UNIVERSITY OF OKLAHOMA

GRADUATE COLLEGE

NUMERICAL SIMULATIONS OF FRACTURE PROPAGATION APPLIED TO PETROLEUM AND GEOTHERMAL RESERVOIR USING FINITE ELEMENT METHOD

A DISSERTATION

SUBMITTED TO THE GRADUATE FACULTY

in partial fulfillment of the requirements for the

Degree of

DOCTOR OF PHILOSOPHY

By

KAI HUANG
Norman, Oklahoma
2015

NUMERICAL SIMULATIONS OF FRACTURE PROPAGATION APPLIED TO PETROLEUM AND GEOTHERMAL RESERVOIR USING FINITE ELEMENT METHOD

A DISSERTATION APPROVED FOR THE
MEWBOURNE SCHOOL OF PETROLEUM AND GEOLOGICAL ENGINEERING

BY

_____
Dr. Ahmad Ghassemi, Chair

_____
Dr. Jamie Rich

_____
Dr. Ahmad Jamili

_____
Dr. Chandra Rai

_____
Dr. Deepak Devegowda

In dedication to my wife Xue and my son Roland and my parents.

Acknowledgements

I would like to express my deepest gratitude to my advisor, McCasland Chair Professor Ahmad Ghassemi, for his advice, guidance and support throughout my study and research at Texas A&M University and University of Oklahoma. I have been fortunate to have a professor who offers freedom to explore, and at the same time the professional guidance and help to crack the difficulties. Without his encouragement and trust this dissertation would never have been accomplished.

I would like also to thank Dr. Jamie Rich, Dr. Ahmad Jamili, Dr. Chandra Rai and Dr. Deepak Devegowda for serving in my thesis committee. I benefited a lot form their pertinent comments and suggestions.

I also want to thank Professor Zhennan Zhang from Shanghai Jiang Tong University, for the support, fruitful discussion and inspiration during the preparation of this dissertation. I greatly appreciate the precious help and encouragement from my past and present colleagues Dr. Jian Huang, Dr. Xiaonan Wang, Dr. Kyoung Min, Yawei Li, Jixiang Huang, Shahla Feizi Masouleh, Varahanaresh Sesetty, Qian Gao, Qinglu Cheng, Jiman Liu, Zhe Ye, who make my Ph.D. study a great experience.

Finally, I would like to thank my wife Dr. Xue Luo, my parents Hao Huang, Naizhen Tao and my parents-in-law Gang Luo, Xiaolan Kang, for their love and continuous trust and encouragement.

Table of Contents

List of Tables

List of Figures

Abstract

Hydraulic fracturing is a major technique in reservoir stimulation to enhance production. Better understanding of mechanisms of hydraulic fracturing is essential for designing hydraulic fracture treatments. Multiple physical processes are involved in hydraulic fracturing propagation and active in determination of the growth of a propagating flow induced fracture. The rock deformation, fracture mechanical responses, fluid flow and thermal diffusion need to be coupled studied to represent the realistic behaviors in the petroleum and geothermal reservoir. In this work, motivated by the limitations of the existing fracture simulators and urgent needs for true 3D hydraulic fracturing model, three-dimensional numerical approaches implemented in finite element method are developed to simulate rock failure and coupled hydraulic and thermal fracture propagation problems.

Due to the complex geological conditions of rock formation such as nonlinearity, anisotropy, heterogeneity and existence of large discontinuity, the behaviors of realistic rock in the reservoir are extremely difficult to be characterized and modeled. Finding a suitable and affordable constitutive model for rocks is a crucial part in the rock mechanics and its applications in petroleum industry. Multi-scale virtual multidimensional internal bonds (VMIB) model and continuum damage model are presented in this work providing solutions from different aspects on solving the nonlinear responses of rock. Moreover, the phenomenon and cause of mesh size sensitivity due to using local strain softening model are introduced. Verified by the simulation results, the mesh size sensitivity is minimized through adopting nonlocal damage theory.

Three dimensional element partition method (3D EPM) is adopted to represent the mechanical behaviors of fracture surface such as contact and friction of closed fracture surfaces. Taking advantage of efficiency and simplicity of 3D EPM, the fracture mechanical response and moving boundary conditions in the hydraulic fracturing process are well represented, especially for true 3D simulation.

Though the fracture process is a fully coupled nonlinear problem, the present dissertation studies the hydraulic and thermal effects separately. The 3D thermal fracture propagation due to transient cooling in quasi-brittle rock is studied using VMIB model combined with 3D EPM. The nonlinearities of mechanical behaviors and thermal parameters of the solid material were captured by introducing nonlinear VMIB model into thermo-mechanical coupled governing equations. On the aspects of fluid flow, poroelastic model and lubrication theory are introduced based on different flow mechanisms. Lubrication theory integrally considered the physical behaviors of both rock formation and fluid. The unknown variables are solved by trial and iterations. Nonlocal damage model and the relative technique are adopted for the first time in hydraulic fracturing simulation. To capture the hydraulic fracture propagation in natural fractured formation, the modified poroelastic model is developed to simulate the hydraulic fracturing especially for the hydraulic fracture problem with complex geometry and boundary conditions such as hydraulic and natural fractures interaction. Though the model needs improvement on the accuracy and stability, the overall tendency of fluid pressure distribution and fracture propagation can be captured considering the computational feasibility and efficiency. The new numerical model is a promising tool for predicting and understanding the complex processes of hydraulic

fracturing and its interaction with natural fractures in unconventional reservoir under finite element method framework.

Chapter 1. Introduction

1.1 Problem Descriptions

Hydraulic fracturing is a stimulation technique that creates fluid induced fracture in the rock matrix by fracturing fluid injection to enhance recovery, which has been widely used in petroleum reservoirs and enhanced geothermal systems. Moreover, nearly all the unconventional gas reservoirs must be hydraulically stimulated to get the commercial feasibility [Valko and Economides, 1995]. Hydraulic fracturing was first experimented in 1947 and then successfully applied commercially in 1949. However, the first hydraulic fracturing was observed and described by [Grebe and Stoesser, 1935; Economids and Nolte, 2000] that the formation was being fractured during acid treatment application in petroleum reservoirs. Each year, varied from low permeability gas and oil reservoirs and naturally fractured reservoirs, thousands of hydraulic fracturing treatments are performed in a wide range of geological formations. Hydraulic fracturing technique is also widely used for other purposes such as in-situ stress measurement [Bredehoeft et al., 1976; Zoback et al., 1992; Hayashi et al., 1997], determination of formation permeability with near wellbore hydraulic fracturing [Bjerrum et al., 1972] and remediation of shallow fine-grained formation [Murdoch and Slack, 2002], etc..

The necessary prediction of the development of fracture geometries helps better design of hydraulic fracturing treatment [Rahman and Rahman, 2010]. The fracture geometries are defined by its length, height, aperture and propagating directions. More important for the naturally fractured reservoir, the interaction and interconnection between the hydraulic and nature fractures along with the geometries eventually impact

the production. However, the complex geological conditions and formations characteristics such as in-situ stress, nonlinearity, anisotropy, heterogeneity and the large discontinuity make hydraulic fracturing problems very difficult to be predicted exactly at greater depths [Gildey et al., 1989]. Therefore, simplified models are used based on the approximated geometries of hydraulic fractures. Although hydraulic fracturing has been implemented for more than 60 years, deeper understandings of the mechanism of fracture propagation in anisotropic and heterogeneous rocks and its interactions with nature fracture or fault are still urgently needed.

Hydraulic fracturing treatments are also common techniques in high temperature petroleum reservoirs and geothermal reservoirs [Sasaki, 1998; Berumen et al, 2000]. The influence of thermo-mechanical processes on fracture initiation and propagation are important to petroleum and geothermal systems development, which result from both the fracturing fluid injection and long term geothermal energy extraction [Wright and Tanigawa, 1994; Ghassemi, 2010]. The fluid injection in the reservoir involves the thermal-poro-chemo-elastic coupled responses that influence the consequent fracture development [Ghassemi et al., 2008]. Cold water injection and heat extraction in the reservoir cause dramatic temperature changes, and then volumetric contraction in the rock. A volumetric expansion or contraction results in rock stress and properties change. The processes of thermal and mechanical coupling occur at various time scales and may have different influences upon the problem of interest. Generally, the thermal effects should be considered during the long term injection owing to low thermal diffusivity of rocks. High tensile stresses are induced by cooling of the rock and fracture surfaces, indicating a potential for extension of the secondary thermal fractures [Bazant and

Ohtsubo, 1979; Tarasovs and Ghassemi, 2014; Feng and Jin, 2009; Tarasovs and Ghassemi, 2011; Huang and Ghassemi, 2012]. There are also experimental investigations [Geyer and Nemat-Nasser, 1982] showing thermally induced cracks in glass. The influence of thermo-poroelastic process on the near wellbore flow and stresses has been addressed analytically [McTigue, 1990] and numerically [Ghassemi and Zhang, 2004; Zhou and Ghassemi, 2009]. In a word, thermal stimulation has been suggested as a means of dramatic thermal stress, deformation change and its induced reservoir conductivity enhancement.

In cases of a homogenous and isotropic formation, the magnitude and orientation of in-situ stress are the dominating factors of hydraulic and thermal fracture propagation. The fracture is intended to grow in the direction of minimum in-situ stress since less restrains and stress to be overcame in this direction. In most conditions of reservoir, the minimum in-situ stress is in horizontal direction because of the high overburden stress in the depth of interest. However, in most cases, the propagation direction in complex geological formation is not only controlled by the in-situ stress. Other impact factors such as heterogeneity and anisotropic rock properties, existing of nature fault and weak plane control the fracture geometry. Therefore, the hydraulic fracturing problem is restricted by the assumption of propagation in horizontal minimum in-situ stress plane. Though two dimensional analyses on horizontal plane provide reasonable suggestions and great computational efficiency, the three dimensional model is necessary for more accurate and realistic simulation. For example, the fracture develops from deviated wellbore needs to consider the near wellbore effects that induce the fracture reorientation and development in a non-planar fracture

geometry [Carter et al., 2000]. Particularly in shale gas reservoir consisted by naturally fractured rock, the hydraulic fracture propagation involves both intact rock fracturing and opening or slip of pre-existing spatially distributed joint that induce tortuous and unpredictable fracture growth.

Therefore, the main objective of this dissertation is to develop a numerical simulator modeling the three dimensional hydraulic and thermal fracture initiation and propagation. The detailed objectives are listed as follows: 1) to find reasonable constitutive models for the rock mass representing the mechanical behavior and failure mechanism; 2) to develop fracture models representing the opening and slippage of fracture surface using three dimensional element partition method; 3) to model the thermally induced rock deformation and fracturing during the cool fluid injection; 4)to build a coupling scheme handling the interaction processes between the mechanical response of rock formation and fluid flow in fracture surface and hence the leakage into formation; and finally 5) to integrate the key points above and develop a reliable numerical simulator for real three dimensional hydraulic and thermal fracturing.

1.2 Modeling Hydraulic and Thermal Fracturing

Massive volume of stimulating fluid are pumped into low permeability rock formation during the hydraulic fracturing treatment in order to create highly conductive propped fracture for channeling and interconnecting storage volume of hydrocarbon. The behavior of hydraulic fracture is initially captured using linear elastic fracture mechanics (LEFM) to calculate the deformations of formation and aperture of fracture. The deformation and opening of rock and fracture are simultaneously used to calculate the fluid flow in the fracture. More importantly, LEFM also serves to calculate the

criterion of propagation and growth direction during the injection. Usually, from the vertical well, the fluid induced fracture has two wings in the direction along the minimum horizontal in-situ stress. Based on this assumed geometry of hydraulic fracture, several fracture propagation models have been proposed. The pioneering models such as Khristianovic-Zheltov [Khristianovic and Zheltov, 1955], Perkins-Kern (PK) [Perkins and Kern, 1961], and Perkins-Kern-Nordgren (PKN)[Nordgren, 1972] adopted the classic elastic solution of plane strain crack by [Sneddon, 1946; Sneddon and Elliot,1946] to solve planar horizontal propagation of hydraulic fracture with constant height and elliptical shape fracture opening including the leak off effects, which are used only when the fracture length is much larger than the fracture height. The Kristonovich-Geertsma-Daneshy (KGD) [Geertsma and de Klerk, 1969] model is used if the fracture height is much larger than the fracture length. The PKN model does not consider the effect of the fracture tips, however, the emphasis is on the fluid flow and pressure gradient. On the other hand, KGD model considered more on the fracture tip region.

A significant amount of analytical solutions have been proposed to provide a better understanding of different mechanisms of fluid-driven fracturing. However, the complexity of hydraulic fractures development due to the uncertainty in subsurface conditions, bring challenges to some classic models such as PKN and KGD model that are based on the assumption of single fracture and homogeneous matrix. Although models such as pseud-3D [Cleary and Wong, 1985] has been developed to simulate a single fracture crossed multiple geological layers, still, the assumption of planar fracture surface limits its application in reservoir with unconventional rock properties such as

mentioned heterogeneity, anisotropy and existing nature joints and faults. These influence facts will change the stress and strain field near hydraulic fractures, hence, induce the irregularity such as curving growth and consequently forming of fracture network.

Fracture propagation problem is not limited to hydraulic fracturing problems in petroleum and geothermal industry. Griffith first explained the failure of brittle materials motivated by the contradictory factors that the stress needed to fracture the bulk glass and theoretical stress needed to break the atomic bonds of the glass [Griffith, 1921 and 1924]. A constant C is expressed in terms of the surface energy of crack by solving a finite crack problem in elastic plate. Griffith initiated the development of linear elastic fracture mechanics (LEFM). There are three basic fracture modes in LEFM classified by the ways of applying loads induce the fracture propagation shown in Figure 1.1. Mode I fracture is opening mode indicating that a tensile stress is applied on the normal direction of the fracture plane. Mode II fracture is in-plane sliding mode under shear load parallel to the fracture plane. Mode III is out-of-plane or tearing mode induced by the shear stress parallel to the crack front. Mode I fracture is the dominate mode of hydraulic fracturing. However, mode II and mode III are equally important since that most fracture are initiated as mixed modes due to that the orientation of initial fracture or perforations are inclined to the direction of maximum in-situ stress. The material anisotropy and existing of nature faults and fractures can also induce mix mode fracture growth.

In the framework of fracture mechanics, the crack propagation is analyzed through the evaluation the mechanical states such as stress intensity factor (SIF) [Irwin,

1948] and strain energy release rate as the fracture propagation and development orientation criterion. The strain energy release rate is the energy dissipation per unit area of newly created fracture. The stress intensity factor is an essential parameter in linear elastic fracture mechanics for integrality evaluation of the magnitude or intensity of singular stress state around the fracture tip by loading [Anderson, 1994], which is usually applied to homogeneous and isotropic material. The strain energy release rate and SIF can be calculated by the stress and strain analysis or the measurement of the energy released by fracture growth through both the analytical and numerical ways. The theoretical concept of J-integral [Rice, 1968, Cherepanov, 1967] represents a solution to calculate the strain energy release rate. The J-integral J presents an energetic contour path integral is independent of chosen path around the fracture tip calculating the strain energy release rate. Later, J is defined as a critical value of fracture energy at large-scale plastic yielding during the fracture extension.

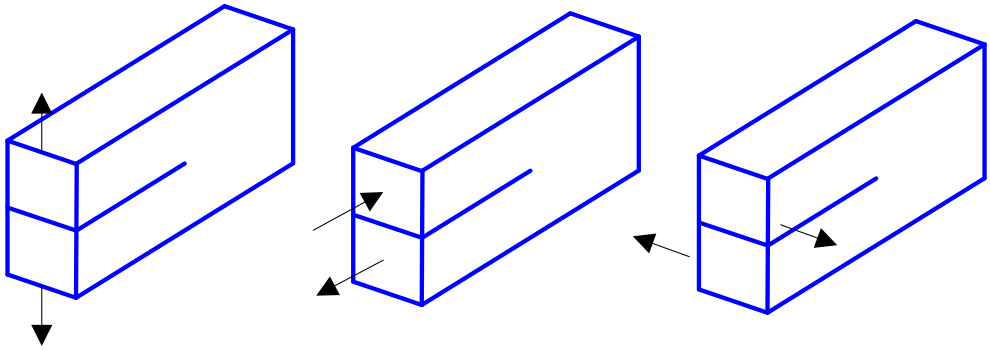

(a) (b) (c)

Figure 1.1. Fracture modes: (a) Mode I: openning; (b) Mode II: sliding; (c) Mode III: tearing [Irwin, 1957].

However, analytical calculation is difficult to be used in the complex and irregular geometries though it has some advantages. On the other hand, the numerical

method requires the mesh refinement to meet the requirement of accuracy of the stress and strain evaluation near the fracture tip. Though several literatures and techniques have been proposed to extract SIF using analytical [Erdogan and Sih,1963, Sih 1974] and numerical analyses by finite element methods or boundary element methods. The requirements for the geometric and boundary conditions make both analytical and numerical methods of SIF calculations very difficult to be performed.

Smeared crack model [Rashid, 1968] was proposed to simulate the quasi-brittle materials like concrete and rock. Generally, a crack is initiated when the stress state satisfies a specified criterion for example the maximum principal stress reaching the tensile strength. A fixed crack orientation is initially assumed. The modified smeared crack models are proposed later [Cope et al., 1980, Gupta and Akbar, 1984, de Borst et al., 2004] using strain soften or strength degrading model instead of the brittle failure. However, the strain softening model is subjected to spurious mesh size sensitivity since that the energy dissipation during the fracture propagation is instable with various chosen element sizes. To solve the element size dependency problem, fictitious crack model is proposed by [Hillerborg, 1976] using fracture energy concept to analyze the fracture growth in concrete. Two regions were defined, which are true crack region and fracture process zone (FPZ). Once the stress of FPZ reached the critical value, the crack propagation in FPZ initiates and the stress level does not drop to zero. As the loading and crack opening displacement (COD) increased, the stress researches zero and cracking process is completed. Blunt crack bond model [Bazant and Oh, 1983] was proposed by introducing a parameter of crack band which is an intrinsic property of specified material. Hence, [Bazant, 1984] introduced nonlinear strain softening curve

into crack band model and found size effect law based on the energy dissipation rate. [Tang, 1997; Tang et al., 2000] adopted damage mechanics model to capture the rock strength degradation during rock failure processes in Weibull distributed [Weibull, 1951] heterogonous rock [Tang et al., 2001]. Realistic fractures pattern was well represented by these models taking advantage of simple and reasonable assumption of strain-stress curve for quasi brittle materials and highly heterogeneity using Weibull distribution. Cohesive crack model [Bilby et al., 1963; Willis, 1967; Elices et al., 2002;], pioneered for concrete named fictitious crack model, has been successfully used to the materials other than concrete including steel and wielded joint [Lin and Heng, 1999] and polymers [Tijssens et al., 2000]. Comparing with other crack model, cohesive crack model is able to predict not only the cracked body but also the behaviors of uncracked and blunt notched material. [Xu and Needleman, 1993] simulated fracture growth using FEM by introducing cohesive surface among the element boundary. The fracture is propagating along mesh boundary and the element keeps intact under loading. The model is well adopted to simulate dynamic fracturing and crack branching.

Several different numerical techniques have been proposed in the past 30 years to solve more complex hydraulically and thermally induced fracture problems. The numerical methods primarily can be classified into several main branches based on the spatial field discretization, which are Finite Element Method (FEM), Boundary Element Method (BEM), Finite Difference Method (FDM) and Discrete Element Method (DEM) etc.. Firstly, BEM is classified into the direct and indirect ones [Kumar, 2013]. The displacement discontinuity method (DDM) is an indirect BEM that has been widely used in the area of fracture mechanics, wellbore stability, hydraulic fracturing [Olsen

and Taleghani, 2009; Weng et al., 2011; McClure, 2012; Sesetty and Ghassemi, 2012, 2013] and thermal fracturing [H. A. Bahr et.al, 1988; Tarasovs and Ghassemi, 2014]. Another popular way is to discretize the whole domain by finite element method (FEM), [Min, 2013] developed coupled thermo-hydro-mechanical FEM model to simulate hydraulic fracture propagation based on brittle damage theory. Besides the mentioned numerical methods, discrete element method (DEM) is also implemented to simulate the hydraulic fracture propagation [Damjanac et al., 2010; Deng, Podgorney and Huang, 2011]. All these models have both advantages and disadvantages when solving different problems of interest. Since that DDM only discretize the fracture, less freedoms of problem significantly save computation volume, especially when simulating a large domain or infinite space. In addition, taking advantage of nature of DDM, hundreds of fractures and their interaction can be simulated in a feasible computational volume [Verde and Ghassemi, 2013]. Nevertheless, DDM still has limitation since that it generates full matrix that requires large storage volume and requires more efficient computational solution for the equation system. Though anisotropic and heterogeneity can be captured by the DDM and BEM, most of DDM analyses assume the rock to be isotropic, homogeneous and elastic solid. The nature of FEM, on the other hand, is to solve the continuum field problem that is easier to capture the inhomogeneity and anisotropy. However, the FEM poses restriction in fracture application and needs special mathematical treatment when fracture or discontinuity in displacement occurred in the field, hence, needs special interpolation and mesh refinement when value concentrate or sharply change at fracture tips for example.

The extended finite element method (XFEM) [Belytschko and Black, 1999; Moes et al., 1999] is a fast growing technique that catches a large amount of attentions. Based on the generalized finite element method and partition of unit method, XFEM extended the classical finite element method by enriching the solution space with discontinuous function for fracture surface and asymptotic function for the fracture tips to partial differential equations. A key advantage of XFEM is that remeshing is not necessary. Moreover, through fracture tips enrichment, singularity of fracture tips can be captured using the original mesh system that increases the accuracy without refining the mesh at the tips. It compensates for the inconvenience of traditional FEM while representing the mechanical properties of the fractured element and the element near the crack tips. However, XFEM has a common disadvantage that its formulations are the typically ill-conditioned system matrix by introducing enrichments representing the displacement discontinuity and fracture tip. Moreover, the tip enrichment as well as the fracture criterion such as calculating J-integral is difficult to implement when fracture propagates irregularly in three dimensional analyses.

On the aspect of material constitutive model, beside the LEFM, many nonlinear models are focused on the damaged or process zone around the fracture tips in quasi-brittle material. Such materials like concrete and rock at the micro scale deform severe nonlinearly because of the heterogeneity and nonlinearity of mechanical properties. The failures in these kinds of materials are accompanied with localization and softening which is manifested by micro-cracking and void formation. Several researchers have studied the concepts of strain softening that are discussed in the following.

The virtual intern bond (VIB) theory introduced by [Gao and Klein, 1998; Klein and Gao, 1998] considering the material softening by multi-scale analysis. VIB considers the solid is discretized into numerous randomized material particles at micro scale. The virtual intern bonds connect the particles. VIB incorporated the fracture criterion directly into the material constitutive formulation that requires no external criteria when simulating fracture propagation. In VIB, only stretch energy potential of bond is considered. [Zhang and Ge, 2005, 2006] introduced virtual multidimensional internal bond (VMIB) extended VIB by considering both stretch and rotation potential energy of bond. The VMIB could represent the different Young's modulus and Poisson's ratio for a wider use of various engineering materials. VMIB model considered that the material is composited the randomized mass particles connected by virtual bond with both normal and shear stiffness. A macro constitutive relation is derived from the cohesive law between material particles that represents the macro nonlinear behaviors.

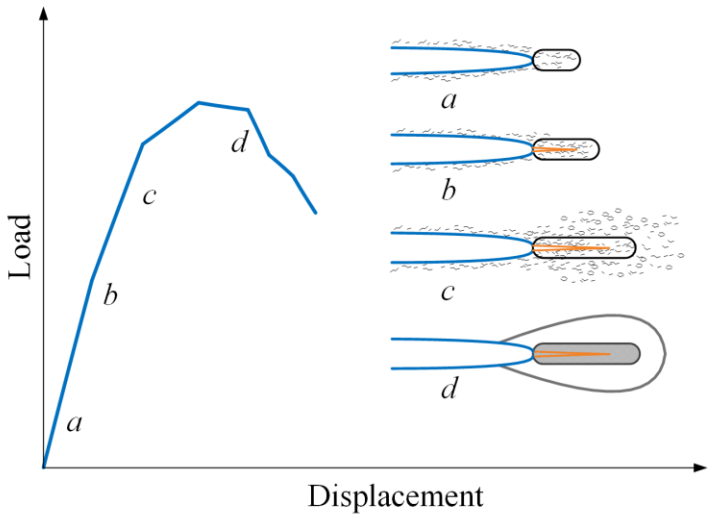

Figure 1.2. Micro-cracking and process zone development identified by acoustic emission in the experiment.

[Kachanov, 1958] initiated the topic of the continuum damage mechanics (CDM) to capture the creeping process of loaded material [Kolari, 2007]. This approach has later been used by several researchers for modeling by choosing a so called damage evolution function. The idea of CDM has significant physical meaning on understanding the inelastic process zone around the crack tip. Contradicting to LEFM, the stress of crack tip in real material cannot be unbounded. The material around the crack tip will proceed into inelastic stage after the elastic limit is reached. Therefore, a process zone always occurs around crack tip where the mechanical response is inelastic interpreted by damage or plastic area. The presence of a long process zone at a crack tip has been observed in many quasi-brittle materials, for example, using acoustic emission [Labuz etc., 1989]. The idea of fracture process zone is shown in Figure 1.2 for Charcoal and Rockville granite. Prior to forming new fracture surface, many micro-cracks gradually develop around crack from status a to c, As the nucleation of micro-cracks, an effective crack or macro fracture is eventually generated shown by the status d in Figure 1.2. However, this localization of strain or damage brings new problems to the CDM approach since that the CDM represent the mechanical behaviors of the damaged and intact parts implicitly in a representative volume that usually controlled by the size of element. It is shown in some numerical experiments that when the strain softening is localized in an infinite small element resulted infinite strain and zero energy dissipation, which contradicts the physics of energy dissipations during fracturing. This phenomenon is called mesh size sensitivity that indicates the results are affected by using different mesh sizes. In order to remedy the mesh size sensitivity of strain-softening in FEM, [Bazant, 1986; Pijaudier-Cabot and Bazant, 1987] proposed nonlocal

formulations for modeling strain softening behavior. Based on nonlocal theory, the stress and strain relation is no longer just considered locally but is assigned to a deformation in a finite volume around the point of interest. In Chapter 2, local and nonlocal continuum damage mechanics will be briefly introduced along with their application in hydraulic fracturing problem in Chapter 7.

1.3 Outlines of the Dissertation

Chapter 1 introduces the basic ideas and developments of hydraulic fracturing, provides detailed literature review of hydraulic fracturing process on the applications and scientific understandings aspects, and discusses the detailed motivations and specific objectives of this research.

Chapter 2 presents the fundamental conceptions and constitutive relationship derivations of virtual multidimensional internal bonds (VMIB) model, the phenomenon and cause of spurious mesh size dependency induced by adopting the strain softening model, and continuum damage mechanics (CDM) for both local and nonlocal formulation, in which nonlocal formulation of damage theory is employed to minimize the mesh size dependency. These constitutive models serve as the significant parts representing the mechanical behaviors of the rock in hydraulic fracturing simulations in the following Chapters.

Chapter 3 introduces the representation of the mechanical response of three dimensional fracture surface using three dimensional element partitioning method (3D EPM). The detailed mathematical derivations and the functional test are given showing that the method effectively represents the behaviors of fracture surface, for example, the surface opening, contacting and slippage.

Chapter 4 presents the methodologies of fluid flow applied in the hydraulic fracturing simulations. Both the mathematical derivations of the fluid flow in the rock formation captured by poroelasticity and fracture surface analyzed by lubrication theory are given. The interaction between the solid and fluid is illustrated and solved by the fully coupled iteration scheme between the deformations of the rock mass and fluid pressure. This chapter also gives the method how to apply the nonlocal damage mechanics in the hydraulic fracturing simulation.

Chapter 5 gives the examples of the numerical simulations for mechanical behaviors of the quasi-brittle materials using virtual multidimensional internal bonds (VMIB) and nonlocal damage mechanics. The results and comparisons with pattern and data from experiments verified these models for the following hydraulic fracturing analyses.

Chapter 6 presents the governing functions for thermal-mechanical coupling processes, shows the simulation results of single thermal fracture propagation, multiple thermal fractures interaction and the fractures emanating from a wellbore by transient cooling induced by long term cold water injection in the borehole.

Chapter 7 presents a series of hydraulic fracturing examples under different in-situ stress states using both VMIB and continuum damage mechanics. The modified poroelastic model is developed to capture both the fracture flow and leak-off during hydraulic fracturing processes. The simulation examples are presented to model the interactions between hydraulic and nature fractures in 3D formation. The influence of anisotropic in-situ stress on propagation direction is also simulated.

Chapter 8 is the summaries and conclusions of this dissertation, and recommendations of future works.

Chapter 2. Constitutive Model of Brittle Rock

Successful capturing the mechanical behaviors of rock is the first and important step for simulating of hydraulic fracturing processes. The basic constitutive law and failure mechanism govern the rock deformation around the fracture tips and therefore determine the fracture initiation and propagation. Generally, various constitutive models such as linear elastic, hyperelatic (nonlinear elastic), elasto-plastic, viscoelastic, damage-plastic, poroelatic, poro-thermo-elastic etc. are adopted to capture the different types of rocks under different conditions. However, the realistic underground rocks are difficult to be characterized since the complex geological conditions and formation such as nonlinearity, anisotropy, heterogeneity and existing of large discontinuity. Moreover, to capture the realistic behavior of rock, more sophisticated constitutive model and failure mechanism are needed, however, lead to insufficient input parameters. In a word, a suitable and affordable constitutive model for the rock is a crucial part in the rock mechanics and its applications in petroleum industry.

In this chapter, virtual multidimensional internal bonds (VMIB) and nonlocal damage theory are briefly described. VMIB model considered that the material is composited by the randomized mass particles connected by virtual bonds with both normal and shear stiffness. According to the concept of VMIB, the macro behavior of material is determined by the bond evolution in micro structure. In other words, a macro constitutive relation derived from the cohesive law between material particles represents the macro nonlinear behaviors. However, from other literatures [Bazant, 1986; Pijaudier-Cabot and Bazant, 1987] and the results of simulation using strain softening model like VMIB, finite element analysis using strain softening model becomes highly

affected by the mesh size and alignment causing non-physical predictions of damage or softening process zone. This phenomenon is so called mesh size dependency or mesh size sensitivity. In this work, the basic conception and mathematical derivation of both local and nonlocal formulation damage mechanics are given. The fundamental theory of damage mechanics is introduced through the local formulation. However, using local formulation, finite element analysis fails to capture energy dissipation due to elemental based strain localization. The energy dissipation becomes unstable since that it is highly affected by the different size of element used in the simulations. Nonlocal formulation abandons the classical assumption that the damage or strength degradation at certain point can only results from the state at the point itself, but the strain-stress state distribution over the whole domain or at least a certain representative volume defined by a characteristic length. The nonlocal damage variable is calculated from a spatial averaging of damage driving force over the representative volume. Therefore, the energy dissipation is no longer controlled by a single element size, but a material constant-the characteristic length.

2.1 Virtual Multidimensional Internal Bonds

2.1.1 Hyperelastic Theory

In the continuum mechanics, a change in the configuration of a continuum body results in displacement. The displacement is composed by rigid-body displacement and deformation. The material points in the undeformed configuration are described by the Lagrangian(Material) coordinates $X = (X_1, X_2, X_3)$. The corresponding material points in the deformed configuration is described by Eulerian (spatial) coordinates $x = (x_1, x_2, x_3)$. The deformation gradient is given by:

$$F_{iI} = \frac{\partial x_i}{\partial X_I} \tag{2.1}$$

From deformation gradient, the Green-Lagrange strain tensor is given by:

$$E_{IJ} = \frac{1}{2}\left(F_{iI}F_{iJ} - \delta_{IJ}\right) \tag{2.2}$$

where δ_{IJ} is the Kronecker delta.

In the hyperelastic theory [Marsden and Hughes, 1983; Ogden, 1984], Φ is the strain energy density function. The Piola-Kitchhoff stress tensor is:

$$S_{IJ} = \frac{\partial \Phi}{\partial E_{IJ}} \tag{2.3}$$

The material elastic tensor is:

$$C_{IJKL} = \frac{\partial S_{IJ}}{\partial E_{KL}} = \frac{\partial^2 \Phi}{\partial E_{IJ}\partial E_{KL}} \tag{2.4}$$

2.1.2 Material Constitution of VMIB

The constitution of material has different representation at different scales, which are continuum based for material at macro scale and the particle based at micro scale, shown as Figure 2.1. The macroscopic mechanical behavior is determined by the material constitution at micro scale. In the VMIB method, the solid is considered as randomized virtual material particles at the micro scale shown in Figure 2.1(b). Virtual internal bonds between the material particles have both normal and shear stiffness as shown in Figure 2.2. The bond constrains both normal displacement and rotation. The interactions of the bonds govern the mechanical response of the material according to the relative displacements of paired particles. These particles and bonds are not necessary to be realistic physical particles such as atom or molecule. In this simplifying of microscopic structure, VMIB avoids the complicated and massive atom simulation.

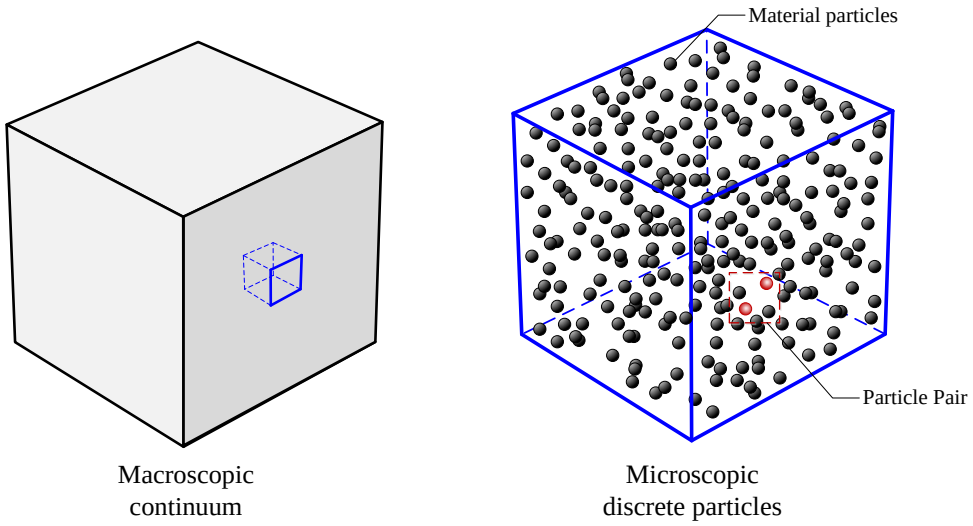

Figure 2.1. Material constitution at (a) macro scale and (b) micro scale consisting of randomized material particles

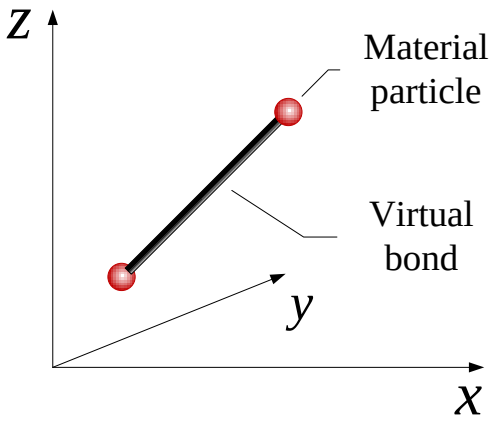

Figure 2.2. Material constitution at (a) macro scale and (b) micro scale consisting of randomized material particles

2.1.3 Relative Displacements and Energy Potentials of Particle Pairs

From micro structure of material, derivation of the macroscopic constitution starts with the relative position and displacements of each virtual particle pair. The relative displacements can be decomposed into bond stretch l and bond rotation with

angle β. Therefore, the virtual bonds between particles are classified as normal bonds and shear bonds due to the different connecting and constraining mechanisms. Normal bonds govern the normal relative displacement and interacting effects of a particle pair. On the other hand, shear bonds restrict the relative rotations. In the small deformation cases, according to Cauchy-Born rule, the stretch of normal bond in $\boldsymbol{\xi}$ direction is

$$l = l_0 \xi_i \varepsilon_{ij} \xi_j \tag{2.5}$$

where l_0 is the original bond length, $\boldsymbol{\xi} = (\sin\theta\cos\phi, \sin\theta\sin\phi, \cos\theta)$ is the unit orientation vector of bond in sphere coordinate system and ε_{ij} is the strain tensor.

The rotation angles of bond towards three coordinate axes are respectively:

$$\begin{cases} \beta_1 = \xi_i \varepsilon_{ij} \eta'_j \\ \beta_2 = \xi_i \varepsilon_{ij} \eta''_j \\ \beta_3 = \xi_i \varepsilon_{ij} \eta'''_j \end{cases} \tag{2.6}$$

where β_1, β_2 and β_3 are the rotation angle towards axis $\mathbf{x}_1$, $\mathbf{x}_2$ and $\mathbf{x}_3$ respectively, $\boldsymbol{\eta}'$, $\boldsymbol{\eta}''$ and $\boldsymbol{\eta}'''$ is the unit vectors perpendicular to the direction indicated by $\boldsymbol{\xi}$ of normal bond. Additionally, $\boldsymbol{\eta}'$, $\boldsymbol{\eta}''$ and $\boldsymbol{\eta}'''$ have to be in same planes determined with their correspondent coordinate axis vectors and $\boldsymbol{\xi}$ respectively. Their mathematical expressions are

$$\begin{aligned} \boldsymbol{\eta}' &= \boldsymbol{\xi} \times (\mathbf{x}_1 \times \boldsymbol{\xi}) \\ &= (\sin^2\theta\sin^2\phi + \cos^2\theta, -\sin^2\theta\cos\phi\sin\phi, -\sin\theta\cos\phi\cos\theta) \end{aligned} \tag{2.7}$$

$$\begin{aligned} \boldsymbol{\eta}'' &= \boldsymbol{\xi} \times (\mathbf{x}_2 \times \boldsymbol{\xi}) \\ &= (-\sin^2\theta\cos\phi\sin\phi, \cos^2\theta + \sin^2\theta\cos^2\phi, -\sin\theta\sin\phi\cos\theta) \end{aligned} \tag{2.8}$$

$$\begin{aligned} \boldsymbol{\eta}''' &= \boldsymbol{\xi} \times (\mathbf{x}_3 \times \boldsymbol{\xi}) \\ &= (-\sin\theta\cos\phi\cos\theta, -\sin\theta\sin\phi\cos\theta, \sin^2\theta) \end{aligned} \tag{2.9}$$

According to two decomposed displacement l and β, the total energy potential U is given as:

$$U = U_l + U_\beta \tag{2.10}$$

where U_l, U_β are the stretch energy potential and rotation potential respectively. U_l and U_β can be written as:

$$U_l = \frac{1}{2} k l^2 = \frac{1}{2} k \left(l_0 \varepsilon_{ij} \xi_i \xi_j \right)^2 \tag{2.11}$$

$$\begin{aligned} U_\beta &= U_{\beta_1} + U_{\beta_2} + U_{\beta_3} \\ &= \frac{1}{2} r \beta_1^2 + \frac{1}{2} r \beta_2^2 + \frac{1}{2} r \beta_2^2 \\ &= \frac{1}{2} \left(\varepsilon_{ij} \xi_i \eta_j' \right)^2 + \frac{1}{2} \left(\varepsilon_{ij} \xi_i \eta_j'' \right)^2 + \frac{1}{2} \left(\varepsilon_{ij} \xi_i \eta_j''' \right)^2 \end{aligned} \tag{2.12}$$

where k is normal bond stiffness, r is the shear bond stiffness coefficient.

2.1.4 Fourth-order Elastic Tensor

The mass particles randomly distribute in the infinitesimal of material according to the assumption above. Therefore, the bonds between the particles are also have randomized distributions and orientations, but following a given spatial distribution density $D(\phi, \theta)$ in the sphere coordinate system. Since the assumption of small deformation cases, E_{IJ} and S_{IJ} reduce to the strain $\boldsymbol{\varepsilon}_{ij}$ and stress σ_{ij} respectively of linear elasticity [Gao and Klein, 1998]. By integrating the total energy potential and assuming the initial length of normal bond is identical, the energy density is written as

$$\Phi = \frac{W_l + W_\beta}{V} \tag{2.13}$$

where V is volume of infinitesimal, W_l is

$$W_l = \int_0^{2\pi}\int_0^{\pi} U_l D(\theta,\phi)\sin(\theta)d\theta d\phi \tag{2.14}$$

, and W_β is

$$\begin{aligned} W_\beta = &\int_0^{2\pi}\int_0^{\pi} U_{\beta_1} D(\theta,\phi)\sin(\theta)d\theta d\phi + \int_0^{2\pi}\int_0^{\pi} U_{\beta_2} D(\theta,\phi)\sin(\theta)d\theta d\phi \\ &+ \int_0^{2\pi}\int_0^{\pi} U_{\beta_3} D(\theta,\phi)\sin(\theta)d\theta d\phi \end{aligned} \tag{2.15}$$

According to Eqs. (2.3) and (2.4), by equaling the energy potential stored in the virtual bonds with the strain energy potential stored on the continuum level in the same volume due to an imposed deformation, the stress tensor is given as:

$$\begin{aligned} \sigma_{ij} = \frac{\partial \Phi}{\partial \varepsilon_{ij}} = &\frac{1}{V}\int_0^{2\pi}\int_0^{\pi} k l_0 \left(\xi_m \varepsilon_{mn} \xi_n\right)\xi_i \xi_j D(\theta,\phi)\sin(\theta)d\theta d\phi \\ &+ \frac{1}{V}\int_0^{2\pi}\int_0^{\pi} r\beta_1 \xi_i \eta_j' D(\theta,\phi)\sin(\theta)d\theta d\phi \\ &+ \frac{1}{V}\int_0^{2\pi}\int_0^{\pi} r\beta_2 \xi_i \eta_j'' D(\theta,\phi)\sin(\theta)d\theta d\phi \\ &+ \frac{1}{V}\int_0^{2\pi}\int_0^{\pi} r\beta_3 \xi_i \eta_j''' D(\theta,\phi)\sin(\theta)d\theta d\phi \end{aligned} \tag{2.16}$$

The fourth-order elastic tensor is written as:

$$\begin{aligned} C_{ijmn} = \frac{\partial^2 \Phi}{\partial \varepsilon_{ij}\partial \varepsilon_{mn}} = &\frac{1}{V}\int_0^{2\pi}\int_0^{\pi} k l_0^2 \xi_i \xi_j \xi_m \xi_n D(\theta,\phi)\sin(\theta)d\theta d\phi \\ &+ \frac{1}{V}\int_0^{2\pi}\int_0^{\pi} r\xi_i \eta_j' \xi_m \eta_n' D(\theta,\phi)\sin(\theta)d\theta d\phi \\ &+ \frac{1}{V}\int_0^{2\pi}\int_0^{\pi} r\xi_i \eta_j'' \xi_m \eta_n'' D(\theta,\phi)\sin(\theta)d\theta d\phi \\ &+ \frac{1}{V}\int_0^{2\pi}\int_0^{\pi} r\xi_i \eta_j''' \xi_m \eta_n''' D(\theta,\phi)\sin(\theta)d\theta d\phi \end{aligned} \tag{2.17}$$

For an isotropic material, the bond distribution density in every direction is uniform, i.e. $D(\theta,\phi)=1$.

In finite element method (FEM), the strain-stress relationship is expressed as:

$$\boldsymbol{\sigma} = \boldsymbol{\Omega} \cdot \boldsymbol{\varepsilon} \tag{2.18}$$

where $\boldsymbol{\sigma}$ is the stress vector, i.e. $\boldsymbol{\sigma} = \left[\sigma_{11}, \sigma_{22}, \sigma_{33}, \sigma_{12}, \sigma_{13}, \sigma_{23}\right]^T$, $\boldsymbol{\varepsilon}$ is the strain vector, i.e. $\boldsymbol{\varepsilon} = \left[\varepsilon_{11}, \varepsilon_{22}, \varepsilon_{33}, \varepsilon_{12}, \varepsilon_{13}, \varepsilon_{23}\right]^T$, and $\boldsymbol{\Omega}$ is the elastic tensor C_{ijmn} written in the elastic matrix form:

$$\boldsymbol{\Omega} = \begin{bmatrix} C_{1111} & C_{1122} & C_{1133} & \frac{1}{2}(C_{1112}+C_{1121}) & \frac{1}{2}(C_{1132}+C_{1123}) & \frac{1}{2}(C_{1113}+C_{1131}) \\ C_{2211} & C_{2222} & C_{2233} & \frac{1}{2}(C_{2212}+C_{2221}) & \frac{1}{2}(C_{2232}+C_{2223}) & \frac{1}{2}(C_{2213}+C_{2231}) \\ C_{3311} & C_{3322} & C_{3333} & \frac{1}{2}(C_{3312}+C_{3321}) & \frac{1}{2}(C_{3332}+C_{3323}) & \frac{1}{2}(C_{3313}+C_{3331}) \\ C_{1211} & C_{1222} & C_{1233} & \frac{1}{2}(C_{1212}+C_{1221}) & \frac{1}{2}(C_{1232}+C_{1223}) & \frac{1}{2}(C_{1213}+C_{1231}) \\ C_{2311} & C_{2322} & C_{2333} & \frac{1}{2}(C_{2312}+C_{2321}) & \frac{1}{2}(C_{2332}+C_{2323}) & \frac{1}{2}(C_{2313}+C_{2331}) \\ C_{1311} & C_{1322} & C_{1333} & \frac{1}{2}(C_{1312}+C_{1321}) & \frac{1}{2}(C_{1332}+C_{1323}) & \frac{1}{2}(C_{1313}+C_{1331}) \end{bmatrix} \tag{2.19}$$

Integrating Eq. (2.17) and substituting to Eq. (2.19) yields

$$\boldsymbol{\Omega} = \begin{bmatrix} 3kl_0^2+2r & kl_0^2-r & kl_0^2-r & 0 & 0 & 0 \\ & 3kl_0^2+2r & kl_0^2-r & 0 & 0 & 0 \\ & & 3kl_0^2+2r & 0 & 0 & 0 \\ & & & kl_0^2+0.5r & 0 & 0 \\ & \textit{symmetric} & & & kl_0^2+0.5r & 0 \\ & & & & & kl_0^2+0.5r \end{bmatrix} \tag{2.20}$$

Equaling Eq. (2.20) with elastic matrix expressed by macroscopic material constants Young's modulus E and Poisson ratio ν, the relationship between microscopic material constants k, r and macroscopic constants can be obtained

$$k = \frac{3EV}{4\pi(1-2\nu)l_0^2} \tag{2.21}$$

$$r = \frac{3EV(1-4\nu)}{4\pi(1+\nu)(1-2\nu)} \tag{2.22}$$

On the contrary, the Young's modulus and Poisson ratio can also be expressed using microscopic material constants k, r, which means the macroscopic mechanical behaviors are determined by the micro bond mechanical properties.

2.1.5 Bond Evolution Mechanism

In the previous sections, the linear VMIB constitutive relationship is derived. For realistic materials such as rocks, normally, the mechanical response can be classified as linear elastic phase, strengthening phase and strain-softening phases as the deformation increases, shown in Figure 2.3. In VMIB system, the bond is not broken when simulating the fracture propagating. The nonlinear macro properties of a material such as softening and degradation are expressed by introducing the strength evolution of internal virtual bonds. Thus, by introducing an evolution function $f(\boldsymbol{\varepsilon})$, the nonlinear elastic tensor is given by:

$$\begin{aligned} C_{ijmn} = \frac{1}{V}\int_0^{2\pi}\int_0^{\pi} f(\boldsymbol{\varepsilon})(kl_0^2\xi_i\xi_j\xi_m\xi_n + r\xi_i\eta_j'\xi_m\eta_n' \\ + r\xi_i\eta_j''\xi_m\eta_n'' + r\xi_i\eta_j'''\xi_m\eta''')D(\theta,\phi)\sin(\theta)d\theta d\phi \end{aligned} \tag{2.23}$$

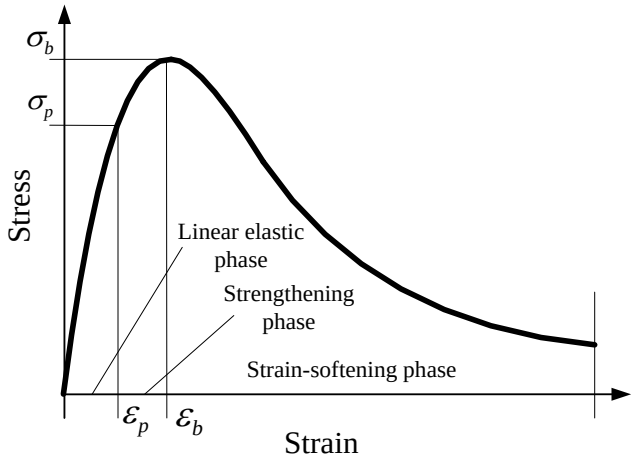

Figure 2.3. Nonlinear mechanical response of material under uniaxial tensile load.

In this work, the strain based evolution function can be written as following:

$$f(\boldsymbol{\varepsilon}) = \exp\left[-c\left(\frac{\left|\boldsymbol{\xi}^T\boldsymbol{\varepsilon}\boldsymbol{\xi}\right|}{\varepsilon_b}\right)^n\right]\cdot\exp\left[-c\left(\frac{\boldsymbol{\xi}^T\boldsymbol{\varepsilon}^T\boldsymbol{\varepsilon}\boldsymbol{\xi}-\left(\boldsymbol{\xi}^T\boldsymbol{\varepsilon}\boldsymbol{\xi}\right)^2}{\varepsilon_b^2}\right)^n\right] \tag{2.24}$$

where ε_b is a micro coefficient, $\varepsilon_b = \varepsilon_t$ if $\boldsymbol{\xi}^T\boldsymbol{\varepsilon}\boldsymbol{\xi} \geq 0$ whereas $\varepsilon_b = \varepsilon_c$ if $\boldsymbol{\xi}^T\boldsymbol{\varepsilon}\boldsymbol{\xi} < 0$. ε_t and ε_c indicate the strain at the peak stress in uniaxial tensile and compressive test, respectively. c , n are the shape coefficients which determine the shape of stress-strain curve. The term $\boldsymbol{\xi}^T\boldsymbol{\varepsilon}\boldsymbol{\xi}$ means the relative normal deformation of bond and the term $\boldsymbol{\xi}^T\boldsymbol{\varepsilon}^T\boldsymbol{\varepsilon}\boldsymbol{\xi}-\left(\boldsymbol{\xi}^T\boldsymbol{\varepsilon}\boldsymbol{\xi}\right)^2$ represents the relative shear deformation of bond shown in the Figure 2.4.

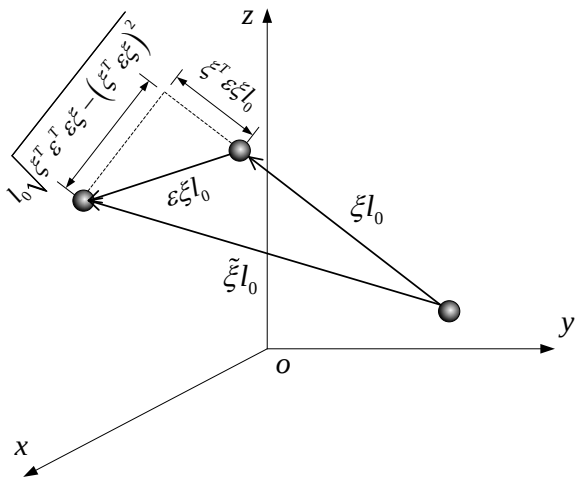

Figure 2.4. Geometrical relationship among undeformed bond vector $\boldsymbol{\xi} l_0$ and deformed bond vector $\tilde{\boldsymbol{\xi}} l_0$

2.1.6 Size Effect and Mesh Size Dependency Associated with VMIB Model

For quasi-brittle materials, the cohesive strength and fracture energy are basic parameters to describe the behaviors of fracture propagation [Park et al., 2008]. It is observed that there is an intermediate region between uncracked and cracked parts

defined as the fracture process zone. The material softening localized in the fracture process zone consumes energy. The relationship between the fracture energy and size of the localization zone has been verified by the experiments. Especially, due to the micro cracks and voids, relatively larger fracture process zone is found in quasi-brittle materials, and results in the difference between the strength measured in laboratory-size sample and the strength of actual structures. This phenomenon is associated with the size effect [Bazant and Planas, 1998]. In addition, in finite element implementation, the size of localization zone is related to the VMIB element size. In other words, in VMIB model, the fracture energy depends on the size of element. This effect is called mesh size dependency or mesh size sensitivity, which is not only found in VMIB model, but also in typical strain softening models. To capture the fracture energy, [Klein and Gao, 1998; Gao and Ji, 2003] introduced the fracture localization zone in virtual internal bond (VIB) model to simulate the fracture process zone of materials. The fracture localization zone is consistent with fracture band model developed by [Bazant and Cedolin, 1979]. As an intrinsic length of materials, the size of fracture localization zone is calculated in conjunction with the J integral.

The bond evolution curve, in this work, is calibrated to match the experiment data for all element size. However, the actual softening curve and fracture energy should integrally consider both the elemental strain-stress curve and the size of fracture process zone (size of element in FEM implements). The quantitative analysis will be highly effected since that the model fails to capture the exact energy dissipation during the fracture propagation. The goal of simulation using VMIB model in present work is to capture the complex mix-mode fracture patterns under shear and compressive

loading. The failure mechanisms and energy dissipation are difficult to be simulated due to the complex strain-stress states and different cracking patterns at locations on the fracture tip in 3D simulation. Nevertheless, the fracture patterns can still be represented by VMIB model verified by the comparison with fracture shape found in the experiments. The quantitative VMIB analysis will be further studied using the concept of fracture localization zone [Klein and Gao, 1998; Gao and Ji, 2003] and the theory of J integral. The present work will employ the nonlocal damage model to capture the fracture energy with an intrinsic characteristic length, in which the size of element does not have to be the size of fracture localization zone that is more convenient for curved fracture propagation.

2.2 Continuum Damage Theory

2.2.1 Local Formulation

Kachanov initially proposed Continuum Damage Mechanics (CDM), to describe creep behavior. Later, it was well adopted to describe the nonlinear responses of various materials due to presence, growth, and nucleation of the micro-cracks and voids. Over 50 years of development, damage theory has been expanded to capture different nonlinear responses in various materials.

To introduce the basic conception of CDM, a cylinder subjected to uniaxial tensile stress is considered and shown in Figure 2.5(a). Initially, in Figure 2.5(b), the material responds elastically and the stress is applied on the original cross section A of cylinder. At this stage, the actual cross section $\overline{A}_1 = A$. As the load is increased, the actual cross section starts to decrease due to appearing of micro crack, namely $\overline{A}_2 < A$ (Figure 2.5(c)). Eventually, at the failure of the cylinder, the actual cross area $\overline{A} = 0$.

The CDM defined the stress applied on the actual cross area $\overline{A}$ as effective stress $\overline{\sigma}_{ij}$, and the stress applied on the initial cross area A as nominal stress σ_{ij}. The force equilibrium yeilds $A\sigma_{ij} = \overline{A}\overline{\sigma}_{ij}$. After rearranging, the relationship between the nominal stress and effective stress are obtained:

$$\sigma_{ij} = \frac{\overline{A}}{A}\overline{\sigma}_{ij} \tag{2.25}$$

Depending on the material property, a scalar/tensor damage parameter or damage density noted as φ / φ_{ij} is used in the CDM to capture the isotropic or anisotropic strengthen degradation, which is normally defined as

$$1-\varphi = \frac{\overline{A}}{A} \tag{2.26}$$

where $\overline{A} = A$ indicates that an intact material is characterized by $\varphi = 0$. Due to the micro fracture initiation and coalescence in the softening process, the effective cross area $\overline{A}$ decreases which results in the growth of damage parameter φ; $\varphi = 1$ indicates complete failure of material with effective cross area $\overline{A} = 0$.

According to the generalized Hooke's law, the effective stress is given by

$$\overline{\sigma}_{ij} = E_{ijkl}\varepsilon_{kl} \tag{2.27}$$

where the variables with bar indicate the ones in the effective configuration.

The strain in the nominal configuration is assumed to be equal to the strain in the effective configuration written as $\overline{\varepsilon}_{ij} = \varepsilon_{ij}$. Thus, combining Eq. (2.25), (2.26) and (2.27) we obtain the constitutive relationship for the nominal stress,

$$\sigma_{ij} = (1-\varphi)E_{ijkl}\varepsilon_{kl} \tag{2.28}$$

Then, to characterize the damage evolution, we can consider strain as damage driving force when calculating damage variable,

$$\varphi = \varphi(\boldsymbol{\varepsilon}) \tag{2.29}$$

To capture the material behaviors during unloading and partial reloading, the damage variable has to be related to the maximum strain reached in the loading history but not to the current strain. Normally, the maximum strain in the history is introduced by a variable κ,

$$\kappa(t_c) = \max_{t \le t_c} \varepsilon(t) \tag{2.30}$$

where t_c is current time.

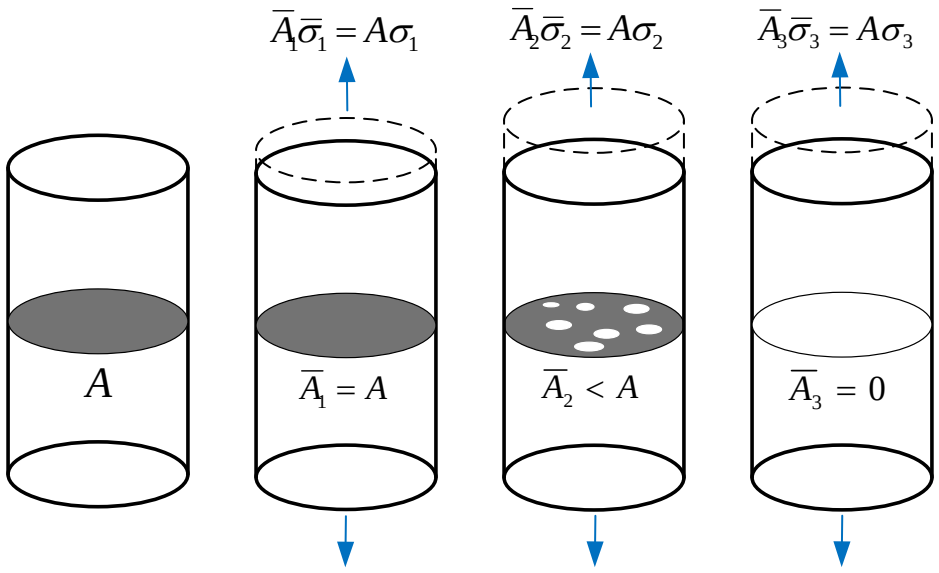

(a) (b) (c) (d)

Figure 2.5. Nominal and effective configuration during damage evolution.

Then, to calculate the damage density, various methods and conceptions are developed. From the uniaxial stress-strain curve, a linear softening damage function $\varphi(\kappa)$ is given by,

$$\varphi(\kappa)=\begin{cases}0 & \text{if } \kappa \le \varepsilon_0 \\ \dfrac{\varepsilon_f}{\varepsilon_f-\varepsilon_0}\left(1-\dfrac{\varepsilon_0}{\kappa}\right) & \text{if } \varepsilon_0 \le \kappa \le \varepsilon_f \\ 1 & \text{if } \varepsilon_f \le \kappa \end{cases} \tag{2.31}$$

and an exponential softening with,

$$\varphi(\kappa)=\begin{cases}0 & \text{if } \kappa \le \varepsilon_0 \\ 1-\dfrac{\varepsilon_0}{\kappa}\exp\left(-\dfrac{\kappa-\varepsilon_0}{\varepsilon_f-\varepsilon_0}\right) & \text{if } \varepsilon_0 \le \kappa \end{cases} \tag{2.32}$$

where ε_0 is the strain at the peak stress indicates when does the damage start to occur. ε_f controls the slope of the post-peak curve that determines the ductile or brittle response the material will perform. Figure 2.6 shows the diagram of strain-stress with linear and exponential softening.

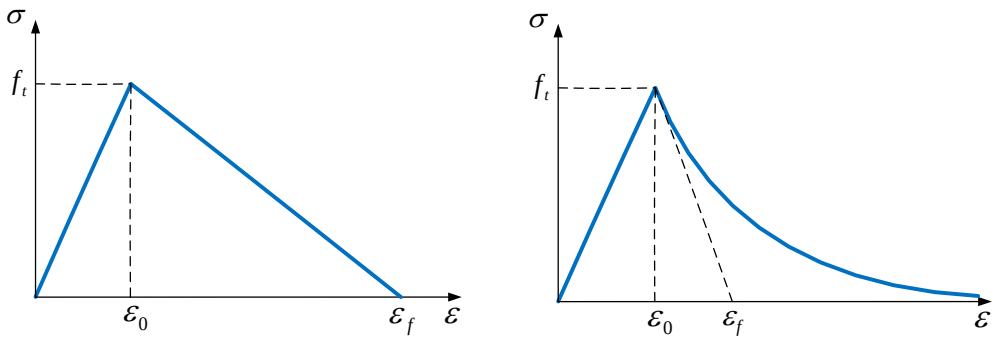

(a) (b)

Figure 2.6. The diagram of strain-stress with (a) linear and (b) exponential softening.

For more complicated loading path or various confining stresses, κ defined above is not a sufficient driving force of damage. Followed with the procedure analogous to the classic plasticity theory, similar driving forces Y in Von Mises, Drucker-Prager forms [Abu Al-Rub and Voyiadjis, 2003] are employed into damage

mechanics. A damage surface function is used to identify damage initiation under current stress-strain states. Then, damage density can be determined by damage flow analogous to plasticity flow rule.

2.2.2 Mesh size sensitivity

In local continuum damage theory, however, the basic assumption is expressed by the micro-cracks and voids are homogenized in an implicit way within a representative volume that usually is the element size in the finite element implement. Since one element size is the minimum representative volume for local damage theory, the damage and softening usually localized in a narrow region that is controlled by the size of the element. Therefore, finite element analysis became highly affected by the mesh size and alignment causing non-physical predictions of damage area.

This phenomenon is so-called mesh size sensitivity [Bazant and Planas, 1998] or mesh size dependency. It has been discussed in numerical results from a spring system with total length L shown in Figure 2.7(a). Figure 2.7(b) shows the softening behavior of a single spring by stretching. Figure 2.8 shows the displacement-force curves from different number of springs used in the system. The post-peak behaviors therefore depend on the number of springs in the system. When n springs are used, the post-peak curve will snap back to $\frac{3}{n}u_0$. The tendency of post-peak curve is turning back to the original point if the number of springs n goes infinite. Additionally, when n approaches zero, the area covered by displacement-force curve and horizontal axial indicating the energy dissipation during the whole loading and failure process tends to be zero, which is physically unrealistic.

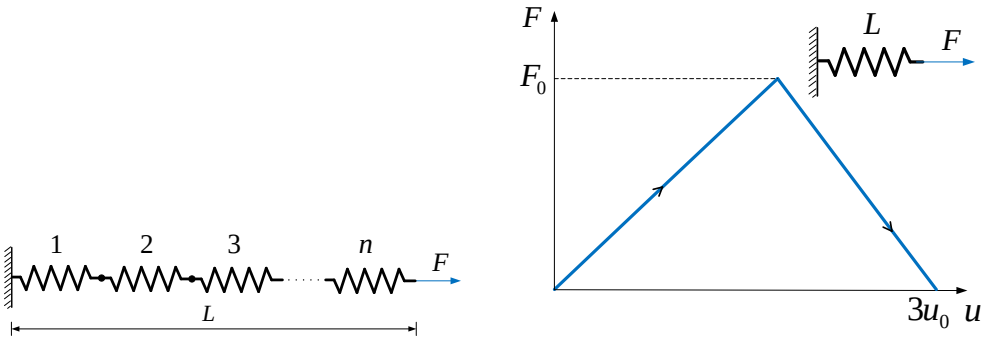

(a) (b)

Figure 2.7. (a) Softening behavior of a single spring; (b) spring system [Bazant and Planas, 1998].

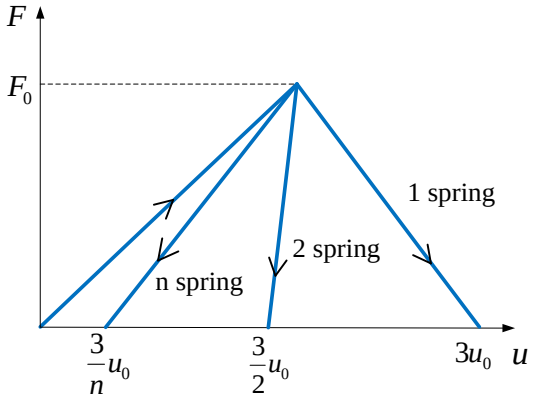

Figure 2.8. Displacement-force diagrams from different number of springs in the system [Bazant and Planas, 1998].

[Jirasek, 2004] presented another mesh size dependency example by modeling three-point-bending test with different element sizes shown in Figure 2.9. The results show that different mesh sizes deliver different results following with the tendency that the smaller element results in weaker strength and smaller envelop. Figure 2.10 illustrates the damage localization in different mesh size during fracture propagation in notched specimen under tensile loading using local CDM. It provides more straightforward expression that the damage or micro crack is implicitly homogenized

within an element in the finite element implement and the damage zone is represented by damage element in local continuum damage theory.

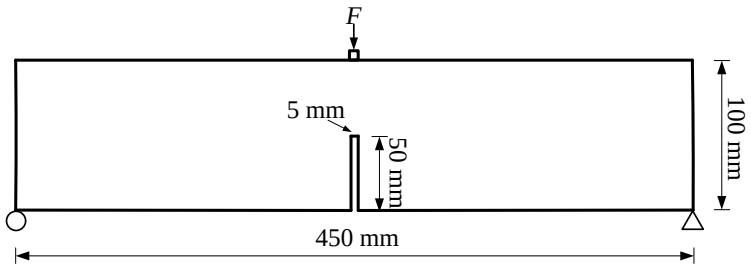

(a)

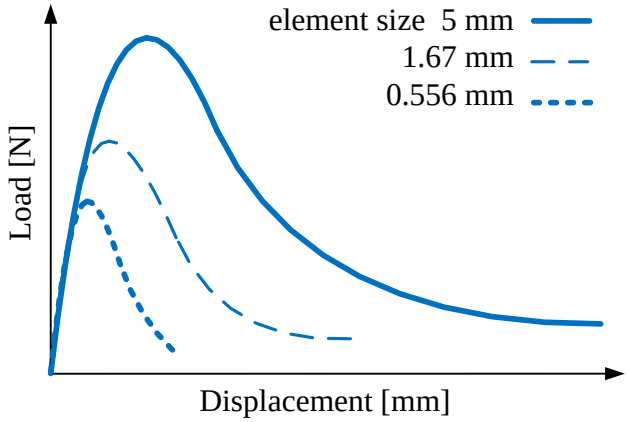

(b)

Figure 2.9. Three-point-bending test simulations with three different mesh sizes: (a) problem geometry and boundary condition; (b) load-displacement curves [Jirasek, 2004].

For quasi-static loading conditions, by including the effect of damage from the surrounding region on the point of interest, a physically meaningful solution can be obtained by enhancing the local damage models by nonlocal measures or homogenizations, which is so called nonlocal average method that will be discussed in the following sections.

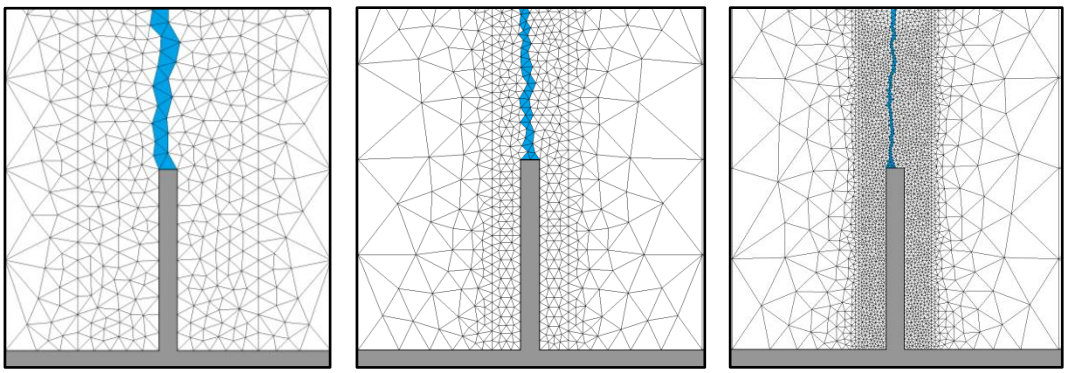

(a) (b) (c)

Figure 2.10. Illustrations of Damage localization (in blue color) in different size meshes: (a) 5mm; (b) 2.5mm; (c) 1mm.

2.2.3 Nonlocal Formulation

For heterogonous materials like concrete and rock, the mathematical and numerical models of failure must correctly represent the energy dissipated in the fracture process zone. Using local formulation, finite element analysis fails to capture energy dissipation due to strain localization. Nonlocal model abandons the classical assumption that damage or strength degradation at certain point can only result from the mechanical state at the point itself, but the strain-stress state distribution over the whole domain or at least a certain representative volume defined by a characteristic length. The principal idea of nonlocal damage theory is that the nonlocal damage variable is calculated from a spatial averaging of damage driving force over the representative volume [Bazant 1986, Pijaudier-Cabot and Bazant 1987]. The nonlocal driving force is written as,

$$\bar{Y} = \frac{1}{V_r}\int_{V_r} w(\xi) Y(x+\xi) dV \tag{2.33}$$

where Y is the damage driving force, which could simply be strain or Von Mises stress in effective configuration for example, V_r is the representative volume governed by the characteristic length collaborated from the experiment, $\overline{Y}$ is the nonlocal averaged damage driving force, $w(\xi)$ is the weight function depends only on the distance ξ to the interest point x within the representative volume. The weight function satisfies the normalizing condition [Bazant and Jirasek, 2002]

$$\frac{1}{V_r}\int_{V_r} w(\xi)dV = 1 \tag{2.34}$$

$w(\xi)$ is expressed in Gauss distribution form

$$w(r) = \frac{1}{l_c\sqrt{\pi}} e^{-\left(\frac{r}{l_c}\right)^2} \tag{2.35}$$

or the quartic polynomial function

$$w(r) = \begin{cases} 0 & \text{if } r > R \\ \left(1-\frac{r^2}{R^2}\right) & \text{if } r \le R \end{cases} \tag{2.36}$$

where l_c is the characteristic length and R is a parameter related to l_c. R is 2~3 times of l_c [Jirasek, 2004].

In finite element analysis, since the field equations have already been discretized into weak form, the averaging and nonlocalization process can be expressed by weighted summing up of values on Gauss points in each region from the following formula [De Vree et al., 1995],

$$\overline{Y}^k = \sum_{i=1}^{nip} \alpha^i J^i w^{ki} Y^i \tag{2.37}$$

where α^i, J^i are the integration weight and Jacobian of isoparametric transformation for number i th Gauss point respectively, and w^{ki} is the weight for nonlocal averaging of i th point respect to point k

$$w^{ki} = \frac{w\left(\left\|\mathbf{x}^k - \mathbf{x}^i\right\|\right)}{\sum_{m=1}^{nip} \alpha^m J^m w\left(\left\|\mathbf{x}^k - \mathbf{x}^i\right\|\right)} \tag{2.38}$$

Then substitute Eq. (2.33) into the constitutive equation Eq. (2.28) yields

$$\sigma_{ij} = (1-\varphi(\bar{Y}))E_{ijkl}\varepsilon_{kl} \tag{2.39}$$

and its tangential form to calculate the incremental stresses,

$$\dot{\sigma}_{ij} = (1-\varphi(\bar{Y}))E_{ijkl}\dot{\varepsilon}_{kl} - \dot{\varphi}(\bar{Y})E_{ijkl}\varepsilon_{kl} \tag{2.40}$$

The weighted summing up brings computational difficulties in the simulation specially expressed by tangential form since time derivative will induce complicated expansion of equation when many time dependent variable involved [De Vree etc., 1995]. Therefore, researchers also introduced the techniques from plasticity research-gradient enhanced theory [de Borst et al., 1993]. $\varphi(x+\xi)$ is expanded into a Taylor series around the point $x=0$ and assuming an isotropic weighting function $w(\xi)$, which results in disappearing of higher-order gradients with odd orders. By neglecting higher than second-order terms, the following expression for $\bar{\varphi}$ can be derived as

$$\bar{\varphi} = \varphi + l^2\nabla^2\varphi \tag{2.41}$$

Eq. (2.41) provides a more straightforward expression of nonlocal damage model. Although calculating average formulas in Eq. (2.37) and (2.38) is a time consuming process associated with the number of element. Fortunately, it can be

calculated once at the beginning since the average formulas are static during the loading process.

2.3 Conclusion

Though the behavior of realistic rock in the reservoir is extremely difficult to be characterized and modeled, multi-scale VMIB model and continuum damage model presented in this chapter provide solutions from different aspects on solving the nonlinear response of rock. The VMIB stem from the discrete microstructure, but eventually turns out the continuum constitutive relationship since that the mechanical properties of the material particles are assembly obtained through statistical averaging. The statistical averaging is very important in reducing the degrees of freedom. On the other hand, the deformation and softening of individual bond are considered integrally and may be diminished, which is proved to be important during the fracture process [Zhang, 2013]. In Chapter 5, the fracture propagation under pure mechanical loading are simulated to test the performance of VMIB on mix mode fracture propagation. Using VMIB model, a three dimensional thermal fracturing model is developed in Chapter 6 and a series of hydraulic fracturing examples are simulated under different in-situ stress conditions in Chapter 7.

Continuum damage model considers the strength degradation resulting from the micro crack and void growth in a representative volume. The nonlocal formulation of damage model for softening materials eliminates spurious mesh size sensitivity and insures proper convergence. Essentially, the nonlocal formulation is to average the energy release rate during damage process over the representative volume of the material. The size of representative volume is governed by the characteristic length l_c

that is an intrinsic property of the material. Consequently, the dissipated energy due to strain-softening damage converges to a finite value. It is physically meaningless and unrealistic that local finite element model with strain softening energy converges to zero as the mesh size approaches infinity small. The characteristic length l_c is a material property related to the size of the process zone due to inhomogeneity, which must be determined and corroborated by results of experiments. Averaging of damage can be introduced in any nonlinear finite element simulation with a strain-softening constitutive model.

However, the determination of material parameters like the characteristic length l_c is still challenging. Beside, though the mesh dependency can be eliminated by using nonlocal theory, the element size is limited to be several times smaller than the characteristic length l_c. In other words, finer mesh is still needed to match the characteristic length l_c in the scale of millimeter or centimeter. If the size of element is larger than characteristic length, the nonlocal averaging treatment is mathematically meaningless. Using nonlocal damage theory in simulating hydraulic fracture, a special treatment of boundary condition on the hydraulic fracture surface is needed. Considering the computational volume, to simulate larger domain, adaptive mesh solution is urgently recommended. In Chapter 4, the detail method of applying nonlocal formulation damage theory in hydraulic fracturing simulation is presented. To verify the nonlocal damage model on minimizing mesh size sensitivity, mode I and mode II fracture examples are presented in Chapter 5. Chapter 7 gives the simulation results of hydraulic fracturing using nonlocal damage model.

Chapter 3. Three Dimensional Representation of Fracture Using Element Partition Method

One of the challenges for 3D fracture simulation is the mechanical representation of pre-existing and newly extended fracture surfaces. Propagating fracture geometry associated with the moving boundary conditions through fracture growth path makes hydraulic fracturing modeling especially difficult. Additionally, besides the opening fracture, the contact and friction of closed fracture surface are also significant mechanical behaviors for pre-existed fracture subjected to the compressive and shear stresses. Several special treatments for fracture surface have been used in the fracture modeling in the framework of finite element method. Remeshing and mesh refining for the newly extended fracture surface and tip are common techniques, which have great advantages on the computational accuracy and efficiency on the linear equation system solving. However, the remeshing and refining scheme implements are difficult to be performed since that it is time consuming and mathematically challenging especially for 3D problems with complex domain and fracture geometry. Extended finite element method (XFEM) [Belytschko and Black, 1999; Moes et al., 1999] based on the generalized finite element method and partition of unit method represents the fracture by enriching the solution space with discontinuous function for fracture surface and asymptotic function for the fracture. The XFEM avoids the remeshing problem and captures the stress singularity using the original mesh system, which compensates the inconvenience of traditional FEM. However, the XFEM still has disadvantage that the added degrees of freedom change the original structure of matrix and sparseness,

numerical integration for each divided parts of element is time consuming and difficult particularly for the element contains multiple fractures.

Different from the XFEM, taking advantage of simple geometry character of triangle and tetrahedron element, element partitioning method (EPM) [Zhang and Chen, 2008, 2009; Huang and Zhang, 2010] construct triple-node and quad-node contact element that needs no remeshing and mesh refinement during the fracture propagation and uses original mesh configuration during the fracture propagation. Therefore, the greatest advantage of EPM saves computational time and is easier to encode since that EPM introduces no additional degree of freedom and global matrix structure remains the same. However, EPM has a limitation that the elastic deformation of partitioned element is not considered. The error is arising with increase of element size . Comparing the computational cost with the other fracture treatment techniques, EPM is still more desirable since that the simulating domain and element size chosen is relative small. In the functional test, performance of 3D EPM will be tested on representing mechanical behaviors of the closed fracture surface subjected to the compressive and shear stress.

3.1 General Idea of Element Partition Method

[Zhang and Chen, 2008, 2009] developed the two-dimensional element partition method (2D EPM) to represent the mechanical behaviors of fractured element cut through by pre-existing and newly extended fracture. Taking advantages of the simple geometrical characteristic of three-node triangular element, the stiffness matrix for a partitioned element is derived to account for the contact and friction effects between fracture faces. Through 2D EPM, the fracture could be represented by transferring intact

element to partitioned element. Since the partitioned element shares the same nodes with intact element, no mesh modification is needed. Based on similar concept, 3D element partition method (3D EPM) is developed by [Huang and Zhang 2010] to describe the opening, contact and friction between the fracture surfaces. The 3D EPM takes advantage of the geometry features of tetrahedron element to construct a four-node contact element. When a fracture cuts through a tetrahedron element, two types of four-node contact element, i.e., Type I and Type II, are formed shown as Figure 3.1. Tetrahedron element is chosen because of its geometric simplicity. Therefore, only type I and II of the contact element with triangular and quadrilateral fracture sections, respectively, will be generated, which avoids the complexity from more types of partition element to be identified and calculated. The geometry aspects will be discussed in the follow sections.

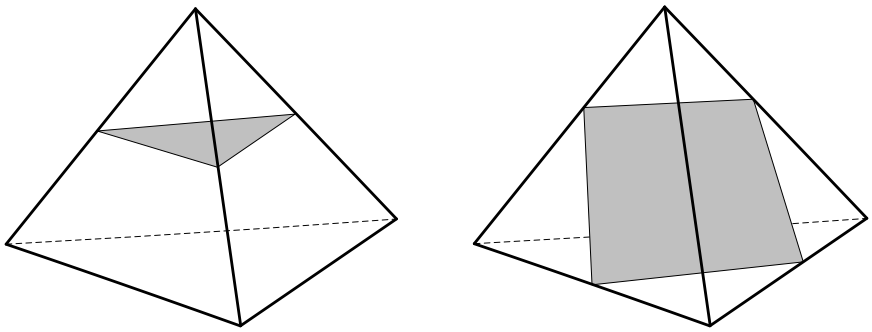

(a) (b)

Figure 3.1. Partition modes of tetrahedron element: (a) type I: triangular fracture plane; (b) type II: quadrilateral fracture plane.

3.2 Derivation of Stiffness Matrix for 3D EPM

To derive the stiffness matrix of 3D EPM, taking type I partition element shown in Figure 3.2 for example, a local coordinate system needs to be established. The original point, x' and y' axis of the coordinate system are on the fracture plane. The z'

axis is perpendicular to the fracture plane. Therefore, the local coordinates x', y' and z' are defined as:

$$
\begin{aligned}
x' &= \left[-\frac{n_1 n_3}{\sqrt{1-n_3^2}}, -\frac{n_2 n_3}{\sqrt{1-n_3^2}}, \sqrt{1-n_3^2} \right] \\
y' &= \left[-\frac{n_2}{\sqrt{1-n_3^2}}, -\frac{n_1}{\sqrt{1-n_3^2}}, 0 \right] \\
z' &= \left[n_1, n_2, n_3 \right]
\end{aligned}
\tag{3.1}
$$

where (n_1, n_2, n_3) is the unit vector indicating the normal direction of the fracture plane calculated by the plane equation $n_1(x-x_0)+n_2(y-y_0)+n_3(z-z_0)=0$. (x_0, y_0, z_0) is the center point on the fracture plane.

The following assumptions are made to derive the stiffness matrix of 3D EPM: (i) all the strain energy is stored in a contact volume with the thickness h and the area A shown in Figure 3.3 if the fracture surface is subjected to compression and shear stress; (ii) the contact volume is linear elastic; (iii) the displacements of points m', m'' and m''' are equal to the displacements of node M, the displacements of point i, j and k are equal to the displacements of I, J and K respectively; (iv) the contact areas $A_{im'}$, $A_{jm''}$ and $A_{km'''}$ shown in Fig. 3 are controlled by contact pairs $i-m'$, $j-m''$ and $k-m'''$ respectively. The displacements of nodes I, J, K and M are denoted as u_x^I, u_y^I, u_z^I, u_x^J, u_y^J, u_z^J, u_x^K, u_y^K, u_z^K, u_x^M, u_y^M and u_z^M respectively.

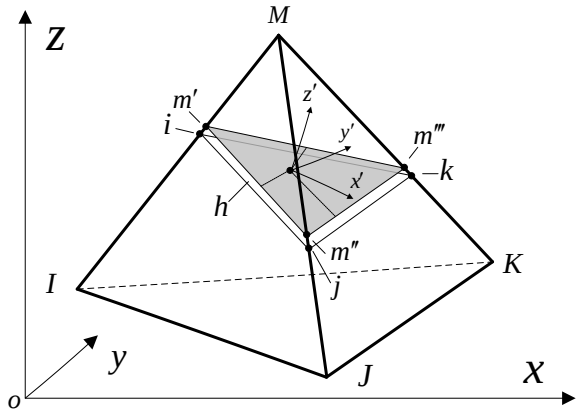

Figure 3.2. Local coordinate system and node pairs for type I partition element.

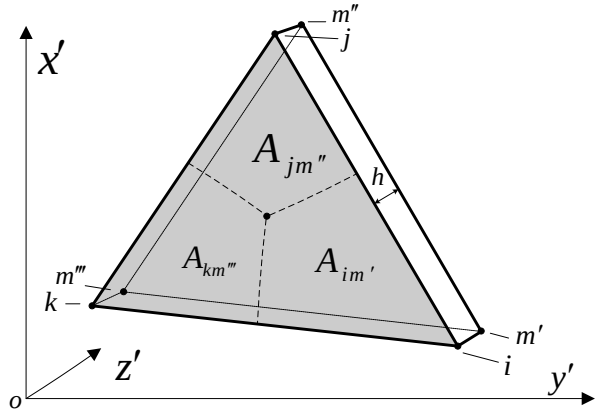

Figure 3.3. Contact volume and contact areas for each node pairs (type I).

Based on a special case that local and global coordinate systems are parallel to each other, the strain energy stored in the contact volume is:

$$W_{im'} = \frac{1}{2} K_n \varepsilon_n^{im'2} A_{im'} h + \frac{1}{2} K_s \varepsilon_s^{im'2} A_{im'} h = \frac{1}{2} \frac{\left(u_z^M - u_z^I\right)}{h} K_n \frac{\left(u_z^M - u_z^I\right)}{h} A_{im'} h$$
$$+ \frac{1}{2} \frac{\left(u_y^M - u_y^I\right)}{h} K_s \frac{\left(u_y^M - u_y^I\right)}{h} A_{im'} h + \frac{1}{2} \frac{\left(u_x^M - u_x^I\right)}{h} K_s \frac{\left(u_x^M - u_x^I\right)}{h} A_{im'} h \tag{3.2}$$

where K_n, K_s are the shear and the normal stiffness coefficients of the contact element respectively. $\varepsilon_n^{im'}$, $\varepsilon_s^{im'2}$ are the normal strain and shear strain of the contact area $A_{im'}$.

Similarly, the strain energy stored in the contact areas $A_{jm''}$ and $A_{km'''}$ are

$$W_{jm''} = \frac{1}{2} K_n \varepsilon_n^{jm''2} A_{jm''} h + \frac{1}{2} K_s \varepsilon_s^{jm''2} A_{jm''} h = \frac{1}{2} \frac{\left(u_z^M - u_z^J\right)}{h} K_n \frac{\left(u_z^M - u_z^J\right)}{h} A_{jm''} h$$
$$+ \frac{1}{2} \frac{\left(u_y^M - u_y^J\right)}{h} K_s \frac{\left(u_y^M - u_y^J\right)}{h} A_{jm''} h + \frac{1}{2} \frac{\left(u_x^M - u_x^J\right)}{h} K_s \frac{\left(u_x^M - u_x^J\right)}{h} A_{jm''} h \tag{3.3}$$

$$W_{km'''} = \frac{1}{2} K_n \varepsilon_n^{km'''2} A_{km'''} h + \frac{1}{2} K_s \varepsilon_s^{km'''2} A_{km'''} h = \frac{1}{2} \frac{\left(u_z^M - u_z^K\right)}{h} K_n \frac{\left(u_z^M - u_z^K\right)}{h} A_{km'''} h$$
$$+ \frac{1}{2} \frac{\left(u_y^M - u_y^K\right)}{h} K_s \frac{\left(u_y^M - u_y^K\right)}{h} A_{km'''} h + \frac{1}{2} \frac{\left(u_x^M - u_x^K\right)}{h} K_s \frac{\left(u_x^M - u_x^K\right)}{h} A_{km'''} h \tag{3.4}$$

where $A_{im'} = A_{jm''} = A_{km'''} = \frac{1}{3} A$, A is the area of fracture plane contained in the partition element.

To capture the opening, contact and slippage of the fracture plane in the partition element, two different conditions are considered. The first condition is that the fracture surface is free to open if it is subjected to tensile stress. The second one is that the fracture surface keeps the normal strength and surface friction to support the closure and represent the slippage resistance respectively, when the fracture is subjected to compressive and shear stresses. Therefore, the total strain energy stored in the contact volume is derived as:

$$W = W_{im'} H\left(u_z^M - u_z^I\right) + W_{jm''} H\left(u_z^M - u_z^J\right) + W_{km'''} H\left(u_z^M - u_z^K\right) \tag{3.5}$$

where $H(x) = \begin{cases} 1 & x \le 0 \\ 0 & x > 0 \end{cases}$. $x \le 0$ indicates the fracture is closed, $x > 0$ indicates the fracture is opened.

Substituting Eqs. (3.2), (3.3) and (3.4) into Eq. (3.5) yields

$$W=\frac{A_{im'}}{2h}\left[K_n\left(u_z^M-u_z^I\right)^2+K_s\left(u_y^M-u_y^I\right)^2+K_s\left(u_x^M-u_x^I\right)^2\right]H\left(u_z^M-u_z^I\right)$$
$$+\frac{A_{jm''}}{2h}\left[K_n\left(u_z^M-u_z^J\right)^2+K_s\left(u_y^M-u_y^J\right)^2+K_s\left(u_x^M-u_x^J\right)^2\right]H\left(u_z^M-u_z^J\right) \quad (3.6)$$
$$+\frac{A_{km'''}}{2h}\left[K_n\left(u_z^M-u_z^K\right)^2+K_s\left(u_y^M-u_y^K\right)^2+K_s\left(u_x^M-u_x^K\right)^2\right]H\left(u_z^M-u_z^K\right)$$

For sake of simplicity, the displacements of element nodes are written as:

$$u_i=\left[u_1,u_2,u_3,u_4,u_5,u_6,u_7,u_8,u_9,u_{10},u_{11},u_{12}\right] \quad (3.7)$$

$$F_i=\left[F_1,F_2,F_3,F_4,F_5,F_6,F_7,F_8,F_9,F_{10},F_{11},F_{12}\right] \quad (3.8)$$

where $u_1=u_x^I, u_2=u_y^I, u_3=u_z^I, u_4=u_x^J, u_5=u_y^J, u_6=u_z^J, u_7=u_x^K, u_8=u_y^K, u_9=u_z^K,$

$u_{10}=u_x^M, u_{11}=u_y^M, u_{12}=u_z^M$ and $F_1=F_x^I, F_2=F_y^I, F_3=F_z^I, F_4=F_x^J, F_5=F_y^J, F_6=F_z^J$

$, F_7=F_x^K, F_8=F_y^K, F_9=F_z^K, F_{10}=F_x^M, F_{11}=F_y^M, F_{12}=F_z^M$.

Using the new notation, Eq. (3.6) can be written as:

$$W=\frac{A_{im'}}{2h}\left[K_n\left(\delta_{12i}u_i-\delta_{3i}u_i\right)^2+K_s\left(\delta_{11i}u_i-\delta_{2i}u_i\right)^2+K_s\left(\delta_{10i}u_i-\delta_{1i}u_i\right)^2\right]H\left(u_{12}-u_3\right)$$
$$+\frac{A_{jm''}}{2h}\left[K_n\left(\delta_{12i}u_i-\delta_{6i}u_i\right)^2+K_s\left(\delta_{11i}u_i-\delta_{5i}u_i\right)^2+K_s\left(\delta_{10i}u_i-\delta_{4i}u_i\right)^2\right]H\left(u_{12}-u_6\right) \quad (3.9)$$
$$+\frac{A_{km'''}}{2h}\left[K_n\left(\delta_{12i}u_i-\delta_{9i}u_i\right)^2+K_s\left(\delta_{11i}u_i-\delta_{8i}u_i\right)^2+K_s\left(\delta_{10i}u_i-\delta_{7i}u_i\right)^2\right]H\left(u_{12}-u_9\right)$$

where δ_{ij} is the Kronecker delta.

The complementary energy Φ is

$$\Phi=W-u_iF_i \quad (3.10)$$

According to the principle of minimum complementary energy in the elasticity theory, the stiffness matrix of type I partition element is derived as:

$$K_{ij}^{(I)} = \frac{\partial^2 \Phi}{\partial u_i \partial u_j}$$

$$= \frac{A_{im'}}{h}\left[K_n(\delta_{12i}-\delta_{3i})(\delta_{12i}-\delta_{3i}) + K_s(\delta_{11i}-\delta_{2i})(\delta_{11i}-\delta_{2i}) + K_s(\delta_{10i}-\delta_{1i})(\delta_{10i}-\delta_{1i})\right]H(u_{12}-u_3) \qquad (3.11)$$

$$+ \frac{A_{jm''}}{h}\left[K_n(\delta_{12i}-\delta_{6i})(\delta_{12i}-\delta_{6i}) + K_s(\delta_{11i}-\delta_{5i})(\delta_{11i}-\delta_{5i}) + K_s(\delta_{10i}-\delta_{4i})(\delta_{10i}-\delta_{4i})\right]H(u_{12}-u_6)$$

$$+ \frac{A_{km'''}}{h}\left[K_n(\delta_{12i}-\delta_{9i})(\delta_{12i}-\delta_{9i}) + K_s(\delta_{11i}-\delta_{8i})(\delta_{11i}-\delta_{8i}) + K_s(\delta_{10i}-\delta_{7i})(\delta_{10i}-\delta_{7i})\right]H(u_{12}-u_9)$$

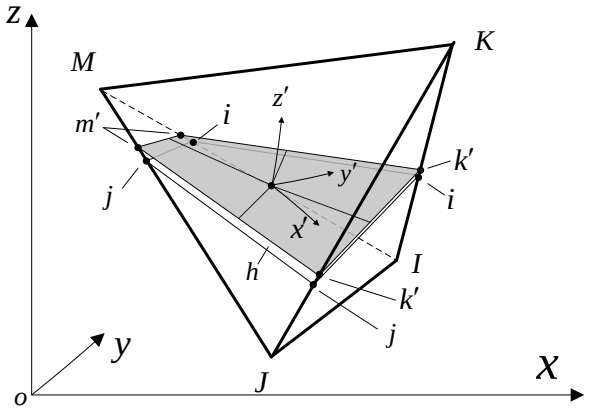

Figure 3.4. Local coordinate system and node pairs for type II partition element.

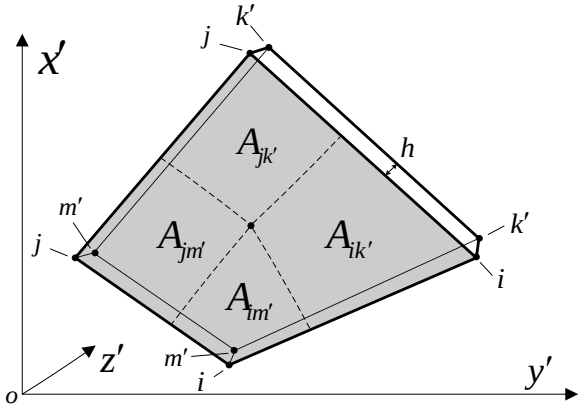

Figure 3.5. Contact volume and contact areas for each node pairs (type II).

Similarly, Figure 3.4 shows the local coordinate system and node pairs for type II partition element. The contact node pairs such as $i-m'$, $j-m', i-k'$ and $j-k'$ control their contact areas $A_{im'}$, $A_{jm'}, A_{ik'}$ and $A_{jk'}$ respectively shown in Figure 3.5. The stiffness matrix of type II partition is derived as

$$
\begin{aligned}
K_{ij}^{(II)} &= \frac{\partial^2 \Phi}{\partial u_i \partial u_j} \\
&= \frac{A_{im'}}{h}\left[K_n(\delta_{12i}-\delta_{3i})(\delta_{12i}-\delta_{3i})+K_s(\delta_{11i}-\delta_{2i})(\delta_{11i}-\delta_{2i})+K_s(\delta_{10i}-\delta_{1i})(\delta_{10i}-\delta_{1i})\right]H(u_{12}-u_3) \\
&+ \frac{A_{jm'}}{h}\left[K_n(\delta_{12i}-\delta_{6i})(\delta_{12i}-\delta_{6i})+K_s(\delta_{11i}-\delta_{5i})(\delta_{11i}-\delta_{5i})+K_s(\delta_{10i}-\delta_{4i})(\delta_{10i}-\delta_{4i})\right]H(u_{12}-u_6) \\
&+ \frac{A_{ik'}}{h}\left[K_n(\delta_{9i}-\delta_{3i})(\delta_{9i}-\delta_{3i})+K_s(\delta_{8i}-\delta_{2i})(\delta_{8i}-\delta_{2i})+K_s(\delta_{7i}-\delta_{1i})(\delta_{7i}-\delta_{1i})\right]H(u_9-u_3) \\
&+ \frac{A_{jk'}}{h}\left[K_n(\delta_{9i}-\delta_{6i})(\delta_{9i}-\delta_{6i})+K_s(\delta_{8i}-\delta_{5i})(\delta_{8i}-\delta_{5i})+K_s(\delta_{7i}-\delta_{4i})(\delta_{7i}-\delta_{4i})\right]H(u_9-u_6)
\end{aligned}
\tag{3.12}
$$

where $A_{im'} = A_{jm'} = A_{ik'} = A_{jk'} = \frac{1}{4}A$.

Based on the stiffness matrixes derived above for special case that the local and global coordinate systems are parallel to each other, the general form of stiffness matrixes can be derived through the coordinate system transformation as follow:

$$K_{ij} = Q^T K' Q \tag{3.13}$$

where Q is the coordinate transform matrix.

3.3 Functional Test

To test the performance of 3D EPM on representing the contact and slippage of the fracture surface, the mechanical behavior of a rock block with a cut-through joint is tested in the section. The object geometry and boundary conditions are shown in Figure 3.6. The number of element and node used in the simulation are 8000 and 3362 respectively. Figure 3.7(a) shows the tetrahedron elements intersected with the joint. Figure 3.7(b) gives the geometrical relationship between vertical and horizontal force components. Two different shear stiffness coefficients K_{s1} and K_{s2} are used in the simulations to test the influence of the coefficients on the slippage response of the joint surface. The material parameters are listed in Table 1. The normal stress applied on the top of object is $\sigma_n = 1.0MPa$. The simulation results are shown in Figure 3.8 indicating

the curve of the resultant force and relative displacements on the joint surface and Figure 3.9 displays the relative slippage between joint surfaces by the deformed mesh configuration.

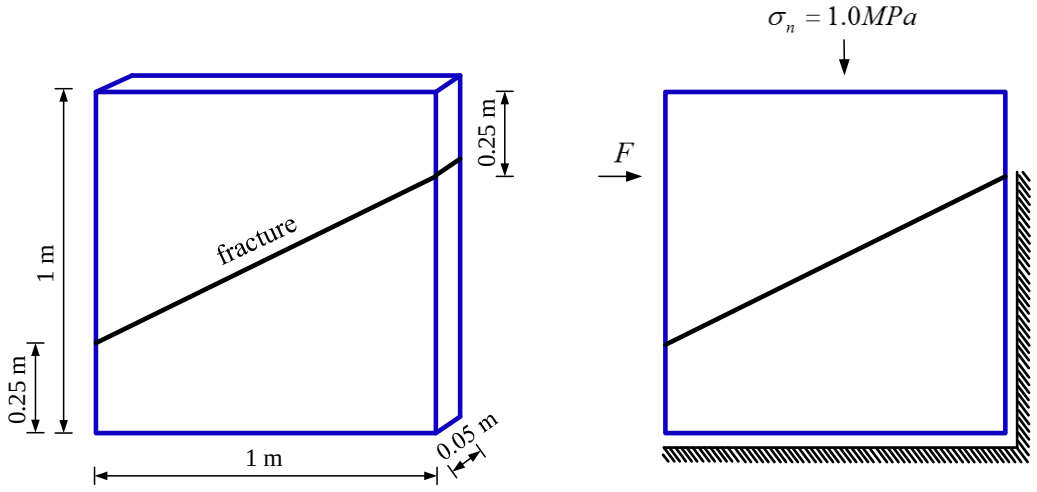

(a) (b)

Figure 3.6. (a) Dimension of simulation object and (b) boundary conditions.

Table 1. Simulation Parameters for 3D EPM Functional Test

Parameters of intact element:	
Young's modulus, E	10.0 GPa
Poisson's ratio, ν	0.16
Tensile strain strength, ε_t	0.1×10^{-3}
Parameters of 3D EPM:	
Normal stiffness coefficient, K_n / h	10.0 GPa/m
Shear stiffness coefficient, K_{s1} / h	10^{-5} GPa/m
Shear stiffness coefficient, K_{s2} / h	10^{-3} GPa/m
Fracture width, h	1.0 mm

According to the geometrical relationship between vertical and horizontal force components, the lateral force balanced with the normal stress on the top is calculated to be $F = 25kN$. Therefore, the slippage initiation forces for two different shear

coefficients are both $F = 25kN$ in Figure 3.8. Due to different shear stiffness coefficients, the consequent tendency of curves of lateral force F and relative slippage are different in slope. When the shear stiffness coefficient K_{s1} is relatively small, the upper block of simulation object is free to slide on the inclined surface due to the existing of cut-through joint. With the increase of relative displacement between upper and lower blocks, shown in Figure 3.8, the lateral force F keeps constant and balanced with the normal stress applied on the top indicating that the slipping surface is smooth. For larger shear stiffness coefficient K_{s2}, the lateral force increases linearly with the relative displacement growth shown in Figure 3.8. In Figure 3.9, the deformed mesh configuration shows the rigid body displacement of upper and lower blocks. The upper block is gradually climbing up along the inclined surface. Therefore, these results verified the capability of 3D EPM of representing the mechanical behavior of contact and slippage of the fracture surfaces.

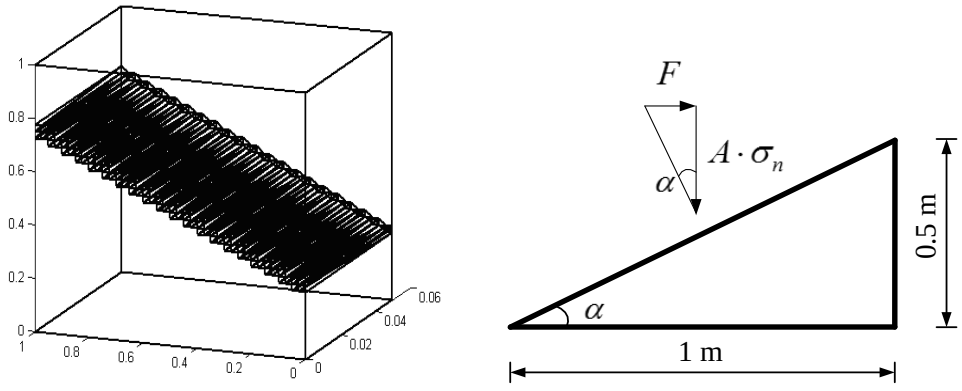

(a) (b)

Figure 3.7. (a) Tetrahedron elements intersected with fracture; (b) illustration of the geometrical relationship between vertical and horizontal force components.

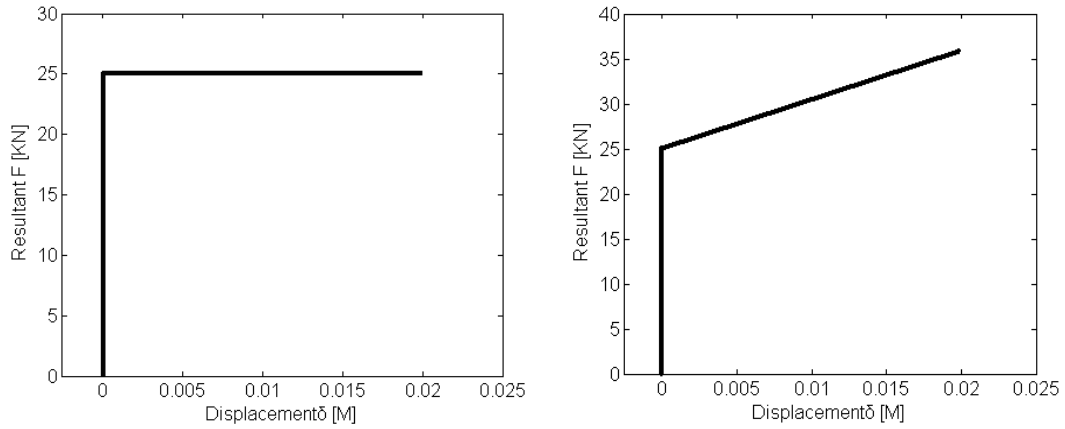

(a) (b)

Figure 3.8. Simulation results: relationship between the applied displacement and the resultant force F : (a) shear stiffness coefficient $K_{s1} = 10^{-5} MPa$; (b) shear stiffness coefficient $K_{s2} = 10^{-3} MPa$.

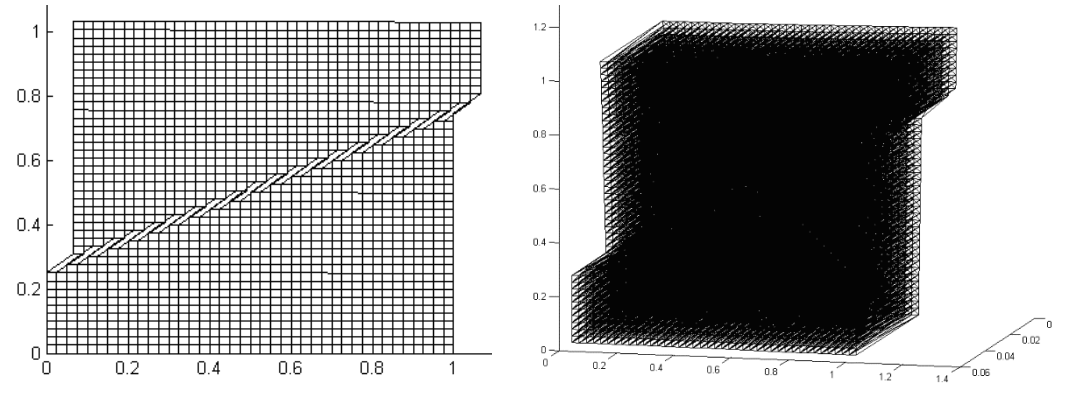

(a) (b)

Figure 3.9. Simulation results: the rigid body displacement indicating relative slippage between joint surfaces.

3.4 Conclusion

The 3D EPM introduces no additional degree of freedom and shares the same nodes with the intact tetrahedron element so that no remeshing is needed. Moreover, the dimension of the elemental stiffness matrix after partition remains the same, which

benefits the global stiffness matrix assembling. Although, the error of 3D EPM is arising with the increase of element size since that elastic deformation of partitioned element is not considered, 3D EPM is still competitive when the simulating domain and element size are relatively small comparing the computational cost with the other fracture treatment techniques. Through the test of a rock block with a cut-through joint, 3D EPM successfully represents mechanical behaviors such as contact and friction of the closed fracture surfaces. A series of simulations of pressurized subsurface fracture and result comparisons presented in Chapter 4 validate that the 3D EPM provides reasonable accuracy for pressurized fracture problem. Another drawback of element partitioning method is that the fracture surface within an element has to be flat. Since the whole fracture surface consists of the fracture segment in each partitioned element, the newly extended curved fracture presentation by 3D EPM could be unsmooth and composes by discontinued surfaces, which brings difficulty to apply moving boundary condition such as fluid pressure during the hydraulic fracturing process.

The greatest advantages of proposed 3D EPM are its efficiency and simplicity that outweigh its disadvantages, especially for its feasibility and applicability on the true 3D hydraulic fracturing simulation. Based on the theory of 3D EPM, the technique is developed with the features of transferring the quasi-static hydraulic loading to the equivalent nodal forces and calculating the fracture opening or aperture by knowing the geometric information of fracture segment in an element during the fracture propagation, which will be detailed introduced in Chapter 4.

Chapter 4. Methodologies of Fluid Flow for Hydraulic Fracture

Sometimes multiple physical processes are involved in hydraulic fracturing propagation and are active in determination of the growth of a propagating hydraulic fracture [Peirce, 2015]. It is very crucial for an effective hydraulic fracturing model to capture all the key physical processes including mechanical behaviors of rock mass and the fluid flow through the fracture and porous media. Moreover, the rock deformation, fracture creation and fluid flow are coupled physical processes that need to be analyzed simultaneously. The injection fluid initially flows from pressurized and perforated borehole. The high pressure fluid induces the rock failure around the perforation hole and creates initial fracture plane. Usually, the hydraulic fracture analysis is performed after the initial fracture plane has been created since that the physical process of the crack initiation form perforation is complicate and less important than the consequent fracture propagation. In this chapter, the methodologies of fluid flow during the hydraulic fracture propagation are discussed based on the different flow mechanisms in the porous rock media and the space between the fracture surfaces respectively. So far as we know, hydraulic fracturing is not only the complex interaction problem of fluid flow and rock mass deformation, but also involves Darcy fluid, non-Newtonian fluid, fluid leak off and more sophisticated turbulence fluid due to the complexity of fracture network and roughness of fracture surfaces. Though capturing the flow mechanisms is very difficult by an integrated method, this chapter focuses on two key aspects of fluid flow and attempts to model the porous media flow and fracture flow using poroelastic theory and lubrication theory respectively.

The detailed theory and mathematical derivation of fully coupled poroelastic model are described by the governing equations of equilibrium and fluid diffusion. The model is presented in a total form and implemented in finite element formulation to analyze the effective stress and deformation of rock mass, pore pressure induced by the fluid diffusion and compaction in a fully couple equation system. On the other hand, the fracture flow can be simulated by fluid flow in a narrow aperture that is much smaller than other dimensions. Additionally, laminar flow exists since the high viscosity of fracturing fluid and small injection rate. Therefore, the popular lubrication flow theory is used to model the pressure gradient and mass conservation inside pressurized fracture. Associated with the fracture description by three dimensional element partitioning method (3D EPM), a moving boundary analysis on the propagating fracture can be implemented by algorithm of creating new fracture surface and applying hydraulic pressure boundary conditions that will be introduced in this chapter.

However, the present work doesn't integrate the two fluid flow mechanisms into one simulation model. The realistic fracturing fluid flows from the injection well through the fracture tip with a pressure degradation since the resistance. Meantime, because of pressure difference, the fluid is going to diffuse into the formation that is so called leak-off. Thus the whole process should be analyzed simultaneously since that the pore and fracture fluid share same pressure boundary condition on the fracture surfaces. However, this is very difficult to be implemented mathematically and numerically. The present work provides the couple schemes and iteration methods for fluid flow in the porous rock mass and fracture separately. More rigorous lubrication theory is emphasized only on the pressure profile along the fracture surface and its

induced fracture growth. The followings are the basic assumptions for lubrication model: the leak-off effects are neglect since inject time are relatively short; the fracture propagates advance to the fluid front, which means there is fluid lag at the fracture tip; the pressure profile is calculated in stationary parallel fracture geometry. On the other hand, the poroelastic model is used to capture the hydraulic fracture propagation with complex geometry and boundary conditions such as hydraulic fracture and natural fractures interaction. The permeability of fractured element is artificially increased to represent the conductivity enhancement by fracture creation. Although this model cannot provide precise fluid pressure along the fracture surface, the overall tendency of fracture and pore pressure distribution and fracture propagation can still be modeled considering the computational feasibility and efficiency.

4.1 Fully Coupled Analysis Using Poroelastic Model

The fully coupled diffusion-deformation mechanism of the porous media is inspired by understanding the problem of consolidation in soil mechanics. The consolidation is the process of soil decrease in volume that results from decrease of water content of saturated soil. [Terzaghi, 1923] firstly developed the theory to capture the quasi-static deformation of soil under surface compressive loading in one-dimension. [Boit, 1935, 1941] developed the theory of dynamic poroelasticity or Biot theory that represents the interactions between the displacement or the volumetric change of the skeleton rock and the pore fluid discharge describes that the motion of the fluid with respect to the skeleton.

4.1.1 Poroelastic Constitutive Relations

Based on the assumption of linear relations between stress σ_{ij} and strain ε_{ij}, pressure p and fluid content ζ respectively, the coupled mechanical equilibrium equations with pore pressure for isotropic porous material could be described by the Biot theory[Biot, 1935, 1941]:

$$\varepsilon_{ij} = \frac{\sigma_{ij}}{2G} - \frac{\nu}{2G(1+\nu)}\sigma_{kk}\delta_{ij} + \frac{\alpha(1-2\nu)}{2G(1+\nu)}p\delta_{ij} \tag{4.1}$$

$$\zeta = \frac{\alpha(1-2\nu)}{2G(1+\nu)}\left(\sigma_{kk} + \frac{3}{B}p\right) \tag{4.2}$$

where the first equation considers the constitutive response for the solid skeleton, the second equation correspond to the behaviors of porous fluid, ε_{ij} is strain tensor that is positive for tension, σ_{ij} denotes the total stress tensor, p and ζ are the pore pressure and the variation of the fluid content per unit volume of the porous media respectively. G is the shear modulus and ν is the Poisson ratio. α is the Biot's coefficient, B is the Skempton's coefficient. α and B are written as

$$\alpha = 1 - \frac{K}{K_s} \tag{4.3}$$

$$B = \frac{3(\nu_u - \nu)}{\alpha(1-2\nu)(1+\nu_u)} \tag{4.4}$$

where K is bulk modulus, K_s is the bulk modulus of solid phase, ν_u is the undrained Poisson ratio.

Eq. (4.1) can be written in terms of stress strain relation,

$$\sigma_{ij} = 2G\varepsilon_{ij} + \frac{2G}{1-2\nu}\varepsilon_{kk}\delta_{ij} - \alpha p\delta_{ij} \tag{4.5}$$

Eq. (4.5) represents the constitutive equation for the linear system, in which we can find the effective stress σ'_{ij} by eliminates the last pore pressure term defined as

$$\sigma'_{ij} = 2G\varepsilon_{ij} + \frac{2G}{1-2\nu}\varepsilon_{kk}\delta_{ij} \tag{4.6}$$

Effective stress σ'_{ij} physically means the resultant stress applied on the rock skeleton. It is the exact stress that the rock skeleton supports.

4.1.2 Balance Law

Two equilibrium considerations compose the conservation law for poroelastic material. Firstly, the static equilibrium leads to stress balance equation or equilibrium equation written as

$$\sigma_{ij,j} = -F_i \tag{4.7}$$

where F_i is the body force per unit volume. Usually the body force is assumed to be ignored if the volume or dimension of objective of interest is small. Second one is the continuity equation for the fluid phase considering the mass conservation:

$$\frac{\partial \zeta}{\partial t} + q_{i,i} = \gamma \tag{4.8}$$

where γ is the density of injection source.

4.1.3 Field Equations

The equations in the previous sections explain the physical meaning of porous material and fluid. However, only field equations lead to useful solution that is derived in this section. Associated with (i) the constitutive equations for the porous rock (Eq. (4.5)) and porous fluid (Eq. (4.2)), (ii) the equilibrium equation and continuity equation defined as Eqs. (4.7) and (4.8) respectively and (iii) Darcy's law that governs the single phase fluid transport in the porous rock, the linear isotropic poroelastic coupling

processes are captured. By ignoring the body force of fluid, the Darcy's law is written as

$$q_i = -\frac{k}{\mu} p_{,i} \tag{4.9}$$

where k is intrinsic permeability and μ is the fluid viscosity.

By combining the strain-displacement relationship under assumption of small deformation,

$$\varepsilon_{ij} = \frac{1}{2}\left(u_{i,j} + u_{j,i}\right) \tag{4.10}$$

with the constitutive equations and the momentum equilibrium. The deformation field equations are obtained as

$$G\nabla^2 u_i + \frac{G}{1-2\nu} u_{j,ji} - \alpha p_{,i} = 0 \tag{4.11}$$

The diffusion equation is derived by substituting Darcy's law (Eq. (4.9)) and constitutive equation (Eq. (4.2)) into fluid mass conservation (Eq.(4.8)) in terms of pore pressure p:

$$-\alpha \frac{\partial \varepsilon_{kk}}{\partial t} - \frac{1}{M}\frac{\partial p}{\partial t} + \frac{k}{\mu}\nabla^2 p = 0 \tag{4.12}$$

where M is the Biot modulus defined as the fluid contents increase results from the unit increase of pore pressure under constant volumetric strain, written as

$$M = \frac{2G\left(\nu_u - \nu\right)}{\alpha^2\left(1-2\nu\right)\left(1-2\nu_u\right)} \tag{4.13}$$

Based on the constitutive relations of porous rock and fluid, static equilibrium and mass conservation and transportation function, the governing equations

representing the fully coupled poroelastic behaviors are therefore derived and written in terms of the displacement $\mathbf{u}$ and pore pressure p as

$$G\nabla^2\mathbf{u}+\frac{G}{1-2\nu}\nabla(\nabla\cdot\mathbf{u})-\mathbf{m}\alpha\nabla p=0 \tag{4.14}$$

$$-\alpha(\nabla\cdot\dot{\mathbf{u}})-\frac{1}{M}\dot{p}+\frac{k}{\mu}\nabla^2 p=Q_i\delta \tag{4.15}$$

where $\mathbf{m}=[1,1,1,0,0,0]^T$ for 3D problems and $\mathbf{m}=[1,1,0]^T$ for 2D problems since the coupling term $\mathbf{m}\alpha\nabla p$ is only active in case of volumetric change of porous solid, Q_i is injection rate at point source, δ is Kronecker delta function.

By solving the field equation system shown as Eqs. (4.14) and (4.15) for the primary unknown variables-displacement $\mathbf{u}$ and pore pressure p, we can then calculate other unknowns such as strain $\boldsymbol{\varepsilon}$, total stress $\boldsymbol{\sigma}$, effective stress $\boldsymbol{\sigma}'$ and flux q according the constitutive relations. However, it is very difficult to get a close form solution due to the complexity of the partial differential equations, except the special cases with simple and symmetric geometries and material properties. Therefore, finding the solution of coupled equations generally relies on numerical techniques, for example, finite element method, boundary element method and finite different method, etc. The problems contain more complicate geometries and various properties of porous solid and fluid such as nonlinearity, anisotropy, heterogeneity could be solved. In this work, we focus on the numerical solution using finite element method.

4.1.4 FEM Formulation

In the following, the finite element solution for the problem of poroelasticity is presented. The field equations (4.14) and (4.15) are spatially discrete by approximating

the field variables of displacement, $\mathbf{u}$, pore pressure p through interpolation functions written as,

$$\mathbf{u} = \mathbf{N}_u \tilde{\mathbf{u}} \tag{4.16}$$

$$p = \mathbf{N}_p \tilde{\mathbf{p}} \tag{4.17}$$

where $\mathbf{N}_u$ and $\mathbf{N}_p$ are the shape functions for the solid displacement and pore pressure fields, respectively. $\tilde{\mathbf{u}}$ and $\tilde{\mathbf{p}}$ are the displacements and pore pressure on nodes in each elements described following an order as

$$\tilde{\mathbf{u}} = [u_x^1, u_y^1, u_z^1, u_x^2, u_y^2, u_z^2, \ldots, u_x^n, u_y^n, u_z^n] \tag{4.18}$$

$$\tilde{\mathbf{p}} = [p^1, p^2, \ldots, p^n] \tag{4.19}$$

The shape functions for displacement and pore pressure are respectively,

$$\mathbf{N}_u = \begin{bmatrix} N_u^1 & 0 & 0 & N_u^2 & 0 & 0 & \ldots & N_u^n & 0 & 0 \\ 0 & N_u^1 & 0 & 0 & N_u^2 & 0 & \ldots & 0 & N_u^n & 0 \\ 0 & 0 & N_u^1 & 0 & 0 & N_u^2 & \ldots & 0 & 0 & N_u^n \end{bmatrix} \tag{4.20}$$

$$\mathbf{N}_p = \left[N_p^1, N_p^2, \ldots, N_p^n\right] \tag{4.21}$$

where n is the node order number depends on the chose type of element.

The strain-displacement relationship expressed as Eq. (4.10) can be written in discretized form,

$$\boldsymbol{\varepsilon} = \mathbf{B}\tilde{\mathbf{u}} \tag{4.22}$$

where

$$\mathbf{B} = \mathbf{L}\mathbf{N}_u \tag{4.23}$$

$$\mathbf{L}=\begin{bmatrix} \frac{\partial}{\partial x} & 0 & 0 & \frac{\partial}{\partial y} & 0 & \frac{\partial}{\partial z} \\ 0 & \frac{\partial}{\partial y} & 0 & \frac{\partial}{\partial x} & \frac{\partial}{\partial z} & 0 \\ 0 & 0 & \frac{\partial}{\partial z} & 0 & \frac{\partial}{\partial y} & \frac{\partial}{\partial x} \end{bmatrix}^T \tag{4.24}$$

According to Eqs. (4.16) through (4.24), using Galerkin's method, the weak form of equation system Eqs. (4.14) and (4.15) can be derived as:

$$\mathbf{K}\tilde{\mathbf{u}}-\mathbf{A}\tilde{\mathbf{p}}=\mathbf{f} \tag{4.25}$$

$$-\mathbf{A}^T\dot{\tilde{\mathbf{u}}}-\mathbf{S}\dot{\tilde{\mathbf{p}}}+\mathbf{H}_H\tilde{\mathbf{p}}=\dot{\mathbf{q}} \tag{4.26}$$

where

$$\mathbf{K}=\int_{V_e}\mathbf{B}^T\mathbf{D}\mathbf{B}dV \tag{4.27}$$

$$\mathbf{A}=\int_{V_e}\mathbf{B}^T\alpha\mathbf{m}\mathbf{N}_p dV \tag{4.28}$$

$$\mathbf{S}=\int_{V_e}\mathbf{N}_p{}^T\frac{1}{M}\mathbf{N}_p dV \tag{4.29}$$

$$\mathbf{H}_H=\int_{V_e}\left(\nabla\mathbf{N}_p\right)^T\frac{k}{\mu}\left(\nabla\mathbf{N}_p\right)dV \tag{4.30}$$

In these equations, V_e is the volume of element, $\mathbf{f}$ is external mechanical loading, $\mathbf{q}$ is the injection rate from a point source. In the following Eq. (4.26) is discretized in time domain since it is first order time dependent. Though incremental formulation of matrix is required for strong nonlinear problem, the present work adopts the total formulation since that the constitutive models (VMIB, nonlocal damage model et al.) for the nonlinear rock behaviors are written in total form. Therefore the temporal discretization of field variables performed between t_0 and t can be expressed as:

$$\lambda \mathbf{K}_t \tilde{\mathbf{u}}_t - \lambda \mathbf{A} \tilde{\mathbf{p}}_t = -(1-\lambda)\mathbf{K}_{t0} \tilde{\mathbf{u}}_{t0} + (1-\lambda)\mathbf{A} \tilde{\mathbf{p}}_{t0} + \lambda \mathbf{f}_t + (1-\lambda)\mathbf{f}_{t0} \tag{4.31}$$

$$-\mathbf{A}^T \dot{\tilde{\mathbf{u}}}_t + (-\mathbf{S} - \Delta t \lambda \mathbf{H}_H) \tilde{\mathbf{p}}_t = -\mathbf{A}^T \dot{\tilde{\mathbf{u}}}_{t0} + [\Delta t(1-\lambda)\mathbf{H}_H - \mathbf{S}] \tilde{\mathbf{p}}_{t0} + \lambda \dot{\mathbf{q}}_t + (1-\lambda)\dot{\mathbf{q}}_{t0} \tag{4.32}$$

where $\Delta t = t - t_0$ is the time interval, λ is a coefficient with the range $0 < \lambda < 1$.

Eqs. (4.31) and (4.32) are written in the matrix form:

$$\begin{bmatrix} \mathbf{K}_t & -\mathbf{A} \\ -\mathbf{A}^T & -\Delta t \lambda \mathbf{H}_H - \mathbf{S} \end{bmatrix} \begin{bmatrix} \tilde{\mathbf{u}}_t \\ \tilde{\mathbf{p}}_t \end{bmatrix} = \begin{bmatrix} \frac{\lambda - 1}{\lambda} \mathbf{K}_{t0} & -\frac{\lambda - 1}{\lambda} \mathbf{A} \\ -\mathbf{A}^T & \Delta t(1-\lambda)\mathbf{H}_H - \mathbf{S} \end{bmatrix} \begin{bmatrix} \tilde{\mathbf{u}}_{t0} \\ \tilde{\mathbf{p}}_{t0} \end{bmatrix} + \begin{bmatrix} \mathbf{f}_t + \frac{1-\lambda}{\lambda} \mathbf{f}_{t0} \\ \Delta t \mathbf{q}_t + \frac{1-\lambda}{\lambda} \Delta t \mathbf{q}_{t0} \end{bmatrix} \tag{4.33}$$

For simplification purpose, set $\lambda = 1$ corresponding to an implicit schemes. Thus, the finite element formulation of field equations through special and temporal discretization in terms of displacement and pore pressure is obtained and Eq. (4.33) is reduced to

$$\begin{bmatrix} \mathbf{K}_t & -\mathbf{A} \\ -\mathbf{A}^T & -\Delta t \mathbf{H}_H - \mathbf{S} \end{bmatrix} \begin{bmatrix} \tilde{\mathbf{u}}_t \\ \tilde{\mathbf{p}}_t \end{bmatrix} = \begin{bmatrix} 0 & 0 \\ -\mathbf{A}^T & -\mathbf{S} \end{bmatrix} \begin{bmatrix} \tilde{\mathbf{u}}_{t0} \\ \tilde{\mathbf{p}}_{t0} \end{bmatrix} + \begin{bmatrix} \mathbf{f}_t \\ \Delta t \mathbf{q}_t \end{bmatrix} \tag{4.34}$$

Finally, by integrating the constitutive equations for the porous rock and fluid, the equilibrium equation, continuity equation and single phase Darcy's law, the fully coupled poroelastic field equations in FEM form are obtained and coded in FORTRAN language. Due to the time dependency of poroelastic problem, using an appropriate time step is especially important. The stress and strain of porous rock propagates relatively faster than fluid diffusion that requires small enough time step for accuracy consideration. However, in fluid flow part, small time step will induce instable because of the pore pressure is nearly unchanged in this small time interval. Meantime, element

size is another influence factor for adopting appropriate time step. Therefore, the time step is determined according to reasonable accuracy and stability.

4.1.5 Validation of Poroelastic Model

To validate the present model for poroelastic model, the numerical solution is compared with the analytical solution of Terzaghi one-dimensional consolidation. Terzaghi consolidation theory provided a solution for the fluid solid interaction in soil saturate with water, which has successfully inspired the following research in soil mechanics and geotechnical engineering. The settlement of a saturated soil column with thickness of h under a constant load from the top surface is analyzed. The column rests on a rigid and impermeable boundary. The constant normal loading with magnitude of P squeezes the pore water out from the top that induces a gradual settlement. The boundary conditions are written as follows:

$$\sigma_{zz} = -H(t)P \qquad z = 0 \tag{4.35}$$

$$p = 0 \qquad z = 0 \qquad \forall t \tag{4.36}$$

$$\frac{\partial p}{\partial z} = 0 \qquad z = h \qquad \forall t \tag{4.37}$$

[Detournay and Cheng 1993; Jaeger, Cook et al. 2009] give the detailed solutions for Terzaghi one-dimensional consolidation. The solutions for pressure distribution are written as:

$$p(z,t) = \frac{B(1+\nu_u)}{3(1-\nu_u)}(-P)\sum_{m\ odd}\frac{4}{m\pi}\left(\sin\frac{m\pi}{2h}z\right)e^{-c\left(\frac{m\pi}{2h}\right)^2 t} \tag{4.38}$$

$$\frac{p(z,t)}{p_0} = 1-\sum_{n=0}^{\infty}(-1)^n\left\{erfc\left[\frac{2nh+z}{(4kt/\mu S)^{0.5}}\right]+erfc\left[\frac{2(n+1)h-z}{(4kt/\mu S)^{0.5}}\right]\right\} \tag{4.39}$$

and the solution for top settlement is

$$w(z,t)=\frac{P}{\lambda+2G}\left[(z-h)+\frac{\alpha^2 Mh}{\lambda+2G+\alpha^2 M}\sum_{n=0}^{\infty}\frac{8}{n^2\pi^2}\cos\left(\frac{n\pi z}{2h}\right)\exp\left(\frac{-n^2\pi^2 kt}{4\mu Sh}\right)\right] \tag{4.40}$$

where h is the thickness of soil column, M is the Biot modulus expressed as Eq. (4.13), B is the Skempton' coefficient written as Eq. (4.4), S is storativity coefficient written as

$$S=\frac{\alpha^2(1-\nu_u)(1-2\nu)(1+\nu)}{3K(1-\nu)(\nu_u-\nu)} \tag{4.41}$$

and $erfc(x)$ is the coerror function (Abramowitz and Stegun, 1970), defined as

$$erfc(x)=\frac{2}{\sqrt{\pi}}\int_x^{\infty}e^{-\eta^2}d\eta \tag{4.42}$$

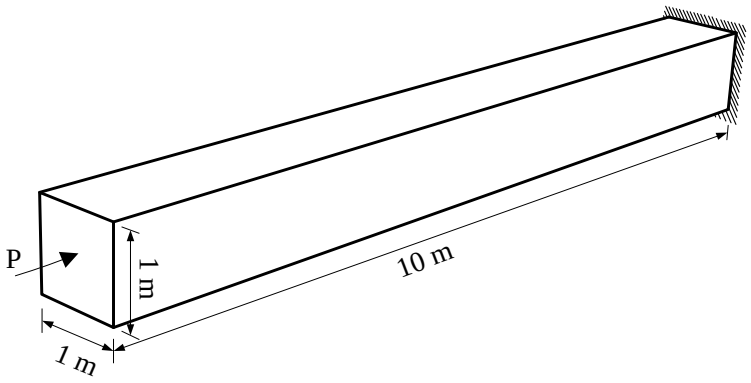

Figure 4.1. Problem geometry and boundary conditions of soil column.

The 3D finite element model with specified boundary conditions is used to reproduce Terzaghi 1D consolidation. The soil column has $1m\times 1m$ cross section and $10m$ height shown in Figure 4.1. The lateral surfaces are impermeable and their normal displacements are confined to fulfill the same boundary conditions as 1D Terzaghi problem. The bottom side is also impermeable with no displacements. The top surface is exposed in air representing zero pore pressure boundary and subjected to a mechanical pressure load P. Therefore, the water is drained from the top during the

loading process. Table 2 lists the input parameters used for analytical and numerical solutions. In the simulation, 38028 four nodes tetrahedron elements with 8556 nodes are used.

Table 2. Input Parameters for Terzaghi 1D Consolidation

Shear modulus, G	12.0 GPa
Poisson's ratio, ν	0.15
Undrained Poisson's ratio, ν_u	0.29
Biot's coefficient, α	1.0
Permeability, k	0.5 md
Fluid viscosity, μ	$3.0\times10^{-4}\,\mathrm{Pa\cdot s}$
Load, P	1.0MPa

The comparisons of the transient pore pressure distributions between analytical and numerical solutions are shown in Figure 4.2. The pore pressure contours at different time are plotted in Figure 4.3. Figure 4.4 shows the transient settlements at various depth comparisons between analytical and numerical solutions. The comparisons indicate well agreement between the analytical and numerical solutions, which enhances the confidence that the model can be adopted to simulate the porous rock and fluid during the hydraulic stimulation in the following sections.

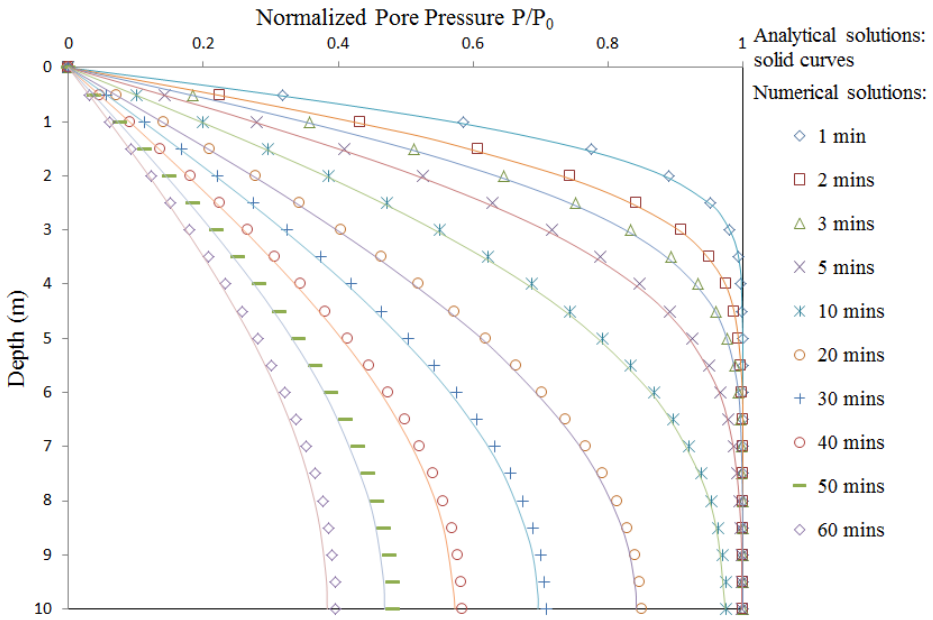

Figure 4.2. The transient pore pressure distributions comparisons between analytical and numerical solution.

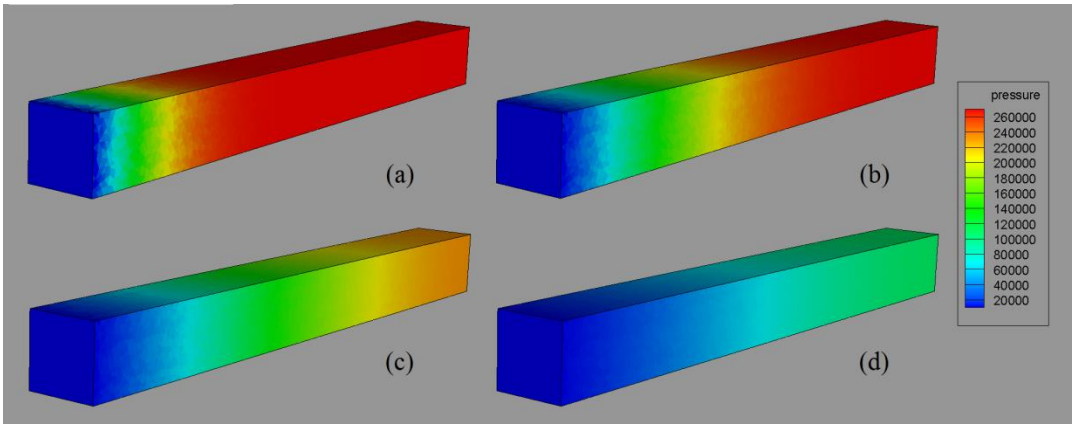

Figure 4.3. The transient pore pressure distributions at (a) 1mins; (b) 5 mins; (c) 20 mins; (d) 60 mins.

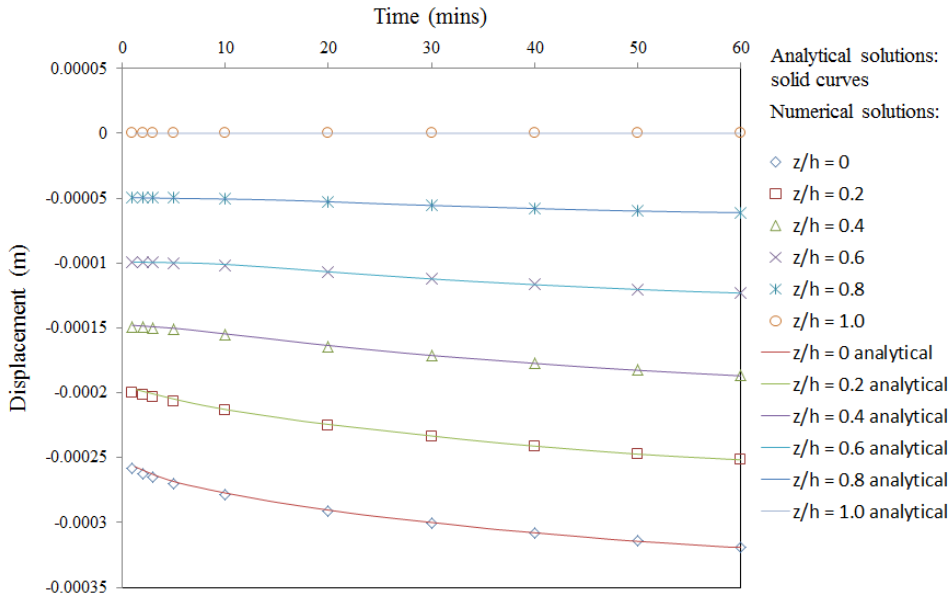

Figure 4.4. The transient settlements at various depth comparisons between analytical and numerical solution.

4.2 Fluid Flow in Fracture Surfaces

Besides the fluid diffusion in the porous matrix, the flow in the fracture surface governs the transient boundary conditions for fracturing fluid pressure and rock deformation, and therefore controls the propagating direction and distance in the hydraulic stimulation. In general, even for simple geometry, modeling the fluid flow induced fracturing has many difficulties due to the moving boundary and nonlinearity of in fracture fluid flow and rock matrix behaviors. The nonlinearity of fluid flow in the fracture not only results from that its conductivity followed the cubic low of the fracture aperture, and also the fluid mass balance considering fluid storage volume due to aperture change. During the simulation, the length of fracture, fracture opening and fluid pressure profile are all time-dependent variables, and more importantly, are mutually interacted. Several steps are involved in the calculation process to reach an

overall convergence. Firstly, next section will introduce the method of applying the fluid pressure on the fracture surface. Then, the coupling scheme and iterations between mechanical response of rock matrix and the pressure profile in the fracture will be briefly illustrated. The last but not the least, newly extended fracture will be located in the damaged bond calculated from the nonlocal damage model, which updates the fracture geometry for next step of simulation. This procedure based on the following assumptions: (i) the fracture propagates advance to the fluid front, which means there is fluid lag at the fracture tip; (ii) the pressure profile is calculated in stationary parallel fracture geometry; (iii) the leak-off effects are neglect in this section since inject time are relatively short.

4.2.1 Representing the Hydraulic Pressure in Fractured Element

This section describes the approach to apply the fracturing fluid pressure on the crack surface in FEM framework. There are other methods [Belytschko and Black, 1999; Olsen and Taleghani, 2009; Weng et al., 2011; McClure, 2012; Sesetty and Ghassemi, 2012, 2013] simulating the hydraulic fracturing by creating new surfaces once the stress or strain states of rock reached the failure criteria. The pressure could be applied on this newly extended surface. The present work employed 3D element partition method (3D EPM) to represent the pre-exciting and newly extended fracture surface within the elements. There is no explicit boundary or extra virtual nodes for applying the pressure boundary conditions. Once the element is divided into two portions by pre-existing or newly extended fracture, the mechanical behaviors are modified by 3D EPM [Huang and Zhang, 2010] algorithm that the opening as well as contact and slipping behaviors of fracture surface can be represented. Thus no explicit

surface or extra nodes are introduced. The pressure applied on the fracture surface is represented by the equivalent nodal force by obtaining the geometry and size of fracture segment and the fluid pressure through the flow analysis. The fracture segment in the element is calculated by the geometry of fracture surface and how it is intersected with the edges of element. Figure 4.5 and Figure 4.6 illustrate the processes to transfer fluid pressure into equivalent nodal forces for each element type.

In the simulation, the forces are applied on the nodes to equivalently represent the fluid pressure. The area of the fracture segment and fluid pressure are respectively denoted as A and $\mathbf{P}$. The resultant force of fluid pressure on the fracture segment is $\mathbf{F} = \mathbf{P} \cdot A$. For the Type I partition element shown in Figure 4.5, for example, the force components $F_{Mx'}$, $F_{My'}$ and $F_{Mz'}$ are balanced with $\mathbf{F}$. The equivalent forces relations of the type I partition element are written as:

$$\mathbf{F} = [F_{Mx'}, F_{My'}, F_{Mz'}] \tag{4.43}$$

$$-\frac{1}{3}\mathbf{F} = [F_{Ix'}, F_{Iy'}, F_{Iz'}] \tag{4.44}$$

$$-\frac{1}{3}\mathbf{F} = [F_{Jx'}, F_{Jy'}, F_{Jz'}] \tag{4.45}$$

$$-\frac{1}{3}\mathbf{F} = [F_{Kx'}, F_{Ky'}, F_{Kz'}] \tag{4.46}$$

The equivalent forces relations of the type II partition element are written as:

$$\frac{1}{2}\mathbf{F} = [F_{Mx'}, F_{My'}, F_{Mz'}] \tag{4.47}$$

$$\frac{1}{2}\mathbf{F} = [F_{Kx'}, F_{Ky'}, F_{Kz'}] \tag{4.48}$$

$$-\frac{1}{2}\mathbf{F} = [F_{Jx'}, F_{Jy'}, F_{Jz'}] \tag{4.49}$$

$$-\frac{1}{2}\mathbf{F}=[F_{Ix'},F_{Iy'},F_{Iz'}] \tag{4.50}$$

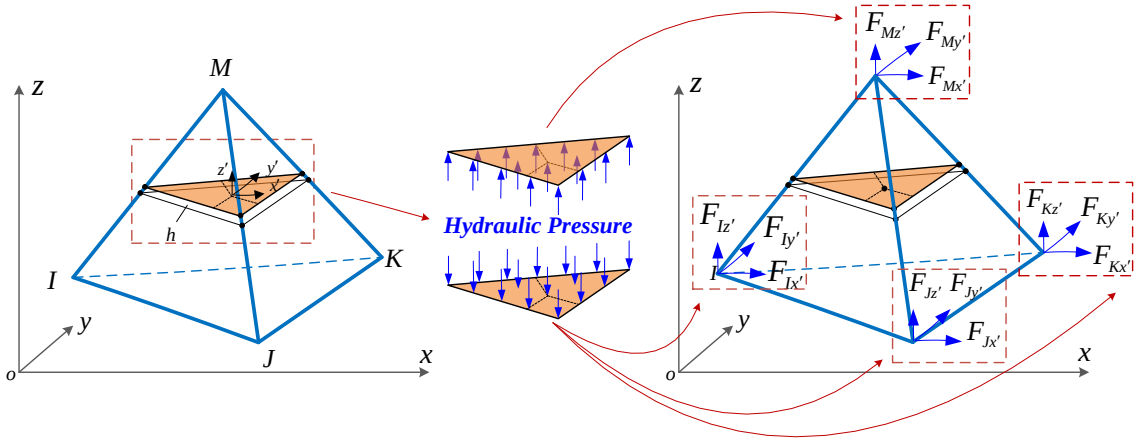

Figure 4.5. Equivalent node force representing the water pressure on the crack surface in the Type I element.

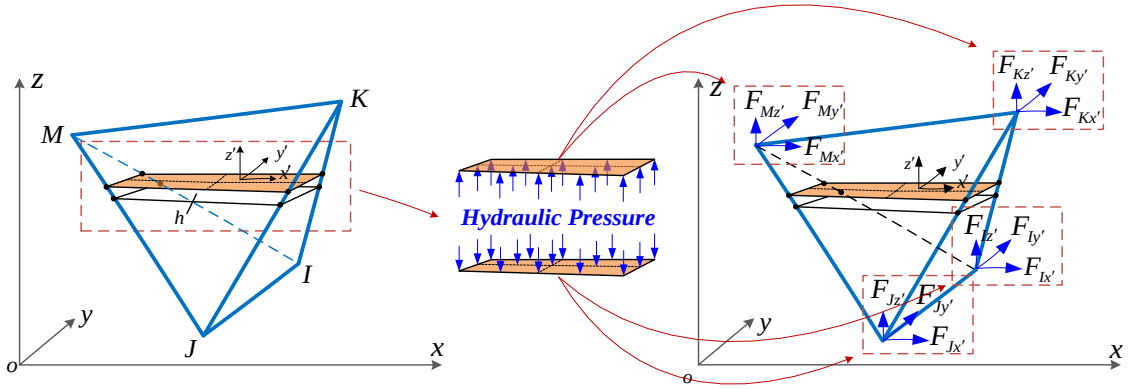

Figure 4.6. Equivalent node force representing the water pressure on the crack surface in the Type II element.

4.2.2 Validation of 3D EPM on Representing Pressurized Fracture

Successfully applying the pressure boundary condition is the key step for hydraulic fracturing simulations. To validate 3D EPM model for pressurized fracture representation, the present model is compared with the numerical [Fu, 2014] and

analytical [Pollard and Holzhausen, 1979] solutions of subsurface pressurized fracture. Figure 4.7 shows the geometry and mesh scheme of 2D pressurized fracture. The red line represents a closed fracture of half-length a that is located at the depth-to-center d below the horizontal free surface of a semi-infinite domain. The dip of the fracture from the free surface is β. Deformations of the free surface with different dip angles are given in [Pollard and Holzhausen, 1979]. Another simulation result provided by [Fu, 2014] using finite element method is compared in this section. This problem is simulated using single layered 3D tetrahedron elements. The out-of-plane displacements along the thickness direction are confined to simulate the plane-strain condition. The size of the domain is $50m \times 50m$. All the normal displacements on the boundary except the top one are fixed. The total number of elements used in this simulation is 126,899. The resolution of mesh is 1 meter in the coarse area and 0.04 meter in the fine area. Table 3 gives the geometrical and material parameters for pressurized fracture problem.

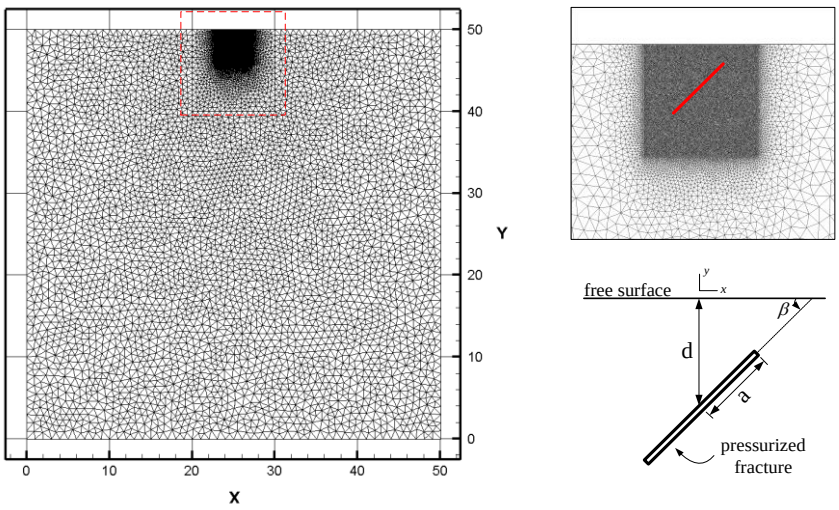

Figure 4.7. Problem geometry for 2D pressurized subsurface fracture.

The vertical displacement and stress contours for different dipping angles are plotted in Figure 4.8 and Figure 4.9. The displacement has been amplified to be visible.

In the figures we observed, the fracture surfaces are not perfect smooth. This is because the displacement discontinuity is represented by the whole fractured element and the elastic deformation of partitioned blocks in single fractured element is neglect. Additionally, the equivalent nodal forces are applied on the adjacent nodes instead of on the fracture surface. Therefore, the stress of fractured element has no mechanical meaning and is blanked in the figures. The comparisons of the surface normal displacement distributions between the present model, the solution by [Fu, 2014] and the exact solution are shown in Figure 4.10. Figure 4.11 shows the solutions by [Pollard and Holzhausen, 1979] provided the suggestion for the overall curve shapes since that an arbitrary constant may be added to these solutions.

Table 3. Geometrical and Material Parameters for Pressurized Surface Fracture

Half length of fracture, a	1.0 m
Depth-to-center d	1.25 m
Half length of fracture in z direction (3D), b	3.0 m
Dip, β	0, 45, 90
Young's modulus, E	$1.0\times10^{6}\,Pa$
Poisson ratio, ν	0.25
Fluid pressure, p_0	1.0 Pa
Shear modulus, μ	$4.0\times10^{5}\,Pa$
Max. normal displacement, $\delta_\infty = p_0 a(1-\nu)/\mu$	1.875×10^{-6}

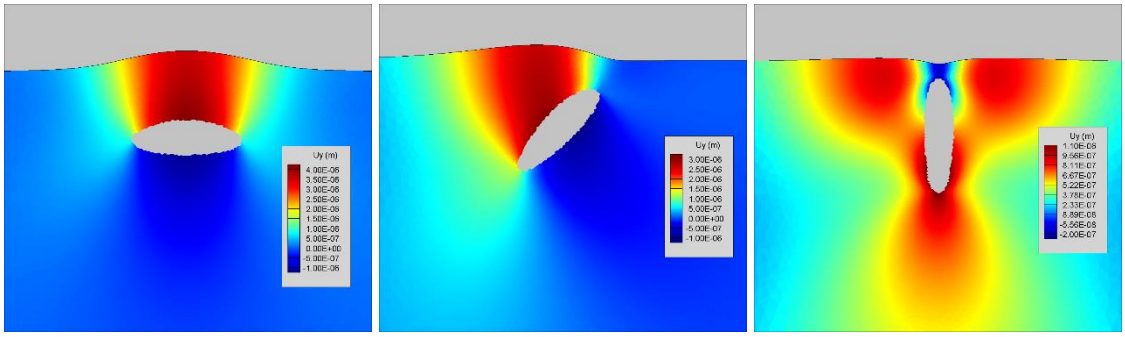

(a) (b) (c)

Figure 4.8. Vertical displacement in 3 different dipping angles of pressurized fracture in 2D: (a) 0 degree; (b) 45 degree; (c) 90 degree.

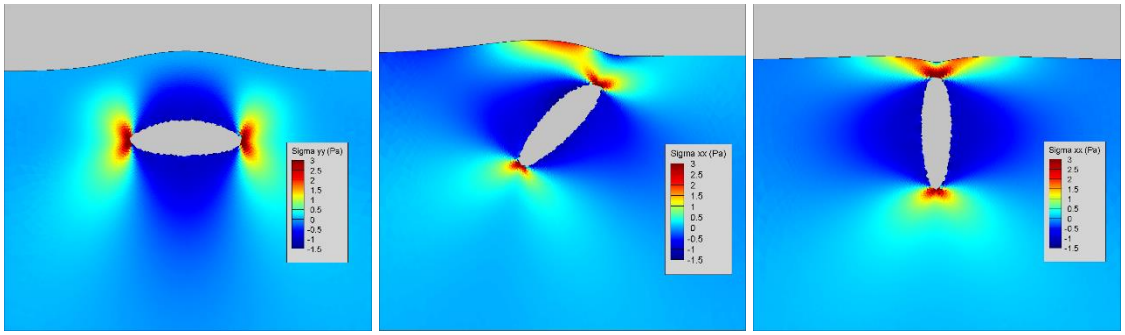

(a) (b) (c)

Figure 4.9. Stress contours in 3 different dipping angles of pressurized fracture in 2D: (a) σ_{yy} for 0 degree ; (b) σ_{xx} for 45 degree; (c) σ_{xx} 90 degree.

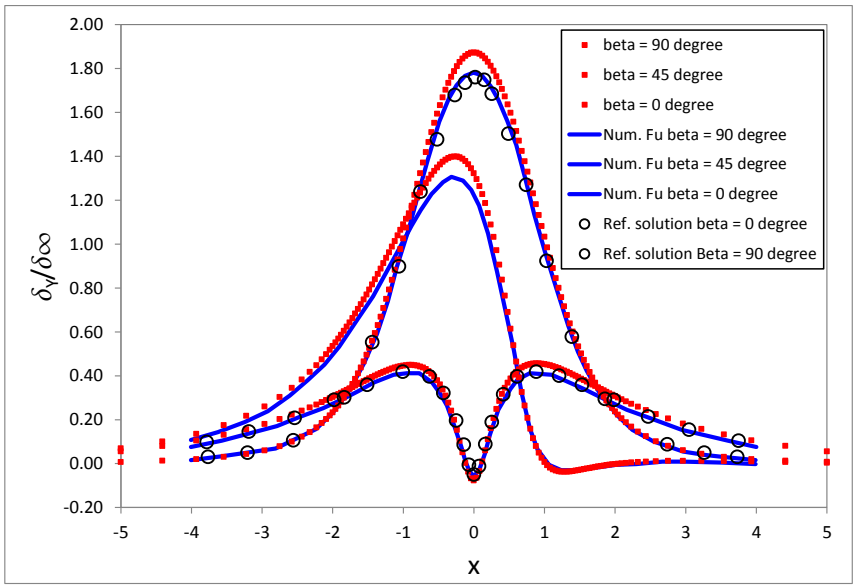

Figure 4.10. Normalized surface displacement in 3 different dipping angles of pressurized fracture in 2D comparing with the results by [Fu, 2014].

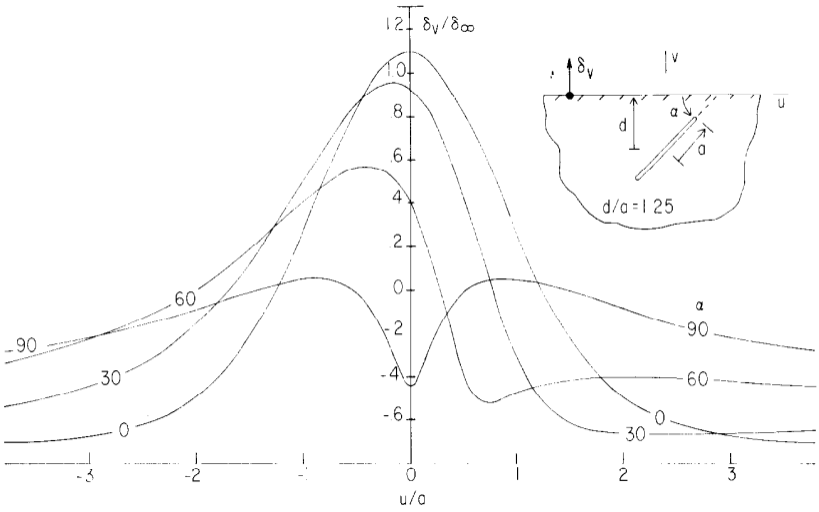

Figure 4.11. Vertical displacements of the surface are normalized and plotted versus position along the surface at different fracture inclinations [Pollard and Holzhausen, 1979]. An arbitrary constant may be added to these displacements.

[Fu, 2014] also presented true 3D simulation examples. Figure 4.12 shows the geometry and mesh scheme of 3D pressurized fracture. The geometric aspect of 3D problem is similar to 2D example except that the fracture is not cut through in z

direction. Parameter b in Table 3 indicates the half-length of fracture in z direction. Half domain is modeled since the symmetry of the problem and its dimensions are $50\text{m} \times 50\text{m} \times 25\text{m}$ on x, y and z axis respectively. This problem is simulated using 3D tetrahedron elements. All the normal displacements on the boundary except the top one are fixed. The total number of elements used in this simulation is 649,647. The resolution of mesh is 3 meter in the coarse area and 0.07 meter in the fine area.

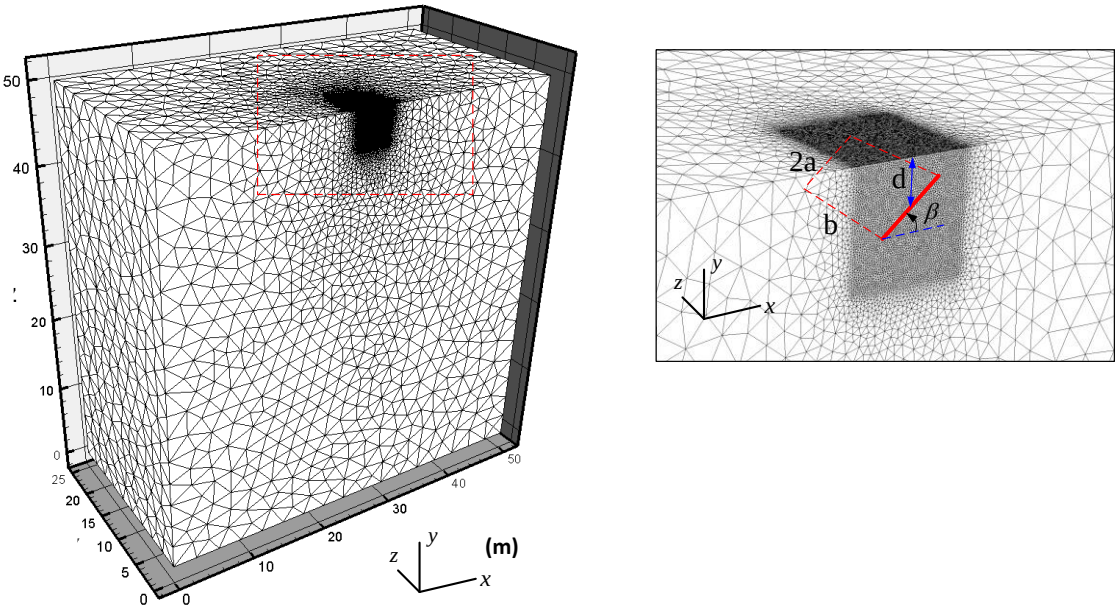

Figure 4.12. Problem geometry for 3D pressurized subsurface fracture.

The simulation results are displayed similar to 2D ones. The vertical displacements and stress contours for different dipping angles are plotted in Figure 4.13 and Figure 4.14. The comparisons of the surface normal displacement distributions between the present model and [Fu, 2014] are shown in Figure 4.15 and Figure 4.16. The original problem takes place in a semi-infinite region. However, the present model can only simulate finite domain. Therefore, the slight difference is observed between two models that are possibly because of different size of simulating domains. The

comparisons for both 2D and 3D problem indicate reasonable agreement that enhanced the confidence that the model can be adopted to simulate the fluid filled fracture during the hydraulic fracturing simulation in the following sections.

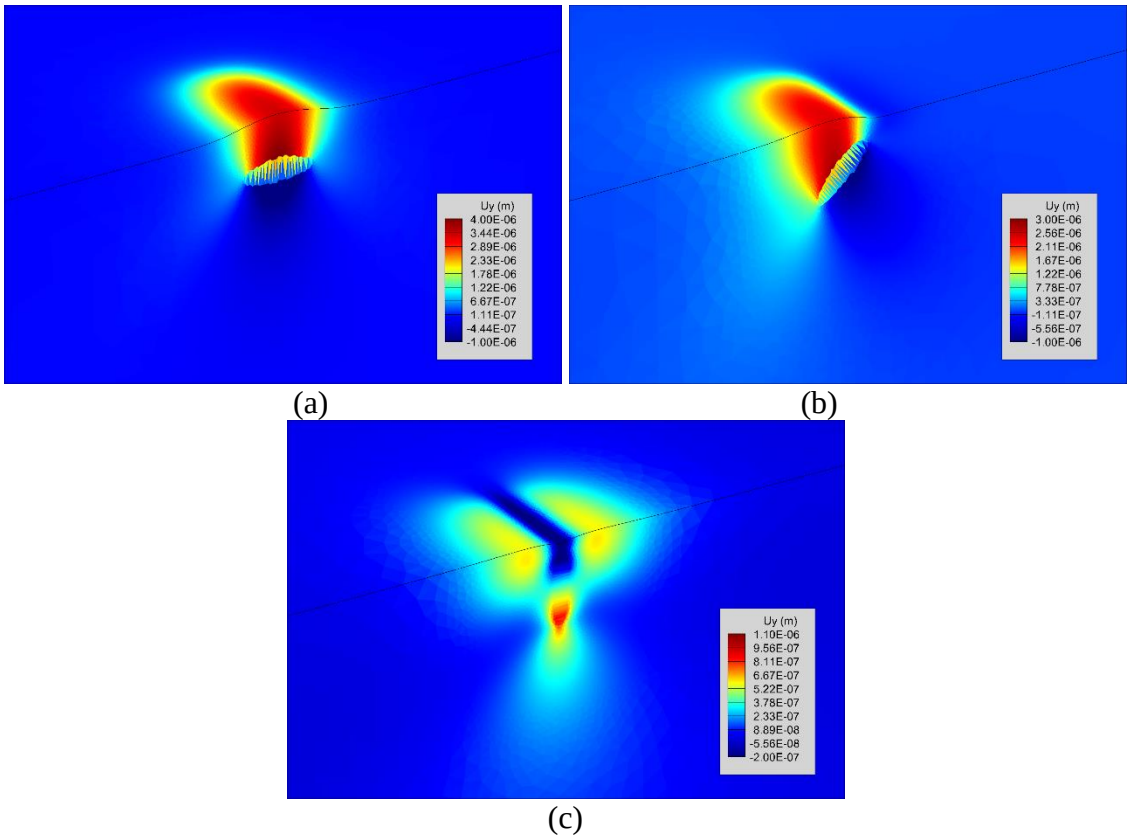

Figure 4.13. Vertical displacement in 3 different dipping angles of pressurized fracture in 3D: (a) 0 degree; (b) 45 degree; (c) 90 degree.

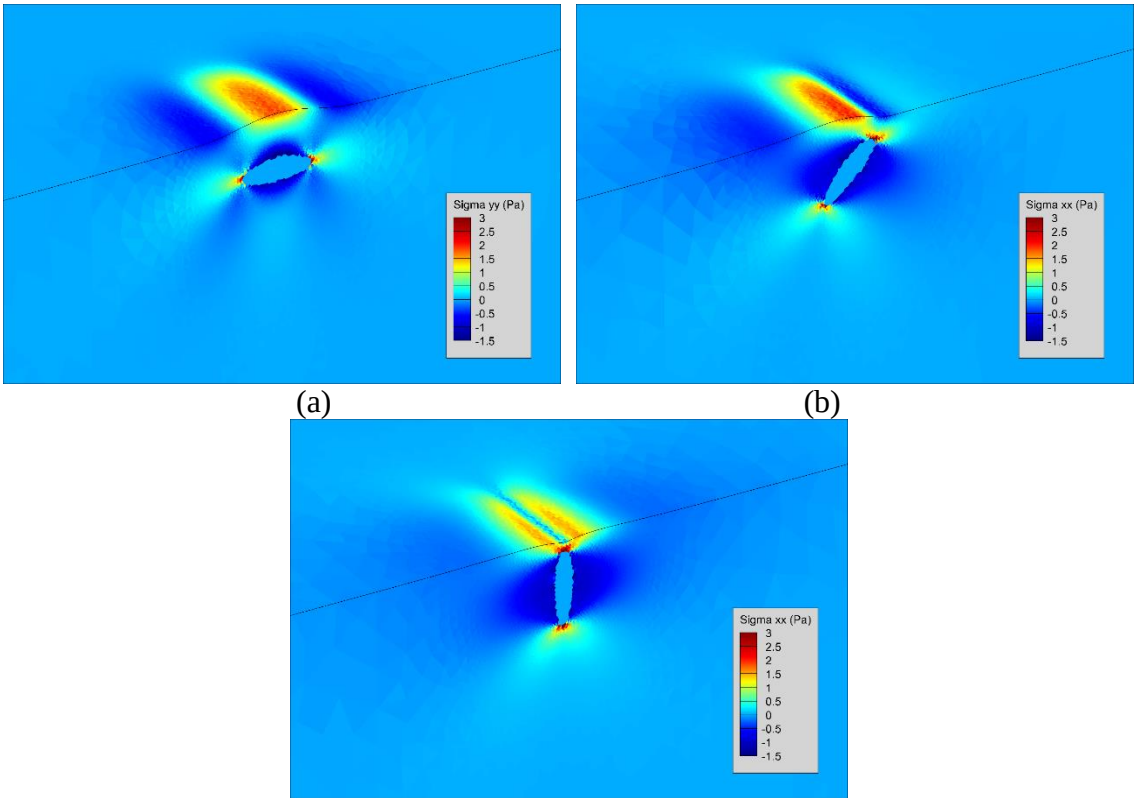

Figure 4.14. Stress contours in 3 different dipping angles of pressurized fracture in 3D: (a) σ_{yy} for 0 degree; (b) σ_{xx} for 45 degree; (c) σ_{xx} 90 degree.

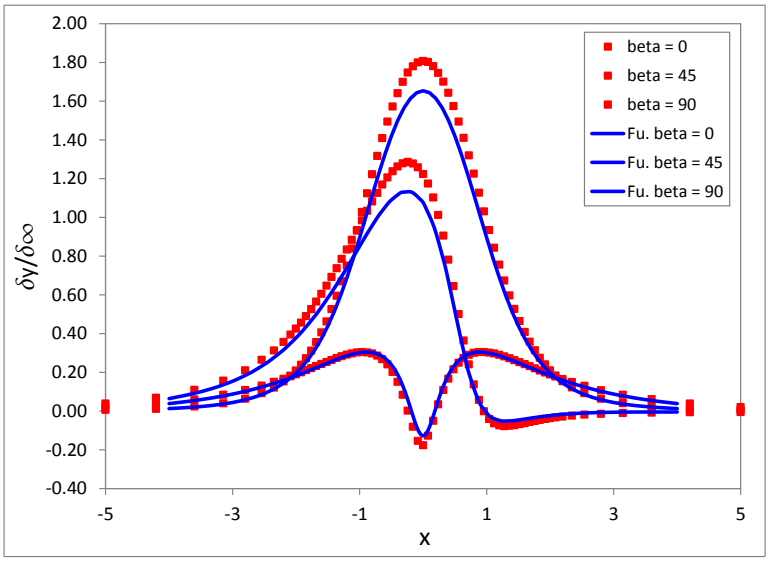

Figure 4.15. Normalized surface displacement along x axis in 3 different dipping angles of pressurized fracture in 3D comparing with the results by [Fu, 2014].

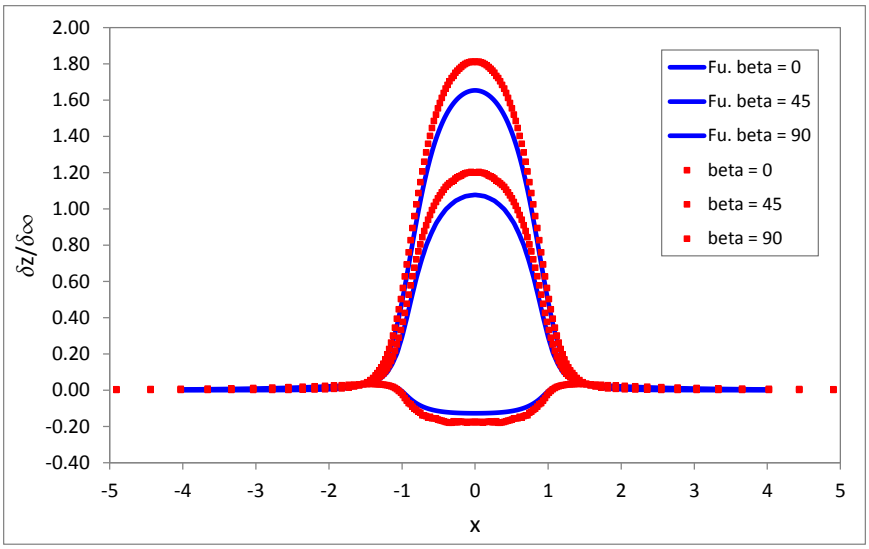

Figure 4.16. Normalized surface displacement along Z axis in 3 different dipping angles of pressurized fracture in 3D comparing with the results by [Fu, 2014].

4.2.3 Mechanical and Fluid Flow Coupling Scheme

The fluid flow in a narrow space between ideal parallel surfaces, in which one dimension is significantly smaller than other one or two dimensions, is described as lubrication flow in fluid dynamic shown in Figure 4.17. Although the fracture is not always flat, the mechanism of the fluid flow in the fracture is similar to the lubrication flow since the aperture is much smaller comparing with the length and height of whole hydraulic fracture. Using this conception, the fracture fluid flow can be captured by lubrication theory. The fracturing fluid is assumed to be incompressible Newtonian fluid from a point source injection, and its velocity and pressure gradient are negligible in normal direction of the fracture. The two-dimensional mass conservation equation is derived as:

$$\frac{\Delta w(x,y,t)}{\Delta t} + \nabla_2 q = Q_i \delta\left(x - x_{inj}, y - y_{inj}\right) \tag{4.51}$$

where w is aperture, q is the flux per unit height. Q_i is the fluid injection rate, ∇_2 is 2D divergence operator, δ is the Dirac delta function, (x_{inj}, y_{inj}) is the coordinates of injection point. Following the cubic law [Witherspoon et al. 1980], the flux for an infinitesimal element of fluid can be written as

$$q = -\frac{w(x,y,t)^3}{12\mu}\nabla_2 p(x,y,t) \tag{4.52}$$

Substituting Eq. (4.52) into Eq. (4.51), we obtain the lubrication equation (Batchelor. 1967),

$$\frac{\Delta w(x,y,t)}{\Delta t} - \nabla_2 \cdot \left[\frac{w(x,y,t)^3}{12\mu}\nabla_2 p(x,y,t)\right] = Q_i \delta\left(x - x_{inj}, y - y_{inj}\right) \tag{4.53}$$

or simplified form,

$$\frac{\Delta w}{\Delta t} - \nabla_2 \cdot \left[\frac{w^3}{12\mu}\nabla_2 p\right] = Q_i \tag{4.54}$$

During the fluid injection and fracturing processes, part of fracturing fluid may diffuse into the formation [Carter, 1957; Wiles, 1986]. Therefore, total volume of injection fluid is basically composed by the fluid storage in the fracture and the leak-off into the reservoir. Hence, unconventional fracturing applications are usually characterized by high leak-off velocity, and significant pore pressure and effective stress change in the region around the wellbore and fracture [Cottrel and Baker, 1983; Settari and Warren, 1994; Ji et al., 2009]. However, in this section, we assume the injection and fracturing time are short enough so the leak-off can be neglected. Therefore, in Eq. (4.54), there is no leak-off term indicating the way we consider the mass conservation that all the fluid is trapped between the fracture surfaces. The

diffusion of fracturing fluid during the period is going to be captured by poroelastic model in the following section.

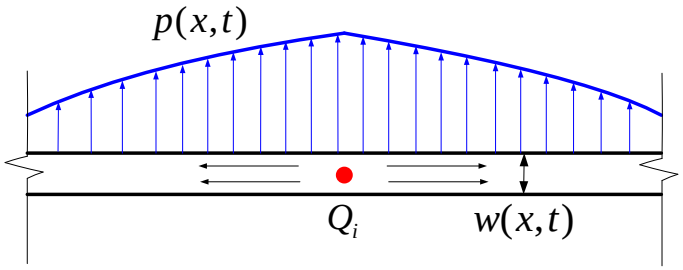

Figure 4.17. Lubrication flow between ideal parallel from a point source injection.

If the fracture is fully filled by the injecting fluid and there is no fluid lag, the assumption of the no flow boundary condition at the fracture tip is valid and realistic. On the other hand, if the fracture propagates faster than fluid [Garagash and Detournay, 2000], there is empty space between the fluid front and fracture tip. However, measuring the length of the fluid lag needs tracking both the locations of fluid front and fracture tip, which is difficult to implement. Neither no flow boundary nor introducing fluid lag is convenient and practical to be implemented in FEM simulation. Even the length of fluid lag is unknown, the pressure in fluid lag is appropriately assumed to be zero. It is practical, and meantime however, compromised that zero pressure is assumed at the fracture tip and neglects the length of the region of fluid lag in FEM implements. The boundary conditions are $Q_i = Q_0$ at injection point, and the net pressure at the fracture tip is zero based on the assumption above. And zero flux boundary condition is discussed in [A Dahi Taleghani, 2009] which is not used in present work. Hence, the opening of fracture tip is zero.

Eq. (4.54) is the local mass conservation condition at each point of fracture plane that needs one more constraint function derived from a global mass balance to determine the time increament between each propagations. By integrating the fracture aperture over the whole fracture plane, and assuming that all fluid injected is rested in the fracture (no leak-off), the global mass constrain equation is written as:

$$Q_i \Delta t = \int_{x_a}^{x_b} \Delta w dx \tag{4.55}$$

for 2D hydraulic fracturing problem and

$$Q_i \Delta t = \int_{A_f} \Delta w dA \tag{4.56}$$

for 3D hydraulic fracturing problem.

Bring the lubrication equation, constitutive equation of mechanical behavior of rock matrix associated with global constrain function together, we obtained the governing equations for hydraulic fracturing problem:

$$E_{ijkl} u_{k,li} + b_j = 0 \tag{4.57}$$

$$\frac{\Delta w}{\Delta t} - \nabla_2 \cdot \left[\frac{w^3}{12\mu} \nabla_2 p \right] = Q_i \tag{4.58}$$

$$Q_i \Delta t = \int_{A_f} \Delta w dA \tag{4.59}$$

During the coupling process and iterations, three variables play importation roles, which are aperture w, fluid pressure p and injection time t. In addition, the physical behaviors of the aperture change due to rock deformation, fluid flow in the fracture and new boundary created by fracture extension are coupled each other, which need to be solved by trial and iterations. The iteration strategy is presented in the next section.

4.2.4 Iteration Strategy for Coupling Processes

In this section, as mentioned above, the iteration processes are introduced to solve the fully coupled solid and fluid interactions. The porous rock is assumed to have very low permeability that the fluid barely diffuses into the rock matrix during the short term injection. Though the equation system shown in Eqs. (4.57)~(4.59) is similar with the fully coupled poroelastic equations, the variables are not as straightforward as the poroelastic problem in frame work of FEM, so that they cannot be solved in one matrix or linear equation system in present model. Eq. (4.57) and (4.58) are written in terms of displacement $\tilde{\mathbf{u}}$ and aperture w respectively. The aperture w is calculated based on the displacement field and location and orientation of fracture surface. Figure 4.18 shows the relative displacements of the nodes in a type I partition element along the normal direction of fracture surface. The displacements of nodes along the normal direction of fracture are written as $\tilde{\mathbf{u}}_e^{\mathbf{n}} = [u_I^{\mathbf{n}}, u_J^{\mathbf{n}}, u_K^{\mathbf{n}}, u_M^{\mathbf{n}}]$. The aperture in this type I partition element can be calculated as following:

$$w_e^{typeI} = \frac{1}{3}\left[(u_M^{\mathbf{n}} - u_I^{\mathbf{n}}) + (u_M^{\mathbf{n}} - u_J^{\mathbf{n}}) + (u_M^{\mathbf{n}} - u_K^{\mathbf{n}})\right] \tag{4.60}$$

and similarly, for type II the aperture is calculated as

$$w_e^{typeII} = \frac{1}{4}\left[(u_M^{\mathbf{n}} - u_I^{\mathbf{n}}) + (u_M^{\mathbf{n}} - u_J^{\mathbf{n}}) + (u_K^{\mathbf{n}} - u_I^{\mathbf{n}}) + (u_K^{\mathbf{n}} - u_J^{\mathbf{n}})\right] \tag{4.61}$$

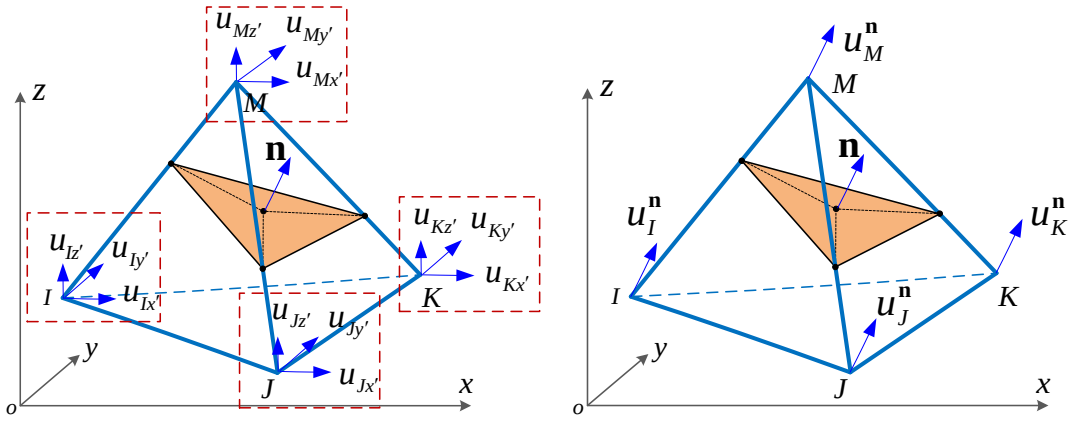

Figure 4.18. Relative displacements of the nodes in a partition element along the normal direction of fracture surface.

The rock deformation and fluid flow are two separate analyses that need establishing a coupled algorithm and transfer the results between two analyses. More important, the fracture geometry is changing during the fracturing processes. Capturing this moving boundary is challenging and crucial. Figure 4.19 helps understanding of interaction between fracture, rock deformation and fluid flow for both straight and curved hydraulic fracture problem. The mesh for lubrication fluid has been generated for the full size of simulation object from the beginning. However, only the nodes (red dots) covered by the fracture are activated. During the fracture propagation, more nodes are activated instead of generating new mesh, which are relatively easier to be implemented. For curved fracture, the length of fluid element will be modified by the inclination of fracture at that location. The moving boundary problem can be solved by activating new nodes in the fluid mesh during the fracture growth. And another challenge is the nonlinear relationship between the aperture and pressure. From Eq. (4.58) we know the pressure distribution is governed by the cubic aperture and local mass conservation term that is the aperture change rate. This fluid driven fracturing

problem has been studied by [Detournay, 2004, Adachi and Detournay, 2008] with simple geometry by assuming the planar fracture surface. [Adachi et al., 2007; A Dahi Taleghani, 2009] structured an iteration scheme using Picard iteration.

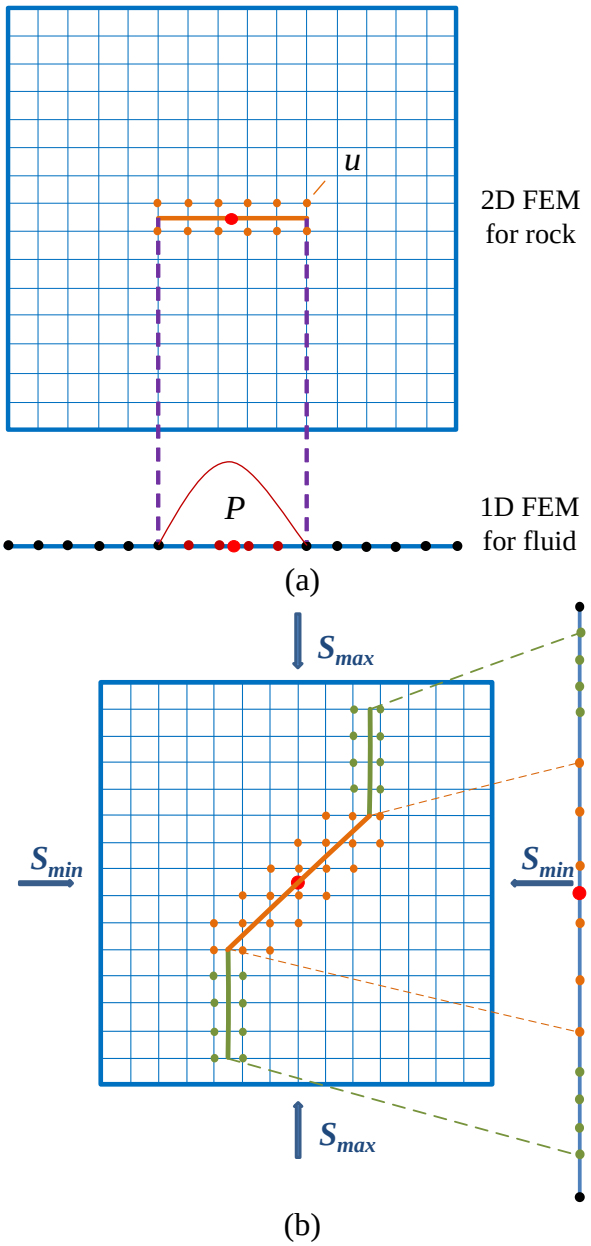

Figure 4.19. Interactions between the rock deformation, aperture and fluid flow for 2D problem: (a) straight fracture; (b) curved fracture.

This dissertation adopts nonlocal damage model to capture the fracture propagation and simulates the coupled hydraulic fracturing problem inspired by these

works. Figure 4.20 shows the flowchart of iteration processes. According to the flowchart, firstly, the model geometry for rock, fluid and fracture, realistic boundary conditions, as well as the material parameters are estimated in the beginning. The iterations and convergence check repeat for each propagating fracture configurations during the injection. The iterative procedures initiate from: (i) estimate an initial trial fluid pressure profile p_0 in the initial fracture. Then, (ii) an initial fracture aperture w_0 is calculated by applying p_0 on the fracture surfaces using Eq. (4.57). (iii) update the injection time Δt_0 through the global fluid mass conservation by solving Eq. (4.59). (iv) update the pressure profile p_1 by solving Eq. (4.58) with Δt_0 and w_0. (v) solve Eq. (4.57) for new fracture aperture w_n and then updates the new injection time Δt_n using global fluid conservation equation (Eq. (4.59)). (vi) check the convergence by comparing the pressure profile in the present iteration with previous one, and examining the average error with a given tolerance. The convergence criterion is written as:

$$\frac{\sum_{i=1}^{NE}\left|p_i^n - p_i^{n-1}\right|}{\sum_{i=1}^{NE} p_i^n} = \varepsilon_f \le \varepsilon_c \tag{4.62}$$

where p_i^n and p_i^{n-1} are the pressure in ith element at the present and previous step respectively, ε_f is the average error, ε_c is the given tolerance. If Eq. (4.62) is not satisfied, solve the fluid flow equation Eq. (4.58) with updated aperture

$$w^{n+1} = (1-\theta)w^{n+1} + \theta w^{n-1} \tag{4.63}$$

where $0 < \theta < 0.5$ and $\theta = 0.2$ is used in this work to stabilize the convergence. The new injection time t^{n+1} is updated by w^{n+1}. The iterations repeat until the solutions

converged in the given tolerance. (vii) the converged pressure profile is then applied on the fracture surfaces to simulate the fracture propagation. (viii) the fracture propagates and updates length or configuration of fracture. Therefore, iterations run again with the new fracture geometry and repeat the steps mentioned above until the target injection time or target length is reached.

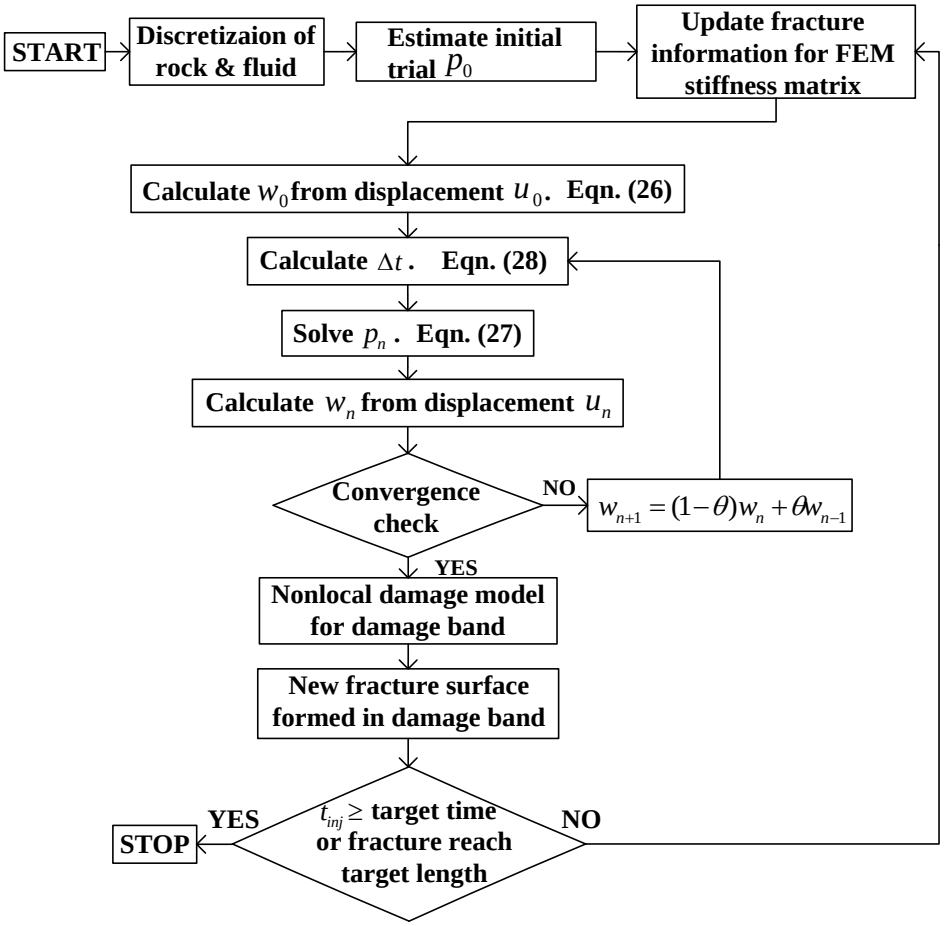

Figure 4.20. Flowchart illustrating the iterations for the fully coupled procedure.

4.2.5 Identification of Newly Extended Fracture in the Damage band

The converged fluid pressure profile is applied as boundary condition to simulate the new fracture growth. In nonlocal damage model, a damage band or fracture process zone will develop at the crack tip. The width of damage band is governed by the

internal radius R, which is composed by several damaged elements. The band shape of damage zone brings difficulty to fluid flow solution and rock mechanical part on applying pressure boundary conditions. To keep the validation of assumptions in the last section, we assume the fluid will choose a most favorable flow path within damage band shown in Figure 4.21. Figure 4.21(a) shows a pre-existing fracture. The orange dots in Figure 4.21(b) represent the centers of damaged element at both crack tips. The most favorable flow path is determined by the polynomial fitting based on these scattered damage element centers. Finally, by knowing the polynomial function from fitting, the newly extended fractures are determined shown as Figure 4.21(d), which serves as new boundary for both rock mechanical and fluid flow solutions in the next coupling processes.

This technique works for 2D hydraulic fracture process and 3D one with a fracture that is cut-through in one of three dimensions. Though 3D simulation could adopt similar conception, the true 3D fracture is mostly propagating with complicate geometric shape due to complex geological conditions. It is very difficult and time consuming to find a fitted spatial curved surface in the damage band. The geometric problem becomes even tougher when the hydraulic fracture is interacting with nature fractures. Meantime, since the element size is required to be smaller than characteristic length l_c or internal radius R with the length of several millimeters, the true 3D simulation using nonlocal damage theory requires large computational volume even for the problem in the domain with length of several meters.

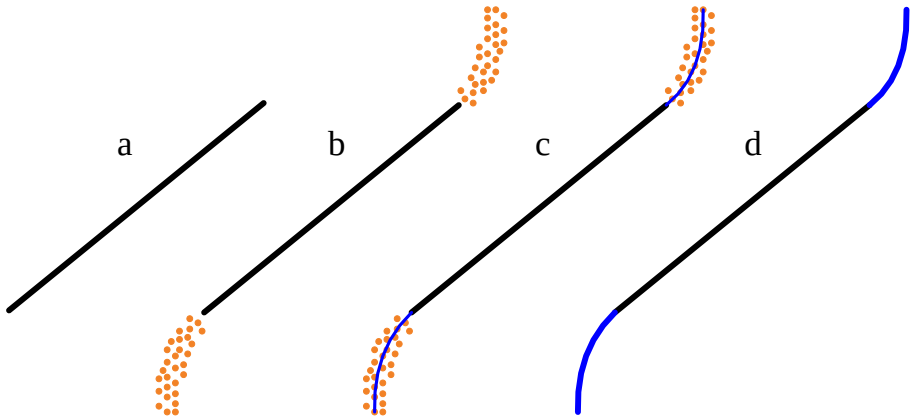

Figure 4.21. Identification of newly extended fracture in the damage band.

4.2 Conclusion

In this chapter, as another crucial aspect of hydraulic fracturing processes, the methodologies of fluid flow for the hydraulic fracture propagation simulation were presented. Generally, the flow mechanisms are very difficult to be captured by an integrated method. The present work introduced two models for fluid analysis using poroelastic model and lubrication theory. For both theories, analysis coupled the fluid flow and deformation of rock mass based on different mechanisms.

Using lubrication theory, the flow in fracture was analyzed to solve the fluid pressure profile in the pre-existing and newly extended fracture. And the physical behaviors of the aperture change, fracture fluid pressure and new boundary created by fracture extension were coupled each other, which need to be solved by trial and iterations. Three coupled equations represented the mechanical equilibrium state of rock mass, continuity equation of fluid following cubic law and global mass conservation respectively. Iteration strategy for coupling processes was also illustrated in this chapter. More importantly, capturing the moving boundary of a propagating fracture was captured by nonlocal damage theory and 3D EPM. A new technique to identify the

most preferable path in the damage band using polynomial fitting is presented so that the 3D EPM can be used on this fitted path. The pressure boundary condition is successfully applied in the fractured element supported by the simulation examples of 3D EPM on pressurized subsurface fracture. The leak-off effects are neglect based on the assumption that the inject time are relatively short.

The fully coupled poroelastic model captures the porous solid deformation and porous fluid diffusion very well. A well agreement was found by comparison between the results from present poroelastic model and the analytical solution of Terzaghi one-dimensional consolidation. However, poroelastic model cannot be claimed as an ideal model to analyze the fluid flow in the fracture. The present work artificially increased the permeability of fractured element to simulate the conductivity enhancement by the fracture opening. The fluid will automatically find the path to the fracture tip and the leak-off phenomenon can be performed by the diffusion equation in poroelastic model. Although this model is not rigorous enough to provide precise fluid pressure along the fracture surface, the overall tendency of fracture and pore pressure distribution and fracture propagation can still be modeled considering the computational feasibility and efficiency, especially for the hydraulic fracture problem with complex geometry and boundary conditions such as hydraulic fracture and natural fractures interaction. The simulation examples of hydraulic fracturing will be presented in Chapter 7.

Chapter 5. Numerical Simulation of Fracture Propagation under Mechanical Loading

Propagation of fractures, especially those emanating from wellbores and closed natural fractures, often involves Mode I and Mode II, and some times Mode III fracture propagation, posing significant challenges to its numerical simulation. When an embedded inclined fracture is subjected to compression, the fracture edge is constrained by the surrounding materials so that its true propagation pattern cannot be simulated by 2D models. Additionally, fracture pattern is usually complex due to many factors such as initial imperfection, grain size of rock and heterogeneity. However, this work generally focuses on the major fracturing pattern of mixed mode fracture adopted the assumption of material homogeneity and isotropy. Take advantage of the nature of finite element method, the elemental based distributed heterogeneity can be conveniently introduced into the model.

Before being adopted in the hydraulic and thermal fracturing modeling especially for 3D problem, the constitutive models must successfully simulate the fracture pattern under mechanical loading. In this chapter, a virtual multidimensional internal bond (VMIB) model is presented to simulate three-dimensional fracture propagation. The model is applied to simulate fracture propagation and coalescence in typical laboratory experiments and is used to analyze the propagation of an embedded fracture. Simulation results for single and multiple fractures illustrate 3D features of the tensile and compressive fracture propagation, especially the propagation of a Mode III fracture. VMIB provides well suggestion on the fracture propagation pattern, however, also has the common disadvantage of the strain softening model that is called mesh size

sensitivity. As introduced in Chapter 2, the phenomenon of mesh size sensitivity is discussed by [Bazant and Planas, 1998] that indicates the results are affected by using different mesh sizes. Continuum damage theory in nonlocal formulation is adopted in this work to remedy the spurious size dependency. Using nonlocal formulation, finite element analysis can successfully calculate energy dissipation during strain localization through capturing stable damage driving force independent with the size of element. A certain representative volume defined nonlocally by a characteristic length l_c that is a dependent material parameter with the grain size of rock. Mode I and mixed mode fracture according the experiments are tested to validate the performance of nonlocal damage model on representing the pre-peak and post-peak mechanical behaviors of rock during the propagation.

5.1 Simulating Fracture Propagation in Different Modes Using VMIB

5.1.1 Mode I fracture

To examine the performance of VMIB and 3D EPM in simulating tensile (Mode I) fractures propagation and their interaction, a cubic specimen with two sawed horizontal rectangular fractures is simulated. The geometry is shown in Figure 5.1. The uniaxial vertical tensile load is applied on the top of the specimen. Table 4 shows the parameters used. The mesh consists of 12, 24 and 34 rows of nodes plotted on the x, y and z direction respectively. The total element number is 41745 and the total node number is 9792. Displacement controlled loading is employed in this simulation.

Table 4. Parameters of Simulations Using VMIB Model

Parameters of intact element:	
Young's modulus, E	30.5 GPa
Poisson's ratio, ν	0.20
Tensile strain strength, ε_t	0.105×10^{-3}
Parameters of 3D EPM:	
Normal stiffness coefficient, K_n / h	10.0 GPa/m
Shear stiffness coefficient, K_s / h	10^{-8} GPa/m
Fracture width, h	1.0 mm
Parameters of 3D VMIB:	
c	0.15
n	4.0

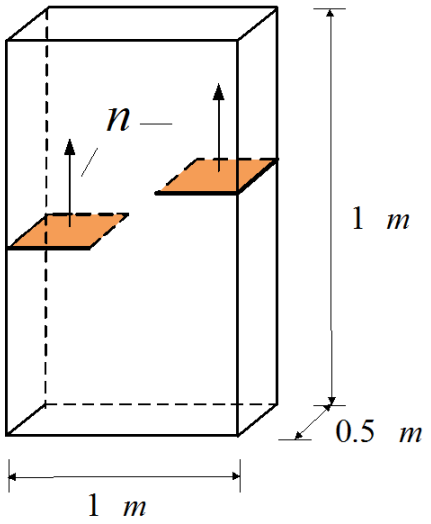

Figure 5.1. Problem geometry and boundary condition of a specimen with two horizontal rectangular fractures, subjected to vertical tension.

Figure 5.2(a) shows the initial and final fracture patterns. From Figure 5.2(b) to (d), the fractures develop from initial crack tips and propagate horizontally as typical Mode I fractures. As the fractures interact with each other, the stress field around the fracture tips is disturbed. Consequently, the newly extended fracture deviates towards

the other one and coalesce. Figure 5.2(e) and (f) show the fracture surface and deformed mesh configuration upon specimen failure.

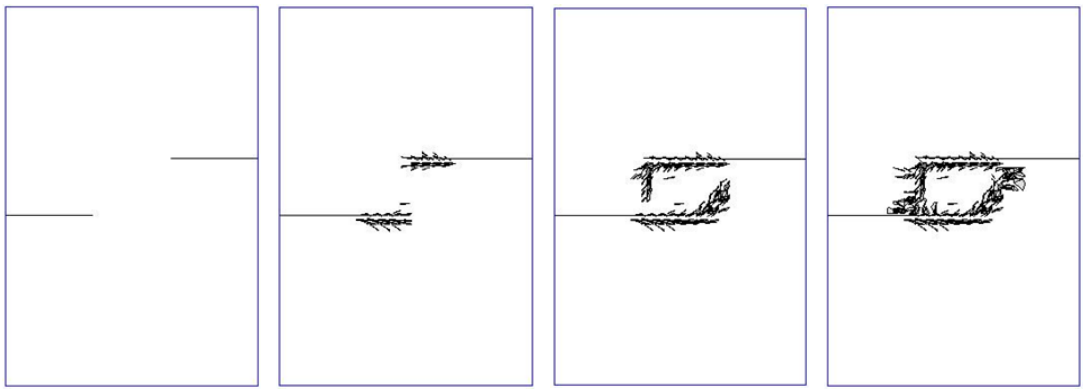

(a) (b) (c) (d)

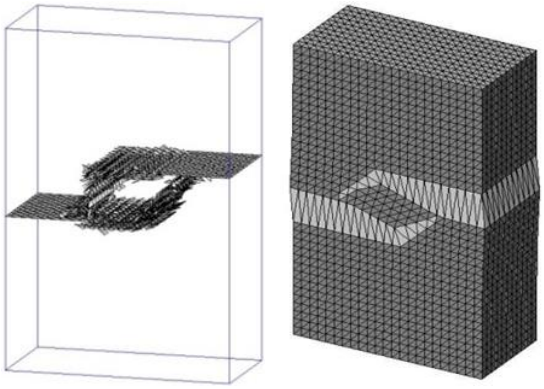

(e) (f)

Figure 5.2. Fracture propagation: (a) initial fracture; (b-d) fracture propagation; (e) fracture surface at failure,and (f) deformed mesh configuration (node displacements magnified 300 times).

5.1.2 Mode II fracture

The second simulation explores Mode II fracture propagation and interaction. A cubic specimen with two sawed inclined rectangular fracture is simulated. The dimensions and boundary conditions are shown as Figure 5.3. Material and model parameters showed in Table 4. The mesh consists of 26 rows of nodes plotted on the

each direction. The total element number is 78125 and the total node number is 17576. Displacement controlled load is used in this simulation. Figure 5.4(a) shows the initial fracture. From Figure 5.4(b) to (d), the fractures propagate from both wings of the initial cracks. The left wing of lower initial fracture and the right wing of upper fracture yield newly-extended fracture firstly along the direction perpendicular to the fracture surface.

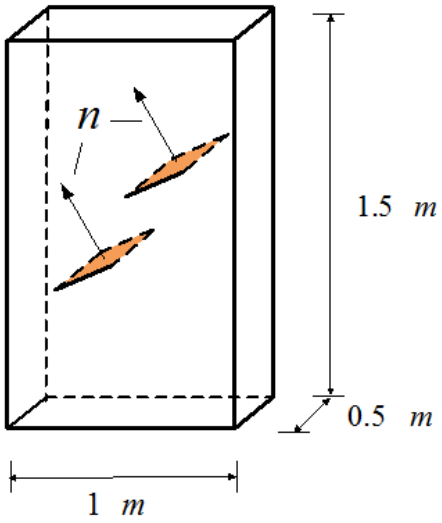

Figure 5.3. Problem geometry and boundary conditions for the cubic specimen with two sawed inclined rectangular fractures, subjected to vertical compression.

Then, the newly extended fractures develop along the vertical direction axis of the specimen in the direction of the applied maximum stress. This agrees with experimental observation [Bobet and Einstein, 1998]. The fractures extend from near side initial fracture tips and converge in the middle of the specimen. Figure 5.4(e), (f) shows the fracture surface and deformed mesh configuration at failure. This agrees with experimental observations in Figure 5.5.

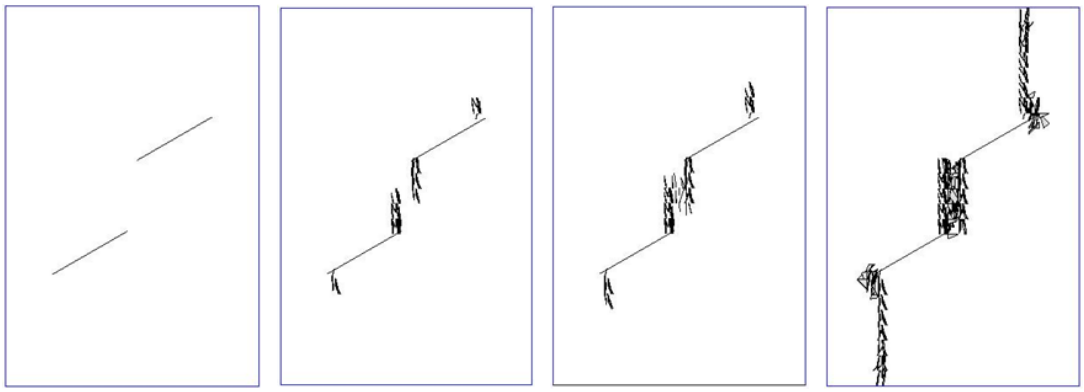

(a) (b) (c) (d)

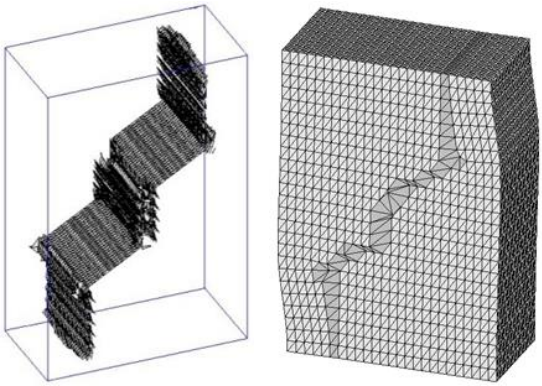

(e) (f)

Figure 5.4. Fracture propagation: (a) initial fracture; (b-d) fracture propagation; (e) fracture surface at failure,and (f) deformed mesh configuration (node displacements magnified 300 times).

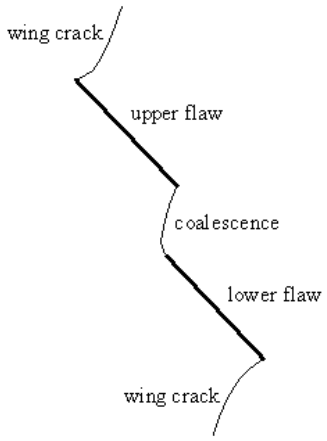

Figure 5.5. Experimental observation of wing crack growth in uniaxial compression [Bobet and Einstein, 1998].

5.1.3 Embedded fracture (Mix Mode-I, II, III)

Simulating the propagation of an embedded fracture subjected to shear stresses is a challenging problem in geomechanics. In this case, the fracture simultaneously involves Modes I, II and III. To model this phenomenon, consider the simulation of embedded elliptical fracture. The dimensions and boundary conditions are shown in Figure 5.6. Material and model parameters are given in Table 4. In presented meshing scheme, there are 45 rows of nodes each plotted on the x, y and z direction. The total element number is 425920 and the total node number is 91125. Figure 5.7(a) shows the initial fracture. The processes of fracture propagation are shown in Figure 5.7(b)~(f). The normal direction of the initial fracture plane is given as 60°.

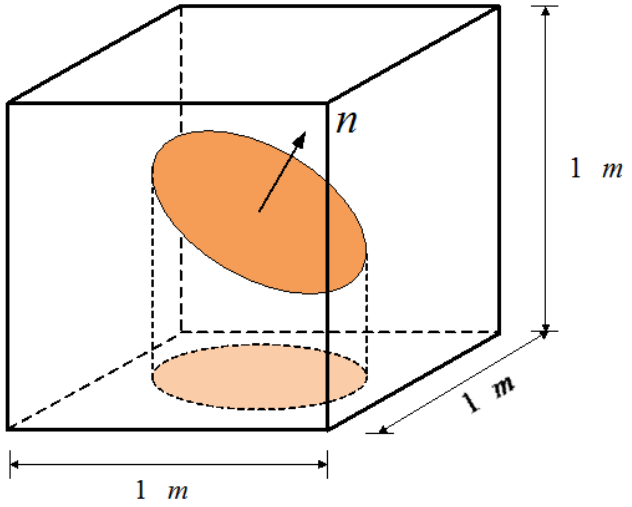

Figure 5.6. Problem geometry and boundary conditions of a cubic specimen with an embedded elliptical fracture.

The appearance of the crack tip after some crack growth has occurred is shown in Figure 5.7(b). It is observed that the crack has not grown by extending its own plane but by generating multiple tiny fracture surfaces which deviate from its original crack front. Similar phenomenon is captured in the experiment for observing the crack propagation in anti-plane shear tested by [Knauss, 1970], which is shown in Figure 5.8. The newly-extended fractures "straddle" the pre-existing straight crack tip. Then these tiny fractures around the original crack tip will form new crack tip which will influence the orientation of consequently opened fracture. Figure 5.7(c)-(f) shows that the fracture develops from upper and lower tips of initial fracture in a typical Mode II fracture. The fracture propagation is slower on the sides tip as it propagates outwardly to the lateral side of specimen. From Figure 5.7, the side fracture that initiated from the side tip rotates from the initial crack tip toward the lateral side of specimen, which represents the Mode III response.

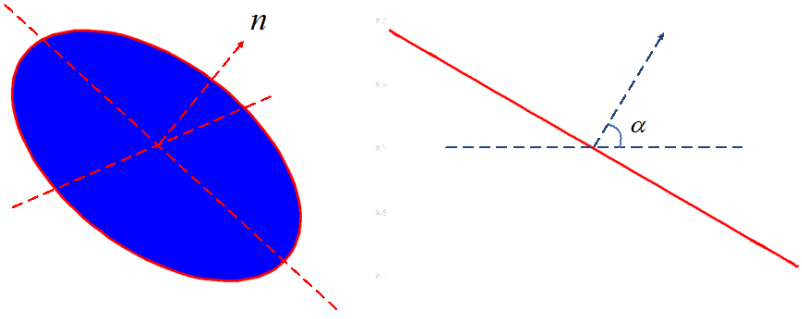

(a)

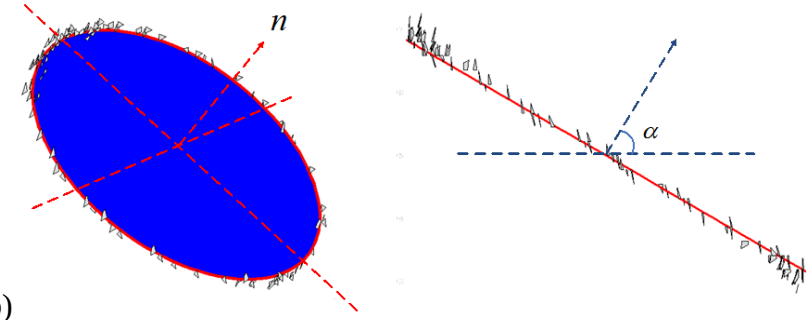

(b)

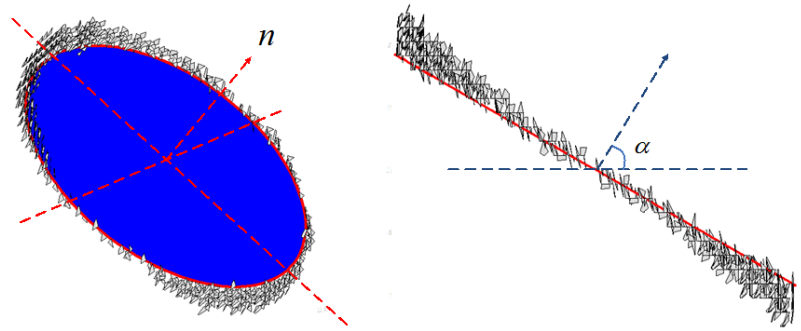

(c)

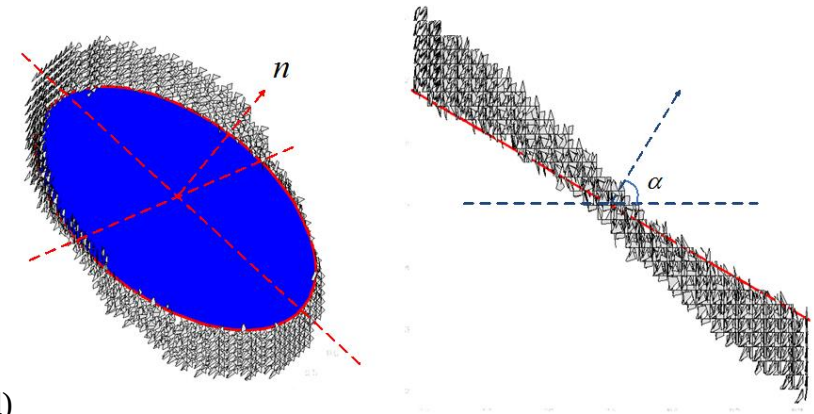

(d)

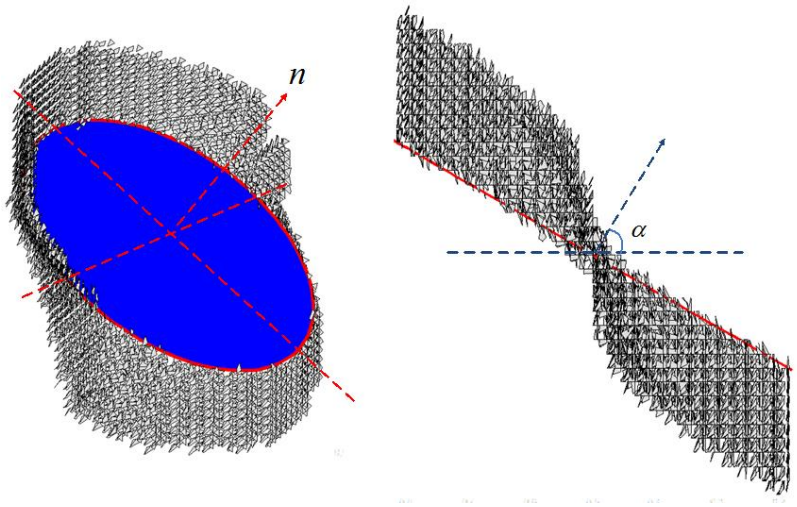

(e)

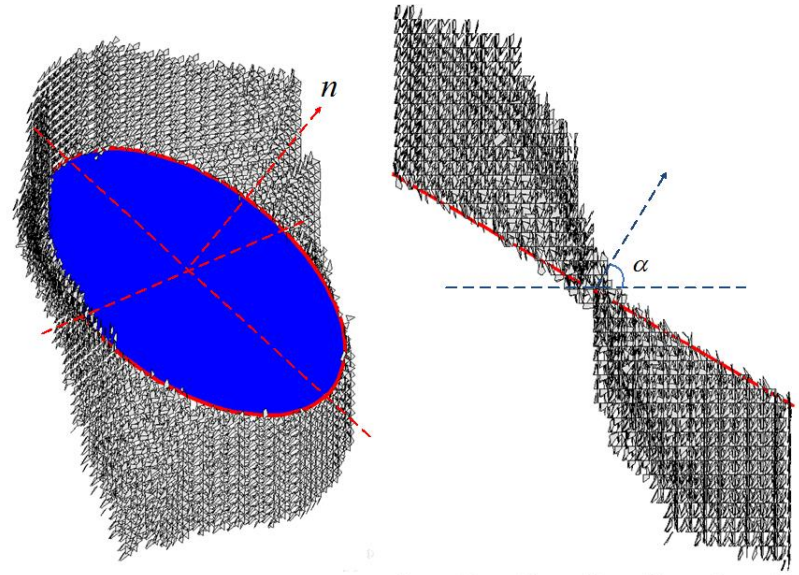

(f)

Figure 5.7. Fracture propagation stages: (a) initial fracture and (b–f) propagated fracture.

Figure 5.9 shows the fracture surface at failure from different viewpoints. For the purpose of visualization, the failure specimen is sliced into 6 pieces which is shown in Figure 5.10 and Figure 5.11. Figure 5.12 indicates the rotation angle of Mode III fracture between the middle slice and lateral surface of specimen. Also, it shows the fracture surface tends to propagate along vertical direction, or the maximum stress direction. As a result, according to the observed phenomenon, if the specimen is large

enough, mode III fracture will gradually turn to be mode I which open in the direction of maximum tensile stress. Mode II fracture has the similar tendency that gradually propagates into mode I pattern which is shown in mode II fracture simulation above.

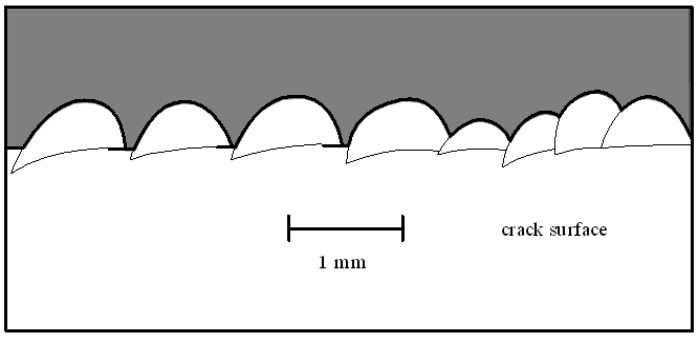

Figure 5.8. Close-up view of crack extension from the direction normal to the original crack as observed in experiments [Knauss, 1970].

This pattern of fracture propagation has been observed in experimental modeling of 3-D crack growth from pre-existing circular crack by [Adams and Sines 1978]. Also, [Dyskin et al., 2003] tested wing crack model using a brittle material with the presence of the contact effect. In their experiments, [Dyskin et al., 2003] observed secondary cracks (called “wings") branched towards the axis of compression from the upper and lower tips of the initial circular crack due to mixed mode of K_{II} and K_{III} related to the contact between pre-existing crack surface (Figure 5.13)

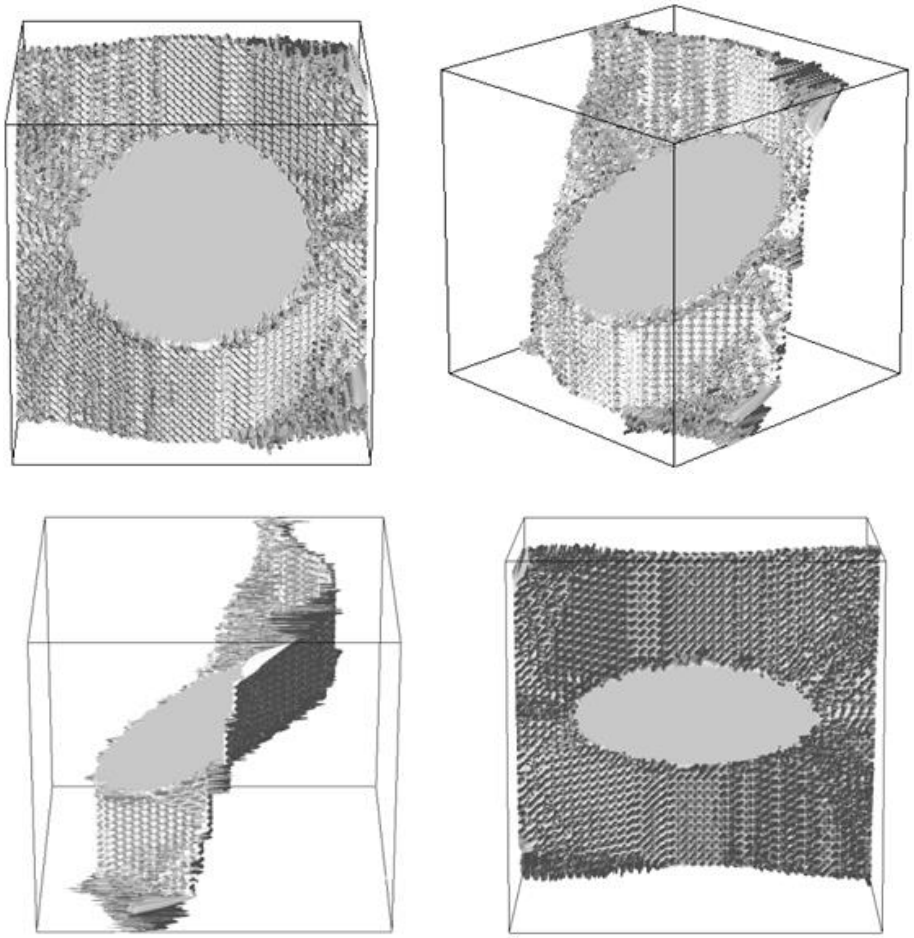

Figure 5.9. Illustration of fracture surface at failure.

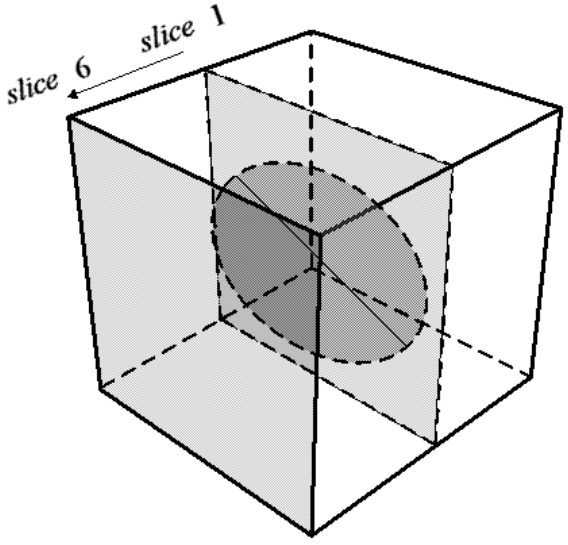

Figure 5.10. Illustration of the location of the slices in the specimen.

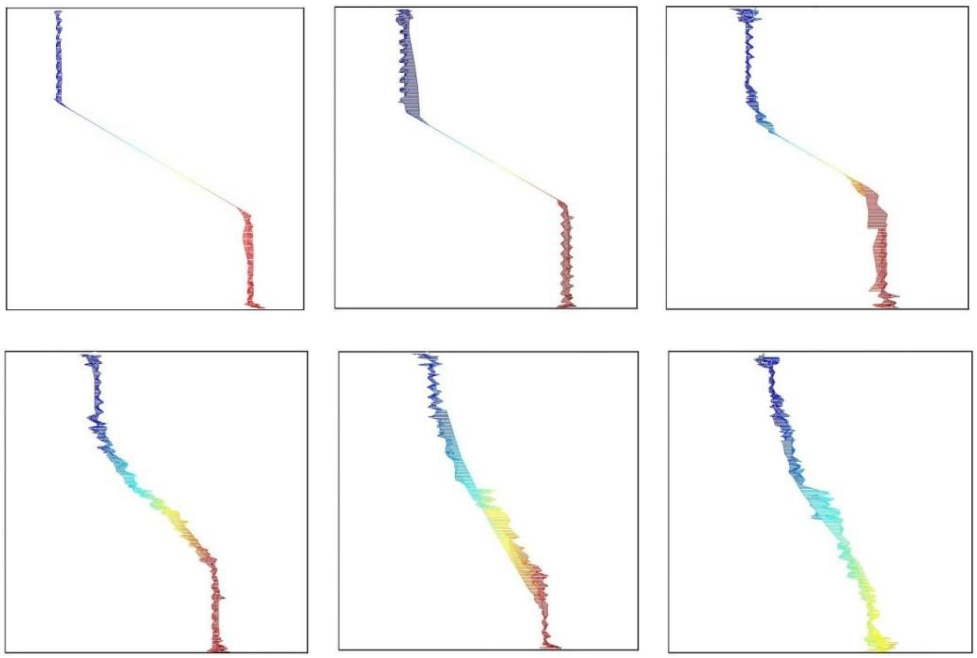

Figure 5.11. Illustration of fracture geometry (surface orientation) in the specimen for different slices from slice 1 to slice 6.

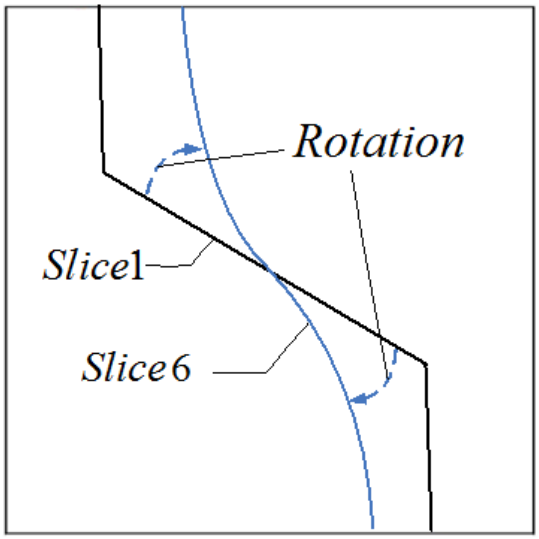

Figure 5.12. The fracture rotates between the middle slice and the side slice of the specimen as it propagates in mode III.

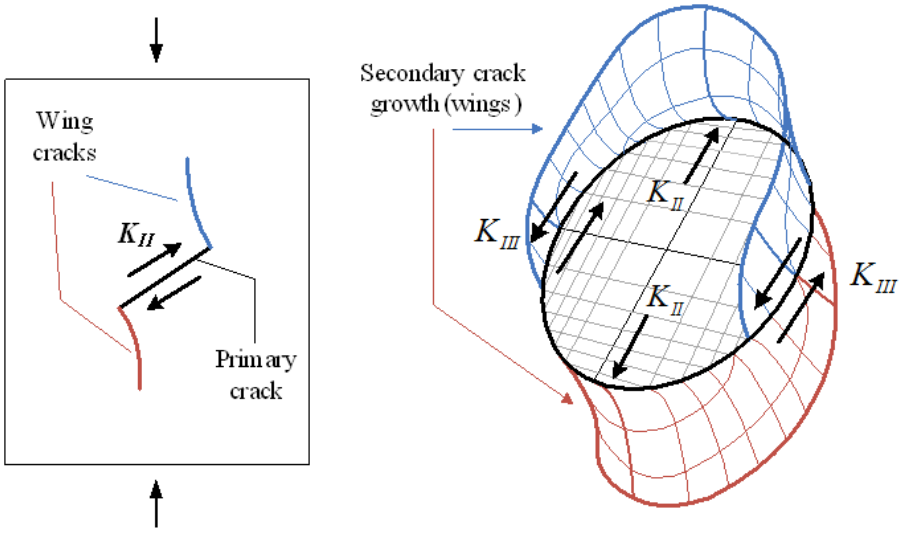

Figure 5.13. Two-dimensional wing crack growth (K_{II}) and 3D wing crack growth (mixed mode of K_{II} and K_{III}).

5.2 Simulating Fracture Propagation Using Nonlocal Damage Model

5.2.1 Three Point Bending Test

To verify the nonlocal formulation of damage model in remedying the spurious mesh sensitivity, the three-point bonding test of notched concrete beam is simulated. The cross section of the beam is 100 mm by 100 mm with the span of 450 mm. To save computational volume, the thickness is reduced from 100 mm to 10 mm. The forces on the loading points are multiplied by 10 and then compared with the test results. The notch is created with 5 mm width and 50 mm height on the lower side of the beam. Figure 5.14 shows the dimensions of the simulated specimen. Three mesh schemes are simulated to describe the effects of different mesh sizes, which are shown in Figure 5.15. Finer meshes are generated near the notch sections with approximate sizes of 5 mm, 2.5 mm and 1 mm respectively.

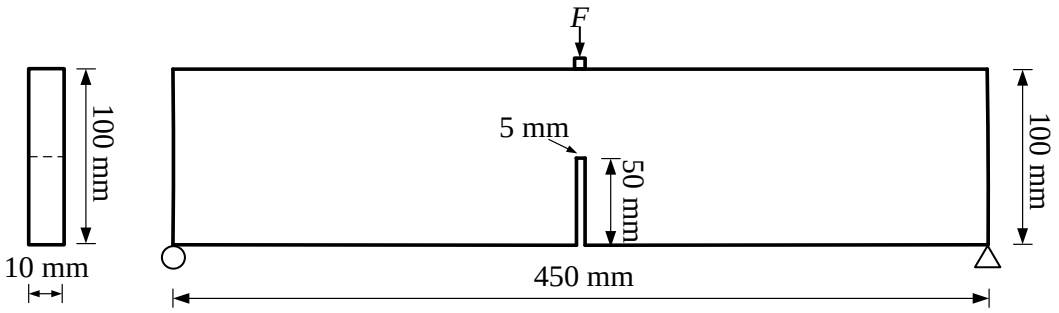

Figure 5.14. The dimensions of the simulated three points bending specimen.

In present numerical tests, the elements are linear tetrahedron element with single integral point, and the Young's modulus and Poisson's ratio are set as $E = 20GPa$ and $\nu = 0.2$ respectively. The damage evolution is represented by nonlocal formulation of exponential softening expressed as Eq. (2.32), in which the parameters are set as $\varepsilon_0 = 9\times10^{-5}$ and $\varepsilon_f = 7\times10^{-3}$. In Eq. (2.32), ε_0 associated with Young's modulus E controls the peak value of elemental strain-stress curve and ε_f governs the total area under strain-stress curve, in other words, is to control the ductility of material. A larger value of ε_f means higher energy consumed during softening and failure process. For nonlocal weight function, a quartic form function is employed shown as Eqn. (2.36). The nonlocal interaction radius is set to be $R = 2.5mm$.

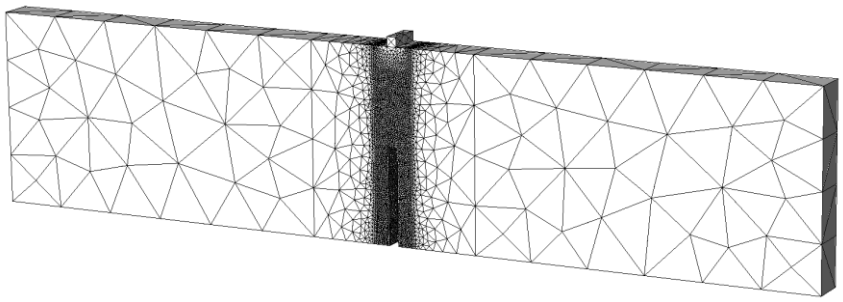

(a)

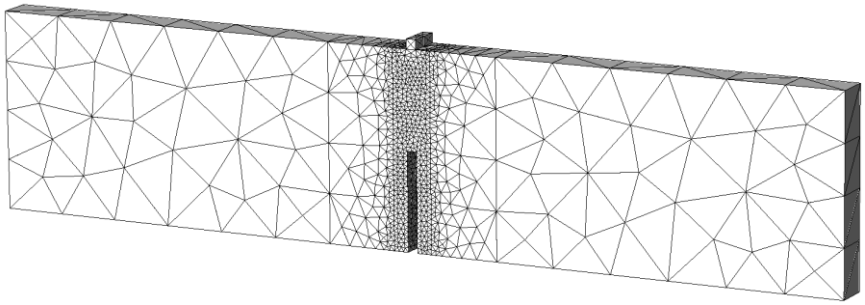

(b)

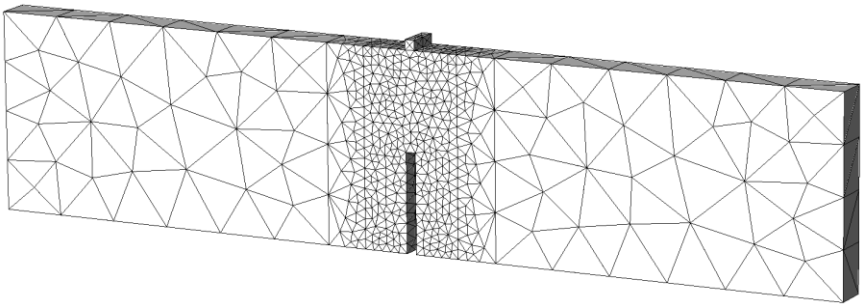

(c)

Figure 5.15. Mesh schemes with element sizes of: (a) 5 mm; (b) 2.5 mm; (c) 1 mm.

Figure 5.16~Figure 5.18 show the numerical results for three-point bending test. Figure 5.16 displays the evolving contours of nonlocal formulated damage density for each mesh scheme. The damage density ranges from zero to one. Zero value of damage density means the intact material shows in white color and zero indicates completely damaged represented by blue color. The damage firstly occurs in the notch tip, and then develops vertically. The overall size of the damage area are still controlled by nonlocal interaction radius R. The highly damage regions, where the damage density is higher than 0.95, can be observed with width around 5 mm that is independent with the element size used in the simulation. The simulated load-displacement curves compared with the experiment envelope are shown in Figure 5.17. All the curves agree with the

experiment curves well and close to each other, especially for the curves result from 2.5 mm and 1 mm element size, which indicate that the nonlocal damage model used has minimized the mesh size dependency. It is logical to consider that 5 mm element size is greater that the preset 2.5 mm interaction radius that induced in some degrees of discordance with the results from other two mesh schemes. Still, 5mm element holds considerable accuracy. [Jirasek, 2004] discussed that inaccuracy occurs when element size is larger than the interaction radius. Figure 5.18 shows the deformed mesh configuration. The largest deformation still concentrates within one element that means the major fracture will be located in most preferable path throughout the damage region. This conception will be used in the following hydraulic fracturing simulation.

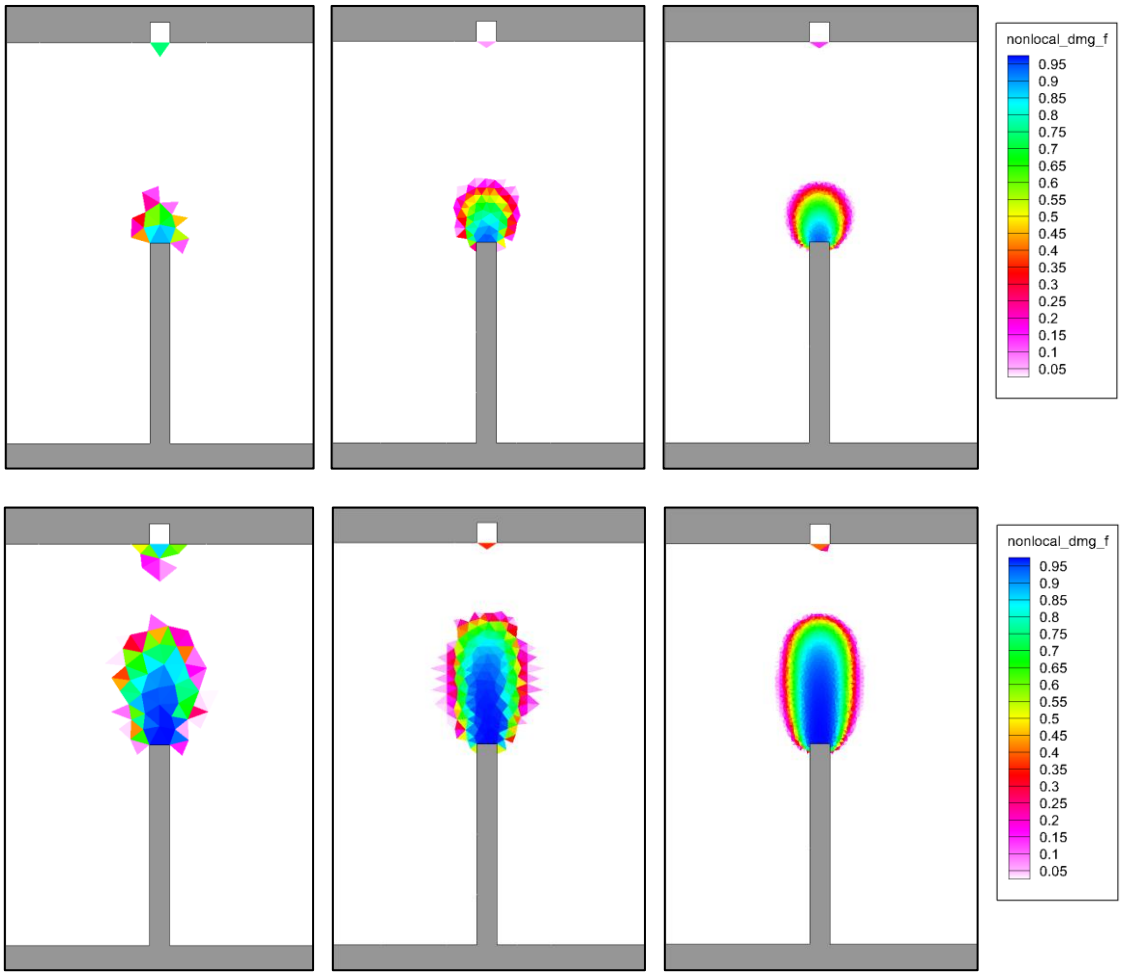

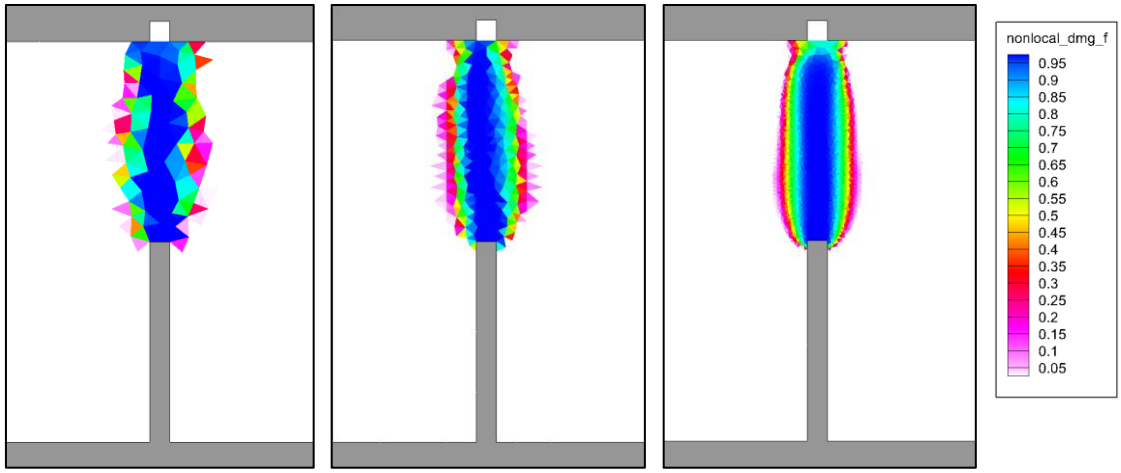

(a) (b) (c)

Figure 5.16. Nonlocal damage density contours of the process zone in simulations with element sizes of (a) 5 mm; (b) 2.5 mm; (c) 1 mm.

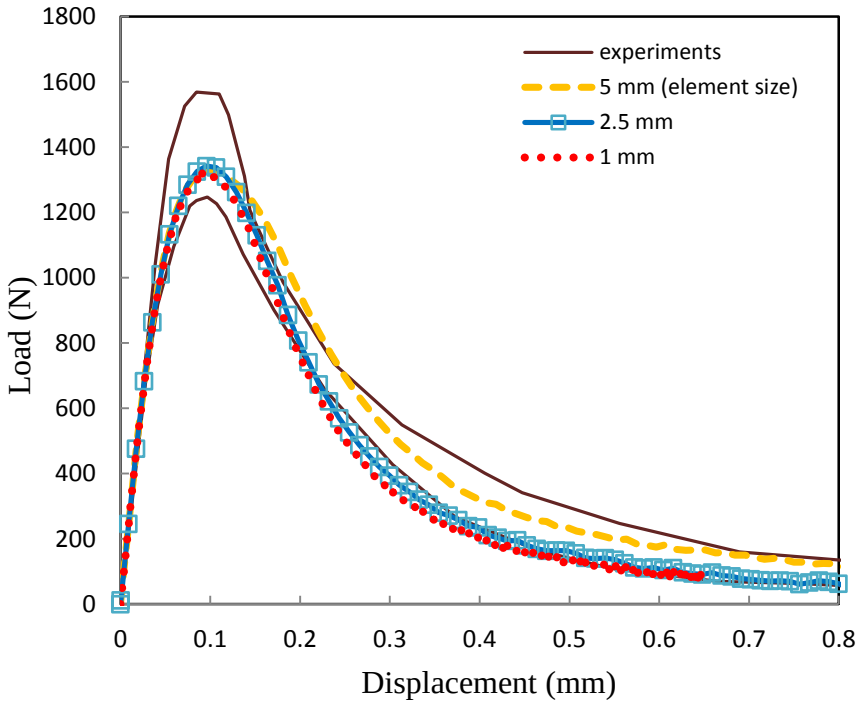

Figure 5.17. Load vs displacement diagram.

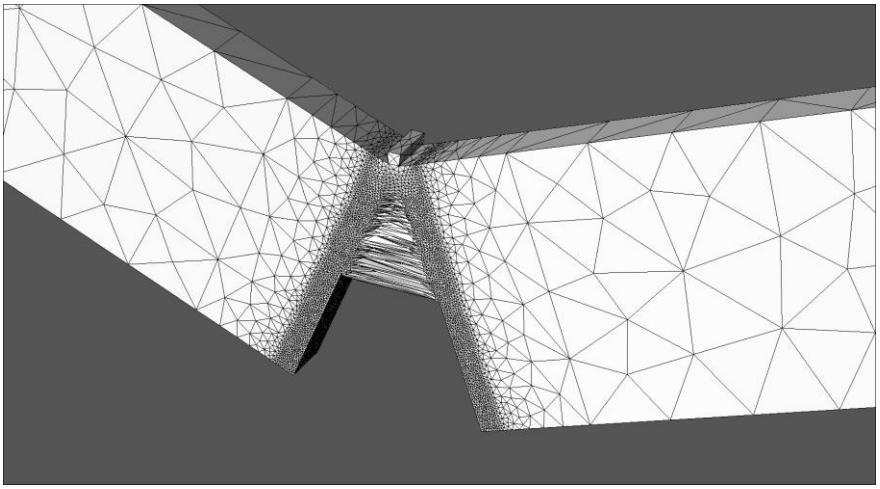

Figure 5.18. Deformed mesh configuration at failure. (amplified by 1000 times).

5.2.2 Mix-mode Test of Double-Edge-Notched Specimen

Beside the pure tensile Mode I fracture, the rock formation is often subjected to a shear and tension or compression combined loading and develops mixed-mode fracture propagation. To test the present model in simulating mixed mode fracture, we are presenting a simulation of the double-edge-notched (DEN) specimen with load-path 6a reported in [Nooru-Mohamed, 1992]. The dimension of DEN is 200 mm by 200 mm with the thickness of 50 mm, with two cut-through 5 mm by 30 mm notches shown in Figure 5.19(a). The displacements on the bottom and lower-right boundary are constrained. Displacement control is used in the experiment. An axial tensile and a lateral compressive load are applied on the top and upper-left side of specimen respectively. The ratio of displacement increment on top and upper-left side is constant and equals to $\delta_1 / \delta_2 = 1$. The Young's modulus and Poisson's ratio are $E = 20GPa$ and $\nu = 0.2$ respectively. For damage evolution function, we use $\varepsilon_0 = 1.2 \times 10^{-4}$ and $\varepsilon_f = 6 \times 10^{-4}$. The nonlocal interaction radius is set to be $R = 2.5mm$.

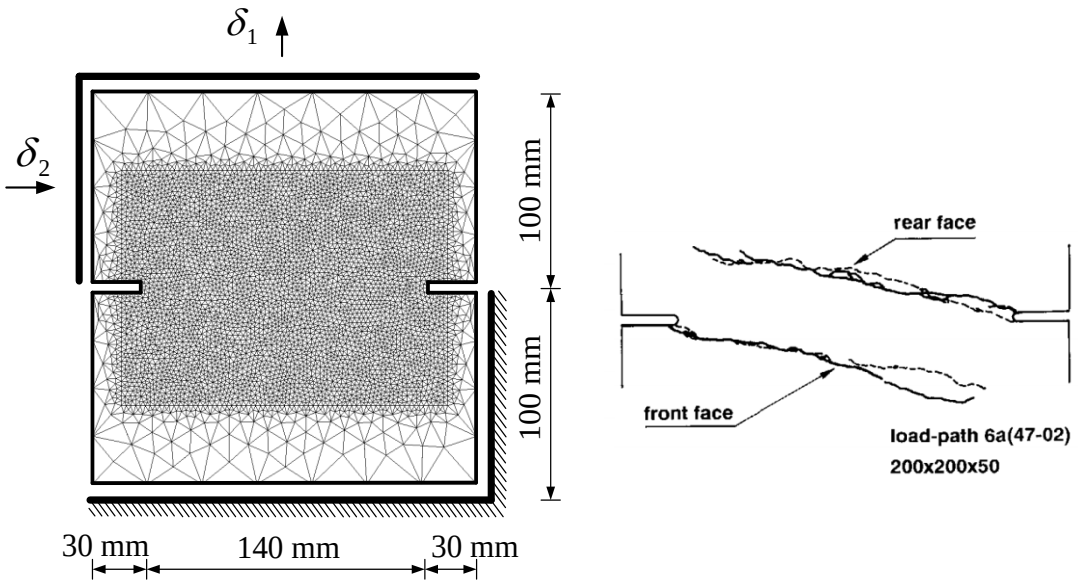

(a) (b)

Figure 5.19. The simulated double-edge notched specimen: (a) dimensions; (b) experimental crack pattern.

Figure 5.20 shows the numerical results. The fracture pattern is represented by the damage density and deformed mesh configuration. The fracture pattern shown in Figure 5.19(b) agrees well with experiment result, which indicates the present model can predict the propagate direction if material is subjected to tensile and shear combined load.

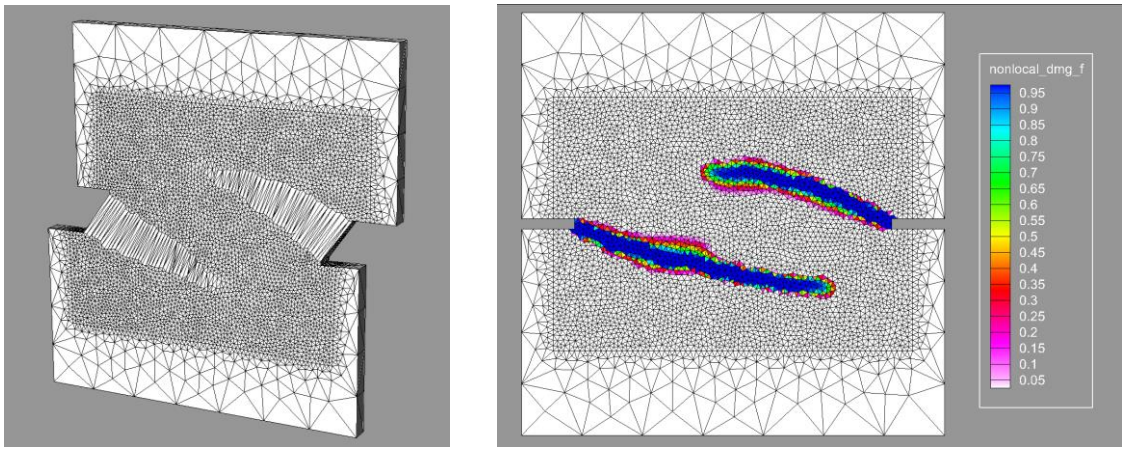

Figure 5.20. Numerical results: (a) crack pattern; (b) nonlocal damage density contour.

5.3 Conclusion

This chapter simulated the mechanical behaviors of rock subjected to mechanical loading using virtual multidimensional internal band model and nonlocal damage model respectively. Mode I, II and III fractures sometimes are involved simultaneously due to various stress status. The failure process of brittle rock was captured using the VMIB evolution function at the micro scale. The results show that typical features of 3D tensile and compressive fracture propagation can be well represented. Especially, simulation results by 3D VMIB and 3D EPM demonstrate the propagation of Mode III fracture. Such simulations improve understanding of 3D fracture propagation mechanisms and provide a means of designing hydraulic fractures for reservoir stimulation, as well as predicting the thermal fracturing in geothermal reservoir. In Chapter 6, VMIB model is employed in the partial coupled thermal mechanical model to simulate the thermal fracturing during the cold fluid injection.

The spurious mesh size sensitivity was minimized using continuum damage model in nonlocal formulation. The results matched well with the experimental

observation, suggesting that the presented method can capture the main features of mode I and II fracture propagation. Though the mesh dependency can be minimized by using nonlocal theory, the element size should be several times smaller than the characteristic length in the scale of mm or cm. The implementation of simulation was feasible on the aspect of computational volume since that the simulating domains in the examples were less than one meter in this chapter. For larger simulation domain such as reservoir scale, however, the simulation using nonlocal damage theory becomes extreme difficult. In Chapter 7, though the model is encoded in true 3D, the simulating domain is a thin plate with the thickness represented by a single layer of element in order to reduce the memory needed for the simulation.

Chapter 6. Modeling 3D Thermal Fracturing Using VMIB

The influences of thermo-mechanical processes on fracture initiation and propagation are observed in enhanced geothermal systems. Cold water injection and heat extraction in the geothermal reservoir will cause dramatic temperature changes and volumetric contraction. A volumetric change results in deformation and stress of rock and sometimes rock failure. The coupling thermal- mechanical processes occur on various time scales and may have different influence upon the problem of interest. Generally, the thermal effects should be considered during long term injection owing to low thermal diffusivity of rocks. High tensile stress are induced by cooling of the rock fractures surfaces and tips, indicating a potential for extension of the secondary thermal fractures. As a result, thermal stimulation has been suggested as a means of enhancing reservoir permeability due to thermal fracture and opening and growth.

Our proposed model is implemented using a FEM and is used to study the development and propagation of 3D thermally-induced fractures in solid. Thermal fractures can result from the nonlinear deformation of the solid in response to thermal stress. Before the rock reaches the final failure stage, material softening and bulk modulus degradation can cause changes in the thermo-mechanical properties of the solid. In order to capture these aspects of the solid fracture, a VMIB-based thermo-mechanical model is derived to track elastic, softening, and the final failure stages of the rock response with the change of its temperature field. The thermo-mechanical properties of rock changes as its bulk modulus evolves are derived from a nonlinear constitutive model. On the other hand, to represent the thermo-mechanical behavior of

pre-existing fractures, the three dimensional element partition method (3D EPM) [Huang and Zhang, 2010] is employed.

6.1 Thermo-mechanical Model

6.1.1 Constitutive Model and Field Equations

Thermally induced strain results from the volumetric change such as expansion with heating and contraction with cooling. Thermal stress arises from cooling or heating when the solid is confined by the surrounding material and/or boundary conditions which will be discussed in the simulation examples. By including an additional thermal term into the governing equations, a nonlinear thermo-mechanical constitutive equation can be obtained as [Nowacki, 1976],

$$\sigma_{ij} = C_{ijmn}\varepsilon_{mn} - \hat{\gamma}\Delta T\delta_{ij} \tag{6.1}$$

where σ_{ij} and ε_{ij} are the components of stress and strain tensor (tension is considered positive), ΔT is the temperature change equal to $(T - T_0)$, in which T and T_0 are the current temperature and initial temperature, respectively. δ_{ij} is the Kronecker's detla. The thermal coefficient $\hat{\gamma}$ in Eq. (6.1) is defined as:

$$\hat{\gamma} = \hat{K}\alpha_m \tag{6.2}$$

where $\hat{K}$ is bulk modulus defined as $\hat{K} = \frac{1}{3}C_{11kl}\delta_{kl} = \frac{1}{3}C_{22kl}\delta_{kl} = \frac{1}{3}C_{33kl}\delta_{kl}$ for an isotropic material, and α_m is the thermal expansion coefficient of solid matrix. The above constitutive equations combined with stress equilibrium and energy balance equations, yield the following Navier's and thermal diffusion field equations,

$$C_{ijkl}u_{k,li} - \hat{\gamma}\Delta T_{,i}\delta_{ij} = 0 \tag{6.3}$$

$$\dot{T} - c^T\nabla^2 T = 0 \tag{6.4}$$

6.1.2 Discretized Field Equations in FE Form

In the following, the finite element method for the nonlinear thermo-mechanical problems is presented. To approximate the field variables of displacement, $\mathbf{u}$, temperature $\mathbf{T}$, and total temperatures change, $\Delta\mathbf{T}$, shape functions are used: $\mathbf{u} = \mathbf{N}_u\tilde{\mathbf{u}}$, $\mathbf{T} = \mathbf{N}_T\tilde{\mathbf{T}}$, $\Delta\mathbf{T} = \mathbf{N}_T\Delta\tilde{\mathbf{T}}$, where $\mathbf{N}_u$ and $\mathbf{N}_T$ are the shape functions for the solid displacement and temperature fields, respectively. $\tilde{\mathbf{u}}$ and $\Delta\tilde{\mathbf{T}}$ are nodal displacements and total temperatures change. These approximations are substituted into Eq. (6.3) and (6.4) (Galerkin method) yielding the following equations

$$\mathbf{K}\tilde{\mathbf{u}} - \mathbf{V}\Delta\tilde{\mathbf{T}} = \tilde{\mathbf{f}} \tag{6.5}$$

$$\mathbf{R}\dot{\tilde{\mathbf{T}}} - \mathbf{U}\tilde{\mathbf{T}} = 0 \tag{6.6}$$

where

$$\mathbf{K} = \int_{V_e} \mathbf{B}^T\mathbf{D}\mathbf{B}dV \tag{6.7}$$

$$\mathbf{V} = \int_{V_e} \mathbf{B}^T\hat{\gamma}\mathbf{m}\mathbf{N}_T dV \tag{6.8}$$

$$\mathbf{R} = \int_{V_e} \mathbf{N}_T{}^T\mathbf{N}_T dV \tag{6.9}$$

$$\mathbf{U} = \int_{V_e} (\nabla\mathbf{N}_T)^T\mathbf{c}^T(\nabla\mathbf{N}_T)dV \tag{6.10}$$

Using Crank-Nicolson method for time approximation scheme to discretize the heat diffusion equation shown as Eq.(6.6) , the final finite element formula can be obtained

$$-(\mathbf{R} + \theta\Delta t\mathbf{U})\Delta\tilde{\mathbf{T}}_n = \Delta t\mathbf{U}\tilde{\mathbf{T}}_{n-1} \tag{6.11}$$

Where $\tilde{\mathbf{T}}_{n-1}$ is the temperature in the previous time step, and $\Delta\tilde{\mathbf{T}}_n$ is the temperature change in the present step.

6.1.3 Representation of Mechanical and Thermal Properties of Fractures

Since the thermal-mechanical problem is not a fully coupled one, i.e., mechanical deformation does not influence the thermal diffusion, the thermal coupling term in the elasticity equations can be taken as a mechanical load caused by temperature changes during the calculation. Once the temperature field is known, the thermal stress load can be obtained. Considering the coupling part, after rearrangement of Eqn. (6.5), the field equation becomes

$$\mathbf{K}\tilde{\mathbf{u}} = \tilde{\mathbf{f}} + \mathbf{V}\Delta\tilde{\mathbf{T}} \tag{6.12}$$

The second term on the right side describes how the temperature changes influences the stress-strain field through displacements.

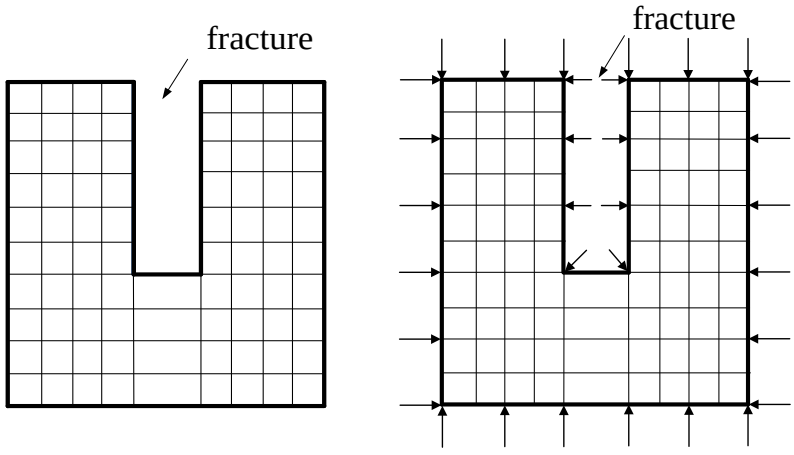

Figure 6.1. Thermo-mechanical response of a fracture in traditional FEM. The arrows show the cooling-induced nodal forces for contraction.

To achieve the volume change such as expansion by heating and shrinking by cooling in the finite element modeling, equivalent node forces (ENFs) caused by the

nodal temperature changes are applied on the corresponding nodes and in the corresponding directions. The mathematical expression of equivalent node forces (ENFs) is shown in Eq. (6.12), which is $\mathbf{V}\Delta\tilde{\mathbf{T}}$. For example, we assume that the temperature over a domain changes instantaneously and uniformly. The ENFs are canceled on the interior nodes because of their same temperature change, and only the enforced ENFs on the boundary nodes will cause a volumetric change (shown in 2D in Figure 6.1 for cooling process).

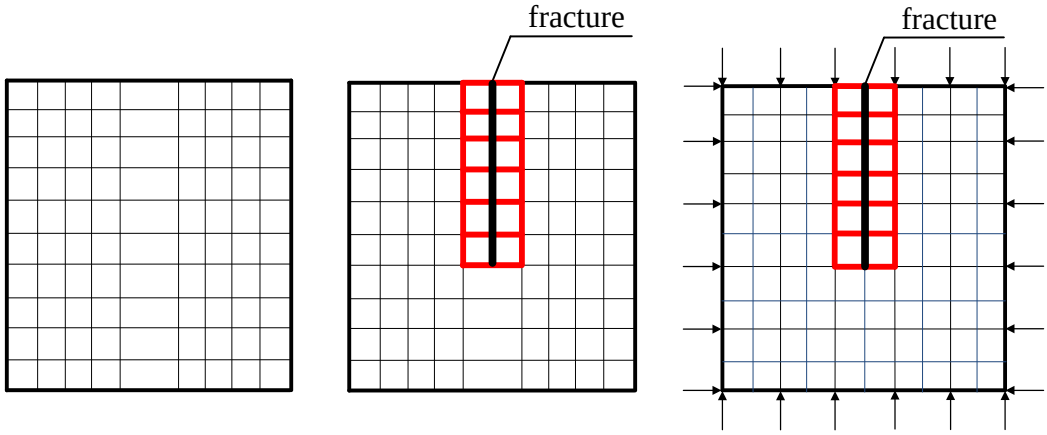

Figure 6.2. Thermo-mechanical response with original thermal properties.

This dissertation uses 3D element partition method (3D EPM) for fracture creation so there is no need to mesh for pre-existing fracture. If the i^{th} element is cut through by a fracture, the element will be transferred to the partition element based on the original structured. The i^{th} element stiffness matrix $\mathbf{K}_i^e$ will be replaced by $\mathbf{K}_i^{EPM}$ before being assembled into global stiffness matrix $\mathbf{K}$. However, the thermal and thermo-mechanical coupling part of the partition element also needs to be modified. In Figure 6.2, the elements with red boundaries have been changed into partition elements after being cut by fracture shown as thick line. Having their original thermal and coupling properties, the object in the figure will perform like a non-fractured one,

because that the ENFs status in Figure 6.2 is equal to the resultant nodal forces in Figure 6.3(a) and (b). If the thermally induced ENFs of the fractured elements are removed, shown in Figure 6.3(a), the resultant nodal force shown in Figure 6.3(b) will be the same as the one in Figure 6.1. Mathematically, before being assembled into the coupling part of global matrix $\mathbf{V}$, the thermo-mechanical coupling term in element level $\mathbf{V}_i^e$ should be multiplied by β which equals 0 if the ith element is fractured. Therefore, the fractured element is now partitioned both with respect to its mechanical properties and its volumetric thermal deformation so that deformation behavior of a fracture under thermo-mechanical load is numerically represented. The same modification will be applied to newly extended fractures. As a result, the fracture will be represented in a blunt sharp that related the size and shape of the fractured elements. This could influence the precision of calculation if the element size is relative large.

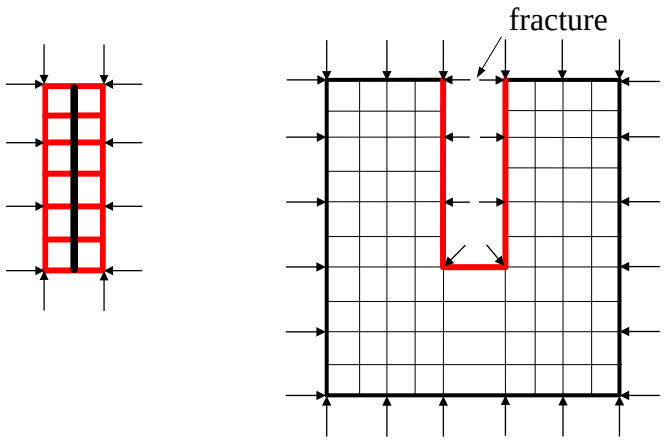

(a) (b)

Figure 6.3. (a) Thermo-mechanical response of fractured element; (b) thermo-mechanical response of partition element after modification.

6.2 Simulation Examples

6.2.1 Functional Test I: Single Fracture

To examine the performance of thermo-mechanical VMIB formulation and 3D EPM in simulating thermal fracture propagation, a cubic sample of rock having a fracture at its top is simulated. The rock block and fracture dimensions are shown in Figure 6.4 Table 5 shows the parameters used in the present simulations. This dissertation assumed no friction between shearing fracture surfaces. Therefore, K_S is set to be very small. A small sample is used so that we may focus on the ability of the new VMIB constitutive model and its numerical implementation to capture softening by thermal stress. Since the size of the object is relatively small, the conduction of heat through the rock sample occurs in a short period of time. Therefore, a uniform cooling is assumed to test the mechanical response due to temperature change without taking into account the transience of temperature diffusion (this is consideration in the next section). The displacements of all rock surfaces except the top one are confined in the direction perpendicular to them. The total number of elements is 156,975 and the total number of node number is 35,280. For each simulation step, a temperature drop of $0.15^{\circ}C$ is used with a total number of 120 steps.

Table 5. Simulation Parameters

Parameters of intact element:	
Young's modulus, E	30.5 GPa
Poisson's ratio, ν	0.20
Tensile strain strength, ε_t	0.105×10^{-3}
Parameters of 3D EPM:	
Normal stiffness coefficient, K_n / h	10.0 GPa/m
Shear stiffness coefficient, K_s / h	10^{-8} GPa/m
Fracture width, h	1.0 mm

Parameters of 3D VMIB:	
c	0.15
n	4.0
Thermal properties of rock	
Thermal diffusivity, c^T	$1.6\times10^{-6} m^2/s$
Thermal expansion coefficient, α_m	$1.8\times10^{-5} K^{-1}$

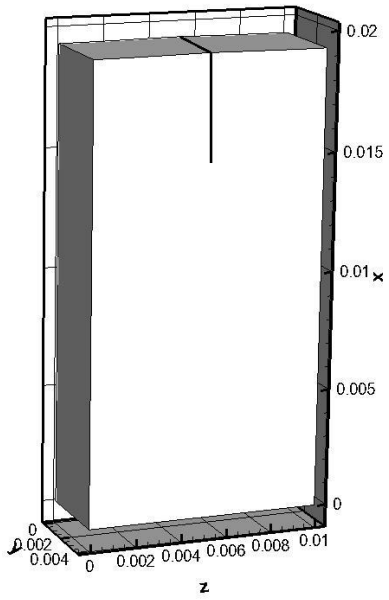

Figure 6.4. The problem geometry showing size and fracture set.

Figure 6.5(a)~(f) shows the deformed mesh configuration amplified 1200 times for different temperature drops. Figure 6.6(a)~(f) shows the middle slice of the maximum principal stress contour in the deformed configuration. Firstly, significant thermally induced volumetric displacements takes place near the pre-existing fracture surfaces due to the shrinkage of rock as shown in Figure 6.5(a). The fracture is forced to open, causing stress concentration at its tip. With increasing cooling, the thermal stress and displacement increase, causing stress concentration at the fracture tip to rise bringing the tip region rock into softening stage, and finally resulting in the formation of a newly extended fracture. Figure 6.7 shows a plot of $\alpha_m K$ verses the maximum principal strain for the element at the initial fracture tip. Bulk modulus K retains its

original value for a few steps and then, gradually degrades as the tensile strain reaches strain level at ultimate strength. This example verifies that the present model is capable of simulating the nonlinear process of thermal fracturing.

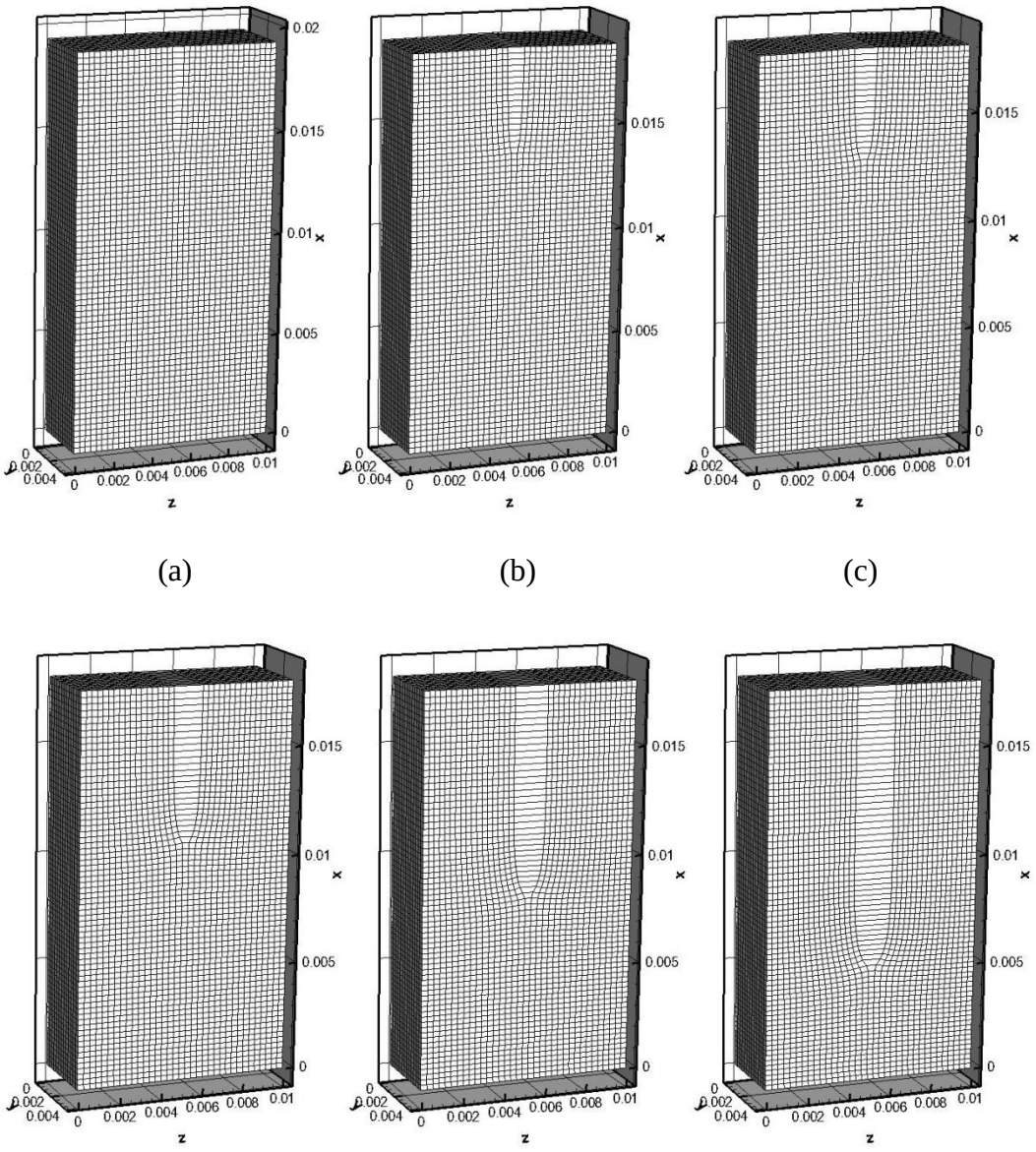

(a) (b) (c)

(d) (e) (f)

Figure 6.5. Deformed mesh configuration (amplified 1200 times) when the rock was cooled by: (a) $-3^{\circ}C$; (b) $-6^{\circ}C$; (c) $-9^{\circ}C$; (d) $-12^{\circ}C$; (e) $-15^{\circ}C$; (f) $-18^{\circ}C$.

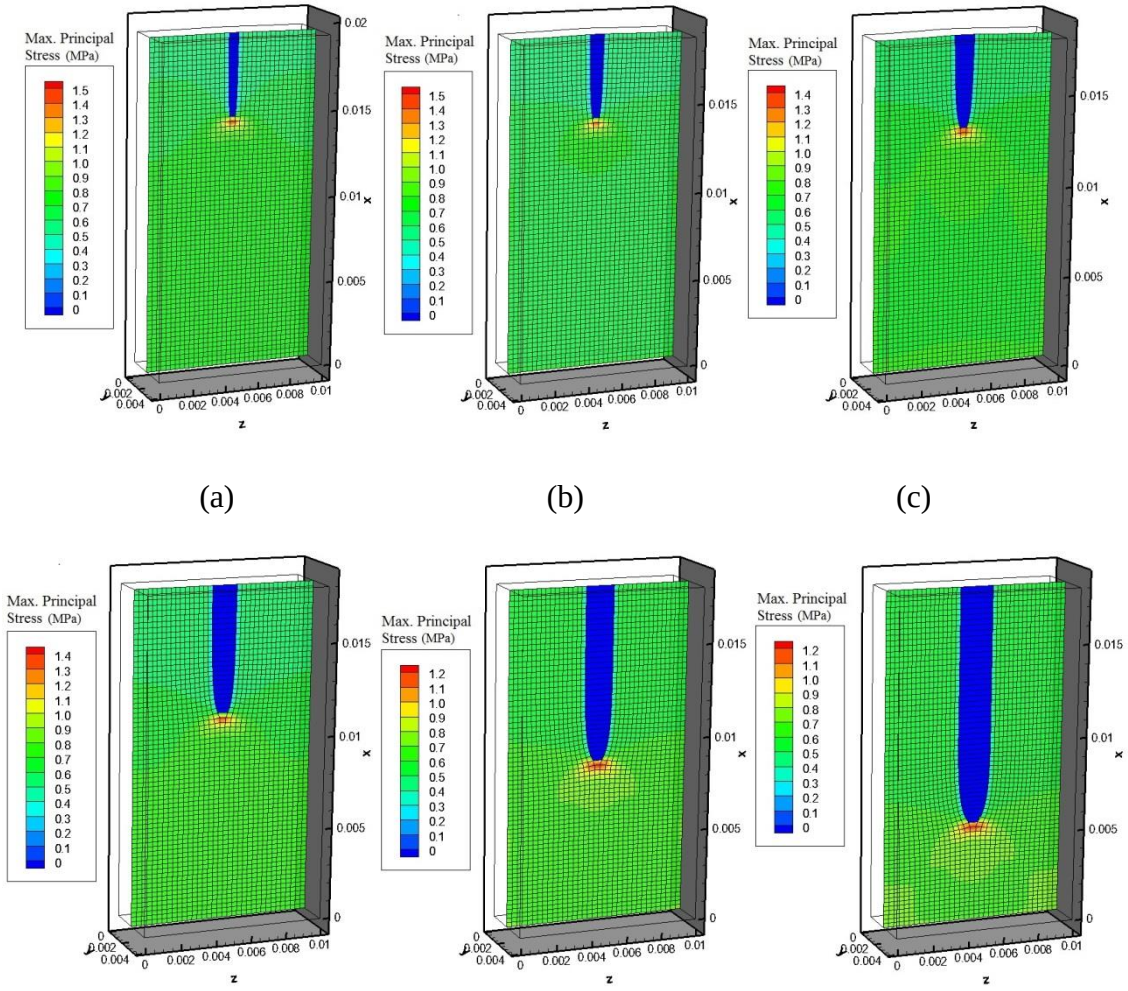

Figure 6.6. The middle slice of maximum principal stress contour with deformed mesh configuration (amplified 1200 times) when the rock was cooled by: (a) $-3^{\circ}C$; (b) $-6^{\circ}C$; (c) $-9^{\circ}C$; (d) $-12^{\circ}C$; (e) $-15^{\circ}C$; (f) $-18^{\circ}C$.

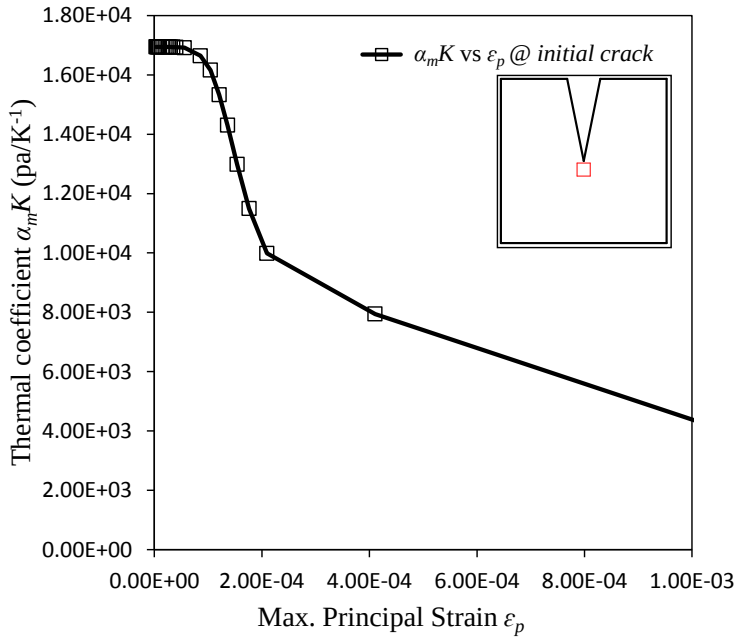

Figure 6.7. Thermal coefficient $\alpha_m K$ verse maximum principal strain for the element at the initial fracture tip.

6.2.2 Functional Test II: Randomly Distributed Multiple Fractures

The second simulation explores thermal fracture propagation and interaction. Taking advantage of 3D EPM to represent thermal response of fractures, multi-fractures can be simulated with a structured mesh without remeshing in the process of fracture propagation. A cubic specimen with 20 randomly distributed small fractures is considered. The dimensions are shown in Figure 6.8 and the material and model parameters are listed in Table 5. As before, uniform cooling is assumed to test the mechanical response of fractures to a temperature change. The total number of element is 380,880 and the total number of node number is 83,300. For each step, the temperature drop is $2.0^{\circ}C$ with a total number of 19 steps.

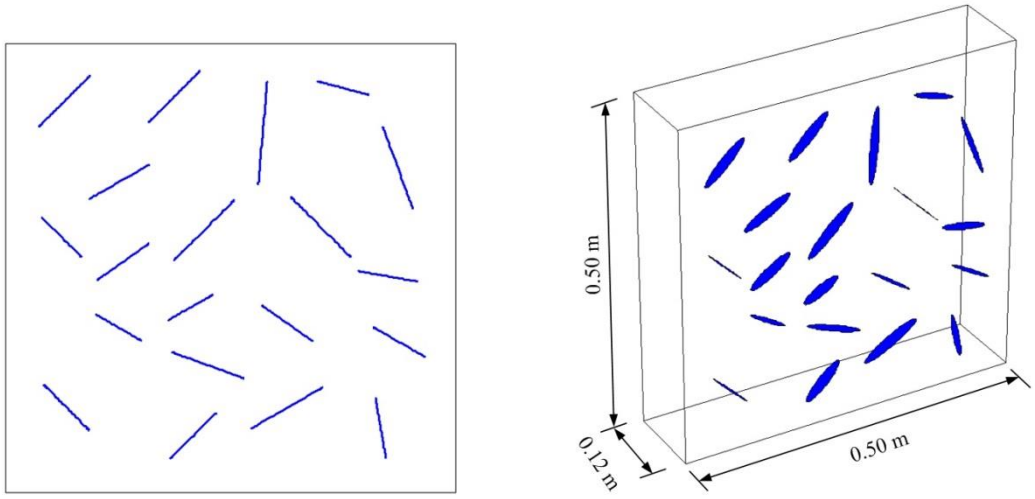

Figure 6.8. The problem geometry showing size and fracture set.

Figure 6.9 shows the propagation of thermal fractures. Initial fractures tend to open in the cooling process and then propagate in their initial plane. However, the displacement and stress fields are changed due to the existence of neighboring fractures. Therefore, fractures tend to converge during the cooling shown red lines in Figure 6.9(c) and red circle in Figure 6.10(c). Figure 6.10(a)~(c) shows the maximum principal stress contour when the rock is cooled by (a) $-28^{\circ}C$, (b) $-34^{\circ}C$, and (c) $-38^{\circ}C$. Thermal stress is concentrated at each fracture tip as the fractures open due to material shrinkage. For the same reason, fracture opening releases the stress on the both side of the fracture surfaces (displayed by green and blue color). Logically, the thermal stress of areas surrounded by the fractures is largely released due to gradual loss of confinement during the propagation of fractures as shown Figure 6.10(c) highlighted in the red dash box.

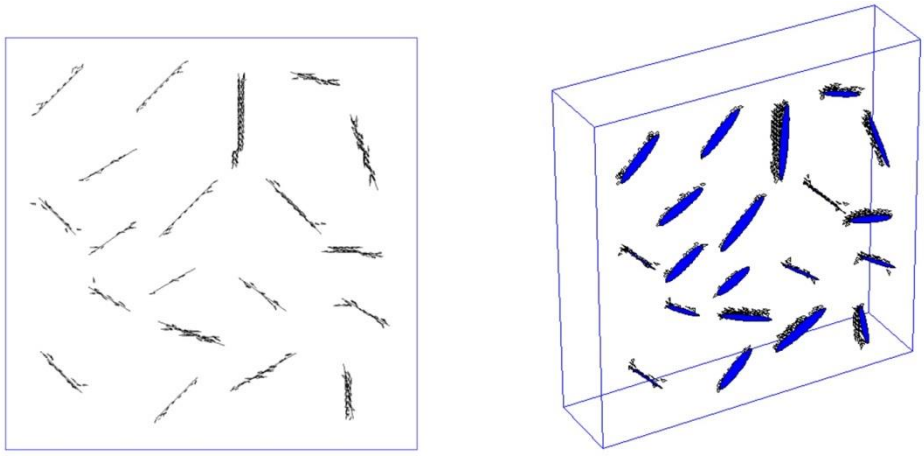

(a)

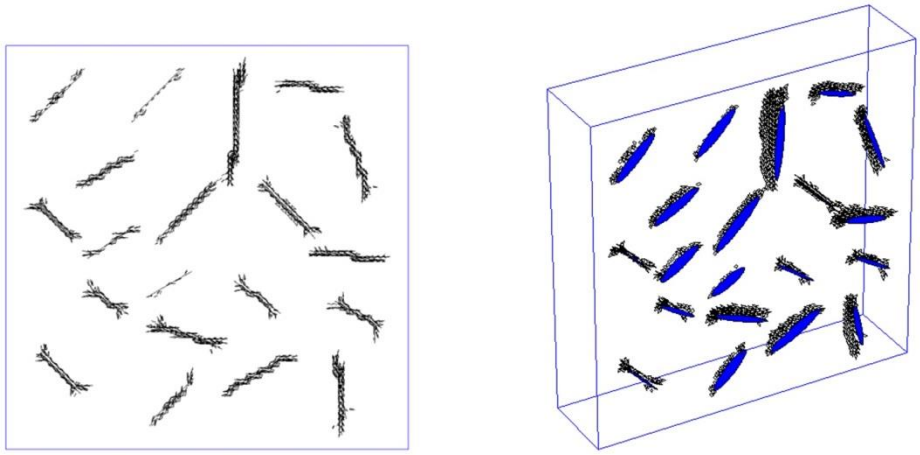

(b)

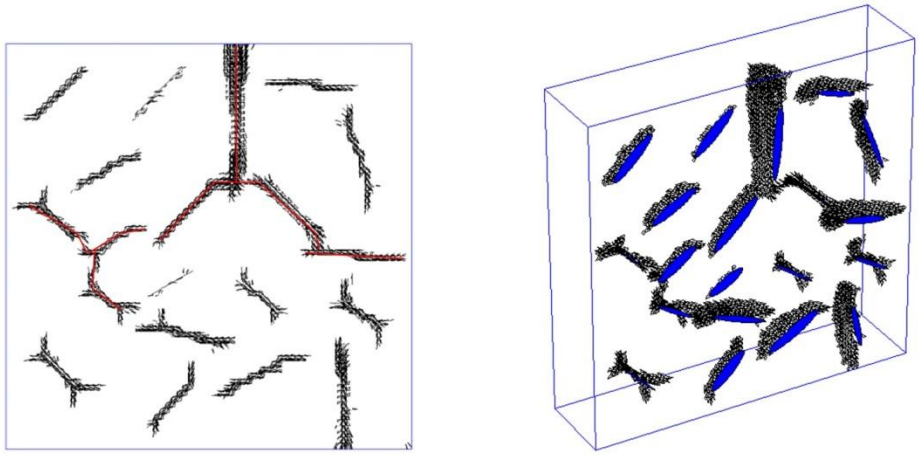

(c)

Figure 6.9. Propagation of thermal fracture when the rock was cooled by: (a) $-28^{\circ}C$; (b) $-34^{\circ}C$; (c) $-38^{\circ}C$.

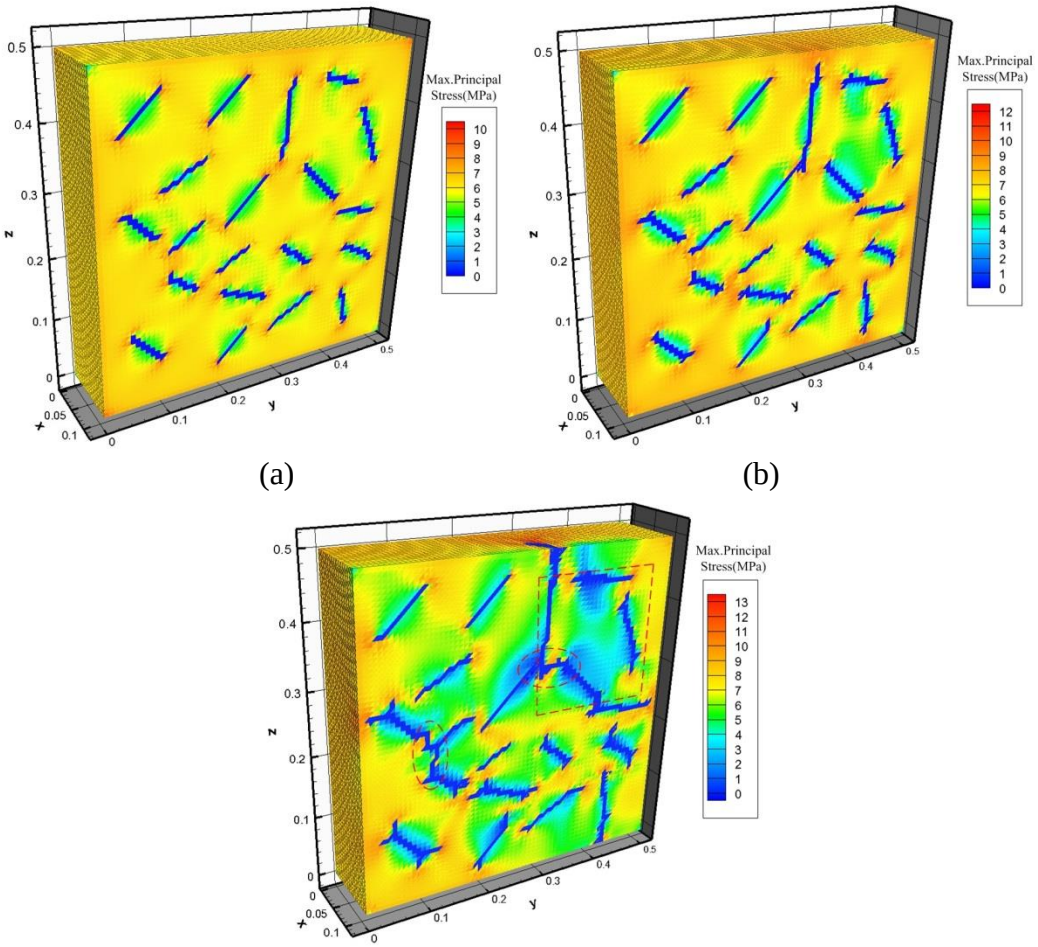

Figure 6.10. Maximum principal stress contour when the rock was cooled by: (a) $-28^{\circ}C$; (b) $-34^{\circ}C$; (c) $-38^{\circ}C$.

6.2.3 Thermo-mechanical Response of a Wellbore

In this example, a linear elastic thermo-mechanical response is studied while considering transient heat diffusion. The problem geometry and dimensions are shown in Figure 6.11. Simulation parameters for this example are listed in Table 5. The initial rock temperature is $250^{\circ}C$, and is set to be $50^{\circ}C$ on the surface of wellbore. Figure 6.12 shows the temperature distribution along the radial direction at different time steps. Figure 6.13 shows the thermal stress distribution along the radial direction in different

time steps. In the present meshing scheme, the total number of elements is 38400 and the total number of nodes is 9225.

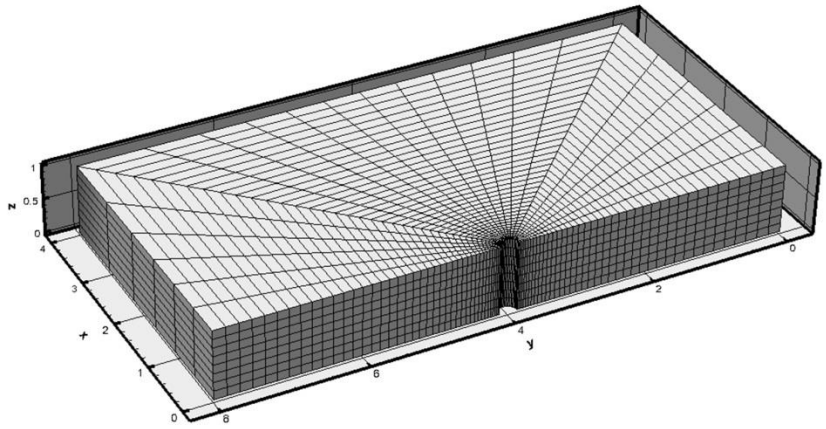

Figure 6.11. The problem geometry .

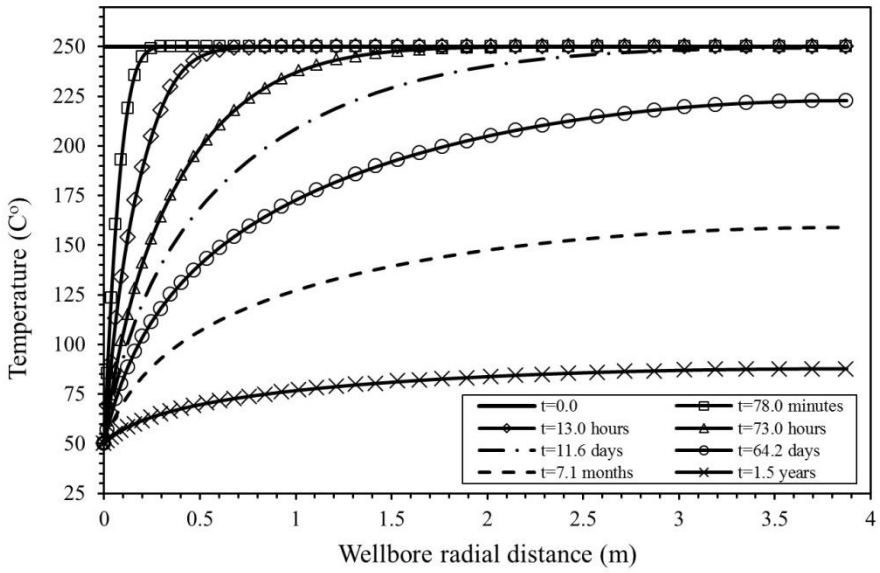

Figure 6.12. Temperature distribution along the radial direction of wellbore.

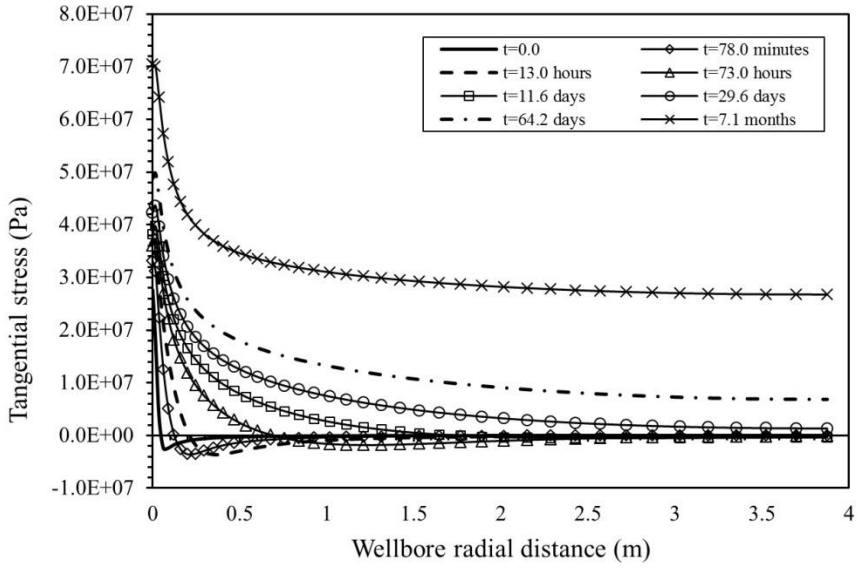

Figure 6.13. Tangential stress distribution along the radial direction of wellbore.

6.2.4 Multiple Fractures Emanating from a Wellbore

Next, a wellbore is simulated with multiple pre-existing cracks emanating from it. A number of 16 initial cracks (3.33 to 4 cm in length) are equally spaced around the wellbore shown in Figure 6.14. Simulation parameters for this example are listed in Table 5. The initial temperature in the matrix is $220^{\circ}C$ and $40^{\circ}C$ on the surface of wellbore. Because it is assumed that all fractures cut through the rock in z direction and propagate in the x-y plane, a single layer of elements in z-direction is used, and all displacements in the z-direction are constrained to be zero. In the present meshing scheme, the total element number is 100,800 and the total node number is 40,800. Since the diffusion rate of temperature tends to become slower as time goes on, a gradually increasing time step scheme is utilized. The initial time step is 2 minutes, and then it is increased to 20 minutes after 20th step, 40 minutes after 50th step, 80 minutes after 100th step, 160 minutes after 150th step, 320 minutes after 200th step, 640 minutes after 250th step, respectively.

To simulate the impact of the in-situ stress, 2 different in-situ stress schemes are used in the examples, which are (a) $S_H = 6MPa$, $S_h = 6MPa$; (b) $S_H = 6MPa$, $S_h = 4MPa$. The results are summarized in Figure 6.15 and Figure 6.16. Figure 6.15 shows the temperature field at 52.4 days after cooling process started. Figure 6.16 displays the maximum principal stress (tensile stress considered positive). The magnitude of thermal stress are indicated by the legends. The lighter shade shows higher thermal stress values (around the wellbore) where the cooling zone is located. Figure 6.16 also shows fracture propagation. Since the fracture creation relieves the stress of a fractured element to zero, the fractures are shown in dark color as they propagate near the wellbore. Moreover, lighter zones are found at the fracture tips where stress concentration occurs due to opening of fractures.

For the isotropic in-situ stress field, in Figure 6.16(a), thermal fractures tend to propagate in radially. In this case, the in-situ stresses have no impact on the main direction of fracture opening. On the other hand, in Figure 6.16(b), for anisotropic stress field, the dominant cracks grow in the direction of SH. It should be noted that the fractures do not propagate symmetrically although the domain is symmetric. This is caused by use of an asymmetric mesh scheme and the EPM in which newly extended fractures are combined with the discontinuous fracture surface of the cracked elements. Moreover, the thermal fracture propagation is very sensitive to the length of the fractures and the space between them, especially when multiple fractures are competing to grow. A higher thermal-induced stress arises at the tips of the longer fractures or the fractures with larger area in between [Tarasovs and Ghassemi, 2014, Geyer and Nemat-Nasser, 1982]. The fractures length and spacing could be slightly different during the

transient cooling so that the thermal fractures propagate in an asymmetric pattern. The contrast in magnitudes of the maximum and minimum in-situ stress still plays the major role on the propagation orientations.

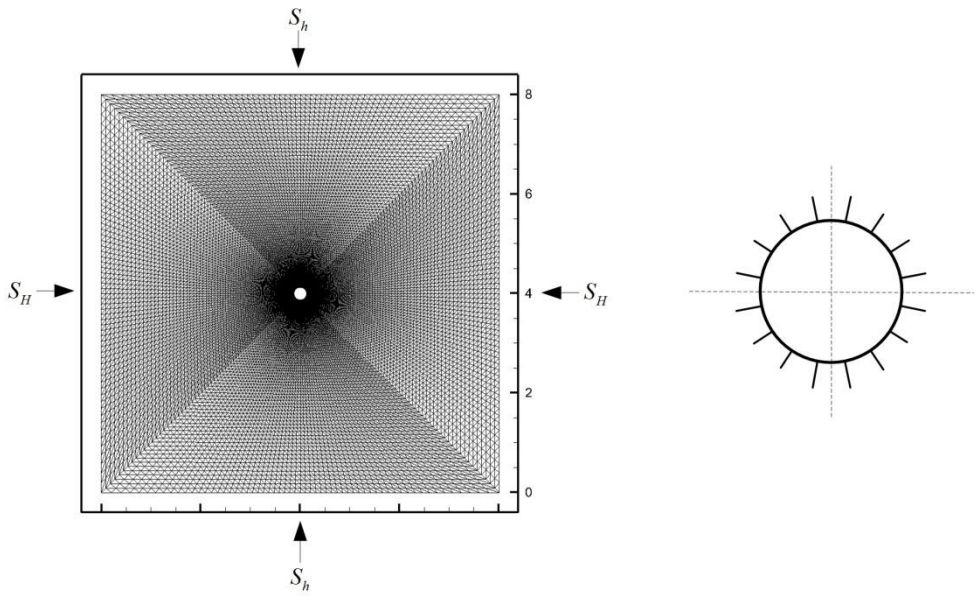

Figure 6.14. (a)The problem geometry and (b)fractures distribution.

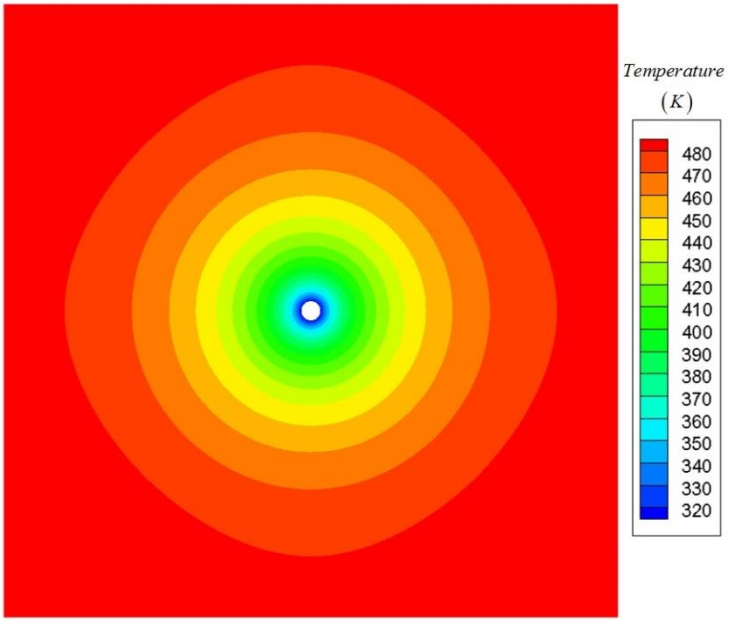

Figure 6.15. Temperature contour at 52.4 days after cooling process started

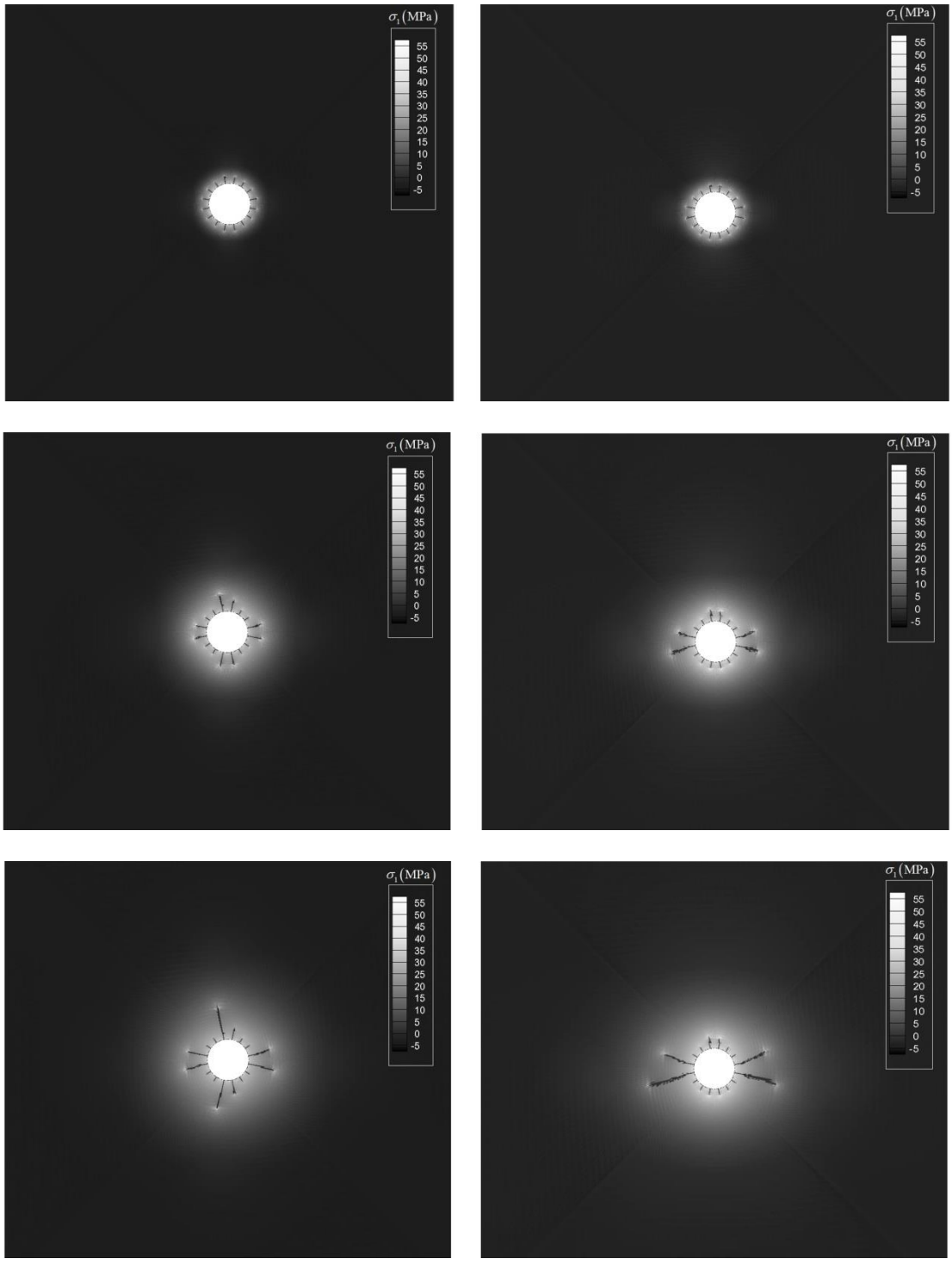
σ_1 (MPa)
55
50
45
40
35
30
25
20
15
10
5
0
-5

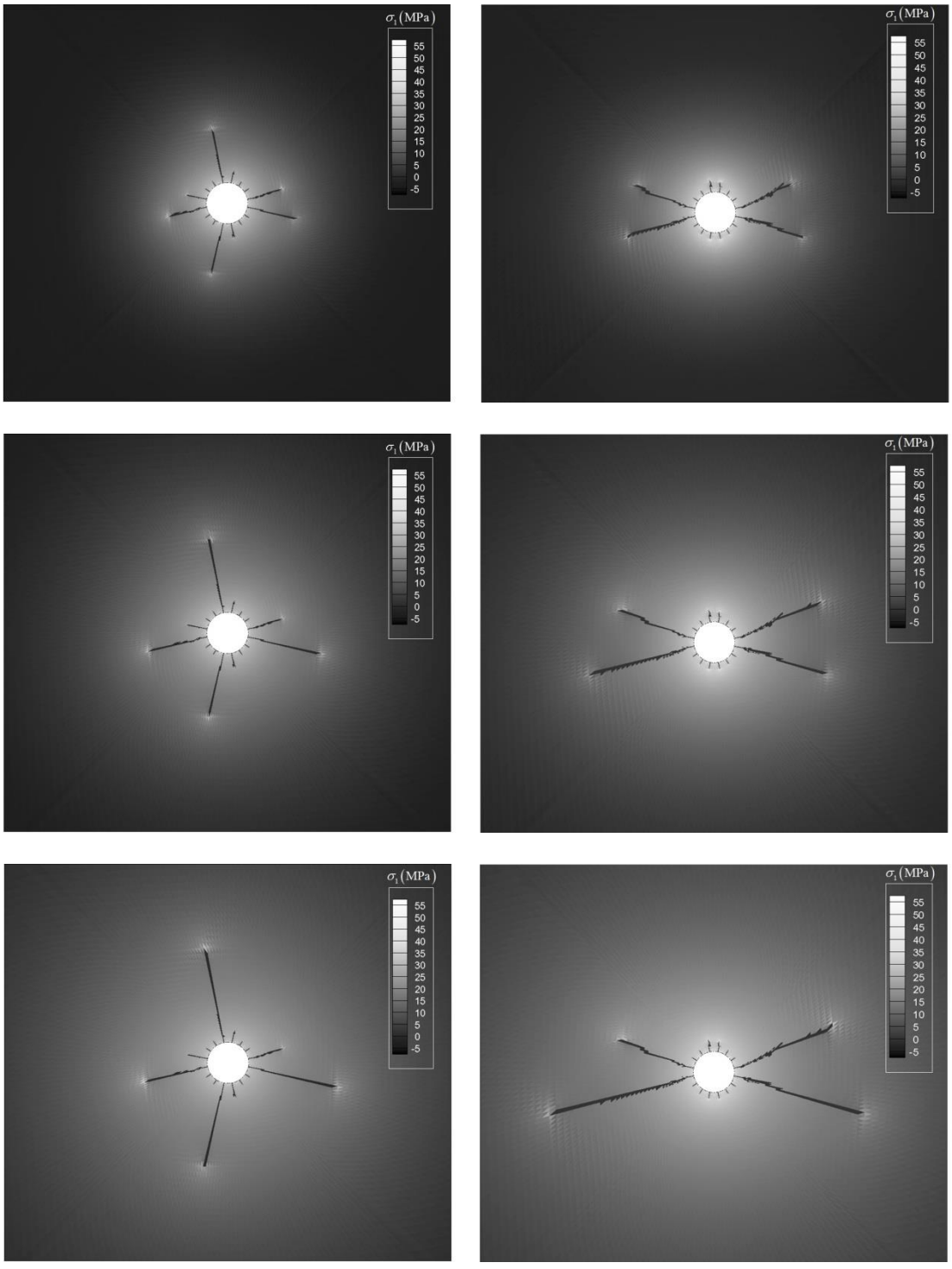

(a) (b)

Figure 6.16. Maximum principal thermal stress contour: (a) $S_H = 6MPa$, $S_h = 6MPa$; (b) $S_H = 6MPa$, $S_h = 4MPa$.

6.3 Conclusion

Numerical simulation of 3D thermal fracture propagation in brittle rock was studied using VMIB model combined with 3D EPM method. Nonlinearities of mechanical behaviors and thermal parameters of the solid material were captured by introducing a nonlinear VMIB constitutive model. The 3D EPM associated with thermal parameters modification for fractured elements provided a simple way to represent the pre-existing fracture in structured mesh. The examples of functional test provided evidences for the validation of presented method. Test I showed the reasonable results of nonlinear thermal response and fracture development of rock when it is under uniform cooling. Test II was designed to perform the ability of the model to treat the random distributed fractures with structured mesh. The simulations in wellbore condition studied the thermal fracturing emanating from wellbore surface and the impact on the propagation patterns from the in-situ stress. The present model provided a new way to predict 3D thermal fracturing.

Chapter 7. Modeling 3D Hydraulic Fracture Propagation

Based on the theoretical and mathematical descriptions in the previous chapters on mechanisms of hydraulic facture processes such as constitutive model of rock, the mechanical representation of fracture surface and the methodologies of the fluid flow in both fracture surface and porous rock formation, in this chapter, a series of numerical simulations are presented based on different assumptions and points of interests. Plus, in this dissertation, more realistic physical phenomena are captured by introducing more physical components into the model from section 7.1 to 7.3.

First series of examples are simulated by virtual multidimensional internal bond (VMIB) model under different in-situ stress conditions. The fracture fluid flow is simplified by applying the gradual increasing uniform hydraulic pressure on the fracture surface. The main targets are testing the performance of VMIB as the constitutive relationship modeling the rock failure during hydraulic stimulation, as well as the influence of in-situ stress on the propagation direction. Secondly, nonlocal damage theory is adopted as rock constitutive model. The fracture flow is captured by lubrication theory. The examples adopt the technique described in Chapter 4 to identify the most preferable path in the damage band using polynomial fitting. The pressure boundary condition is successfully applied in the fractured element supported by the simulation examples of 3D EPM on pressurized subsurface fracture shown in Chapter 4. The leak-off and fluid diffusion in the formation are neglected. Last but not the least, the modified poroelastic model is introduced based on classic poroelastic model and 3D element partition method (3D EPM). Take advantage of modified poroelastic model, the fracture fluid is flowing through the high permeability fractured element without

specified flow meshing. The real-time hydraulic pressure is applied on the fracture surface using the matrix implanted in the global matrix. In this way, true 3D simulation of hydraulic fracture propagation and interaction with natural fracture under FEM framework are carried out. The examples of natural and hydraulic fracture interaction show the excellent performance of the model on predicting the propagating fracture with complex geometry.

7.1 Modeling 3D Hydraulic Fracture Propagation Using VMIB

7.1.1 Problem Descriptions

The hydraulic fractures in geothermal reservoirs and unconventional petroleum resources are subjected to high in-situ stresses that highly influence the fracture propagation. To examine this, consider an embedded elliptical fracture of finite area that is driven by a uniform hydraulic pressure in an infinite underground space. The problem geometry is shown in Figure 7.1, and the material and the corresponding model parameters are listed in Table 4. To increase the efficiency of the simulation, half of the embedded fracture is simulated using the problem symmetry. In the presented meshing scheme, there are 26 rows of nodes plotted on x direction, and both 42 rows of nodes on y and z direction. The total element number is 210125 and the total node number is 45864. Initially, a hydraulic pressure p_0 is applied to the fracture. Then the fracture is increasingly pressurized by an increment of $\Delta p = 0.07\text{MPa}$. A series of fracture propagation case are studied using the following four in-situ stresses:

Case I: $\sigma_V = 0.8$, $\sigma_h = 0.8$, $\sigma_H = 0.8$, $p_0 = 1.6\text{MPa}$;

Case II: $\sigma_V = 1.6$, $\sigma_h = 0.8$, $\sigma_H = 0.8$, $p_0 = 2.4\text{MPa}$;

Case III: $\sigma_V = 2.0$, $\sigma_h = 0.8$, $\sigma_H = 0.8$, $p_0 = 2.8\text{MPa}$;

Case IV: $\sigma_V = 2.4$, $\sigma_h = 0.8$, $\sigma_H = 0.8$, $p_0 = 3.2\text{MPa}$.

In Case I the angle of inclination α, is set to be 45 degree to decrease the boundary effect. α in other cases is set to be 30 degree. The simulation results for these cases are shown in Figure 7.2 to Figure 7.4.

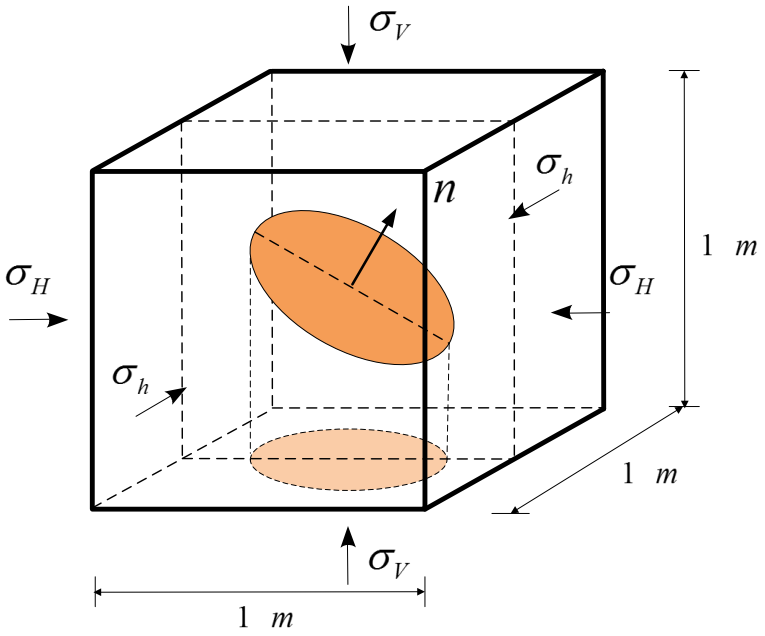

Figure 7.1. Problem geometry and in-situ stress directions.

7.1.2 Simulation Results

When the fracture is pressurized, both the strain and the stress are concentrated near its tip. However, in case of the 3D embedded elliptical fracture, the fracture tip is an ellipse, and the stress strain state is different along the tip contour depending on the certain geometry and in situ stress. Thus, different fracture propagation modes might occur at different locations of the fracture tip contour. Figure 7.2a shows the fracture propagation in the isotropic stress field (Case I). As the applied stress state is symmetric for the 45-degree crack, the fracture propagates on its original plane under the action of the applied stress field. The fracture advances straightforward when the applied uniform

hydraulic pressure exceeds the normal stress on the plane of the fracture. Figure 7.2b shows the fracture propagation for the Case II. The upper and lower fracture tips develop slightly inclined to the vertical direction, that is, the maximum stress direction. This can be observed more clearly in Case III, shown in Figure 7.2c. The final path is steeper than that of Case II, tending to the maximum in situ stress direction. As σ_V increases, the pattern of fracture propagation at the upper and lower wings of original fracture changes from Mode I to combined Modes I and II. To illustrate this, the middle slice of the rock block, which contains only the upper and lower end tips, is considered, and the resulting fracture path is shown for each stress state in Figure 7.3. Figure 7.4 shows the final propagation of the half elliptical fracture. In Case I, shown in Figure 7.4a, the fracture propagates as Mode I despite the location of the fracture tip. From Figure 7.4b–c, mixed mode propagation (Modes I and II) occurs at both upper and lower edges of the original fracture. On the side tips, the fracture develops outward and connects with the fractures on the upper and lower ends to form a curved surface, a typical behavior of Mode III fracture.

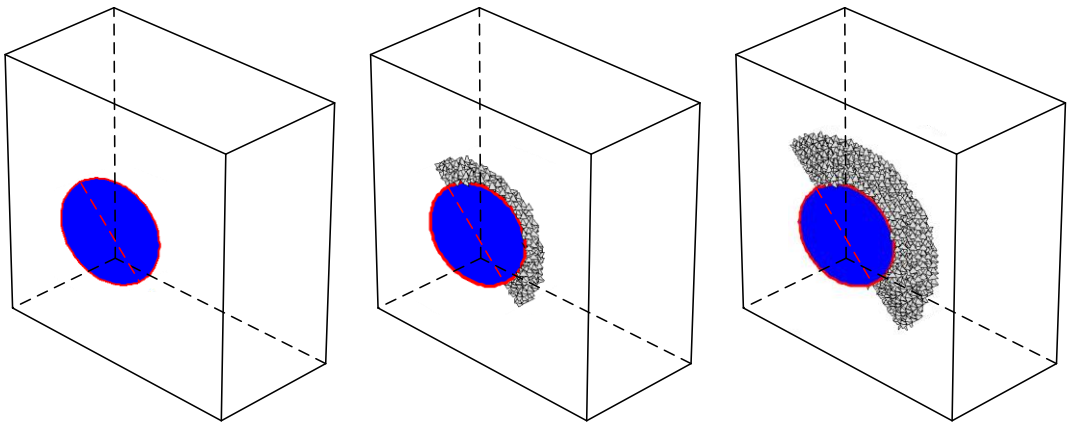

(a)

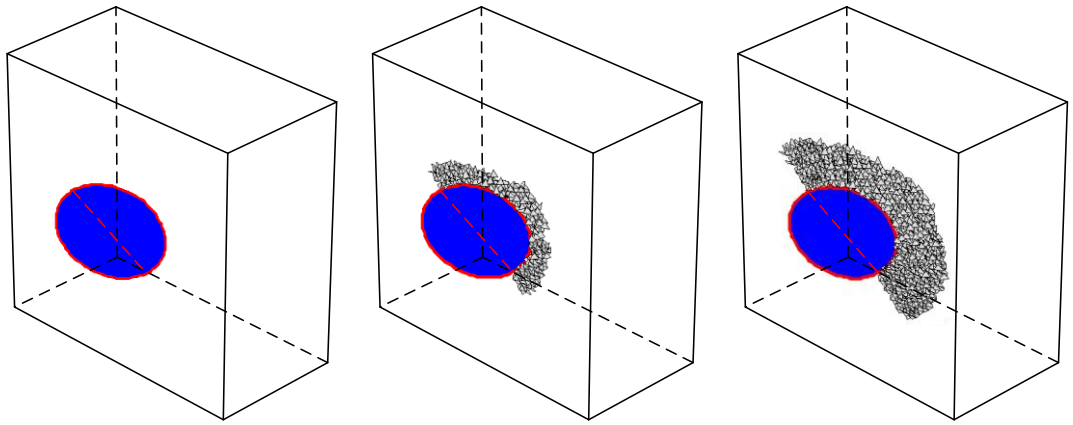

(b)

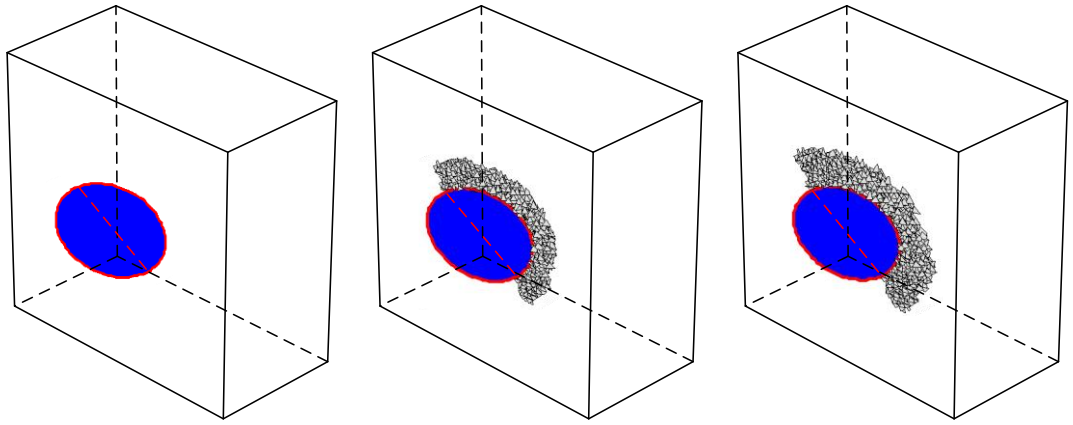

(c)

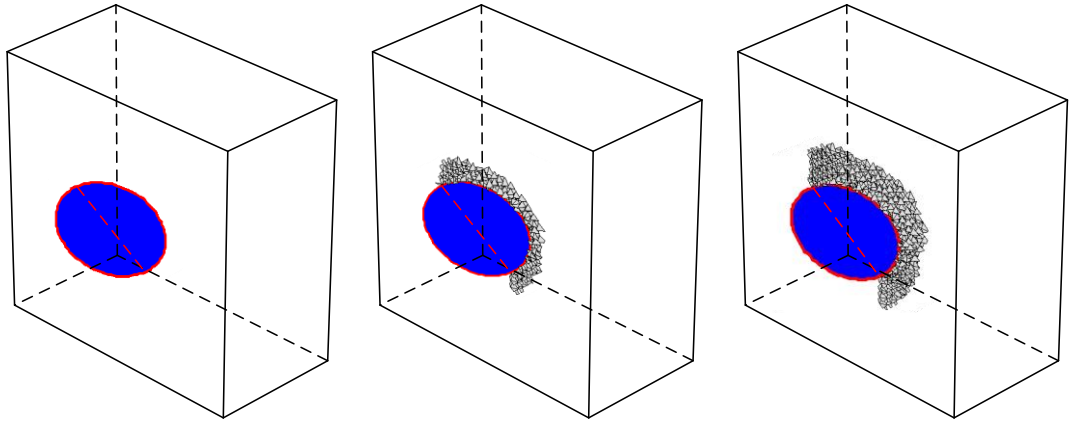

(d)

Figure 7.2. Simulated hydraulic fracture propagation paths: (a) Case I, (b) Case II, (c) Case III, and (d) Case IV

Case IV, when σ_V is three times σ_h and σ_H, is particularly interesting. As shown in Figure 7.3d and Figure 7.4d, the tips of the upper and lower wings develop parallel to the vertical in situ stress. However, the fracture propagation is different on the side tip. Two separate fractures are formed at the side tip shown in Figure 7.4d. The reason for this is the strong tendency of the fracture propagation at the upper and lower tips to develop vertically. Moreover, hydraulic pressure in the newly extended fracture tends to force the fracture open in the direction normal to the hydraulic pressure. Consequently, the new fracture on the side tip cannot connect the upper and lower parts of fracture. In other words, the upper and lower parts are more favorable to propagate in their own direction, resulting in segmentation on the fracture front. This is an important aspect of Mode III fracture propagation that is very challenging to numerically simulate.

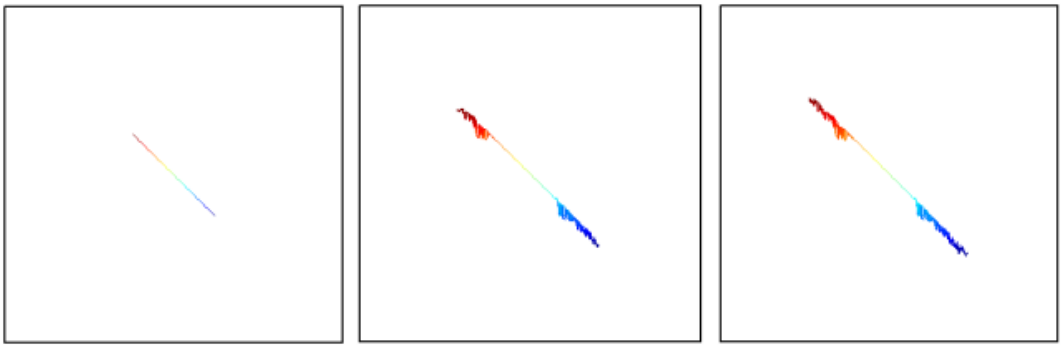

(a)

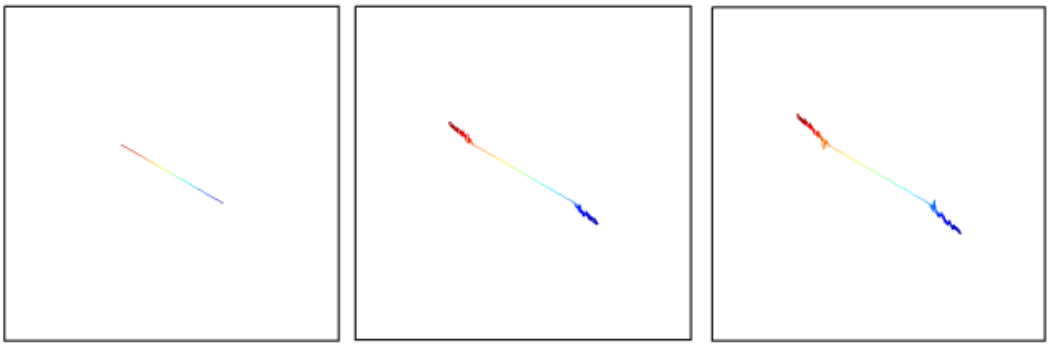

(b)

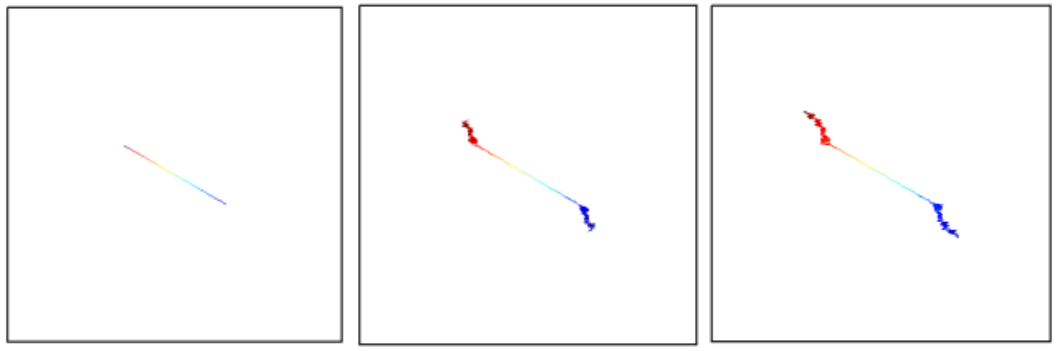

(c)

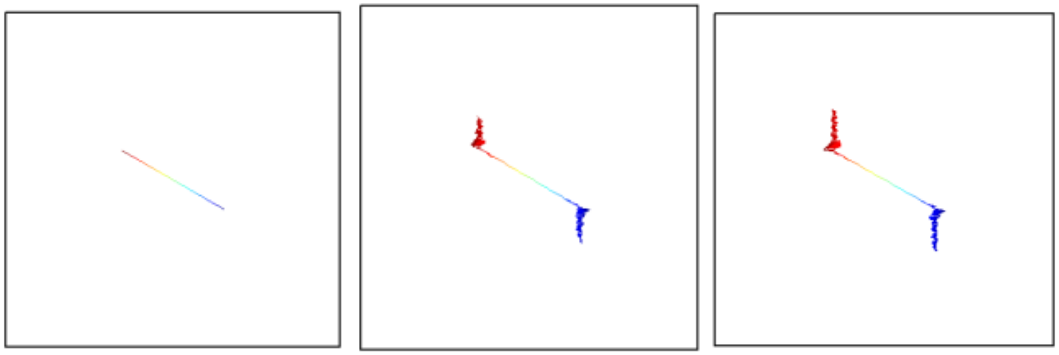

(d)

Figure 7.3. . Illustration of fracture propagation path for the middle slice: (a) Case I, (b) Case II, (c) Case III, and (d) Case IV.

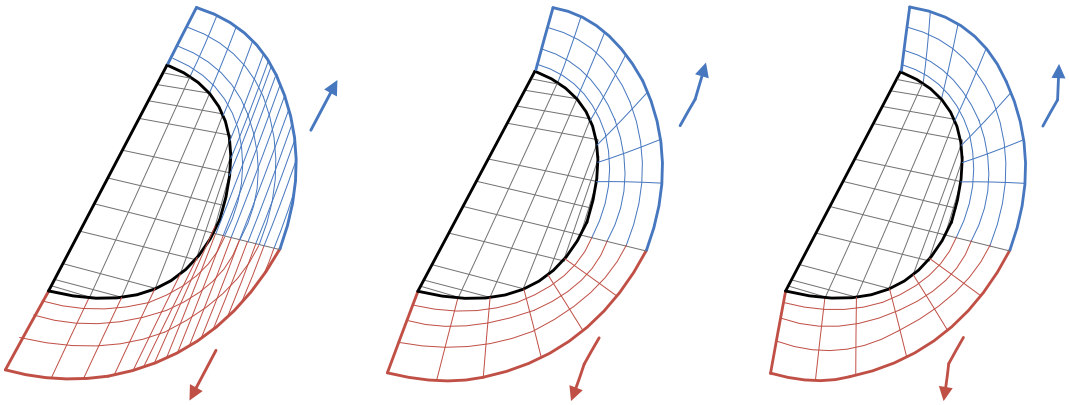

(a) (b) (c)

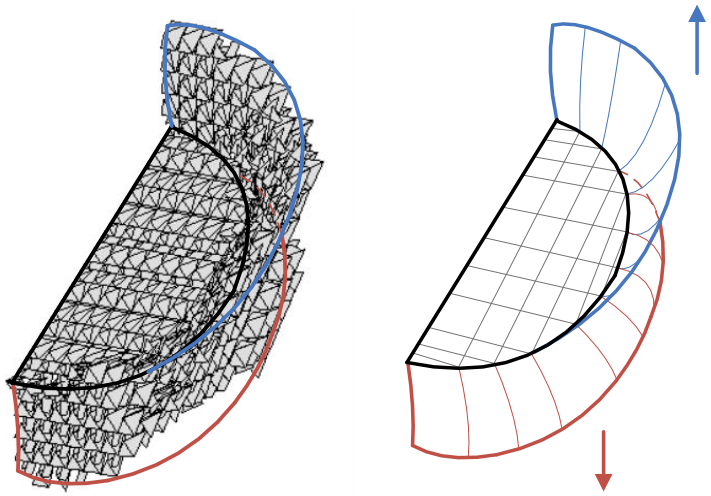

(b)

Figure 7.4. . Final shape of propagated hydraulic fracture: (a) Case I, (b) Case II, (c) Case III, and (d) Case IV.

7.2 Modeling 3D Hydraulic Fracture Propagation Using Nonlocal Damage Model

7.2.1 Problem Descriptions

A series of hydraulic fracturing examples under different in-situ stress states are simulated using nonlocal damage model in this section. It is well known that the in-situ stress state is one of the dominate factors that controls the propagation direction. Hydraulic fracture is going to propagate along the direction of maximum in-situ stress S_H regardless of the angle of initial perforations. However, the ratio of in-situ stress anisotropy still controls how fast the fracture growth will turn parallel to the direction of S_H . The sharpness of turning will influence the transportation of proppant and production. The problem geometry is shown in Figure 7.5. The red dot indicates the injection point and the blue line is initial fracture with 30 degree inclination to the horizontal direction. The present model is built in three-dimension, but the following examples are only use single layer of volumetric element considering the computational

volume. All the degrees of freedom on thickness direction are fixed. Moreover, these examples are not simulating any specific rock type that only uses common reasonable material parameters. To capture the behavior of a real rock, a careful calibration for all parameters in nonlocal damage model is needed through the results of laboratory test. The Young's modulus and Poisson's ratio are set as $E = 20GPa$ and $\nu = 0.2$ respectively. And $\varepsilon_0 = 1.2\times10^{-4}, \varepsilon_f = 6\times10^{-4}$ for damage evolution function. Since in three-point-bending test the 5 mm element is providing a reasonable accuracy, the present simulations use 5 mm element in the mesh-refined area. The nonlocal interaction radius is set to be $R = 2.5mm$. For fluid parameters, the viscosity is $\eta = 0.01pa\cdot s$, the injection rate is constantly $Q_i = 0.01m^2/s$. A series of hydraulic fracturing scenarios are carried out using the following four in-situ stress cases:

Case I: $S_H = 1.0MPa$, $S_h = 1.0MPa$ Case II: $S_H = 2.0MPa$, $S_h = 1.0MPa$

Case III: $S_H = 3.0MPa$, $S_h = 1.0MPa$ Case IV: $S_H = 4.0MPa$, $S_h = 1.0MPa$

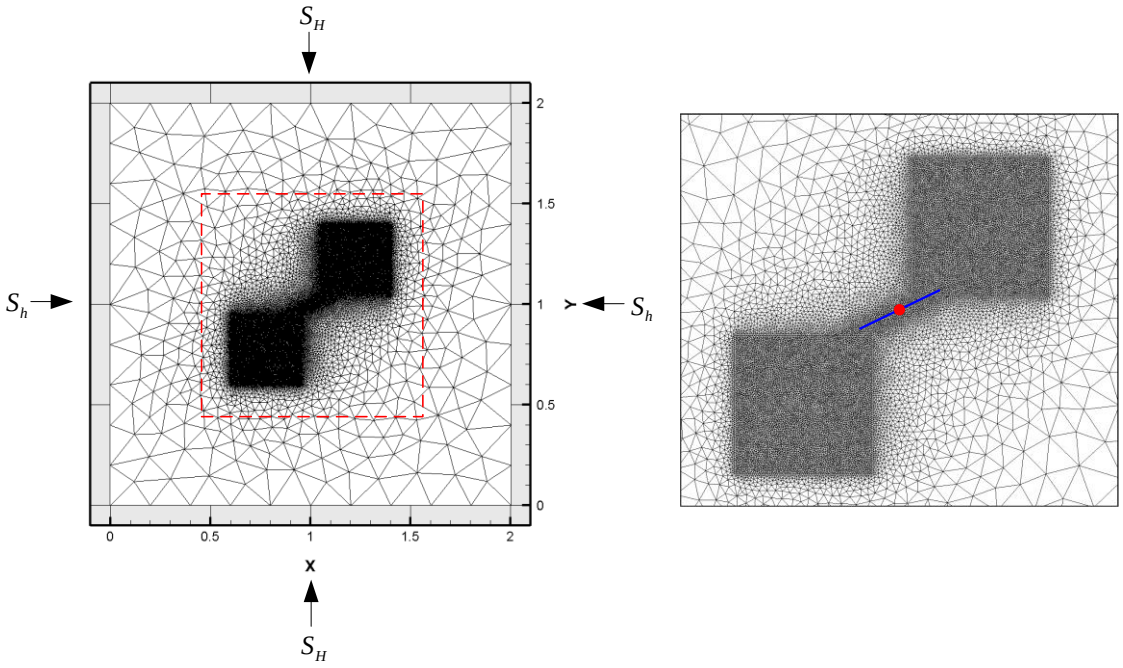

Figure 7.5. Problem geometry and in-situ stress directions.

7.2.2 Simulation Results

Figure 7.6~Figure 7.9 show the numerical results for hydraulic fracturing simulation. In Figure 7.6, the contours of nonlocal formulated damage density for each case are displayed, which indicate the directions of propagation gradually change with different in-situ stress from maintaining its original direction in case I to a sharp turning directly forwards the direction of minimum in-situ stress. The assumption that final direction of hydraulic fracture growth is parallel to S_H is proved by the results. Moreover, the turning angles vary with different ratio of stress anisotropy. This is indeed important if there are natural fractures existing near wellbore. The hydraulic fracture growth path will affect the interaction between hydraulic and natural fractures. The principal stress contours during the fracture propagation for each in-situ stress are shown in Figure 7.7. Figure 7.8 and Figure 7.9 display the aperture and pressure profiles for each in-situ stress case. The horizontal axials of these diagrams in Figure 7.8 and

Figure 7.9 mean the locations along the fractures, in which the ranges marked by red lines indicate initial fracture and blue lines indicate the newly extended fracture. Each colored curve represents the profile in real time fracture length during the propagation.

From Figure 7.8 we get the aperture profiles. When $S_H = S_h$, the fracture is growth in pure tensile load (mode I) and the aperture profile of the fracture is continuous shown in Figure 7.8(a). As S_H increased, tensile and shear combined load at the tip forces the fracture propagates in mode II pattern. The gradual severe aperture jumps between initial and newly extended fracture observed in Figure 7.8(b-d). From problem geometry, the initial fracture inclined faces to S_H. On the other hand, the newly extended fractures are gradually turning to direction of S_H. According to the elementary mechanics, fewer angles between the direction of surface and compressive pressure leads to less compressive pressure that will be applied on the normal direction of surface. As S_H increased, the compressive pressure applied on initial fracture is increased as well that forces fracture to close. Therefore, most obvious aperture bounding happens in case IV Figure 7.8(d), in which the newly extended fracture propagated almost parallel to direction of S_H subjected least compressive pressure from S_H.

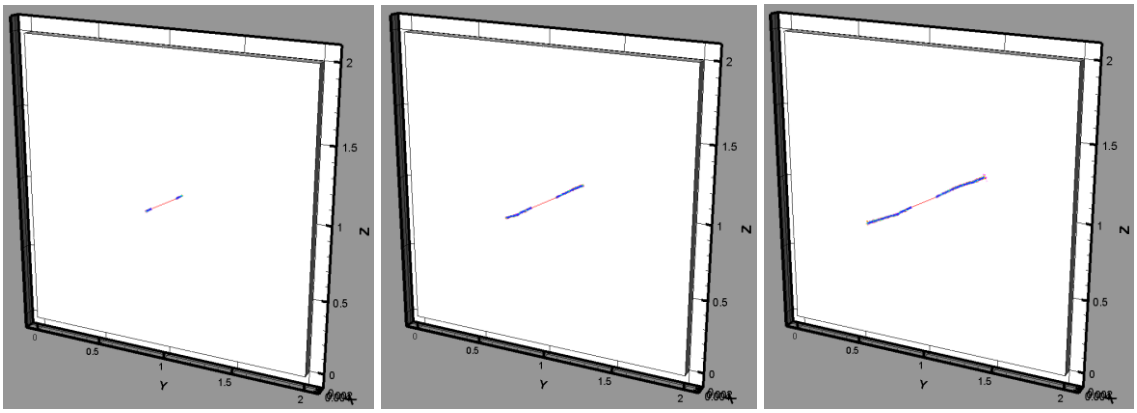

(a)

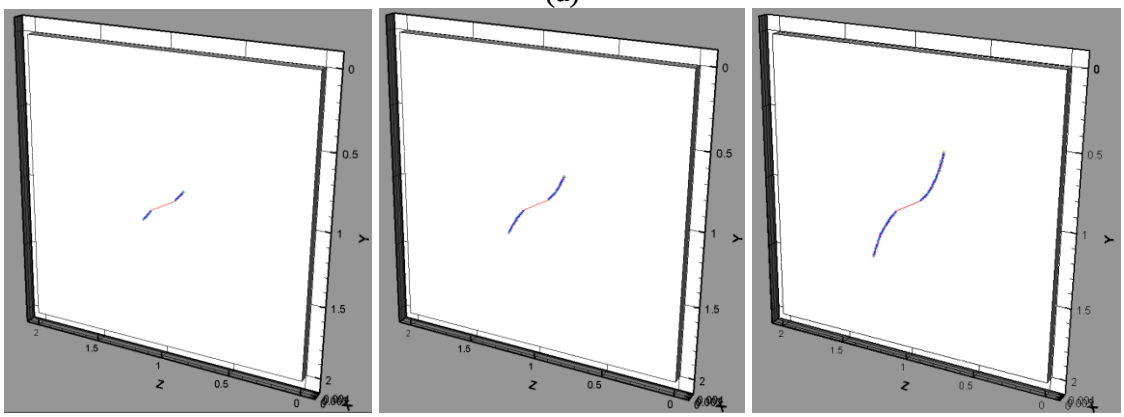

(b)

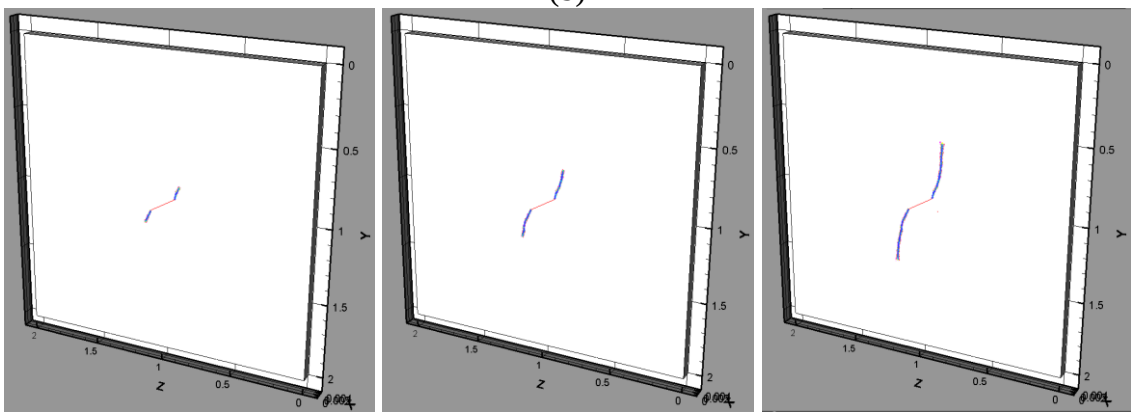

(c)

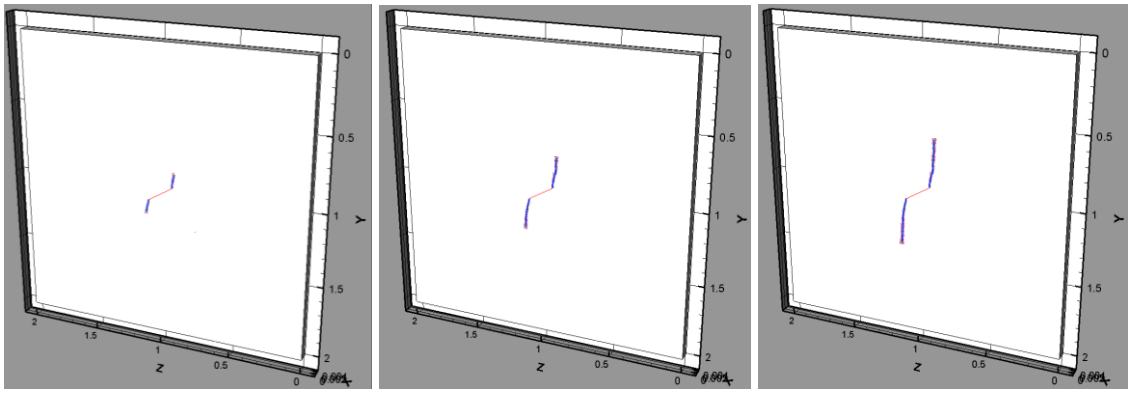

(d)

Figure 7.6. Nonlocal damage density contours of the process zone for (a) case I; (b) case II; (c) case III; (d) case IV.

Figure 7.9 are the pressure profiles. Since the pressure follows the cubic law of aperture, the pressure gradient from the injection point to fracture tip is steeper at the beginning and gradually becomes flatter as the aperture increasing. Therefore, the pressure at injection point is decreasing as the fracture propagating, which is also observed in the field hydraulic fracturing treatment. In addition, the pressure at injection point is higher if larger amount of S_H applied under the same injection rate. In other words, a higher inject pressure is needed in higher in-situ stress field in order to inject same rate inject.

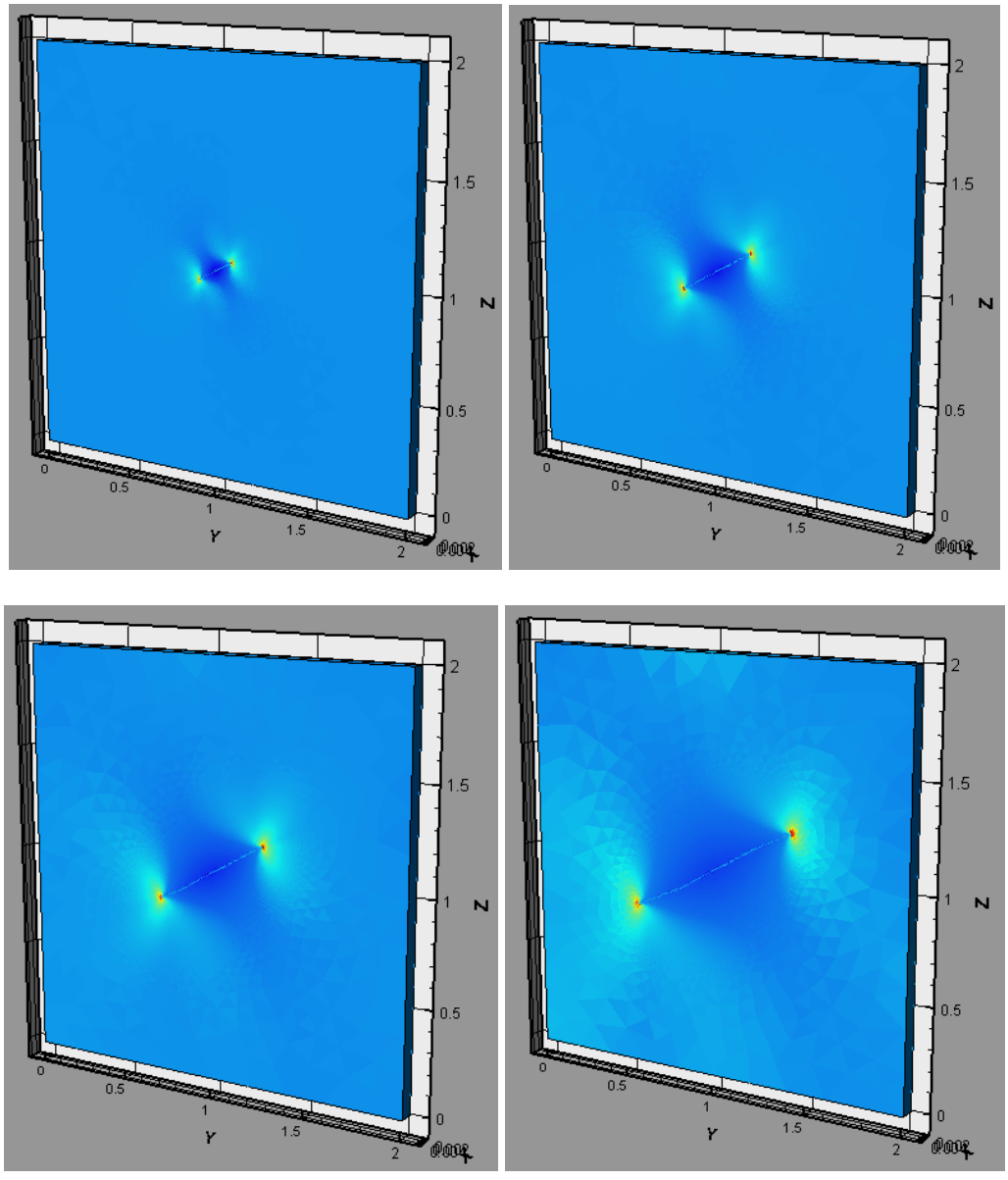

(a)

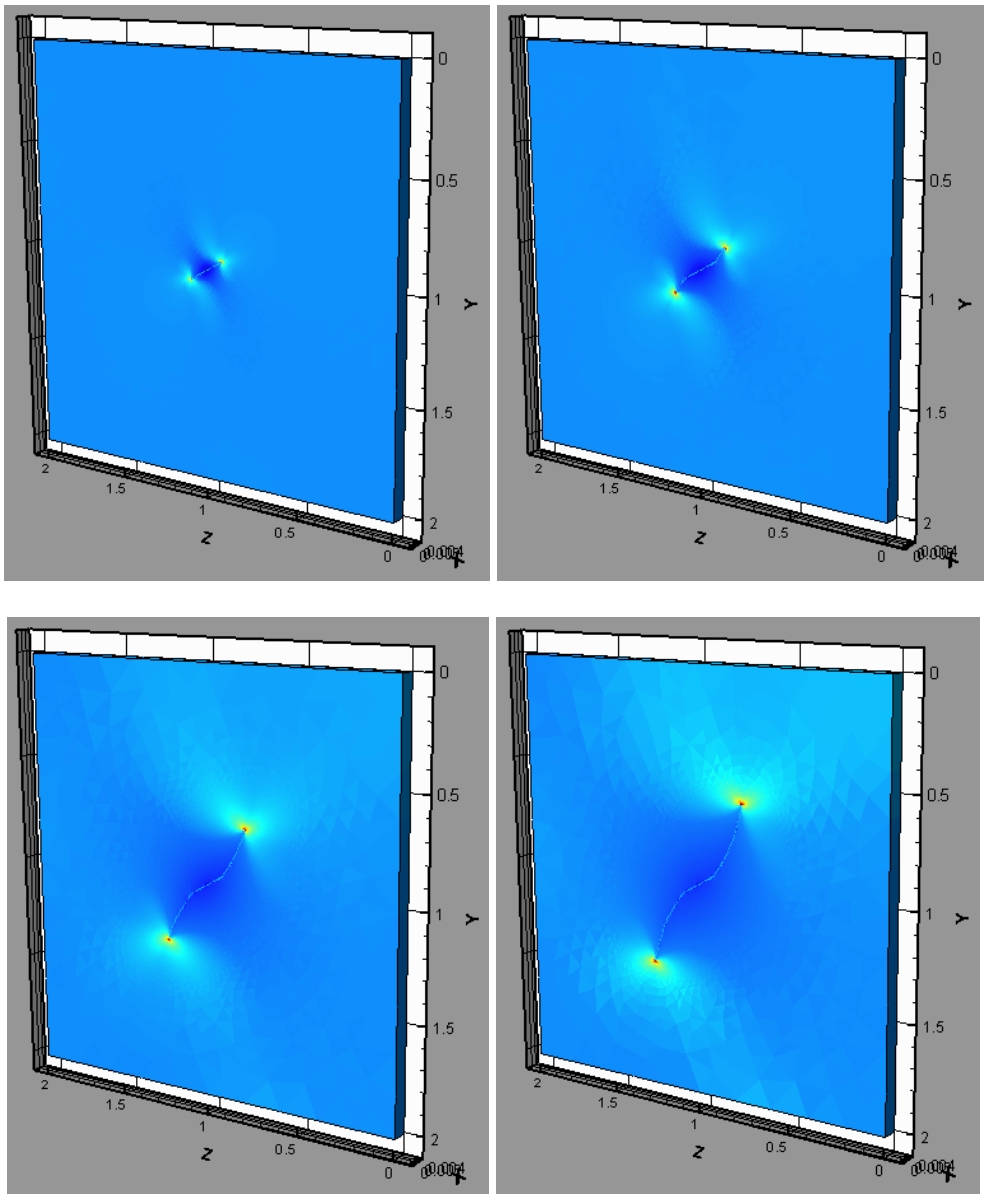

(b)

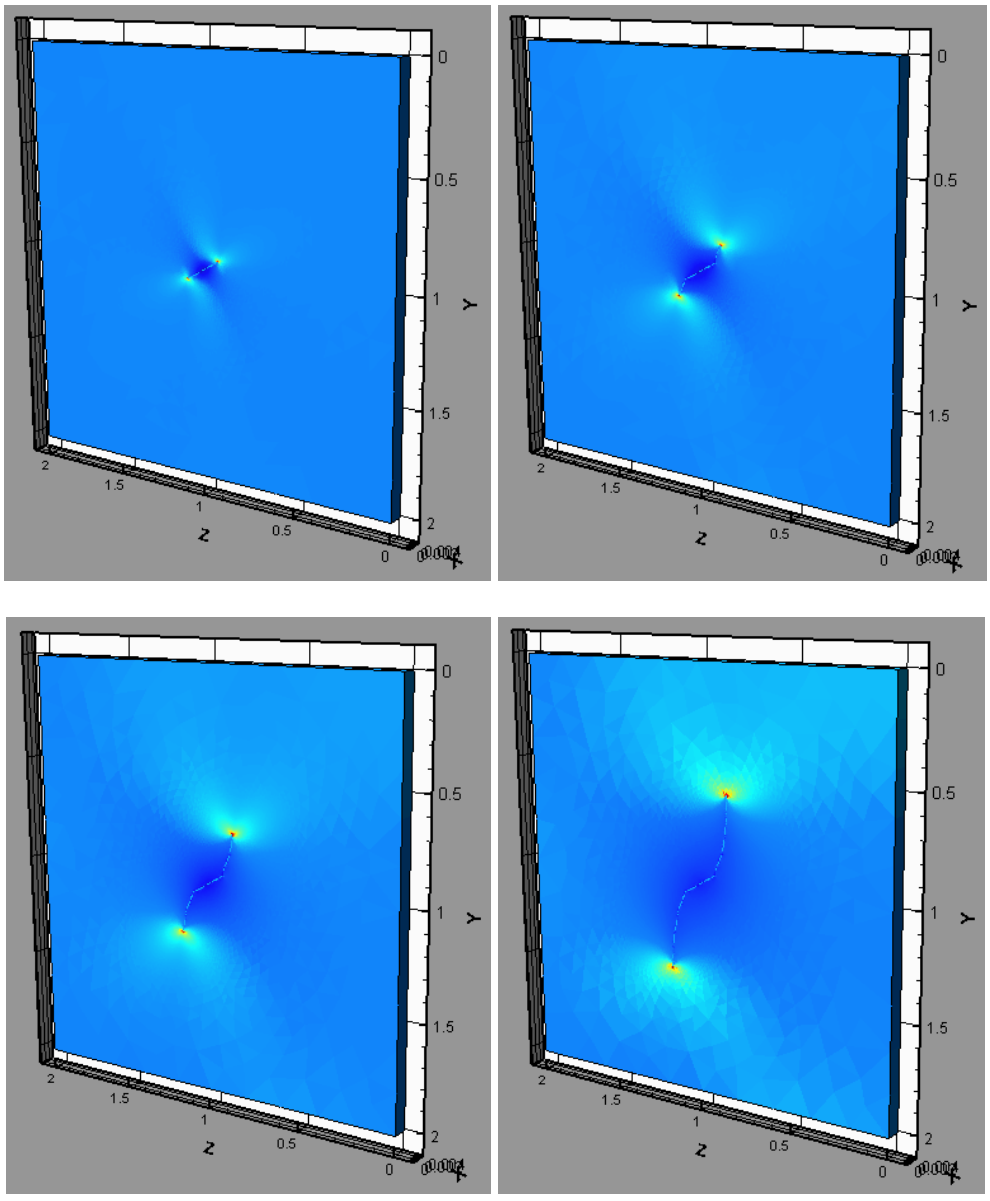

(c)

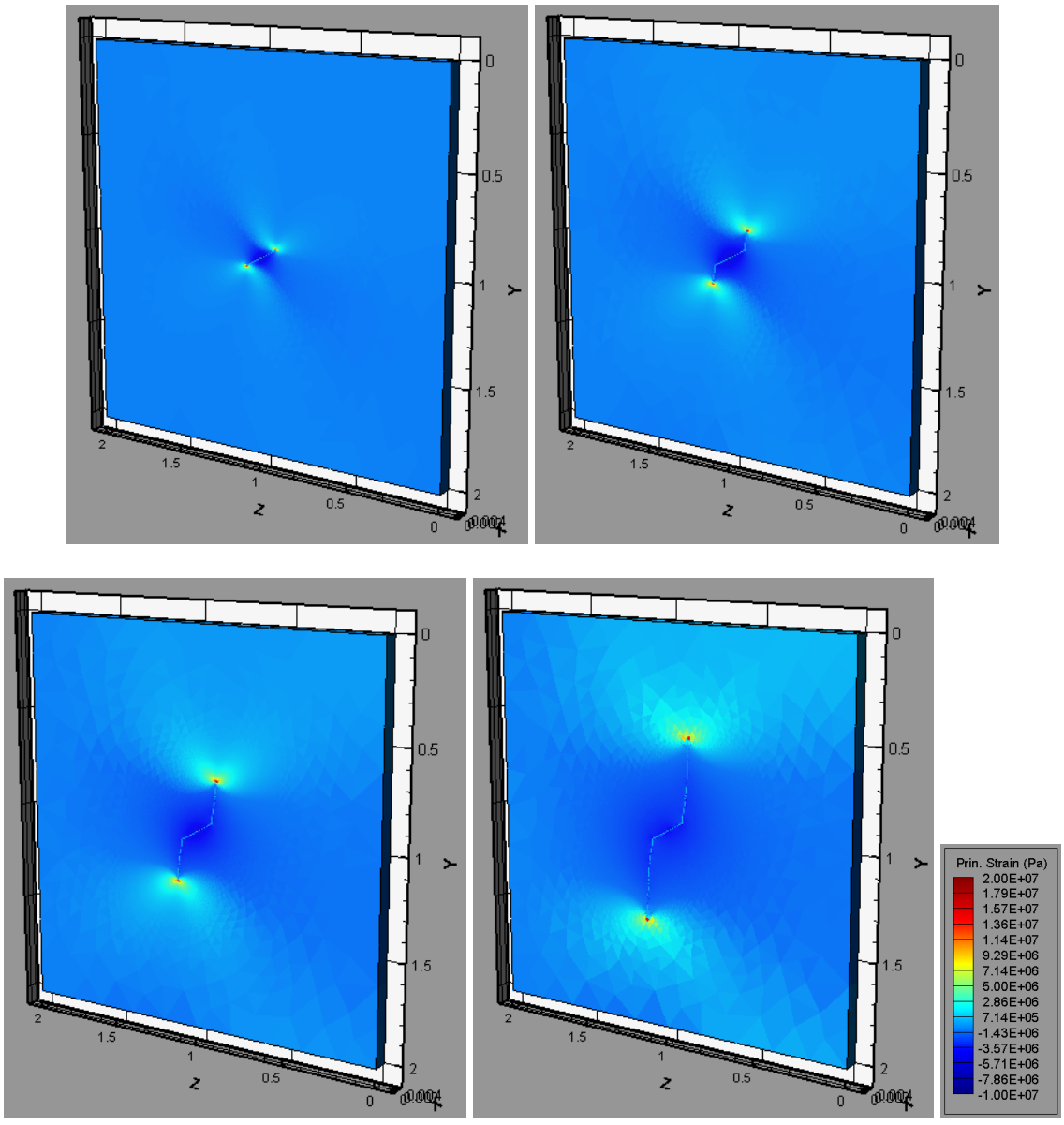

(d)

Figure 7.7. The principal stress contour during the fracture propagation for each in-situ stress: (a) case I;(b)case II; (c)case III; (d)case IV.

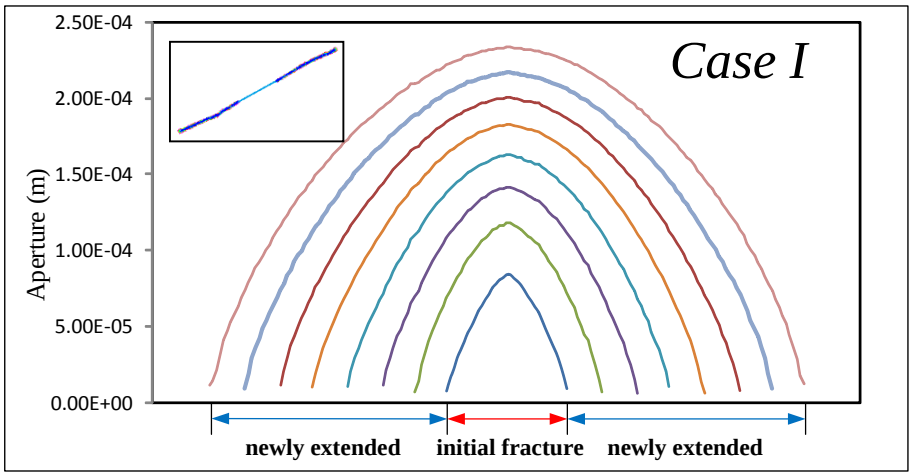
Case I
Aperture (m)
2.50E-04
2.00E-04
1.50E-04
1.00E-04
5.00E-05
0.00E+00
newly extended
initial fracture
newly extended

(a)

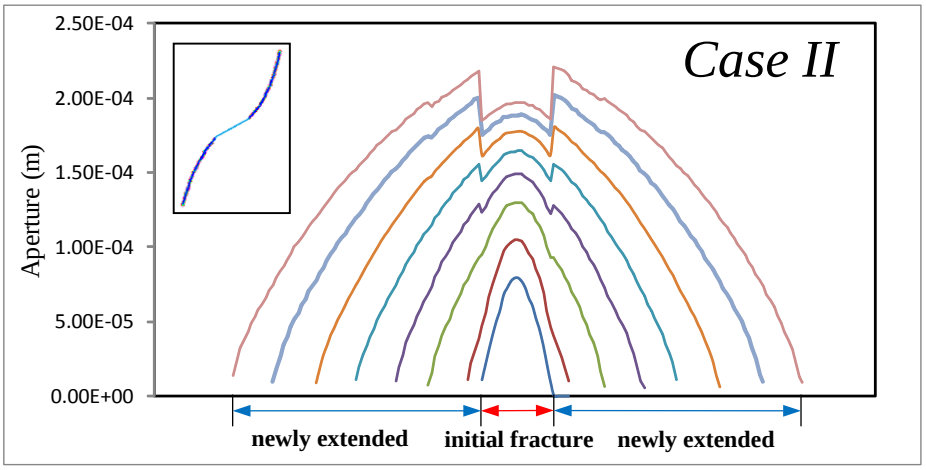
Case II
Aperture (m)
2.50E-04
2.00E-04
1.50E-04
1.00E-04
5.00E-05
0.00E+00
newly extended
initial fracture
newly extended

(b)

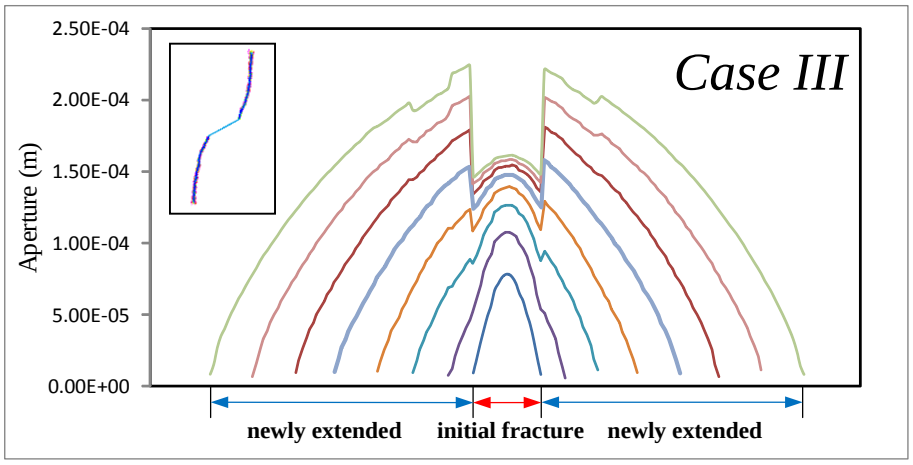
Case III
Aperture (m)
2.50E-04
2.00E-04
1.50E-04
1.00E-04
5.00E-05
0.00E+00
newly extended
initial fracture
newly extended

(c)

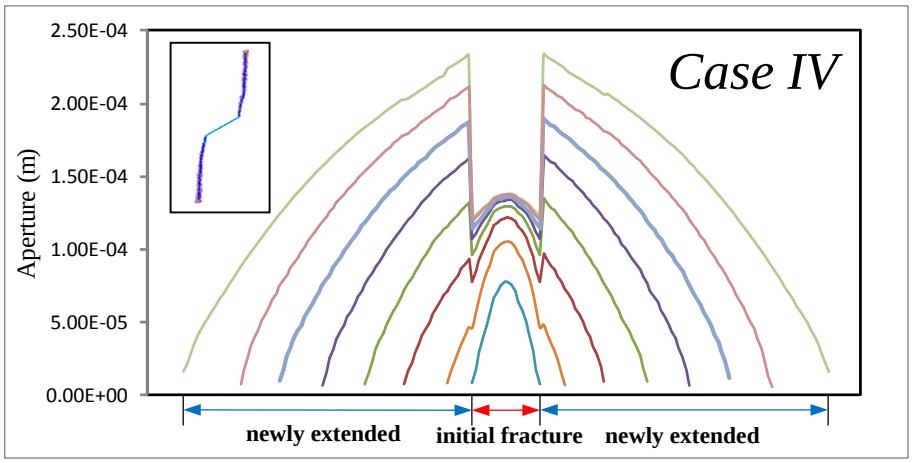

(d)

Figure 7.8. Aperture profiles for each in-situ stress case: (a)Case I; (b)Case II; (c)Case III; (d)Case IV.

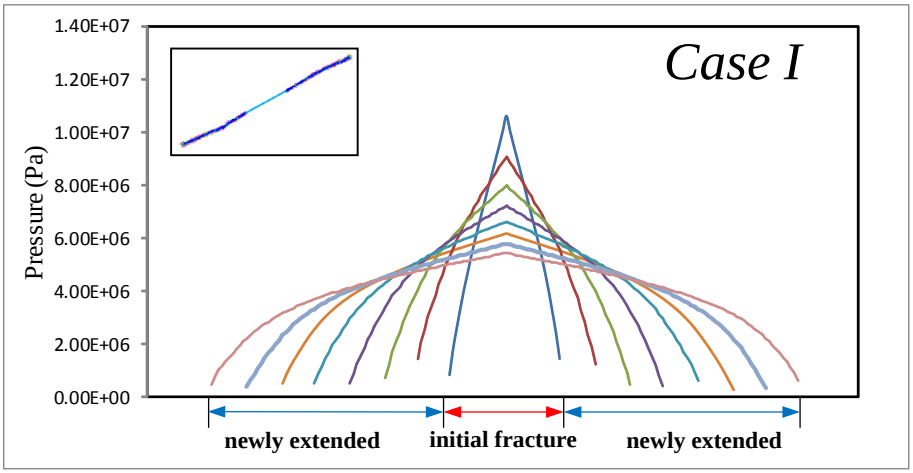

(a)

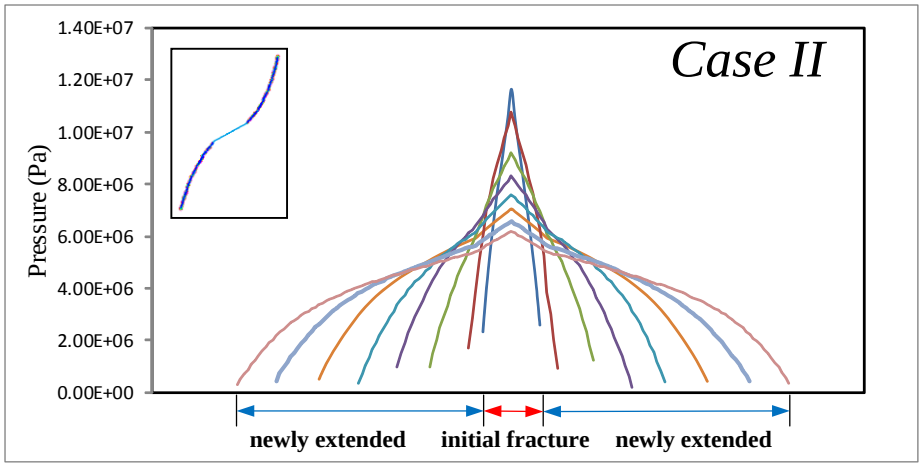

(b)

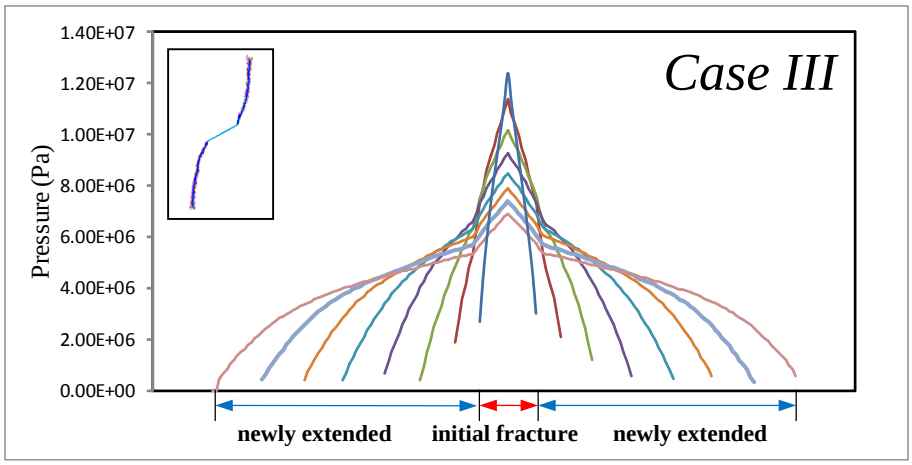

(c)

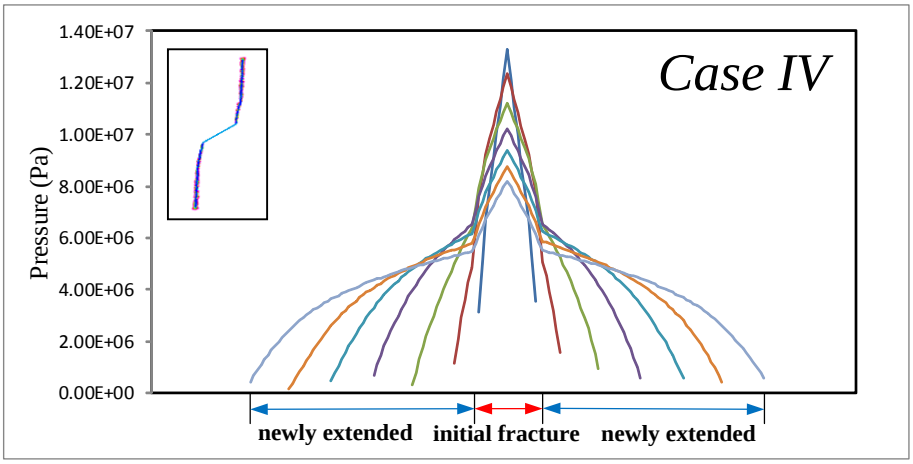

(d)

Figure 7.9. Pressure profiles for each in-situ stress case: (a)Case I; (b)Case II; (c)Case III; (d)Case IV.

7.3 Interaction between Hydraulic Fracture and Nature Fracture in 3D Formation

7.3.1 Modified Poroelastic Model

In Chapter 4, the theoretical aspects and mathematical derivation of classic poroelastic model are presented. The model is continuum-based and well explains the coupled process of the porous fluid flow and rock mass deformation for intact rock formation. However, to simulate the hydraulic fracturing process, a modification is necessarily needed because of the different flow mechanisms and boundary condition

due to discontinuity of fracture surface. The fundamentals of fully coupled poroelastic model is not valid in the element that contains a fracture. On the aspect of fluid flow only, according to the assumption in Chapter 4, the permeability of fractured element is artificially increased to represent the conductivity enhancement by fracture creation. The pressure distribution along the fracture and diffusion in the rock formation can be calculated using an equation system. The challenge problem is applying the calculated pressure profile as pressure boundary on the fracture surface during the propagation process. As mentioned, the coupling parts of poroelastic model is not valid for the fractured element though the fluid diffusion part is still used to calculate the fluid pressure. Therefore, the modification is made on the coupling part of poroelastic model. The original coupled part $-\mathbf{A}$ in Eq. (4.34) is replaced with a new matrix derived based on the way of applying hydraulic pressure on the fracture surface using 3D EPM. The original poroelastic equations system is written as:

$$\begin{bmatrix} \mathbf{K}_t & -\mathbf{A} \\ -\mathbf{A}^T & -\Delta t\lambda\mathbf{H}_H - \mathbf{S} \end{bmatrix} \begin{bmatrix} \tilde{\mathbf{u}}_t \\ \tilde{\mathbf{p}}_t \end{bmatrix} = \begin{bmatrix} 0 & 0 \\ -\mathbf{A}^T & -\mathbf{S} \end{bmatrix} \begin{bmatrix} \tilde{\mathbf{u}}_{t0} \\ \tilde{\mathbf{p}}_{t0} \end{bmatrix} + \begin{bmatrix} \mathbf{f}_t \\ \Delta t\mathbf{q}_t \end{bmatrix} \tag{7.1}$$

In Eq. (7.1), $\mathbf{A}$ is the fully coupled term representing the porous fluid and solid mutual interaction. Eq. (7.1) is used for the intact element. For the fractured element, the following equation system is used:

$$\begin{bmatrix} \mathbf{K}_t^{EPM} & -\mathbf{A}^{EPM} \\ 0 & -\Delta t\lambda\mathbf{H}_H - \mathbf{S} \end{bmatrix} \begin{bmatrix} \tilde{\mathbf{u}}_t \\ \tilde{\mathbf{p}}_t \end{bmatrix} = \begin{bmatrix} 0 & 0 \\ 0 & -\mathbf{S} \end{bmatrix} \begin{bmatrix} \tilde{\mathbf{u}}_{t0} \\ \tilde{\mathbf{p}}_{t0} \end{bmatrix} + \begin{bmatrix} \mathbf{f}_t \\ \Delta t\mathbf{q}_t \end{bmatrix} \tag{7.2}$$

In Eq. (7.2), the stiffness matrix of solid $\mathbf{K}_t^{EPM}$ has been changed to the one calculated by 3D EPM and is no longer fully coupled with the porous fluid. The fluid flow in the fracture element will only follows the Darcy's law. In other words, the solid

deformation will not influence the fluid pressure. The fluid pressure will affect the solid deformation in a one-way manner. Next, Eq. (7.2) is rearranged as

$$\begin{bmatrix} \mathbf{K}_t^{EPM} & 0 \\ 0 & -\Delta t\lambda \mathbf{H}_H - \mathbf{S} \end{bmatrix} \begin{bmatrix} \tilde{\mathbf{u}}_t \\ \tilde{\mathbf{p}}_t \end{bmatrix} = \begin{bmatrix} 0 & 0 \\ 0 & -\mathbf{S} \end{bmatrix} \begin{bmatrix} \tilde{\mathbf{u}}_{t0} \\ \tilde{\mathbf{p}}_{t0} \end{bmatrix} + \begin{bmatrix} \mathbf{f}_t \\ \Delta t \mathbf{q}_t \end{bmatrix} + \begin{bmatrix} \mathbf{A}^{EPM} \tilde{\mathbf{p}}_t \\ 0 \end{bmatrix} \tag{7.3}$$

After rearranging of Eq. (7.3), $\mathbf{A}^{EPM} \cdot \tilde{\mathbf{p}}_t$ term can be considered as nodal forces applied on the right hand side of equation system. Meantime, the pressure boundary condition on the fracture surface can be successfully applied if $\mathbf{A}^{EPM}$ is well constructed. Another advantage is that the pressure boundary will be possibly applied real-timely since that displacement and pressure are calculated simultaneously. Let's recall the method of representing the hydraulic pressure in fractured element presented in Chapter 4, which is helpful for understanding the mathematical and mechanical meaning of $\mathbf{A}^{EPM} \tilde{\mathbf{p}}_t$. The hydraulic pressure $\mathbf{P}$ in an element is represented by the equivalent nodal forces $\mathbf{F} = \mathbf{P} \cdot A$, where A is the area of fracture in one element. Take type I partition element for example, the pressure in the fracture surface uses the averaged value of the pressure on these 4 nodes written as

$$\mathbf{P} = \frac{1}{4}(\tilde{p}_t^I + \tilde{p}_t^J + \tilde{p}_t^K + \tilde{p}_t^M) \cdot \mathbf{n} \tag{7.4}$$

where $\mathbf{n} = \left[n_x, n_y, n_z \right]$ is the direction vector indicating the normal direction of fracture surface.

As shown in Figure 4.5, similar with Eq.(4.43)~(4.46), the equivalent nodal forces are rewritten as

$$\begin{aligned} \mathbf{F} &= [F_{Mx'}, F_{My'}, F_{Mz'}] \\ &= \mathbf{P} \cdot A = \frac{1}{4}(\tilde{p}_t^I + \tilde{p}_t^J + \tilde{p}_t^K + \tilde{p}_t^M) \cdot \mathbf{n} \cdot A \end{aligned} \tag{7.5}$$

$$-\frac{1}{3}\mathbf{F} = [F_{Ix'}, F_{Iy'}, F_{Iz'}] = -\frac{1}{3}\mathbf{P}\cdot A = -\frac{1}{3}\frac{1}{4}(\tilde{p}_t^I + \tilde{p}_t^J + \tilde{p}_t^K + \tilde{p}_t^M)\cdot\mathbf{n}\cdot A \tag{7.6}$$

$$-\frac{1}{3}\mathbf{F} = [F_{Jx'}, F_{Jy'}, F_{Jz'}] = -\frac{1}{3}\mathbf{P}\cdot A = -\frac{1}{3}\frac{1}{4}(\tilde{p}_t^I + \tilde{p}_t^J + \tilde{p}_t^K + \tilde{p}_t^M)\cdot\mathbf{n}\cdot A \tag{7.7}$$

$$-\frac{1}{3}\mathbf{F} = [F_{Kx'}, F_{Ky'}, F_{Kz'}] = -\frac{1}{3}\mathbf{P}\cdot A = -\frac{1}{3}\frac{1}{4}(\tilde{p}_t^I + \tilde{p}_t^J + \tilde{p}_t^K + \tilde{p}_t^M)\cdot\mathbf{n}\cdot A \tag{7.8}$$

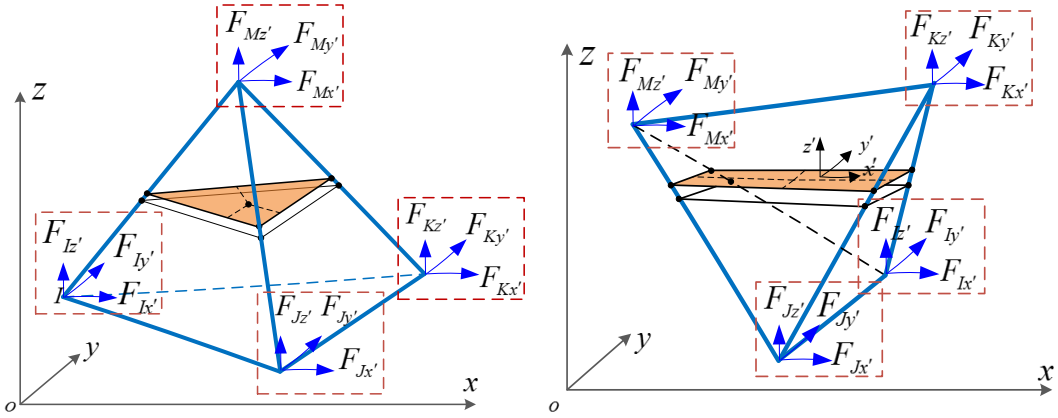

(a) (b)

Figure 7.10. Equivalent nodal forces representing hydraulic pressure for (a) type I partition element; (b) type II partition element.

Write Eq. (7.5)~(7.8) in matrix form shown as following

$$[F_{Mx'}, F_{My'}, F_{Mz'}] = \mathbf{A}_{typeI}^{M}\tilde{\mathbf{p}}_t^e = \begin{bmatrix} \frac{1}{4}An_x & \frac{1}{4}An_x & \frac{1}{4}An_x & \frac{1}{4}An_x \\ \frac{1}{4}An_y & \frac{1}{4}An_y & \frac{1}{4}An_y & \frac{1}{4}An_y \\ \frac{1}{4}An_z & \frac{1}{4}An_z & \frac{1}{4}An_z & \frac{1}{4}An_z \end{bmatrix} \begin{bmatrix} \tilde{p}_t^I \\ \tilde{p}_t^J \\ \tilde{p}_t^K \\ \tilde{p}_t^M \end{bmatrix} \tag{7.9}$$

$$[F_{Ix'}, F_{Iy'}, F_{Iz'}] = \mathbf{A}_{typeI}^{I} \tilde{\mathbf{p}}_t^e = \begin{bmatrix} -\frac{1}{12}An_x & -\frac{1}{12}An_x & -\frac{1}{12}An_x & -\frac{1}{12}An_x \\ -\frac{1}{12}An_y & -\frac{1}{12}An_y & -\frac{1}{12}An_y & -\frac{1}{12}An_y \\ -\frac{1}{12}An_z & -\frac{1}{12}An_z & -\frac{1}{12}An_z & -\frac{1}{12}An_z \end{bmatrix} \begin{bmatrix} \tilde{p}_t^I \\ \tilde{p}_t^J \\ \tilde{p}_t^K \\ \tilde{p}_t^M \end{bmatrix} \tag{7.10}$$

$$[F_{Jx'}, F_{Jy'}, F_{Jz'}] = \mathbf{A}_{typeI}^{J} \tilde{\mathbf{p}}_t^e = \begin{bmatrix} -\frac{1}{12}An_x & -\frac{1}{12}An_x & -\frac{1}{12}An_x & -\frac{1}{12}An_x \\ -\frac{1}{12}An_y & -\frac{1}{12}An_y & -\frac{1}{12}An_y & -\frac{1}{12}An_y \\ -\frac{1}{12}An_z & -\frac{1}{12}An_z & -\frac{1}{12}An_z & -\frac{1}{12}An_z \end{bmatrix} \begin{bmatrix} \tilde{p}_t^I \\ \tilde{p}_t^J \\ \tilde{p}_t^K \\ \tilde{p}_t^M \end{bmatrix} \tag{7.11}$$

$$[F_{Kx'}, F_{Ky'}, F_{Kz'}] = \mathbf{A}_{typeI}^{K} \tilde{\mathbf{p}}_t^e = \begin{bmatrix} -\frac{1}{12}An_x & -\frac{1}{12}An_x & -\frac{1}{12}An_x & -\frac{1}{12}An_x \\ -\frac{1}{12}An_y & -\frac{1}{12}An_y & -\frac{1}{12}An_y & -\frac{1}{12}An_y \\ -\frac{1}{12}An_z & -\frac{1}{12}An_z & -\frac{1}{12}An_z & -\frac{1}{12}An_z \end{bmatrix} \begin{bmatrix} \tilde{p}_t^I \\ \tilde{p}_t^J \\ \tilde{p}_t^K \\ \tilde{p}_t^M \end{bmatrix} \tag{7.12}$$

The nodal force vector on the right hand of elemental matrix system is written as:

$$\mathbf{f} = [F_{Ix'}, F_{Iy'}, F_{Iz'}, F_{Jx'}, F_{Jy'}, F_{Jz'}, F_{Kx'}, F_{Ky'}, F_{Kz'}, F_{Mx'}, F_{My'}, F_{Mz'}] \tag{7.13}$$

Combining and rearranging Eq. (7.9)~(7.13) yield

$$\mathbf{f} = \mathbf{A}_{typeI}^{EPM} \tilde{\mathbf{p}}_t^e \tag{7.14}$$

where $\mathbf{A}_{typeI}^{EPM} = \begin{bmatrix} \mathbf{A}_{typeI}^{I} & \mathbf{A}_{typeI}^{J} & \mathbf{A}_{typeI}^{K} & \mathbf{A}_{typeI}^{M} \end{bmatrix}^T$ for type I partition element.

Similarly, for type II partition element,

$$[F_{Mx'}, F_{My'}, F_{Mz'}] = \mathbf{A}_{typeII}^{M} \tilde{\mathbf{p}}_t^e = \begin{bmatrix} \frac{1}{8}An_x & \frac{1}{8}An_x & \frac{1}{8}An_x & \frac{1}{8}An_x \\ \frac{1}{8}An_y & \frac{1}{8}An_y & \frac{1}{8}An_y & \frac{1}{8}An_y \\ \frac{1}{8}An_z & \frac{1}{8}An_z & \frac{1}{8}An_z & \frac{1}{8}An_z \end{bmatrix} \begin{bmatrix} \tilde{p}_t^I \\ \tilde{p}_t^J \\ \tilde{p}_t^K \\ \tilde{p}_t^M \end{bmatrix} \tag{7.15}$$

$$[F_{Kx'}, F_{Ky'}, F_{Kz'}] = \mathbf{A}^{K}_{typeII}\tilde{\mathbf{p}}^{e}_{t} = \begin{bmatrix} \frac{1}{8}An_x & \frac{1}{8}An_x & \frac{1}{8}An_x & \frac{1}{8}An_x \\ \frac{1}{8}An_y & \frac{1}{8}An_y & \frac{1}{8}An_y & \frac{1}{8}An_y \\ \frac{1}{8}An_z & \frac{1}{8}An_z & \frac{1}{8}An_z & \frac{1}{8}An_z \end{bmatrix} \begin{bmatrix} \tilde{p}^{I}_{t} \\ \tilde{p}^{J}_{t} \\ \tilde{p}^{K}_{t} \\ \tilde{p}^{M}_{t} \end{bmatrix} \tag{7.16}$$

$$[F_{Ix'}, F_{Iy'}, F_{Iz'}] = \mathbf{A}^{I}_{typeII}\tilde{\mathbf{p}}^{e}_{t} = \begin{bmatrix} -\frac{1}{8}An_x & -\frac{1}{8}An_x & -\frac{1}{8}An_x & -\frac{1}{8}An_x \\ -\frac{1}{8}An_y & -\frac{1}{8}An_y & -\frac{1}{8}An_y & -\frac{1}{8}An_y \\ -\frac{1}{8}An_z & -\frac{1}{8}An_z & -\frac{1}{8}An_z & -\frac{1}{8}An_z \end{bmatrix} \begin{bmatrix} \tilde{p}^{I}_{t} \\ \tilde{p}^{J}_{t} \\ \tilde{p}^{K}_{t} \\ \tilde{p}^{M}_{t} \end{bmatrix} \tag{7.17}$$

$$[F_{Jx'}, F_{Jy'}, F_{Jz'}] = \mathbf{A}^{J}_{typeII}\tilde{\mathbf{p}}^{e}_{t} = \begin{bmatrix} -\frac{1}{8}An_x & -\frac{1}{8}An_x & -\frac{1}{8}An_x & -\frac{1}{8}An_x \\ -\frac{1}{8}An_y & -\frac{1}{8}An_y & -\frac{1}{8}An_y & -\frac{1}{8}An_y \\ -\frac{1}{8}An_z & -\frac{1}{8}An_z & -\frac{1}{8}An_z & -\frac{1}{8}An_z \end{bmatrix} \begin{bmatrix} \tilde{p}^{I}_{t} \\ \tilde{p}^{J}_{t} \\ \tilde{p}^{K}_{t} \\ \tilde{p}^{M}_{t} \end{bmatrix} \tag{7.18}$$

Combining and rearranging Eq. (7.13) and Eq. (7.15)~(7.18) yield

$$\mathbf{f} = \mathbf{A}^{EPM}_{typeII}\tilde{\mathbf{p}}^{e}_{t} \tag{7.19}$$

where $\mathbf{A}^{EPM}_{typeII} = \begin{bmatrix} \mathbf{A}^{I}_{typeII} & \mathbf{A}^{J}_{typeII} & \mathbf{A}^{K}_{typeII} & \mathbf{A}^{M}_{typeII} \end{bmatrix}^{T}$ for type II partition element.

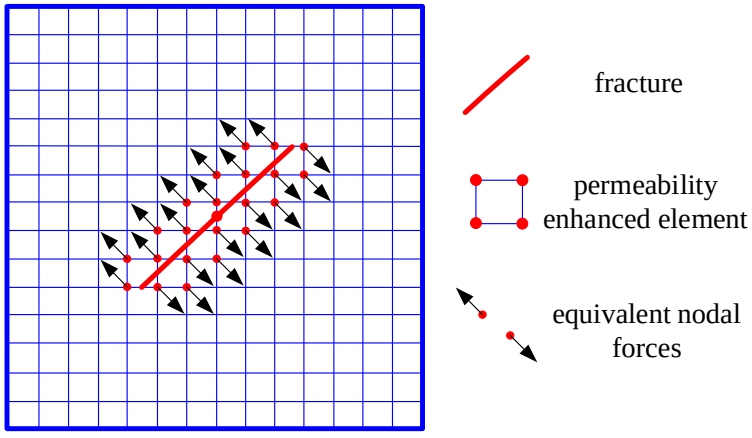

Figure 7.11. Illustration of modified poroelastic model

Finally, the modified poroelastic model is derived and illustrated in Figure 7.11. In Figure 7.11, the red line indicates a fracture. The blue rectangular with the red dot corner displays the permeability enhanced element cut by the fracture. The arrows show the equivalent nodal forces normal to the fracture surface. The fully coupled poroelastic model shown in Eq. (7.1) is adopted to simulate the fluid diffusion and deformation in the intact rock formation. The modified poroelastic model shown in Eq. (7.2) changed the matrix component based on 3D EPM that is capable to apply real-time hydraulic pressure calculated simultaneously in the same equation system. For newly extended fracture, the elemental matrix will be changed to 3D EPM formulation if the element is cut by the new fracture surfaces.

In traditional poroelastic modeling, the time step Δt is predetermined to fit the problem of interests. However, for hydraulic fracture simulation, the time step between each propagation step has specific physical meaning that governs the fracture pressure distribution and leak-off volume into the formation. Therefore, a reasonable value of Δt is required. In present model, the injection time increment Δt in Eq. (7.1) and (7.2) is calculated using the similar way as the one used in lubrication theory written as $\Delta t = \int_{A_f} \Delta w dA / Q_i$. The equation means that the Δt only takes account in the fluid volume that stays in the fracture surface. The volume of diffuse fluid is neglect in Δt calculation since that the leak-off volume is difficult to get especially for complex fracture surface and moving boundary during the fracture propagation. Therefore, Δt is underestimated and needs more work in the future.

In section 7.2, a series of examples under different in-situ stress are presented. Using lubrication flow theory, the fluid flow in the fracture can be well captured with

rigorous physical foundation. However, smooth fracture surface and specific meshing are required that are extremely difficult for real 3D hydraulic fracture problem with complex geometry. Besides, the nonlocal damage model adopted in section 7.2 requires that the element size is smaller than characteristic length in the scale of millimeters. This limitation makes the computational volume really large for real 3D problem even with domain of several cubic meters. In the following simulations, the modified poroelastic model and damage model in local formulation are employed. The damage evolution follows Eq. (2.32). Taking advantage of modified poroelastic model, the fracture fluid is flowing through the high permeability fractured element without specified flow meshing. The real-time hydraulic pressure is applied on the fracture surface using the matrix implanted in the global matrix. The simulations will subject to the mesh size dependency because of using local damage theory. The computational volume can be reduced to be acceptable without the limitation of element size. Nevertheless, due to the complication of true 3D hydraulic fracture problem, the present model provides a novel and feasible way to predict the fracture propagation and fluid diffusion pattern of true 3D hydraulic fracture propagation and its interaction with natural fractures.

7.3.2 One Natural Fracture

In section 7.2, the simulated fracture propagation was primarily influenced by the magnitude and orientation of the in-situ stress. In the following two sections, the examples of 3D hydraulic fracture propagation and its interaction with natural fracture are presented. The existing of natural fractures is another crucial factor that controls the propagating direction. After connecting between hydraulic and natural fracture, natural

fracture becomes part of newly extended hydraulic fracture with complex curved surface that makes the assumption of planar fracture surface in classic hydraulic fracture model invalid. This example designs a natural fracture located near the initial hydraulic fracture in a $10m \times 10m \times 10m$ cubic domain. The problem geometry is shown in Figure 7.12. The red dot indicates the injection point and the circular plane with red outline is initial fracture. A natural fracture is located nearby initial hydraulic fracture shown by the circular plane with blue outline. Figure 7.13 gives detailed geometry from the top and lateral views. The diameters for hydraulic and natural fractures are both 3 meters. Natural fracture is 45 degree inclined to the horizontal plane. The initial pore pressure of whole domain is 1.0 MPa. The Young's modulus E and Poisson's ratio ν are set as $27.6GPa$ and 0.15 respectively. And $\varepsilon_0 = 0.3 \times 10^{-3}$, $\varepsilon_f = 4.0\varepsilon_0$ for damage evolution function. The permeability of intact and fractured element are $k_{\text{intact}} = 0.5\text{md}$, $k_{\text{fractured}} = 1.0\text{e}^3 k_{\text{intact}}$. For fluid parameters, the viscosity is $\mu = 0.3 \times 10^{-3}\,\text{Pa} \cdot \text{s}$,the injection rate is constantly $Q_{inj} = 2.0 \times 10^{-3}\,\text{m}^3/\text{s}$. The total element number is 1916782 and the total node number is 304045.

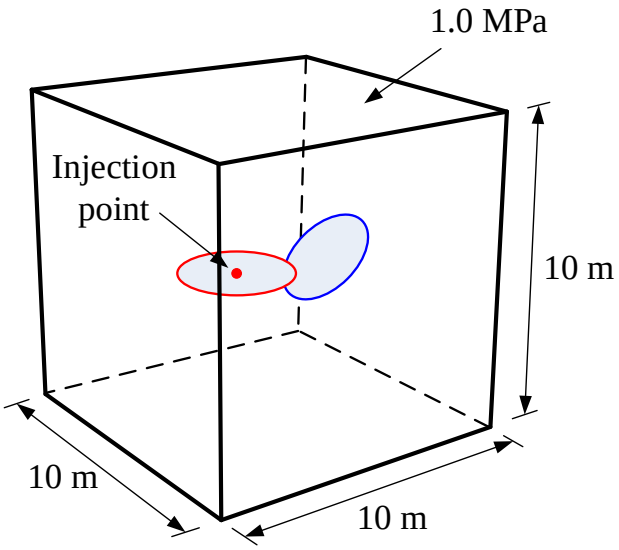

Figure 7.12. Problem geometry and initial fractures.

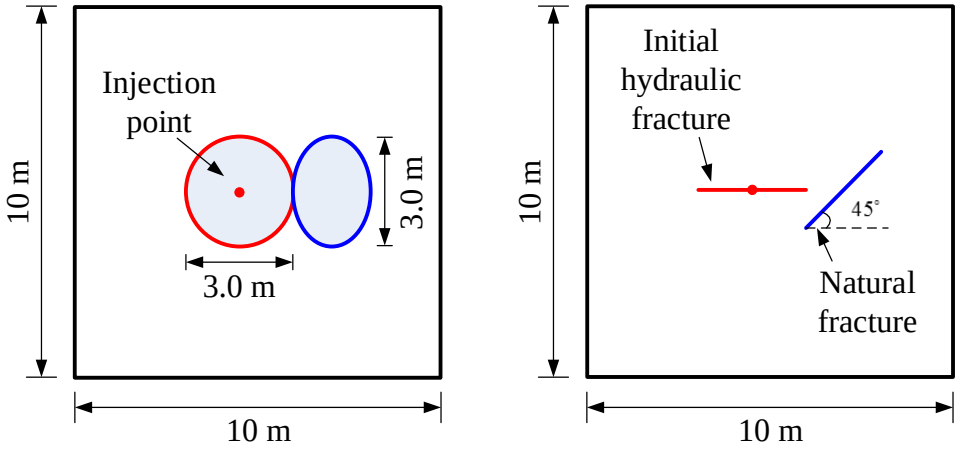

(a) (b)

Figure 7.13. Detailed spatial geometry of two fractures from (a) Top view and (b) lateral view.

Figure 7.14~Figure 7.17 show the numerical results for hydraulic fracturing test. In Figure 7.14, the pattern of fracture propagation is represented by the damaged elements shown in blue color. Lateral views of middle slice of domain are also displayed in the figure that help the understanding of geometry of propagating fracture. Two red circles indicate the initial fractures. The pore pressure distributions in the

fracture surface and formation during the propagation process are shown in Figure 7.15. The displacement discontinuity represented by 3D EPM is shown by the contour of displacement in z direction. The fracture apertures are shown in Figure 7.16. It takes 26.71 seconds injection time to create final fracture shown in Figure 7.14(g).

Figure 7.14~Figure 7.17 are integrally described for better understanding of the whole process of hydraulic fracturing and the interaction with natural fracture. The injection point is located in the center of horizontal fracture. The arising of pore pressure along initial fracture surface is induced by the fluid injection shown in Figure 7.15(a). So far we observe, the natural fracture is not connected with the hydraulic fracture and is still closed. The pressure in fracture surface is applied as the pressure boundary condition. Figure 7.16(a) and Figure 7.17(a) indicate the opening of the fracture subjected to the pressure shown in Figure 7.15(a). Therefore, shown in Figure 7.14(a), fracture propagates radially induced by the hydraulic pressure. Then, the fracture continually propagates and consequently connects with the natural fracture in Figure 7.14(c). The newly extended fracture between hydraulic and natural fracture is slightly inclined due to the stress disturbed by the discontinuity of natural fracture. At that time, the pore pressure contour shown in Figure 7.15(f), in which pressure drop at injection point and fracture surface is found. The pressure drop is reasonable and expected due to new channel created by the connection with natural fracture and constant injection rate. During the hydraulic fracture propagation, the pressure drop is also found in the examples using lubrication theory in section 7.2 since that the aperture is larger during growth of fracture provide more storage room and less resistance for flow.

In further propagation, in Figure 7.14(d)~(g), we found the major and faster region of fracture growth is still located around initial hydraulic fracture because its higher pressure distribution. The connection line between hydraulic and natural fracture cuts in the middle of the natural fracture. In Figure 7.14(g), the natural fracture is only propagating on its upper end. The aperture contours show the opening occurs in the upper part of natural fracture from the connection line shown in Figure 7.17(h). The reason for this phenomenon is that the lower part of natural fracture is covered in the compressive zone of the major hydraulic fracture. The compression from the major fracture neutralizes the pressurizing of lower part and forces the fracture at that area to close. As mentioned above, the major propagation after interconnecting occurs around the initial hydraulic fracture. The fracture growth on the further end of natural fracture is much slower. Moreover, observed from Figure 7.17(a)~(h), we found the fracture tends to growth in circular shape since that the fracture is propagating from a circular initial fracture and the in-situ stress is isotropic. The fracture is primarily propagating on the narrow side of the fracture until the fracture shape becomes circular again, even that the fracture shape becomes irregular after connected with the natural fracture,.

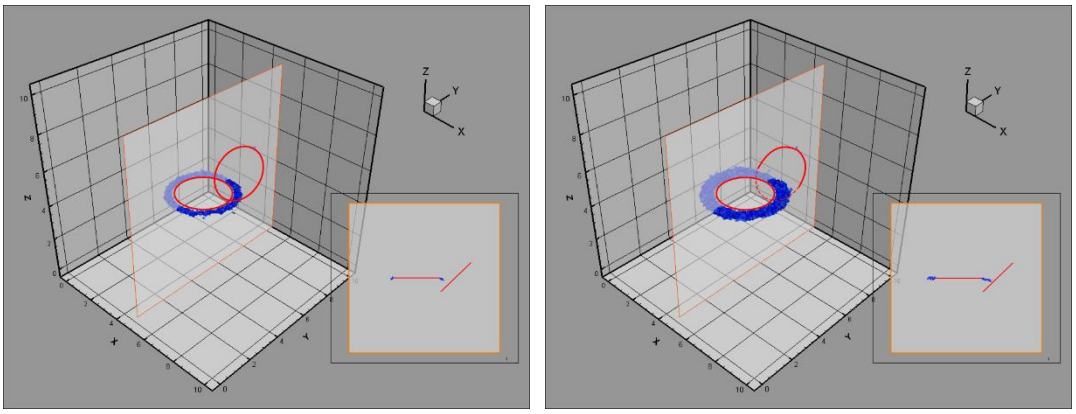

(a) (b)

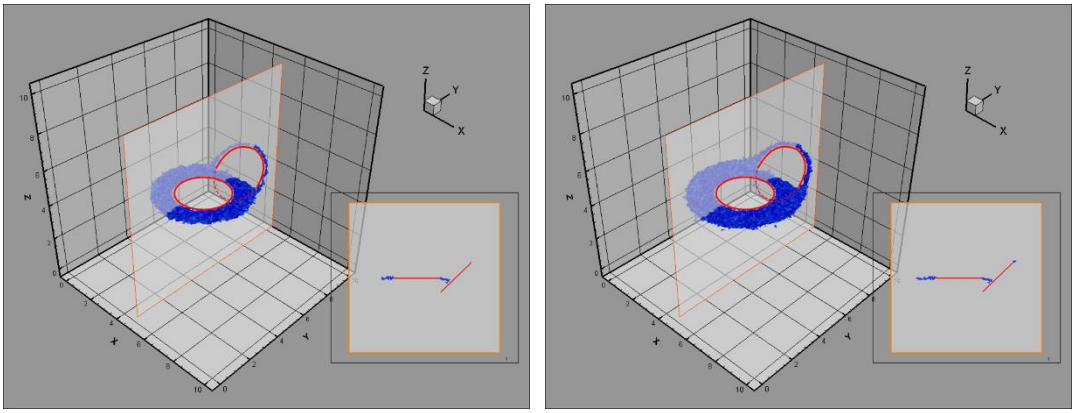

(c) (d)

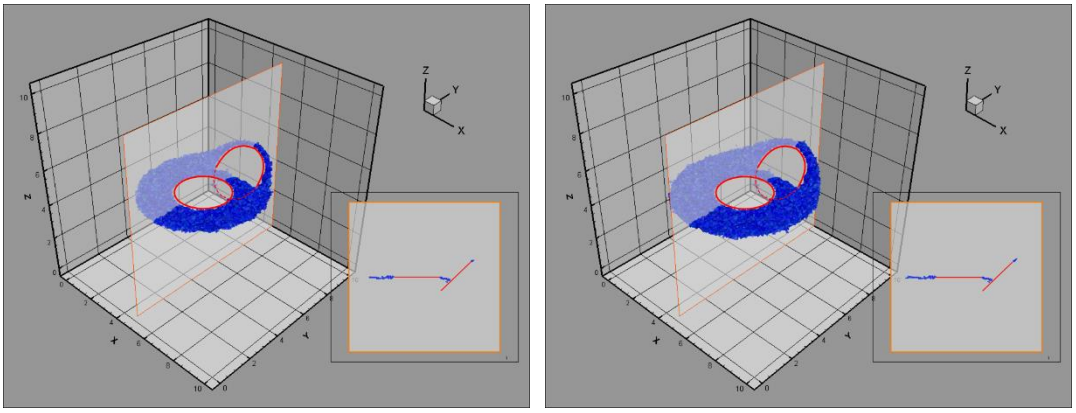

(e) (f)

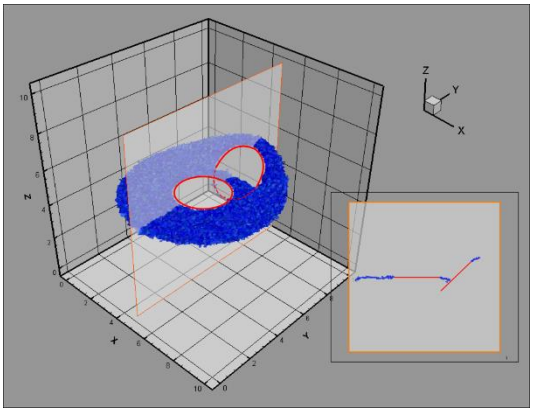

(g)

Figure 7.14. The pattern of fracture propagation displayed by damaged element.

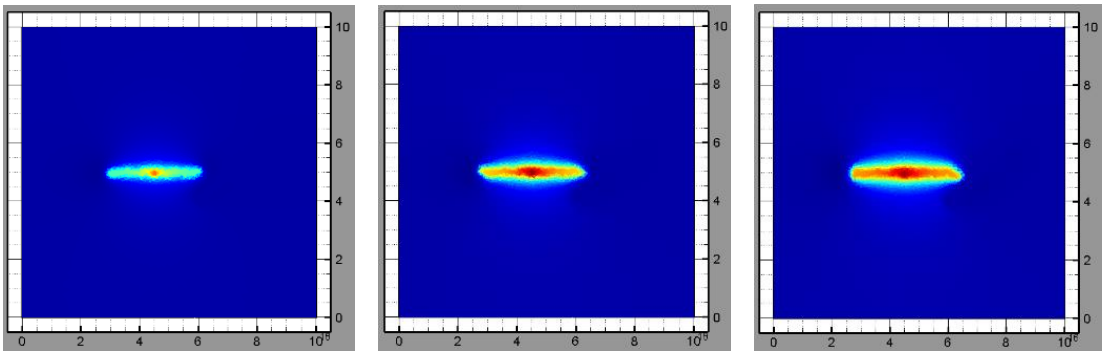

(a) (b) (c)

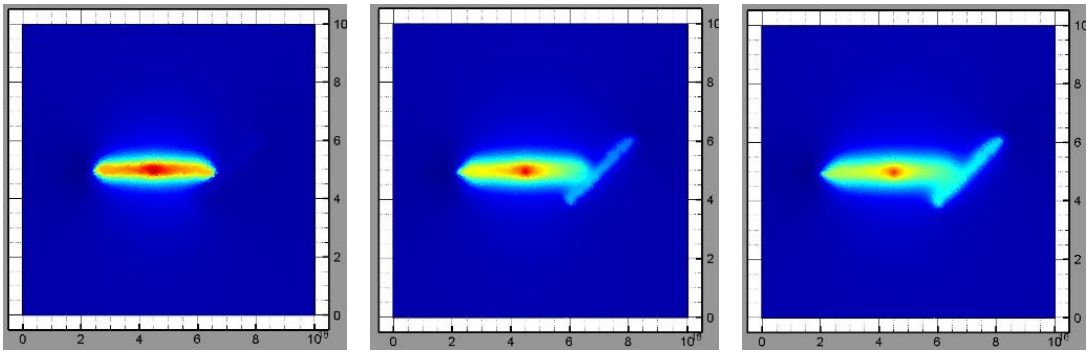

(d) (e) (f)

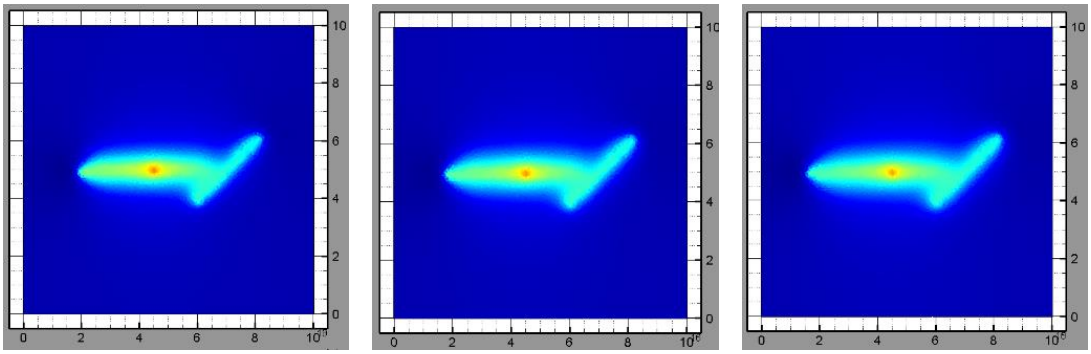

(g) (h) (i)

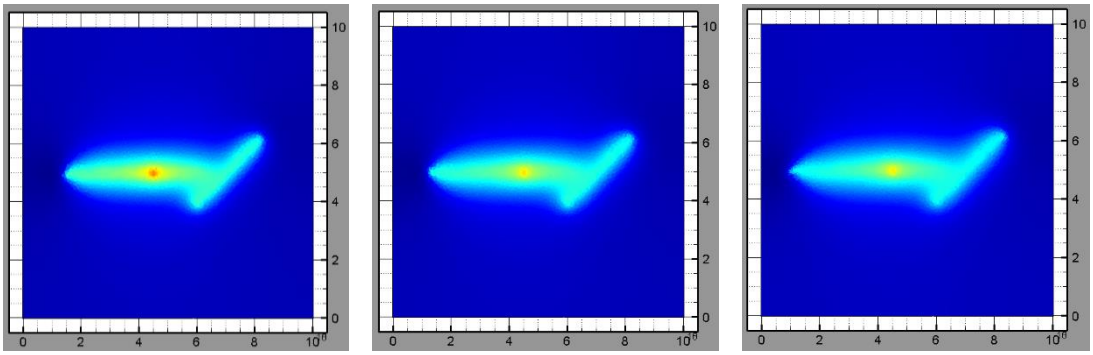

(j) (k) (l)

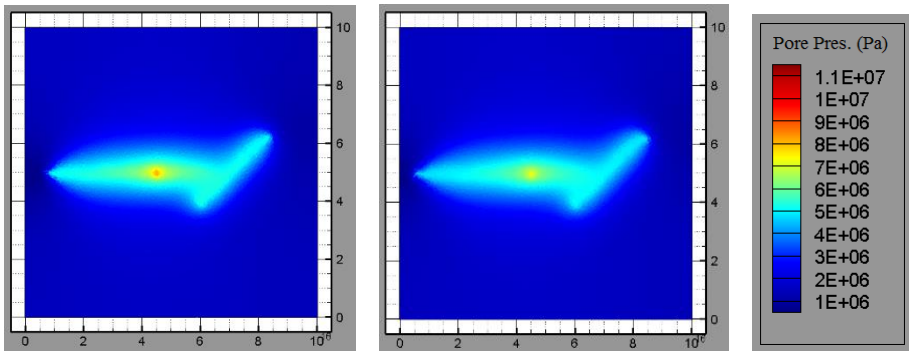

(m) (n)

Figure 7.15. Pore pressure contour slice in the middle of domain during the fracture propagation.

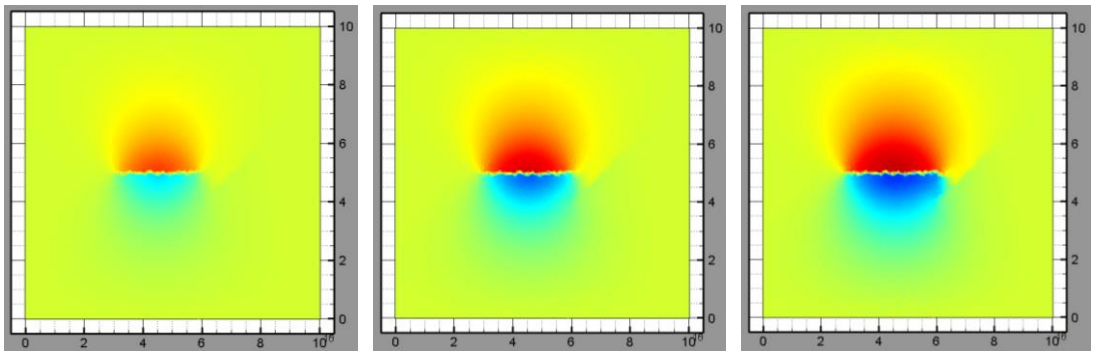

(a) (b) (c)

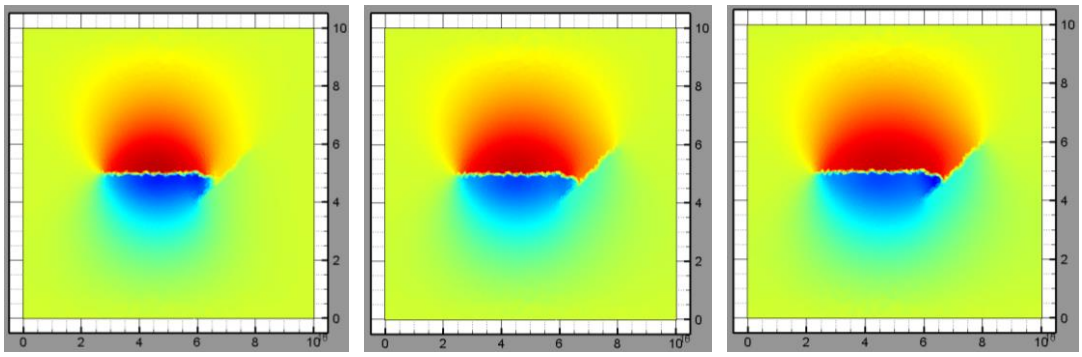

(d) (e) (f)

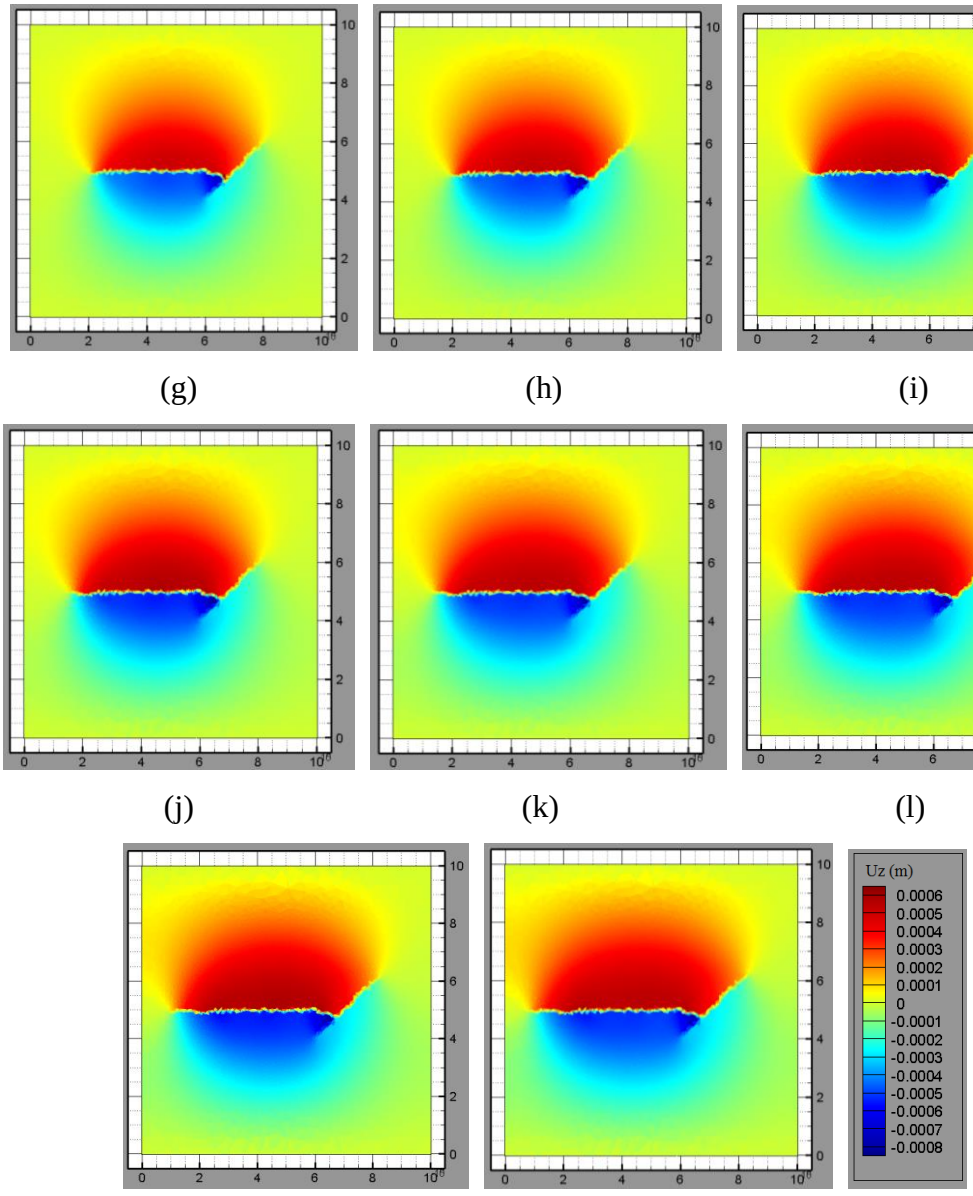

(g) (h) (i)

(j) (k) (l)

(m) (n)

Figure 7.16. The contour of displacement in z direction on the middle slice of domain during the fracture propagation.

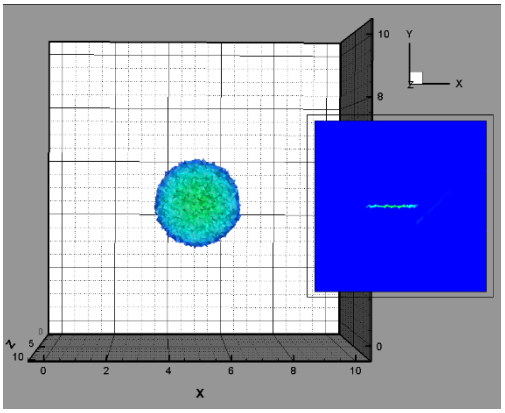
Y
X
Z
10
8
0
5
10
0
2
4
6
8
10
X

(a)

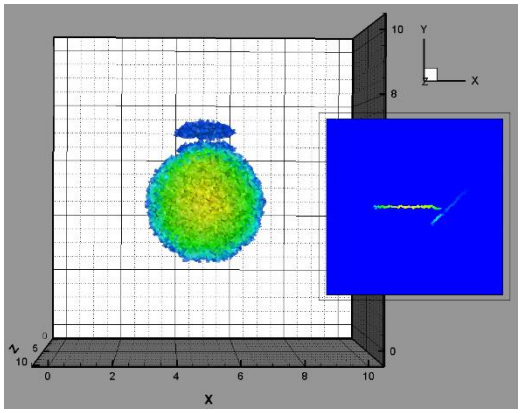
Y
X
Z
10
8
0
5
10
0
2
4
6
8
10
X

(b)

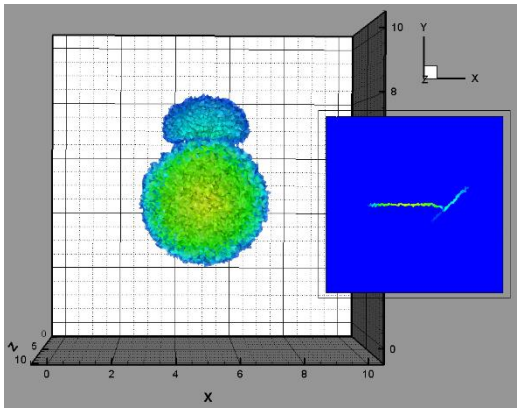
Y
X
Z
10
8
0
5
10
0
2
4
6
8
10
X

(c)

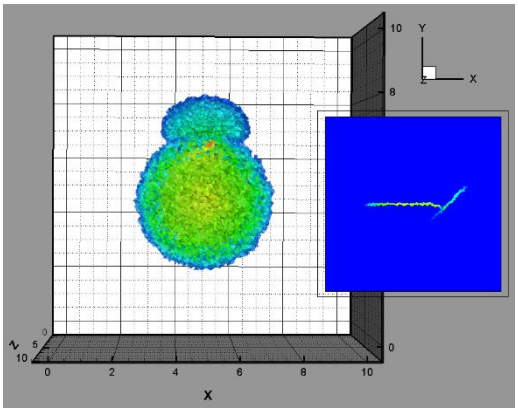
Y
X
Z
10
8
0
5
10
0
2
4
6
8
10
X

(d)

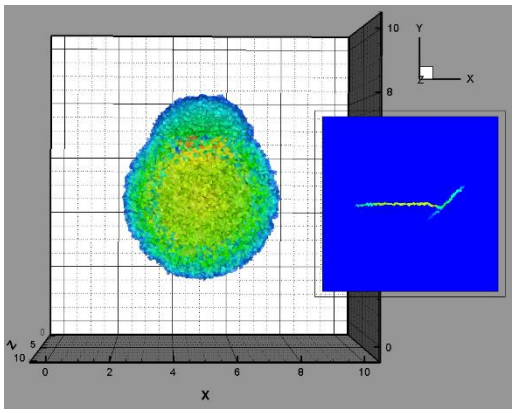
Y
X
Z
10
8
0
5
10
0
2
4
6
8
10
X

(e)

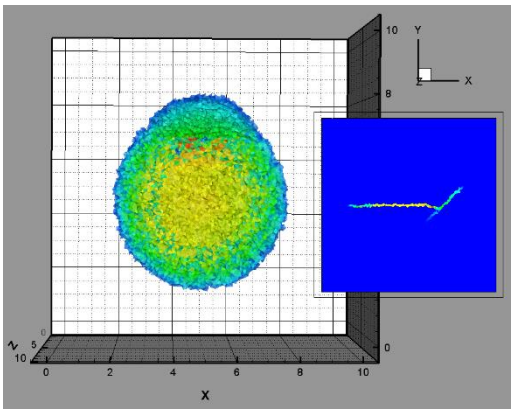
Y
X
Z
10
8
0
5
10
0
2
4
6
8
10
X

(f)

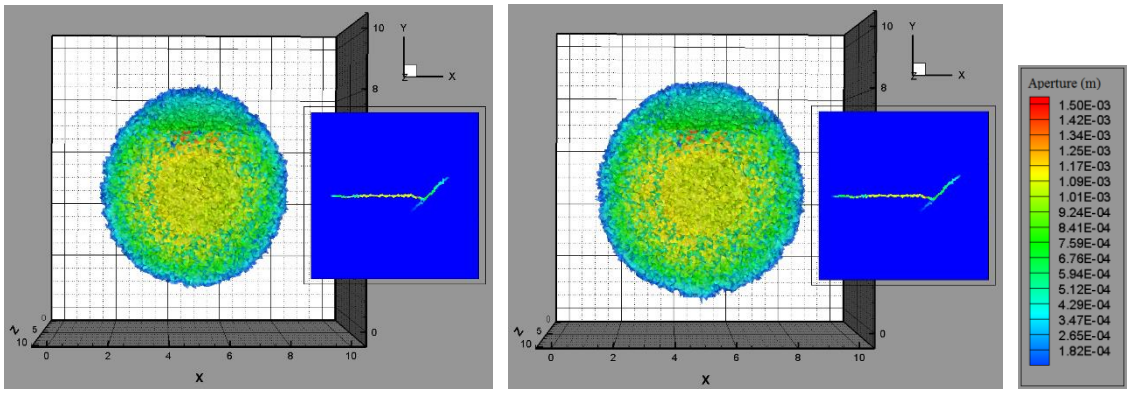

(g) (h)

Figure 7.17. Fracture aperture distribution from the top and lateral views.

7.3.3 Multiple Natural Fractures

Previous section presents the example of single natural and hydraulic fracture interaction. The results display the potential of the modified poroelastic model and 3D EPM on prediction of fracture propagation pattern with complex geometry. More complex realistic geological conditions in natural fractured unconventional reservoir make 3D numerical simulation extremely difficult due to existing of multiple natural fractures. Most results of hydraulic and natural fracture interaction are presented in 2D [Dahi-Taleghani, 2009; McClure, 2012; Verde and Ghassemi, 2013]. This example designs 10 natural fractures located near the initial hydraulic fracture in a $10m \times 10m \times 10m$ cubic domain. The problem geometry is shown in Figure 7.18. The red dot indicates the injection point and the circular plane with red outline is initial fracture. Ten natural fractures are located nearby initial hydraulic fracture shown by the circular plane with blue outline. The geometric details of these natural fractures are not given here. In Figure 7.19, the relative locations of the natural fractures are given by their intersecting lines with slice a and b indicated in Figure 7.18. The diameter for hydraulic and natural fractures range from 0.9 to 1.0 meter. The initial pore pressure of

whole domain is 1.0 MPa. All the flow and mechanical properties and mesh scheme are the same as the ones in section 7.3.1.

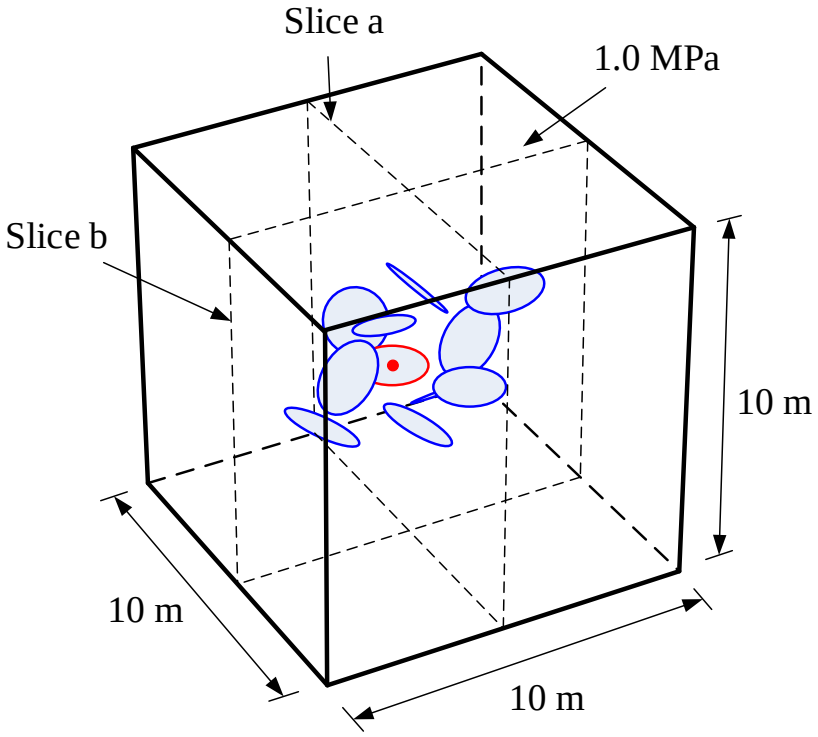

Figure 7.18. Problem geometry and initial fractures.

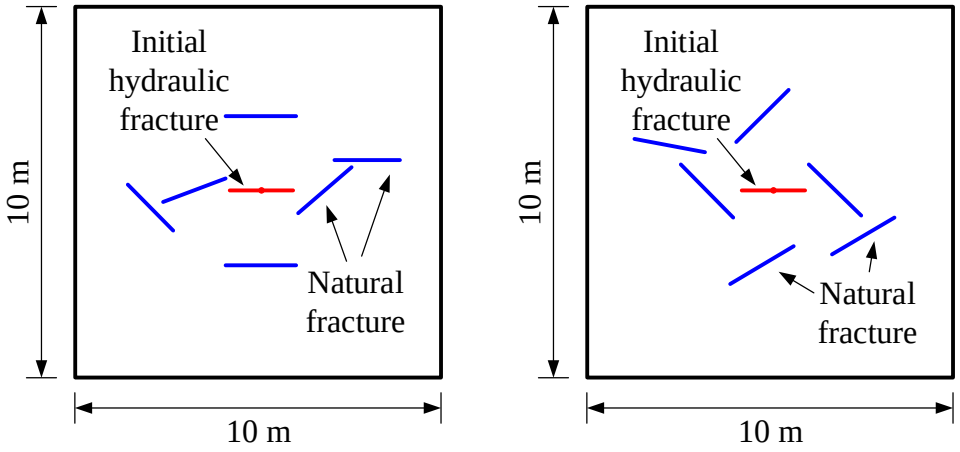

(a) (b)

Figure 7.19. Detailed spatial geometry of multiple fractures from (a) slice a and (b) slice b.

The numerical results are shown in Figure 7.20~Figure 7.22. In Figure 7.20, the pattern of fracture propagation is represented by the damaged element shown in blue color. The middle slices a and b are also displayed in the figure that help the understanding of and geometry of propagating fracture and their interactions. Red circles indicate the initial fractures. The specific spatial locations of 10 natural fractures are difficult to be described. Therefore, we gradually introduced the red circles into Figure 7.20 when the growing fracture is approaching and interconnecting with initial natural fractures. The middle slice of pore pressure contour during the propagation process is shown in Figure 7.21. The contours of displacement in z direction are shown in Figure 7.22. Total injection time is 26.51 seconds to create final fracture shown in Figure 7.14(j).

The fracture is propagating radially from the initial fracture with injection point (Figure 7.20(a)). The newly extended fracture is gradually approaching the neighbor natural fractures and finally connects with them (Figure 7.20(c)). The consequent propagation form natural fractures is not from the both end. The snap-back parts of natural fractures are forced to close by the compression from the major fracture and will not propagate anymore. After the major fracture connected 4 neighbor fractures and filled the space between them, it starts to grow from the further end of natural fractures until it hit the peripheral natural fractures (Figure 7.20(h)). In the previous section we found that the fracture tends to grow in circular shape. This phenomenon is also found in this example. Although the shape of major fracture becomes irregular and curved during the interconnection with natural fracture, the further end of connected natural fracture is not propagating until the major fracture forms an approximate circular shape.

In Figure 7.20(j) we found, there are two natural fractures remain inactivated during the stimulation since that the major propagation direction is along the horizontal direction, shown as circles with black outline. In the middle slices a and b shown in Figure 7.20, the fracture propagation results are similar to the ones presented by 2D simulations. Spatial fracture propagation is not always generate the fracture cut-through the formation that induces failure of plane strain assumption and error on the length of fracture growth, and more important, the energy needed to create the target length of hydraulic fracture. Therefore, true 3D simulation is urgently needed.

The pore pressure evolution is shown in Figure 7.21. The pressure located on the fracture surface can be considered as the hydraulic pressure induced by injection pressurizing the fracture surface. The pressure of the intact formation is the pore pressure increase due to the fracturing fluid diffusion and leak-off. Figure 7.21(a) and (b) show the pressure contour before major fracture connects with the neighbor natural fractures. Server pressure drops are found when the growing fracture contacts the natural fractures shown from Figure 7.21(c) to (i). The pressure at injection point finally drops to half of initial pressure when the injection and propagation just started. The pressure in two natural fractures located above and below respectively the major fracture remains initial pore pressure. The fluid is not flow in these fractures since that they are not activated and interconnected with the major fracture.

Due to the complex geometry of fracture shape, the aperture contour of propagating fracture may be confusing by its spatial location and is decided to be not shown in this work. Instead, the contours of displacement in z direction are shown in Figure 7.22, which also represent the approximate fracture opening. In the figure, the

displacement discontinuity is well represented in the model by 3D EPM not only for the opening major fracture, but also the isolated natural fractures. The different color on the both sides of fracture indicates the separation and slippage of fracture surface. In Figure 7.22, displacement jump is found on the both sides of isolated fracture above the major fracture because of that fracture surface represented by 3D EPM will be able to contact and slip under compressive and shear stress.

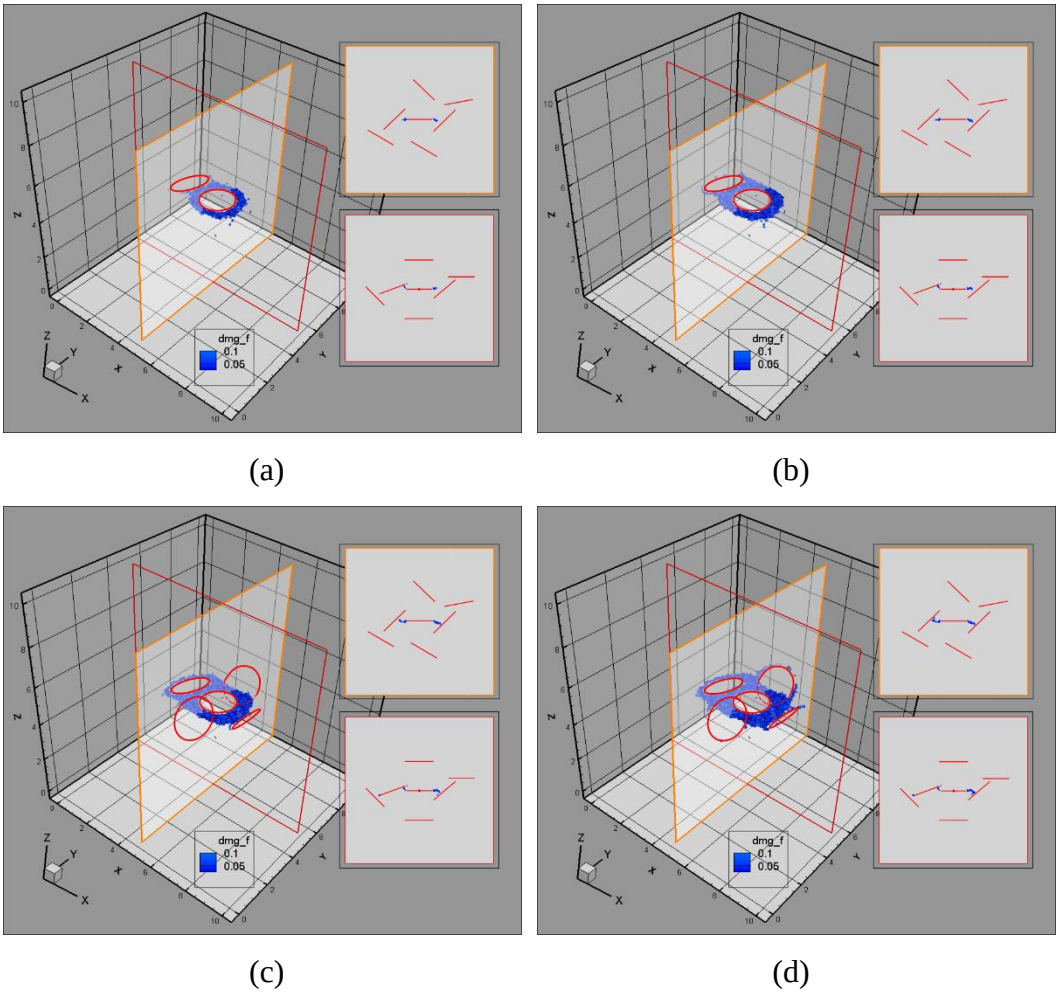

(a) (b)

(c) (d)

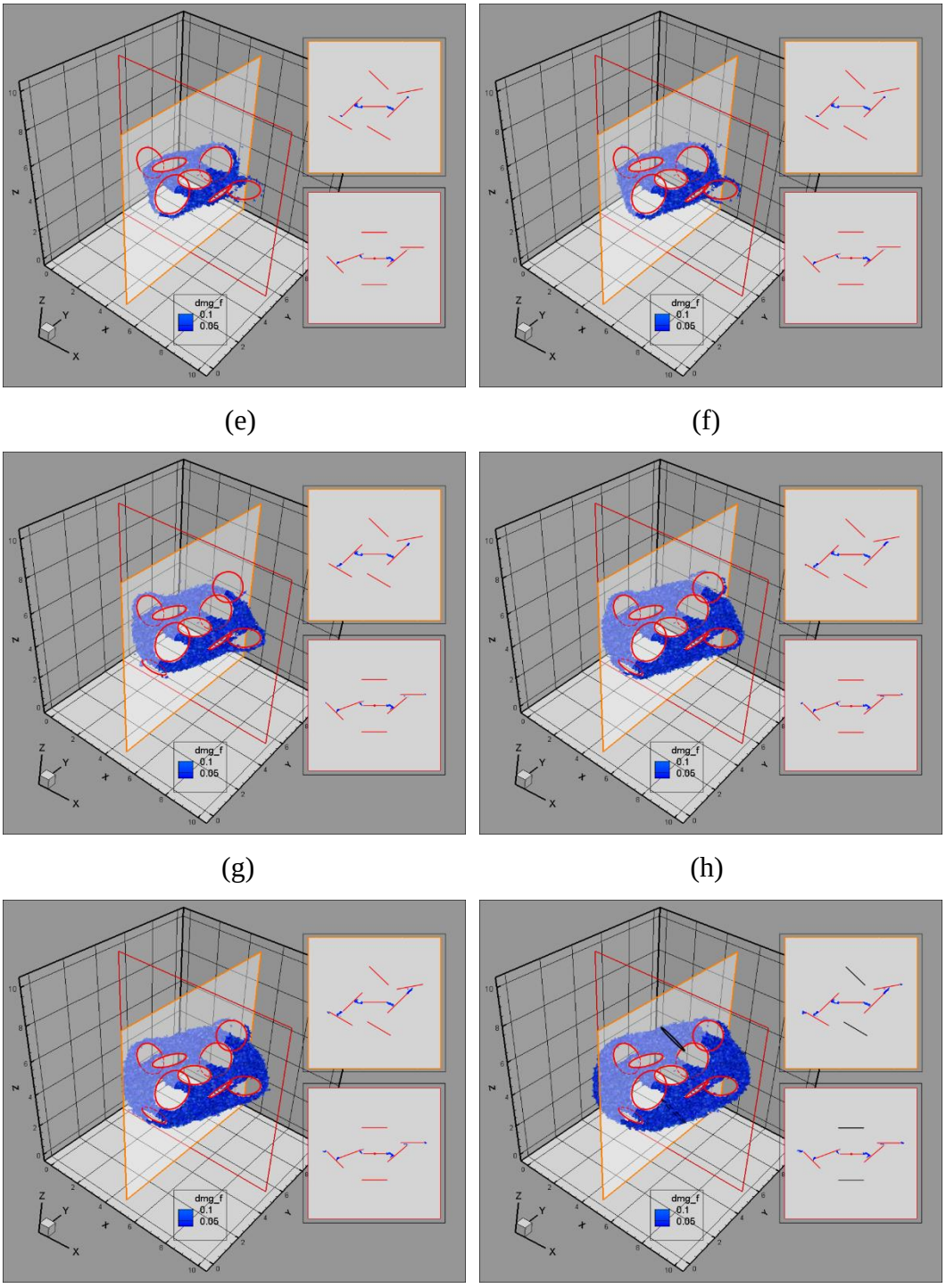

(e) (f)

(g) (h)

(i) (j)

Figure 7.20. The pattern of fracture propagation displayed by damaged element.

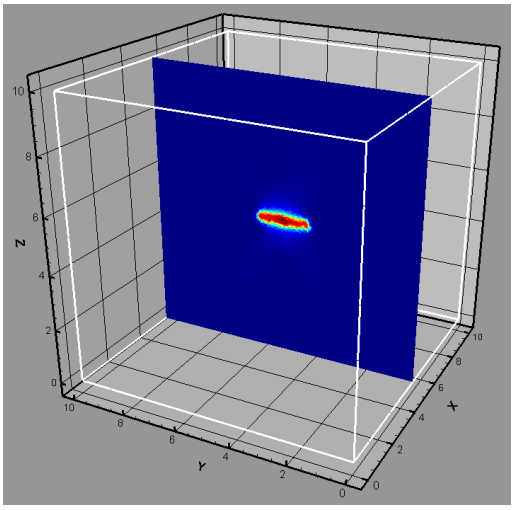

(a)

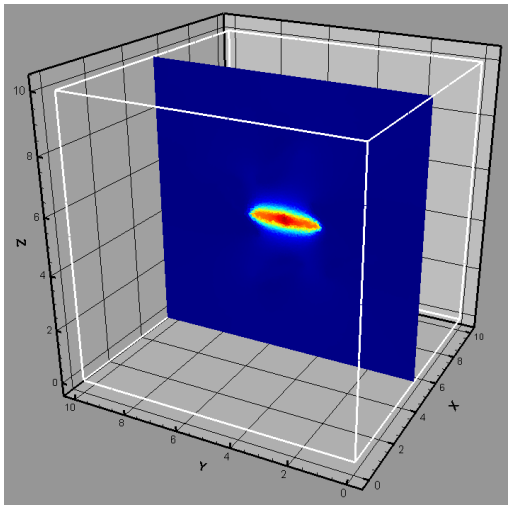

(b)

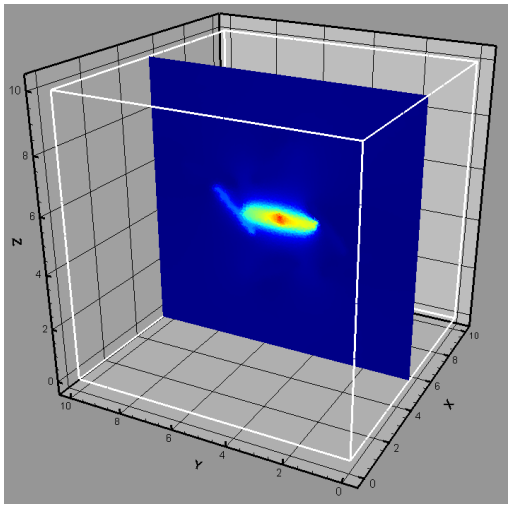

(c)

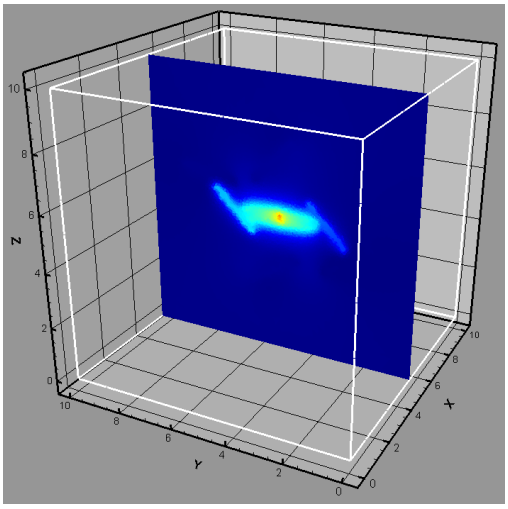

(d)

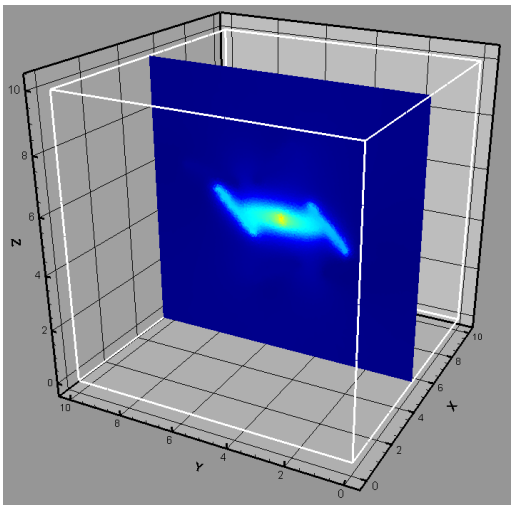

(e)

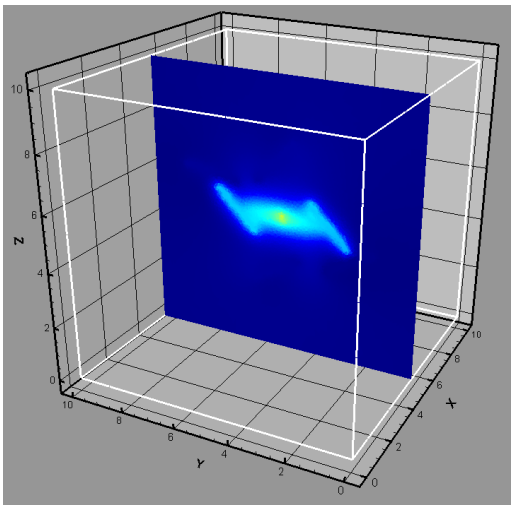

(f)

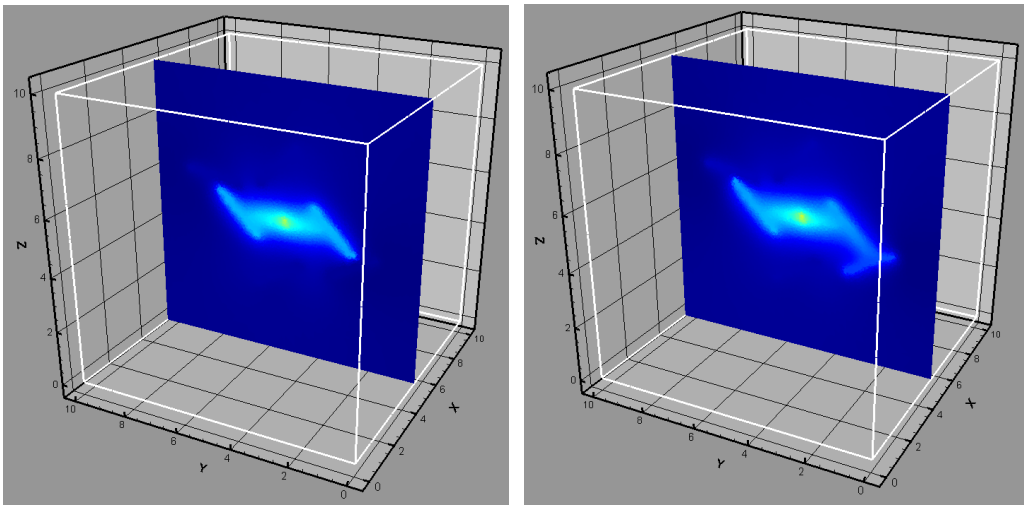

(g) (h)

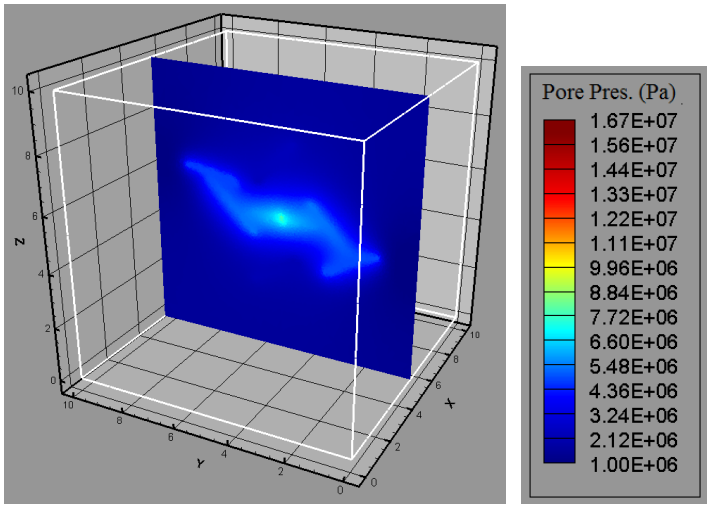

(i)

Figure 7.21. Pore pressure evolution on the middle slice of domain during the fracture propagation.

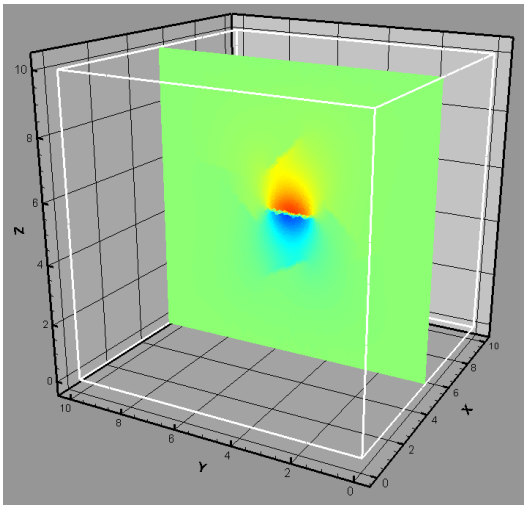

(a)

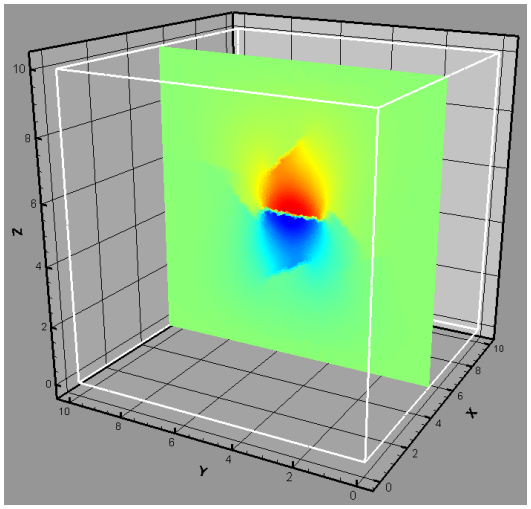

(b)

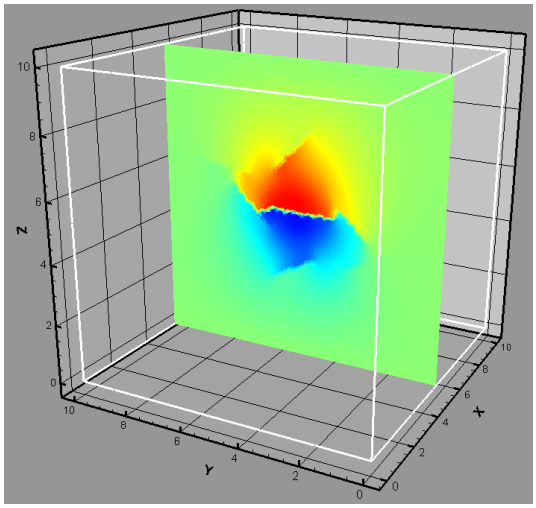

(c)

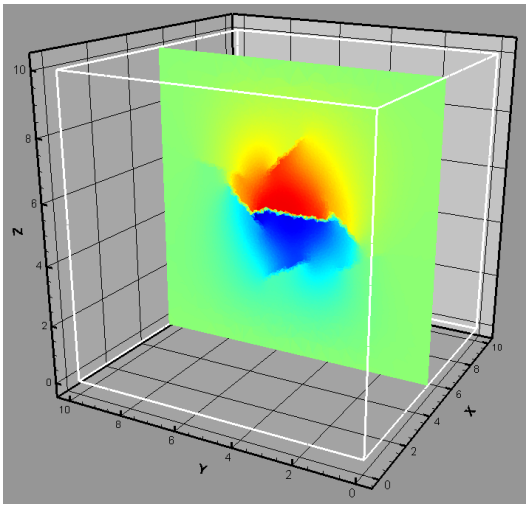

(d)

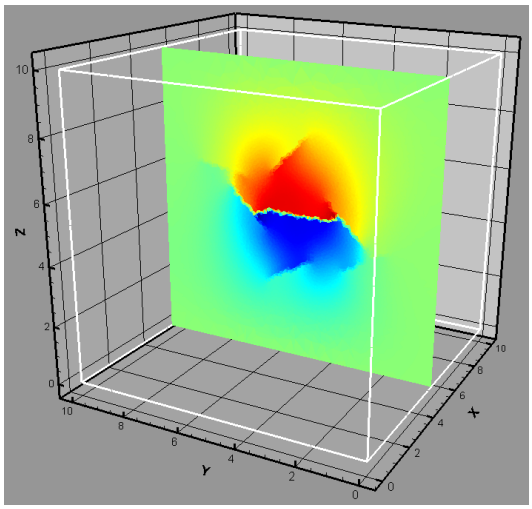

(e)

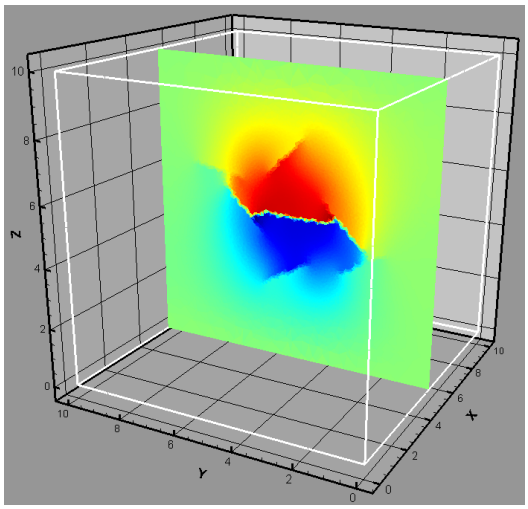

(f)

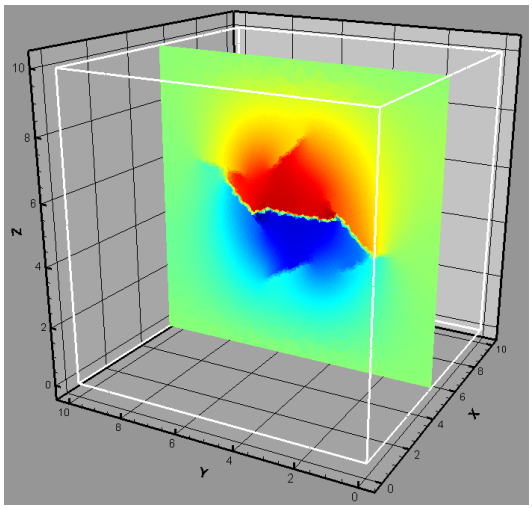

(g)

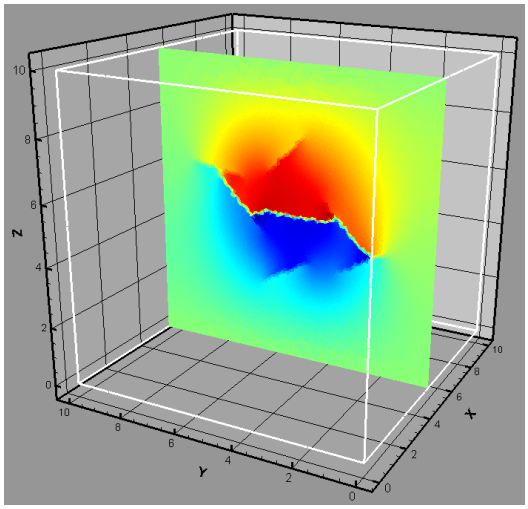

(h)

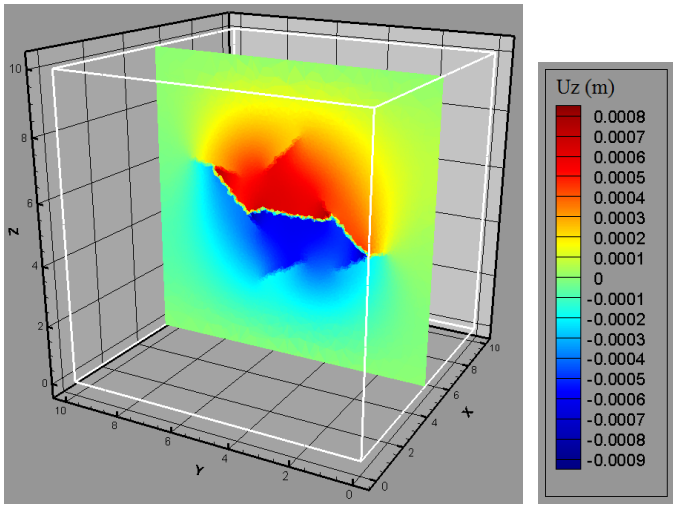

(i)

Figure 7.22. The contour of displacement in z direction on the middle slice of domain during the fracture propagation.

7.3.4 Hydraulic Fracturing under Anisotropic In-situ Stress

In-situ stress anisotropy is a key factor determining the propagation direction of hydraulic fracture. In this section, the influence of anisotropic in-situ stress and its induced tortuousness of newly extended fracture will be primary studied. The example designs two natural fractures located on the upper and lower side of initial hydraulic fracture in a $10m \times 10m \times 10m$ cubic domain. The problem geometry is shown in Figure

7.23. The maximum in-situ stress is the overburden stress with the magnitude of 6.0 MPa. The horizontal in-situ stresses in two directions are both 2.0 MPa. The red dot indicates the injection point and the circular plane with red outline is initial hydraulic fracture. Two natural fractures are shown by the circular plane with blue outline. In Figure 7.24, the relative locations of the natural fractures are given by their intersecting lines with slice indicated by dash outline in Figure 7.23. The diameters for hydraulic and natural fractures are 2.4 meters. The initial pore pressure of whole domain is 1.0 MPa. The injection rate is All the flow and mechanical properties and mesh scheme are the same as the ones used in the simulations of section 7.3.1.

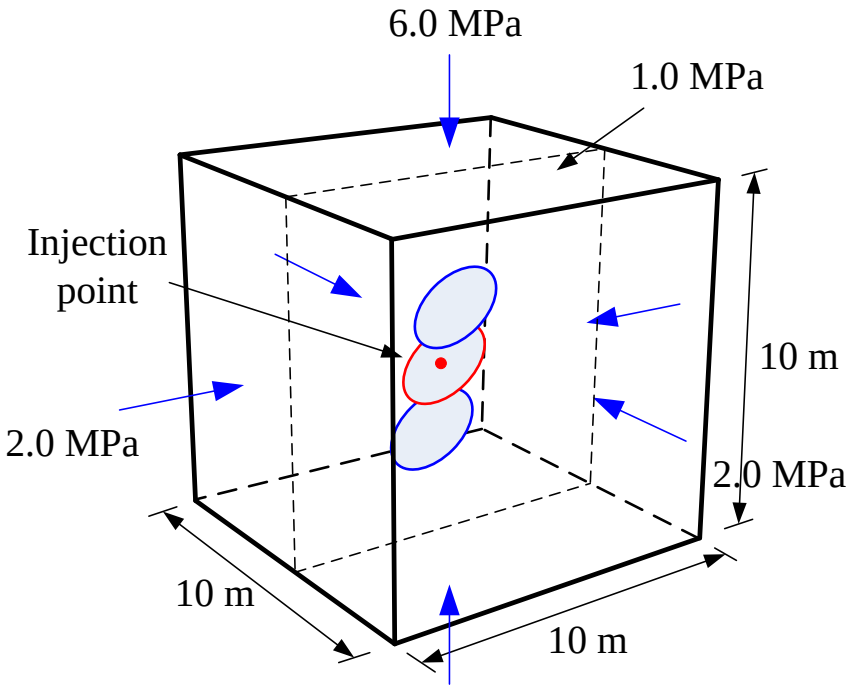

Figure 7.23. Problem geometry and initial fractures.

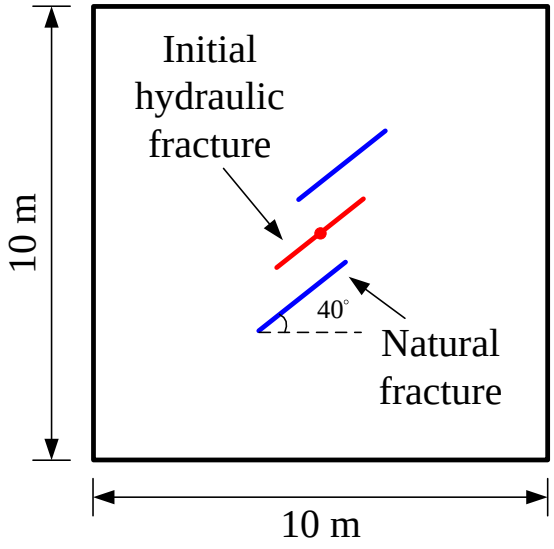

(a) (b)

Figure 7.24. Detailed spatial geometry of multiple fractures on the slice in the middle of object.

The numerical results are shown in Figure 7.25~Figure 7.29. In Figure 7.25, the pattern of fracture propagation is represented by the damaged elements shown in blue color. The red dash line indicates initial hydraulic fracture and the gray solid lines show the initial natural fractures. The detail spatial configuration of 3D fracture surface is difficult to be clearly illustrated. Figure 7.26 shows the final shape of hydraulic fracture that helps the understanding of and geometry of propagating fracture. The middle slices of pore pressure contour during the propagation process are shown in Figure 7.27. The contours of displacement in z direction are shown in Figure 7.28. Total injection time is 5.29 seconds to create final fracture shown in Figure 7.25 (f).

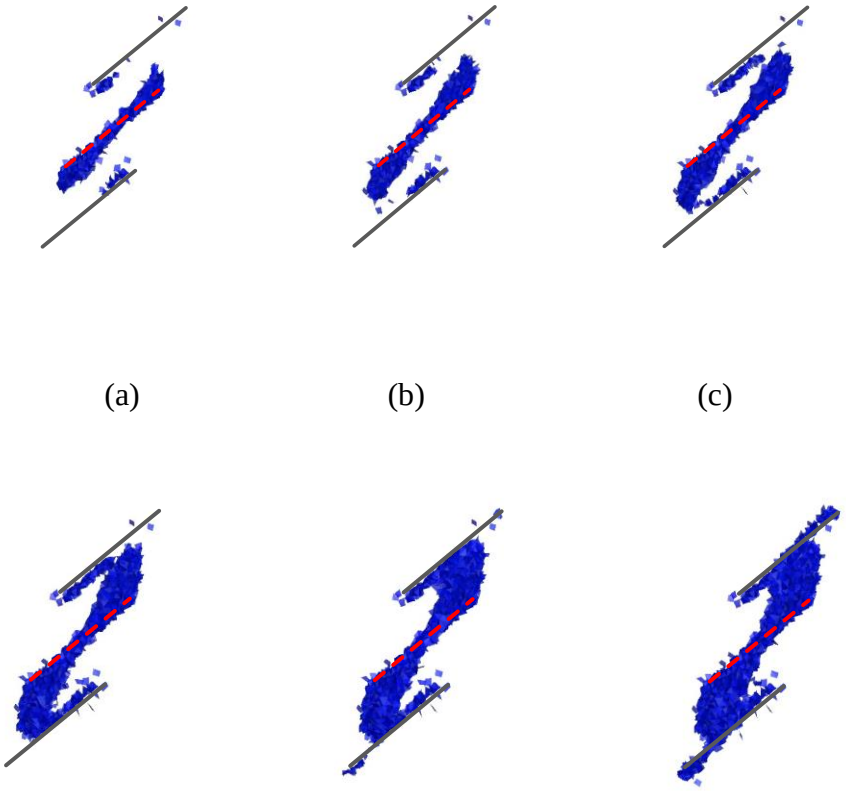

(a) (b) (c)

(d) (e) (f)

Figure 7.25. The pattern of fracture propagation displayed by damaged elements.

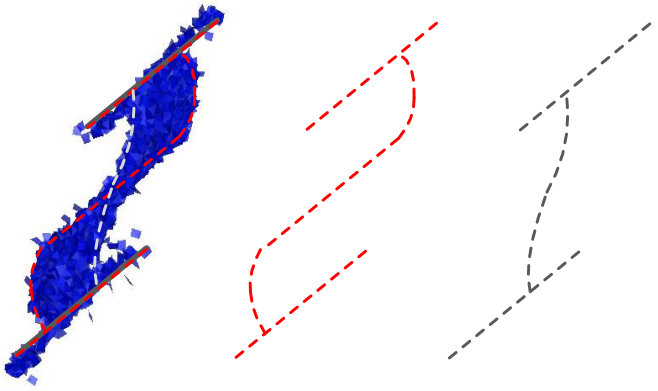

(a) (b) (c)

Figure 7.26. Detailed spatial geometry of final fracture: (a) lateral view of whole fracture; (b) intersecting line between fracture surface and middle slice shown as red dash line; (c) fracture lateral edge by gray dash line.

Subjected to isotropic in-situ stress, the fracture is propagating radially along the original direction of initial fracture before approaching neighbor fracture according to the results in previous sections. In that case, only cause of fracture tortuousness is the exciting of natural fractures. In Figure 7.25, under anisotropic in-situ stress, the newly extended fracture is propagating upwardly on the upper edge and downwardly on the lower edge. In other words, the fracture is growing and turning to the direction of maximum in-situ stress. The phenomenon has been observed and explained in section 7.2. The resistance for the fracture opening on the vertical plane is less since less in-situ stress on the horizontal direction compressing the fracture surface. Therefore, on any vertical plane, the fracture is easier to open and propagate. Consequent opened fracture is gradually approaching the neighbor natural fractures and finally connects with them. Comparing the fracture patterns in Figure 5.7 and Figure 7.25, the final shape of hydraulic fracture is similar to the simulation results in the pure mechanical loading test

of embedded fracture subjecting to compressive loading in section 5.1.3. Since the similar stress states, mode II and mode III fractures occur at similar places on the edge of fracture illustrated in Figure 5.13. Using the same conception of Figure 5.12, Figure 7.26 is plotted to describe the geometry of curved fracture surface. The red dash line is the intersecting line between fracture surface and middle slice. The grey dash line represents the lateral edge of fracture. These two lines indicate a gradual rotation of fracture surface.

It is difficult to plot a straightforward contour of pore pressure evolution in 3D space. We plot the pore pressure evolution contour on the middle slice of domain during the fracture propagation in Figure 7.27. The pressure result on the fracture surface is applied as the hydraulic pressure pressurizing the fracture surface. Beside the pressure change along the fracture surface, the pore pressure of the intact formation near the fracture is increased due to fracturing fluid diffusion. Figure 7.27(a)~(d) show the pressure contour prior to major fracture connected with the neighbor natural fractures. A curved propagating path with high fluid pressure indicates the location of fracture surface and permeability enhancement of the fractured elements. Server pressure drop is found when the growing fracture contacted the lower natural fracture shown in Figure 7.27(e). In Figure 7.27(f), the pressure drops again to lower level after the fracture contacted the upper natural fracture. After fully connected with natural fractures, the pore pressure along the fracture surface builds up again shown in Figure 7.27(g) and (h). The contours of displacement in z direction are shown in Figure 7.28, which represent the relative displacement around the fractures. The jump of contour color represents the discontinuity of fracture surface that provides another clue of the location

and relative displacement like opening and slippage of fracture surface. Figure 7.29 plots the contour on 9 planes from x=5.0 to x=6.6 that supports the information given in Figure 7.26 about the fracture surface rotation.

In Figure 7.25(f) we observe that the damage occurs on the further ends of both natural fractures indicating further propagation direction and pattern of hydraulic fracture. However, meantime, damage also happens in the rock formation between initial hydraulic and natural fractures that induces numerical instability of present model. Specifically, some of the elements in that region are subjected to the applied nodal force from the fracture pressure. If those elements are fully damaged, the numerical model will not converge and deliver unrealistic large displacements on the nodes since that the damaged elements are too weak to support the hydraulic loads. Therefore, the present model fails to simulate the consequent fracture propagation beyond the stage shown in Figure 7.25(f). Future work is emphasized on the stability of the model under similar conditions like highly anisotropic in-situ stress and complex fracture geometry.

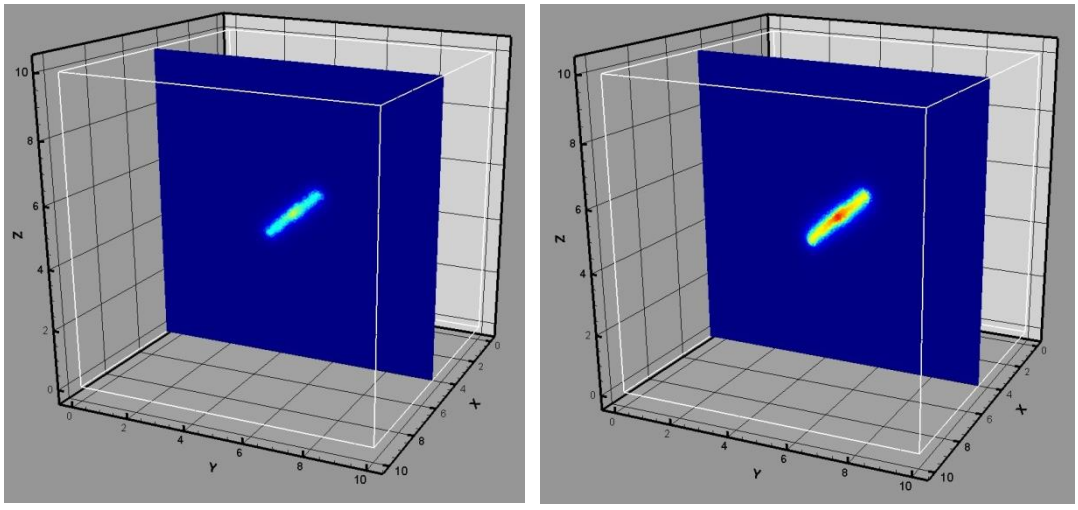

(a) (b)

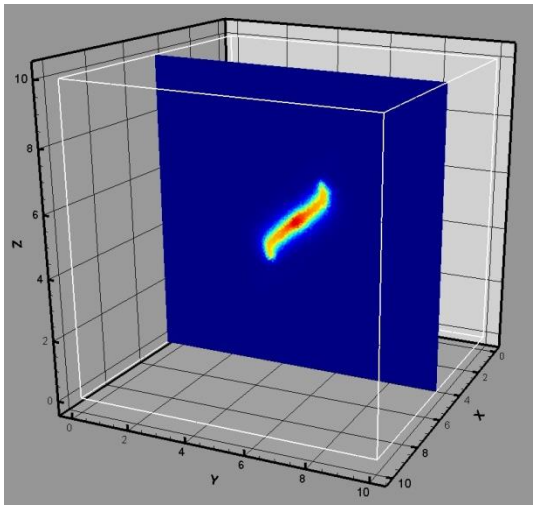

(c)

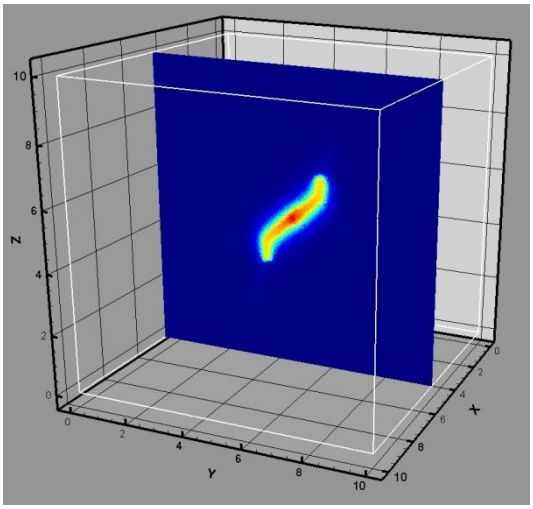

(d)

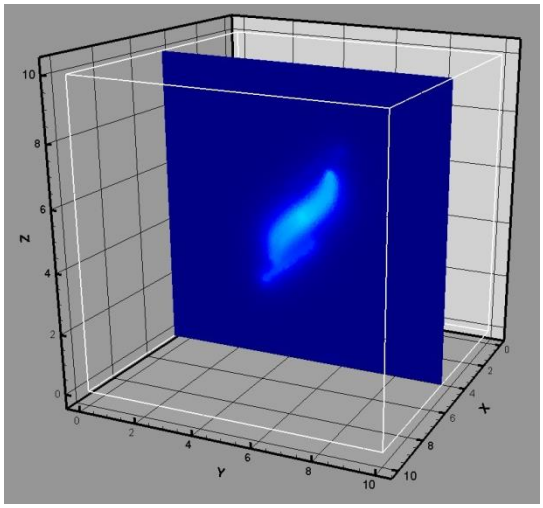

(e)

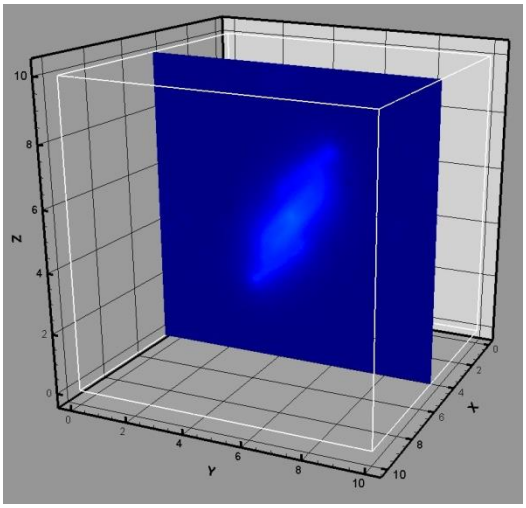

(f)

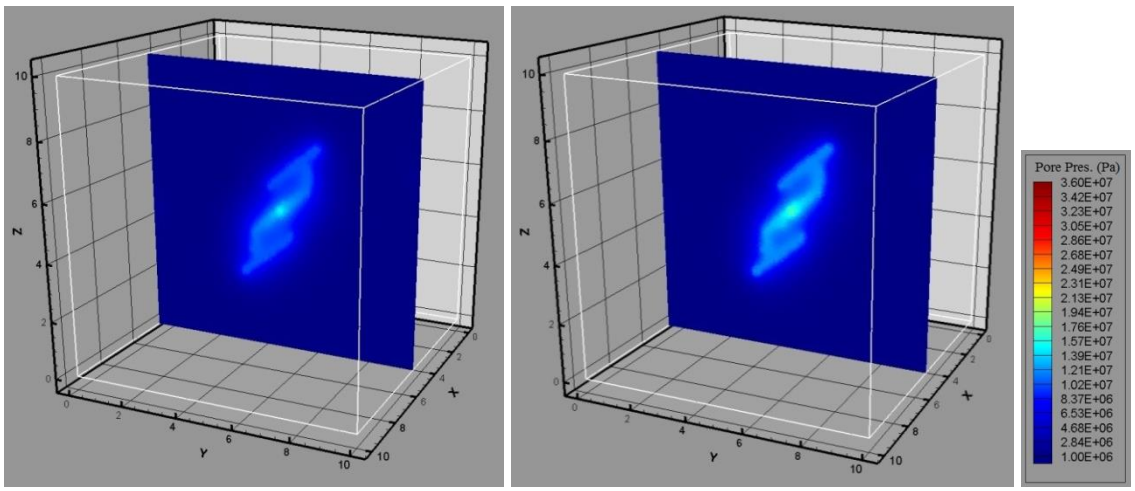

(g) (h)

Figure 7.27. Pore pressure evolution on the middle slice of domain during the fracture propagation.

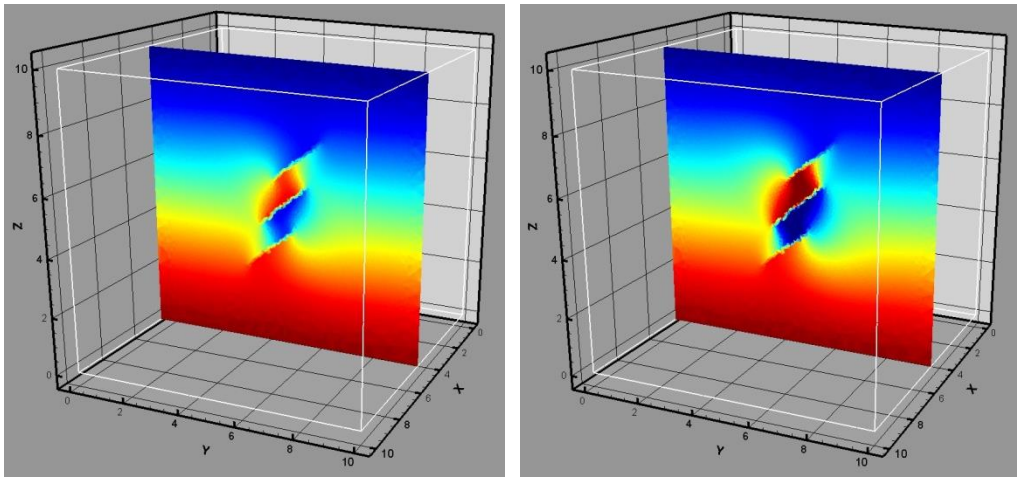

(a) (b)

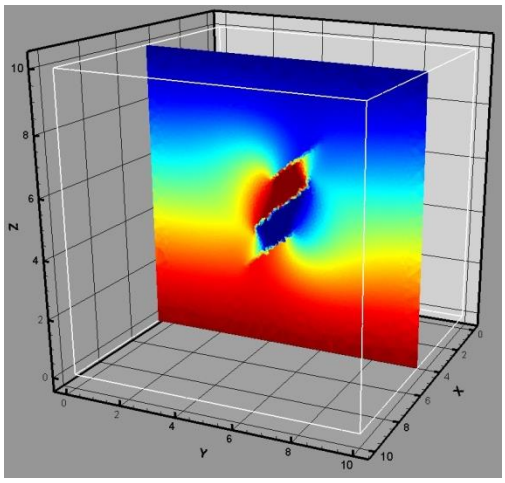
Z
Y
X

(c)

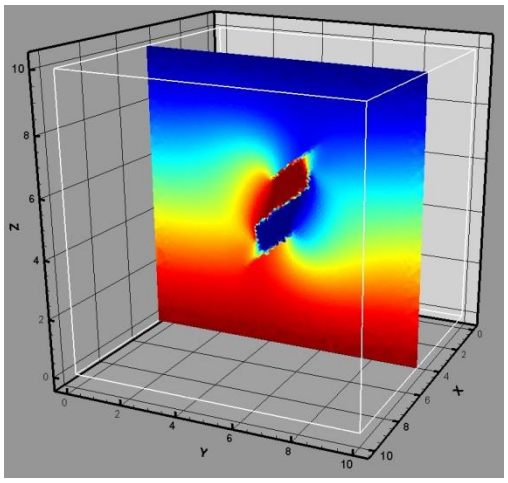
Z
Y
X

(d)

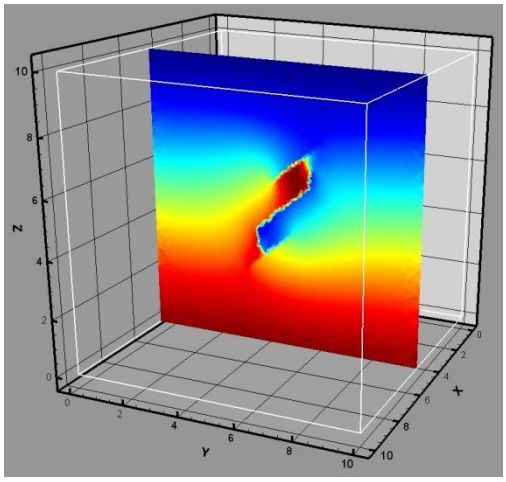
Z
Y
X

(e)

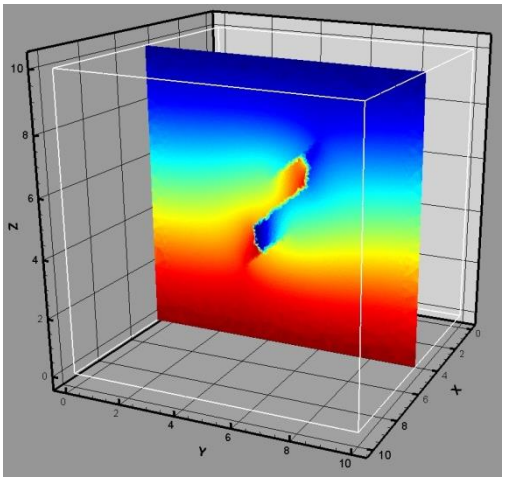
Z
Y
X

(f)

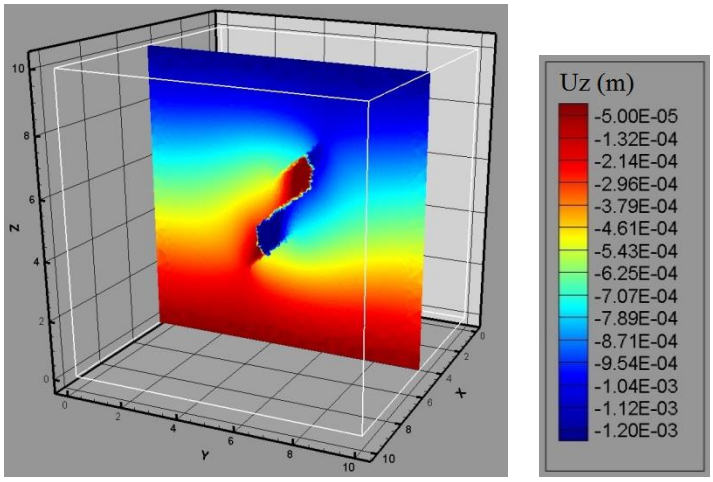
Z
Y
X
Uz (m)
-5.00E-05
-1.32E-04
-2.14E-04
-2.96E-04
-3.79E-04
-4.61E-04
-5.43E-04
-6.25E-04
-7.07E-04
-7.89E-04
-8.71E-04
-9.54E-04
-1.04E-03
-1.12E-03
-1.20E-03

(g)

Figure 7.28. The contour of displacement in z direction on the middle slice of domain during the fracture propagation.

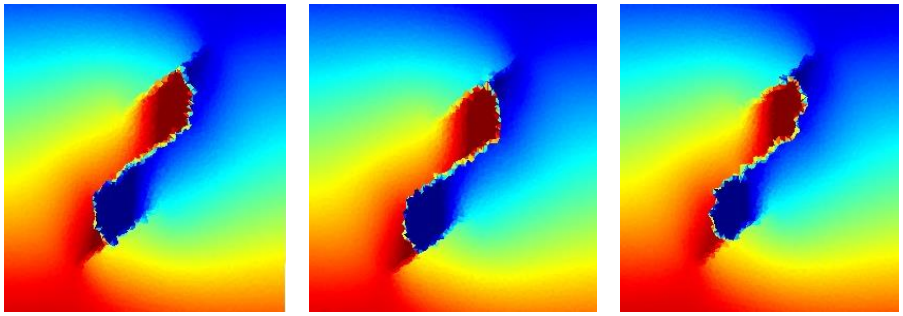

(a) (b) (c)

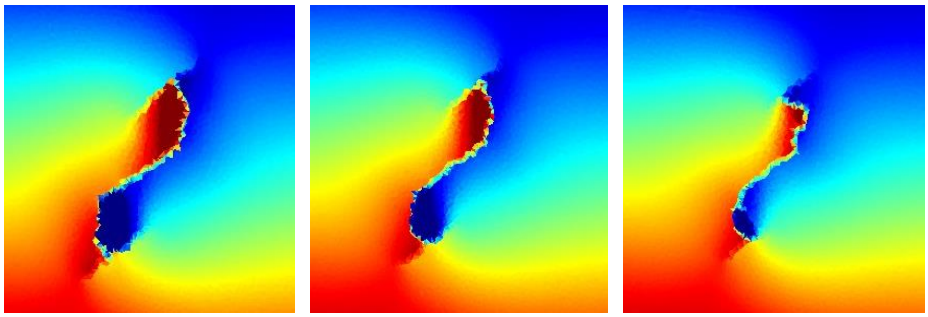

(d) (e) (f)

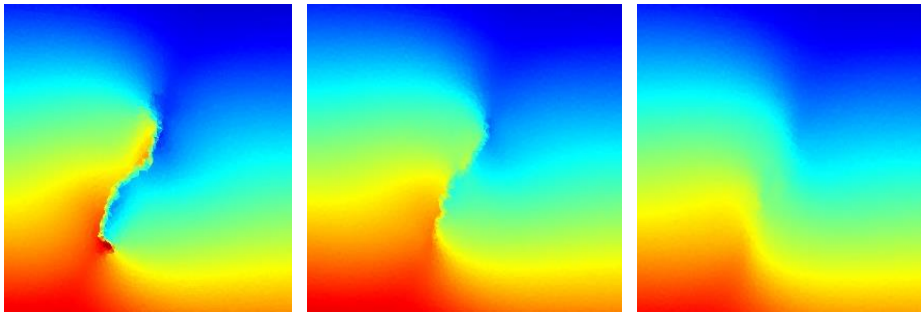

(g) (h) (i)

Figure 7.29. Final fracture shape represented by the displacement discontinuity on the plane of:.(a) x=5.0; (b) x=5.2; (c) x=5.4; (d) x=5.6; (e) x=5.8; (f) x=6.0; (g) x=6.2; (h) x=6.4; (i) x=6.6..

7.4 Conclusions

As the first stage of hydraulic fracturing simulation, the fluid pressure was assumed to be uniform and was increasing linearly each load step on the pre-existing and newly extended fracture surface. Plus, the simulation domain was one cubic meter that was not realistic to represent the real problem in hydraulic fracturing treatment. However, the examples provided suggestions on the fracture patterns and modes under various in-situ stresses. Under isotropic in-situ stress, mode I fracture was propagating along the direction of original fracture surface. As the vertical in-situ stress increased, mode II and mode III were gradually involved in growth of fracture. Took advantage of VMIB model on representing the mechanical nonlinearity, no extra fracture criteria were needed in the simulation especially when the mixed mode fracture propagation involved. Such simulations improved understanding of 3D fracture propagation mechanisms and provided a means of designing hydraulic fractures for reservoir stimulation. In addition, an interesting manner of hydraulic fracture propagation in Mode III was observed showing the formation of multiple fractures from the original crack. The fluid flow analysis was introduced into the model in the following sections to represent more rigorous multiple physics phenomena including the fracture flow and diffusion in the porous rock media.

However, the strain softening model like VMIB will subject to the spurious mesh size sensitivity. It is physically meaningless and unrealistic that strain energy dissipation converges to zero as the mesh size approaches infinity small using local model. The nonlocal damage model for softening materials minimized spurious mesh sensitivity and insured proper convergence validated by the simulation results in

Chapter 5. The results of section 7.2 showed the examples of applying nonlocal damage theory in hydraulic fracturing simulation for the first time. Associated with lubrication theory, the fluid flow was well captured.

The technique worked for 2D hydraulic fracturing and 3D one with cut-through fracture. However, true 3D fracture is propagating with complicate geometric shape due to complex geological conditions. Finding a fitted spatial curved surface in the damage band becomes very difficult and time consuming. The geometric problem becomes even tougher when the hydraulic fracture is interacting with nature fractures. Meantime, since that the element size is required to be smaller than characteristic length, the true 3D simulation using nonlocal damage theory requires large computational volume even for the problem in the domain with length of several meters. If one plans to use nonlocal damage theory in simulating hydraulic fracture, the special treatment of boundary condition on the hydraulic fracture surface is needed. Considering the computational volume, to simulate larger domain, adaptive mesh solution is suggested. A real three-dimensional model is still a challenging problem. Firstly, dramatic increment of finite element number is great obstacle for executing of the code on normal workstation, especially for nonlocal damage theory. Moreover, the fracture propagates in curved shape in 2D simulation that can be captured by curved line to calculate the fluid flow, while in 3D space the fracture subjected to anisotropic in-situ stress could develop in a complex spatial curved surface. This complex sharp of fracture brings difficulties to both mechanical and flow behavior representation.

Therefore, in section 7.3, the modified poroelastic model and damage model in local formulation were employed to reasonably avoid the mentioned difficulties.

Though the simulations were subjected to the mesh size dependency because of using local damage theory, the computational volume was reduced to be acceptable without the limitation of element size in nonlocal damage theory. According to the assumption in modified poroelastic model, the fracture fluid is flowing through the high permeability fractured element without specified flow meshing. Also, the real-time hydraulic pressure is applied on the fracture surface using the matrix implanted in the global matrix. The simulation examples presented the results of hydraulic fracture interacting with single and multiple natural fractures in true 3D domain. The existing natural fractures were the primary influential factors in the propagation processes under isotropic in-situ stress. The results of interaction between hydraulic and 11 natural fracture showed the potential and stability of the present model dealing with complicated geological conditions. Although this model cannot provide precise fluid pressure along the fracture surface, the overall tendency of fracture and pore pressure distribution and fracture propagation can still be modeled considering the computational feasibility and efficiency. Last example studied hydraulic fracturing in rock domain subjected to anisotropic in-situ stress using modified poroelastic model and damage theory. Though fracture is eventually propagating primarily in mode I pattern after turned to the direction of maximum in-situ stress, mixed mode fracture still plays a key role in the region near the wellbore and when the propagating fracture is approaching the natural fractures. Due to the convergence issue of present model, further propagation after the mix mode hydraulic fracture connected with the natural fractures was not presented. Future work focuses on the stability of the model under highly anisotropic in-situ stress with complex fracture geometry. Nevertheless, the new model

is a promising tool for predicting and understanding the complex processes of hydraulic fracturing and its interaction with natural fractures in the stimulated unconventional reservoir.

Chapter 8. Conclusions and Recommendations

8.1 Conclusions

In this work, the hydraulic and thermal fracture mechanisms associated with fluid flow and thermal diffusion were studied. This work motivated by the limitations of the existing fracture simulators and urgent needs for true 3D hydraulic fracturing model from petroleum and geothermal industry. Multiple physical processes are involved in hydraulic fracturing propagation and are active in determination of the growth of a propagating hydraulic fracture. The whole process was modeled using solid, thermal and fluid flow interaction analysis that includes fluid flow, thermal response and mechanical behavior of rock and fracture.

The real underground rocks are difficult to be characterized due to the complex geological conditions of formation such as nonlinearity, anisotropy, heterogeneity and existing of large discontinuity. Though the behavior of real rock in the reservoir is extremely difficult to be characterized and modeled, multi-scale VMIB model and continuum damage model presented in this work provided solutions from different aspects on solving the nonlinear responses of rock. The VMIB stems from the discrete microstructure, however, eventually turns out the continuum constitutive relationship since that the mechanical properties of the material particles are assembly obtained through statistical averaging. The performance of VMIB on simulating the mix mode fracture propagation under pure mechanical loading was tested. Using VMIB model, a three dimensional thermal fracturing model was developed and a series of hydraulic fracturing examples were simulated under different in-situ stress conditions.

However, using strain softening model like VMIB, the simulation was subjected to the spurious mesh size sensitivity. In other words, finite element analysis became highly affected by the mesh size and alignment causing non-physical predictions of softening area. Through the theoretical details and simulation validation, the nonlocal formulation of damage model for softening materials effectively eliminated spurious mesh size sensitivity and ensured proper convergence. Essentially, the so-called nonlocal formulation uses an averaged value of damage driving force over the representative volume of the material during damage process. The characteristic length is an intrinsic material property that governs size of representative volume, which must be determined and corroborated by results of experiments. Consequently, the dissipated energy due to strain-softening damage converges to a stable value. The nonlocal damage theory was used for the first time in the hydraulic fracturing simulation.

Three dimensional element partition method (3D EPM) was adopted to represent the mechanical behaviors of fracture surface. The 3D EPM successfully represented the mechanical behaviors such as contact and friction of closed fracture surfaces. Plus, no additional degrees of freedom were introduced. The partitioned element shares the same nodes with the intact tetrahedron element so that no remeshing is needed. Therefore, the dimension and structure of the elemental stiffness matrix after partition remains the same that needs no extra sorting during the simulation. Taking advantage of efficiency and simplicity of 3D EPM, especially for its feasibility and applicability on the true 3D hydraulic fracturing simulation, the technique was developed with the features of transferring the quasi-static hydraulic loading to the equivalent nodal forces and

calculating the fracture aperture by knowing the geometric information of fracture during the fracture propagation.

Numerical simulation of 3D thermal fracture propagation due to transient cooling in quasi-brittle rock was studied using VMIB model combined with 3D EPM method. By introducing nonlinear VMIB model into thermo-mechanical coupled governing equations, the nonlinearities of mechanical behaviors and thermal parameters of the solid material were captured. The 3D EPM associated with thermal parameters modification for fractured elements provides a simple way to represent the pre-existing and newly extended fracture in structured mesh. The examples for functional test provide evidences for the validation of presented method. The examples of multiple thermal fractures emanate from wellbore were simulated that were aimed on the impact on the propagation patterns from the in-situ stress. The present model provides a way to predict 3D thermal fracturing.

On the aspects of fluid flow, the present work introduced two models for fluid analysis using poroelastic model and lubrication theory. For both theories, analysis coupled the fluid flow and rock mass deformation based on different mechanisms.

The lubrication theory integrally considered the physical behaviors of the aperture change, fracture fluid pressure and new boundary created by fracture extension. The governing equations represented the mechanical equilibrium state of rock mass, continuity equation of fluid following cubic law and global mass conservation respectively that need to be solved by trial and iterations. The iteration strategy for coupling processes was also illustrated. The technique was introduced to identify the flow path in the damage band using polynomial fitting is presented. The pressure

boundary condition was equivalent to nodal forces that was successfully applied on propagating fracture surfaces under 3D EPM framework.

The poroelastic model is an ideal tool to analyze the coupled behaviors of porous flow and rock deformation in intact rock, but not for the fracture flow. This work presented the modified poroelastic model to simulate the hydraulic fracturing especially for the hydraulic fracture problem with complex geometry and boundary conditions such as hydraulic fracture and natural fractures interaction. Taking advantage of modified poroelastic model, the fracture fluid is flowing through the high permeability fractured element without specified flow meshing. The real-time hydraulic pressure is applied on the fracture surface using the matrix implanted in the global matrix. Though this model is not rigorous enough to provide precise fluid pressure along the fracture surface, the overall tendency of fracture and pore pressure distribution and fracture propagation can still be captured considering the computational feasibility and efficiency. The new numerical model is a promising tool for predicting and understanding the complex processes of hydraulic fracturing and its interaction with natural fractures in the stimulated unconventional reservoir under FEM framework.

8.2 Future Recommendations

Due to the complexities and difficulties involved in the hydraulic fracturing simulation, the simplifications and assumptions were made based on the feasibility and efficiency of the aspects of theories, programming and computational volume in this work. The future work will emphasize on improvement of the basic assumption and cracking the limitation of present model. In the followings are the main topics that are recommended for the future work.

1. The formation is not homogenous because of the components of rock such as grains, mineral crystals, voids and natural crack. The failure mechanism and constitutive model are recommended to include the reservoir heterogeneity of mechanical and fluid flow properties. Especially, in shale reservoirs, the rock typically exhibits strong anisotropic mechanical behaviors since their thin parallel layered structure. Therefore, the anisotropy is another crucial aspect of capturing shale deformation and failure, as well as their fluid flow mechanism.

2. The fracture process is a fully coupled nonlinear problem. The present work studied the hydraulic and thermal effects separately. A fully coupled hydro-thermo-mechanical model is desired.

3. The error of 3D element partition method arises with the increment of element size since that elastic deformation of partitioned element is not considered. Since the whole fracture surface consists of the fracture segments in each partitioned elements, the newly extended curved fracture presentation by 3D EPM is unsmooth and composed by discontinued surfaces, which brings difficulty in applying moving boundary condition such as fluid pressure. [Zhang et al. 2013; Zhang et al. 2013] presented the novel partition element methods considered the elastic deformation of partitioned element and fracture tip in 2D that provided the guideline of future work to solve the mentioned problem.

4. In this work, the single phase Newtonian fluid was assumed in the fluid flow analysis, which is not realistic in the deep, high temperature and high pressure reservoir. Multi-Phase flow occurs with the change of temperature and pressure. Plus, the fracturing fluid usually mixes with proppants providing fracture wall support and

remaining the fracture conductivity. Therefore, multiphase flow behaviors should be considered in the simulations.

5. Though the mesh dependency can be eliminated by using nonlocal damage theory, the element size is limited to be several times smaller than the characteristic length that is usually in the scale of several millimeters for most rocks. The element size is too small compared with the hydraulic stimulation domain that is normally several hundred cubic meters. Considering the computational volume, to simulate larger domain, adaptive mesh solution is urgently recommended.

6. The present work didn't integrate the fluid flow mechanisms of fracture and porous flow into one simulation model. The simulation examples using lubrication theory neglected the leak-off effect and pore pressure change in the formation near the hydraulic fracture. The modified poroelastic model considered the fracture conductivity enhancement by increasing the permeability of fracture element to a constant value independent with the fracture aperture that is reasonable but is only an approximation. An integrated fluid flow model is needed to provide the precise solution for pressure boundary condition on the fracture surface that is crucial for fracture propagation simulation.

References

Abu Al-Rub, R. K., Voyiadjis, G. Z., 2003. On the coupling of anisotropic damage and plasticity models for ductile materials. *International Journal of Solids and Structures*. 40(11), 2611-2643.

Adachi, J. I., Detournay, E., 2008. Plane strain propagation of a hydraulic fracture in a permeable rock. *Engineering Fracture Mechanics*. 75(16), 4666-4694.

Adachi, J., Siebrits, E., Peirce, A., and Desroches, J., 2007. Computer simulation of hydraulic fractures. *International Journal of Rock Mechanics and Mining Sciences*, 44(5), 739-757.

Adams, M., Sines, G., 1978. Crack extension from flaws in a brittle material subjected to compression. *Tectonophysics*. 49(1), 97-118.

Anderson, T. L., 1994. *Fracture Mechanics: Fundamentals and applications, 2nd edition*, CRC.

Bahr, H. A., Weiss, H. J., Maschke, H.G., and Meissner, F., 1988. Multiple crack propagation in a strip caused by thermal shock. *Theoretical and Applied Fracture Mechanics*. 10:219–226.

Batchelor, G. K., 1967. *An introduction to fluid mechanics*, 515 pp., Cambridge University Press, New York.

Bazant, Z. P., and Cedolin L., 1979. Blunt crack band propagation in finite element analysis. *Journal of the Engineering Mechanics Division*. 105.2: 297-315.

Bazant, Z. P., and Jirásek, M., 2002. Nonlocal integral formulations of plasticity and damage: survey of progress. *Journal of Engineering Mechanics*. 128(11), 1119-1149.

Bažant, Z. P., and Oh, B. H., 1983. Crack band theory for fracture of concrete. *Matériaux et construction*, 16(3), 155-177.

Bazant, Z. P., and Planas, J., 1998. *Fracture and size effect in concrete and other quasibrittle materials*, CRC, Boca Raton.

Bazant, Z. P., 1984. Size effect in blunt fracture: concrete, rock, metal. *Journal of Engineering Mechanics*. 110(4), 518-535.

Bažant, Z. P., 1986. Mechanics of distributed cracking. *Applied Mechanics Reviews*. 39(5), 675-705.

Bažant, Zdeněk P., Hideomi Ohtsubo, and Kazuo Aoh., 1979. Stability and post-critical growth of a system of cooling or shrinkage cracks. *International Journal of Fracture*. 15.5: 443-456.

Belytschko T, Black T., 1999. Elastic crack growth in finite elements with minimal remeshing. *International Journal for Numerical Methods in Engineering*. 45(5): 601-620.

Berumen, S., Tiab, D., and Rodriguez, F., 2000. Constant rate solutions for a fractured well with an asymmetric fracture. *Journal of Petroleum Science and Engineering*. 25(1), 49-58.

Bilby, B. A., Cottrell, A. H., and Swinden, K. H., 1963. The spread of plastic yield from a notch. Proceedings of the Royal Society of London. *Series A. Mathematical and Physical Sciences*. 272(1350), 304-314.

Biot, M. A., 1935. Effect of certain discontinuities on the pressure distribution in a loaded soil. *Journal of Applied Physics.* 6(12), 367-375.

Biot, M. A., 1941. General theory of three dimensional consolidation. *Journal of applied physics*. 12(2), 155-164.

Bjerrum, L., Nash, J. K. T. L., Kennard, R. M., and Gibson, R. E., 1972. Hydraulic fracturing in field permeability testing. *Geotechnique*. 22(2), 319-332.

Bobet, A., and Einstein, H. H., 1998. Fracture coalescence in rock-type materials under uniaxial and biaxial compression. *International Journal of Rock Mechanics and Mining Sciences*. 35(7), 863-888.

Borst, R. D., Remmers, J. J., Needleman, A., and Abellan, M. A., 2004. Discrete vs smeared crack models for concrete fracture: bridging the gap. *International Journal for Numerical and Analytical Methods in Geomechanics*. 28(7-8), 583-607.

Bredehoeft, J. D., Wolff, R. G., Keys, W. S., and Shuter, E., 1976. Hydraulic fracturing to determine the regional in situ stress field, Piceance Basin, Colorado. *Geological Society of America Bulletin*. 87(2), 250-258.

Carter, B. J., Desroches, J., Ingraffea, A. R., and Wawrzynek, P. A., 2000. Simulating fully 3D hydraulic fracturing. *Modeling in geomechanics*. 525-557.

Carter, R.D., 1957. Derivation of general equation for estimating the extent of fracture area. *Drilling and Prod. Practice, API*. pp. 261-270.

Cherepanov, G. P., 1967. Crack propagation in continuous media: PMM vol. 31, no. 3, 1967, pp. 476–488. *Journal of Applied Mathematics and Mechanics*. 31(3), 503-512.

Cleary, M. P., and Wong, S. K., 1985. Numerical simulation of unsteady fluid flow and propagation of a circular hydraulic fracture. *International Journal for Numerical and Analytical Methods in Geomechanics*. 9(1), 1-14.

Cope, R. J., Rao, P. V., Clark, L. A., and Norris, P., 1980. Modelling of reinforced concrete behavior for finite element analysis of bridge slabs. *Numerical Methods for non-linear Problems*. 1, 457-470.

Cottrell, C. W., & Al Baker, S. A., 1983. The simulation of water-injection performance for a well with a propagating fracture. *In SPE Annual Technical Conference and Exhibition. Society of Petroleum Engineers*.

Dahi-Taleghani, A., 2009. *Analysis of hydraulic fracture propagation in fractured reservoirs: an improved model for the interaction between induced and nature fractures*. PhD dissertation, The University of Texas at Austin, Austin, Texas.

Damjanac, B., Gil, I., Pierce, M., Sanchez, M., Van As, A., and McLennan, J., 2010. A new approach to hydraulic fracturing modeling in naturally fractured reservoirs. *In 44th US Rock Mechanics Symposium and 5th US-Canada Rock Mechanics Symposium. American Rock Mechanics Association*.

De Borst, R., L. J. Sluys, H-B. Muhlhaus, and Jerzy Pamin., 1993. Fundamental issues in finite element analyses of localization of deformation. *Engineering computations.* 10, no. 2: 99-121

De Vree, J. H. P., W. A. M. Brekelmans, and M. A. J. Van Gils., 1995. Comparison of nonlocal approaches in continuum damage mechanics. *Computers & Structures*. 55.4: 581-588.

Deng, S., Podgorney, R., and Huang, H., 2011. Discrete element modeling of rock deformation, fracture network development and permeability evolution under hydraulic stimulation. *36 the Workshop on Geothermal Reservoir Engineering, Stanford University, Stanford, California.*

Detournay, E., Cheng, A.H.-D., 1993. Fundamentals of poroelasticity. *In: Hudson, J.A. (Ed.), Comprehensive Rock Engineering: Principles, Practices and Projects, vol. 2. Pergamon Press, Oxford, UK*. pp. 113–171.

Detournay, E., 2004. Propagation regimes of fluid-driven fractures in impermeable rocks. *International Journal of Geomechanics*. 4(1), 35-45.

Dyskin, A. V., Sahouryeh, E., Jewell, R. J., Joer, H., and Ustinov, K. B., 2003. Influence of shape and locations of initial 3-D cracks on their growth in uniaxial compression. *Engineering Fracture Mechanics*. 70(15), 2115-2136.

Economides, M. J. and K. G. Nolte, eds. 2000. *Reservoir Stimulation. 3rd ed*. Houston: Schlumberger Educational Services.

Elices, M., Guinea, G. V., Gomez, J., and Planas, J., 2002. The cohesive zone model: advantages, limitations and challenges. *Engineering fracture mechanics*. 69(2), 137-163.

Erdogan, F., Sih, G. C., 1963. On the crack extension in plates under plane loading and transverse shear. *Journal of Fluids Engineering*. 85(4), 519-525.

Feng, Y., and Jin Z., 2009. Thermal fracture of functionally graded plate with parallel surface cracks. *Acta Mechanica Solida Sinica*. 22.5: 453-464.

Fu, P., 2014. *Surface deformation from a pressurized subsurface fracture - problem description*. PowerPoint presentation, Lawrence Livermore National Laboratory.

Gao, H., Ji, B., Jäger, I. L., Arzt, E., and Fratzl, P., 2003. Materials become insensitive to flaws at nanoscale: lessons from nature. *Proceedings of the national Academy of Sciences*, 100(10), 5597-5600.

Gao H, Klein P., 1998. Numerical simulation of crack growth in an isotropic solid with randomized internal cohesive bonds. *Journal of Mechanics, Physics, Solids*. 46(2), 187-218.

Garagash, D., and Detournay, E., 2000. The tip region of a fluid-driven fracture in an elastic medium. *Journal of applied mechanics*. 67(1), 183-192.

Geertsma, J., and De Klerk, F., 1969. A rapid method of predicting width and extent of hydraulically induced fractures. *Journal of Petroleum Technology*. 21(12), 1-571.

Geyer, John F., and S. Nemat-Nasser., 1982. Experimental investigation of thermally induced interacting cracks in brittle solids. *International Journal of Solids and Structures*. 18.4: 349-356.

Ghassemi, A., and Zhang Q., 2004. A transient fictitious stress boundary element method for porothermoelastic media. *Engineering analysis with boundary elements*. 28.11: 1363-1373.

Ghassemi, A., Nygren, A., and Cheng, A., 2008. Effects of heat extraction on fracture aperture: A poro–thermoelastic analysis. *Geothermics*. 37(5), 525-539.

Ghassemi, A., Zhou, X. X., and Rawal, C., 2010. 3D poroelastic analysis of rock failure around a hydraulic fracture. *In 44th US Rock Mechanics Symposium and 5th US-Canada Rock Mechanics Symposium. American Rock Mechanics Association*.

Gidley, J.L., Holditch, S.A., Nierode, D.E., and Veatch Jr., R.W., 1989. Recent advances in hydraulic fracturing. *SPE Monograph Series*, Vol.12, 452 pp

Grebe, J. J., and Stoesser, M., 1935. Increasing crude production 20,000,000 bbl. from established fields. *World Petroleum J*. August, 473-82.

Griffith, A. A., 1921. The phenomena of rupture and flow in solids. *Philosophical transactions of the royal society of london. Series A, containing papers of a mathematical or physical character*. 163-198.

Griffith, A.A., 1924. Theory of rupture. *In: Proceedings of the First International Congress of Applied Mechanics, Delft*. pp. 55-63.

Gupta, A. K., and Akbar, H., 1984. Cracking in reinforced concrete analysis. *Journal of Structural Engineering*. 110(8), 1735-1746.

Hayashi, K., Sato, A., and Ito, T., 1997. In situ stress measurements by hydraulic fracturing for a rock mass with many planes of weakness. *International Journal of Rock Mechanics and Mining Sciences*. 34(1), 45-58.

Huang K., Zhang Z., 2010. Three dimensional element partition method and numerical simulation for fracture subjected to compressive and shear stress. *Engineering Mechanics*, 27(12):51-58. (In Chinese)

Huang, K., and Ghassemi, A., 2011. Modeling 3D hydraulic fracture propagation and Thermal fracturing using virtual multidimensional internal bonds. *Presented at the 36th Workshop on Geothermal Reservoir Engineering, Stanford University, Stanford, California*.

Huang, K., Zhang Z., and Ghassemi A., 2012. Modeling three-dimensional hydraulic fracture propagation using virtual multidimensional internal bonds. *International Journal for Numerical and Analytical Methods in Geomechanics*. 37(13), 2021-2038.

Irwin, G. R., 1957. Analysis of stresses and strains near the end of a crack traversing a plate. *SPIE MILESTONE SERIES MS*. 137, 167-170.

Irwin, G.R., 1948. *Fracture dynamics. Fracturing of Metals*. American Society of Metals, Cleveland, p. 147

Jaeger, J. C., Cook, N. G., and Zimmerman, R., 2009. *Fundamentals of rock mechanics*. John Wiley & Sons.

Ji, L., Settari, A., and Sullivan, R. B., 2009. A novel hydraulic fracturing model fully coupled with geomechanics and reservoir simulation. *SPE Journal*. 14(03), 423-430.

Jirásek, M., 2004. Non-local damage mechanics with application to concrete. *Revue française de génie civil*. 8(5-6), 683-707.

Kachanov, L. M., 1958. Time of the rupture process under creep conditions. *Isv. Akad. Nauk. SSR. Otd Tekh. Nauk*.8, 26-31.

Khristianovic, S. A., and Zheltov, Y. P., 1955. Formation of vertical fractures by means of highly viscous liquid. *In Proceedings of the fourth world petroleum congress, Rome.* 579, p. N586.

Klein, P, Gao H., 1998. Crack nucleation and growth as strain localization in a virtual-bond continuum. *Engineering Fracture Mechanics*. 61(1), 21-48.

Knauss, W. G., 1970. An observation of crack propagation in anti-plane shear. *International Journal of Fracture Mechanics*. 6(2), 183-187.

Kolari, K., 2007. *Damage mechanics model for brittle failure of transversely isotropic solids: Finite element implementation*. VTT Technical Research Centre of Finland.

Kumar, D., 2013. *Development and Validation of Thermo-hydro-mechanical Simulator Model for Enhanced Geothermal Systems*. Ph.D. dissertation, Colorado School of Mines.

Labuz, J. F., Shah, S. P., and Dowding, C. H., 1989. Measurement and description of tensile fracture in granite. *Journal of engineering mechanics*. 115(9), 1935-1949.

Lin, G., Meng, X. G., Cornec, A., and Schwalbe, K. H., 1999. The effect of strength mis-match on mechanical performance of weld joints. *International journal of fracture*. 96(1), 37-54.

Marsden, T.J.R. Hughes, 1983. *Mathematical Foundations of Elasticity*, Prentice-Hall, Englewood Cliffs, NJ.

McClure, M. W. 2012. *Modeling and characterization of hydraulic stimulation and induced seismicity in geothermal and shale gas reservoirs*. Ph.D. dissertation, Stanford University.

McTigue, D. F., 1990. Flow to a heated borehole in porous, thermoelastic rock: Analysis. *Water Resources Research*. 26.8: 1763-1774.

Moes N, Dolbow J, Belytschko T., 1999. A finite element method for crack growth without remeshing. *International Journal for Numerical Methods in Engineering*. 46:131–150.

Murdoch, L. C., and Slack, W. W., 2002. Forms of hydraulic fractures in shallow fine-grained formations. *Journal of Geotechnical and Geoenvironmental Engineering*. 128(6), 479-487.

Nooru-Mohamed, M. B., 1992. *Mixed mode fracture of concrete: an experimental approach*. Ph.D. Thesis, Delft University.

Nordgren, R. P., 1972. Propagation of a vertical hydraulic fracture. *Society of Petroleum Engineers Journal*. 12(04), 306-314.

Nowacki, W., 1976. Dynamic problems of diffusion in solids. *Engineering Fracture Mechanics*. 8(1), 261-266.

Ogden, R. W., 1984. Non-linear elastic deformations. *Engineering Analysis*. 1(2), 119.

Olson, J. E., and Taleghani, A. D., 2009. Modeling simultaneous growth of multiple hydraulic fractures and their interaction with natural fractures. *Hydraulic Fracturing Technology Conference,. SPE*. Vol. 119739.

Park, K., Paulino, G. H., and Roesler, J. R., 2008. Virtual Internal Pair-Bond Model for Quasi-Brittle Materials. *Journal of engineering mechanics*. 134(10), 856-866.

Peirce, A., 2015. Modeling multi-scale processes in hydraulic fracture propagation using the implicit level set algorithm. *Computer Methods in Applied Mechanics and Engineering*. 283, 881-908.

Perkins, T. K., and Kern, L. R., 1961. Widths of hydraulic fractures. *Journal of Petroleum Technology*. 13(09), 937-949.

Pijaudier-Cabot, G., and Bazant, Z. P., 1987. Nonlocal damage theory. *Journal of Engineering Mechanics*. 113(10), 1512-1533.

Rahman, M. M., and Rahman, M. K., 2010. A review of hydraulic fracture models and development of an improved pseudo-3D model for stimulating tight oil/gas sand. *Energy Sources, Part A: Recovery, Utilization, and Environmental Effects*. 32(15), 1416-1436.

Rashid, Y. R., 1968. Ultimate strength analysis of prestressed concrete pressure vessels. *Nuclear engineering and design*. 7(4), 334-344.

Rice, J. R., 1968. A path independent integral and the approximate analysis of strain concentration by notches and cracks. *Journal of applied mechanics*. 35(2), 379-386.

Sasaki, S., 1998. Characteristics of microseismic events induced during hydraulic fracturing experiments at the Hijiori hot dry rock geothermal energy site, Yamagata, Japan. *Tectonophysics*. 289(1), 171-188.

Sesetty, V., Ghassemi, A., 2012. Modeling and analysis of stimulation for fracture network generation. *In Proceedings of the 37th workshop on geothermal reservoir engineering, Stanford University, Stanford, CA*.

Sesetty, V., Ghassemi, A., 2013. Numerical simulation of sequential and simultaneous hydraulic fracturing. *Effective and Sustainable Hydraulic Fracturing*.

Settari, A., and Warren, G. M., 1994. Simulation and field analysis of waterflood induced fracturing. *Proceedings, SPE/ISPM Meeting "Rock Mechanics in Petroleum Engineering", Delft, Aug. 29-31, Balkema Publ., 1994.* Pp. 435-445.

Sih, G. C., 1974. Strain-energy-density factor applied to mixed mode crack problems. *International Journal of fracture*. 10(3), 305-321.

Sneddon, I. N., Elliot, H. A., 1946. The opening of a Griffith crack under internal pressure. Quart. *Appl. Math*, 4(3), 262-267.

Sneddon, I.,1946. The distribution of stress in the neighbourhood of a crack in an elastic solid. *Proceedings of the Royal Society of London. Series A. Mathematical and Physical Sciences*. 187(1009), 229-260.

Tang, C. A., Lin, P., Wong, R. H. C., and Chau, K. T., 2001. Analysis of crack coalescence in rock-like materials containing three flaws-part II: numerical approach. *International Journal of Rock Mechanics and Mining Sciences*. 38(7), 925-939.

Tang, C. A., Liu, H., Lee, P. K. K., Tsui, Y., and Tham, L. G., 2000. Numerical studies of the influence of microstructure on rock failure in uniaxial compression-part I: effect of heterogeneity. *International Journal of Rock Mechanics and Mining Sciences*. 37(4), 555-569.

Tang, C., 1997. Numerical simulation of progressive rock failure and associated seismicity. *International Journal of Rock Mechanics and Mining Sciences*. 34(2), 249-261.

Tarasovs, A., Ghassemi A., 2014. Self-similarity and scaling of thermal shock fractures. *Physical Review E*. 90 (1), 012403-1-6.

Tarasovs, S., Ghassemi A., 2012. On the role of thermal stress in reservior stimulation. *Thirty-seventh Workshop on Geothermal Reservoir Engineering, Stanford University*.

Tarasovs, S., Ghassemi A., 2011. Propagation of a system of cracks under thermal stress. *45th U.S. Rock Mechanics / Geomechanics Symposium, 26-29 June, San Francisco, California*.

Terzaghi, K., 1923. Die Berechnung der Durchlässigkeitsziffer des Tones aus dem Verlauf der hydrodynamischen Spannungserscheinungen Sitzungsber. *Akad. Wiss. (Wien)*, Abt. 2a, 132, pp. 125–138.

Tijssens, M. G. A., Van der Giessen, E., and Sluys, L. J., 2000. Modeling of crazing using a cohesive surface methodology. *Mechanics of Materials*. 32(1), 19-35.

Valkó, Peter, and Michael J. Economides, 1995. *Hydraulic fracture mechanics*. New York, NY: Wiley.

Verde, A., Ghassemi, A., 2013. Efficient Solution of Large-Scale Displacement Discontinuity Problems using the Fast Multipole Method. *Proceedings of the 47th US rock mechanics/geomechanics symposium (American Rock Mechanics Association). San Francisco, CA. 2013*.

Weibull, W., 1951. A statistical distribution function of wide applicability. *J. Appl. Mech.-Trans. ASME.* 18 (3): 293–297.

Weng, X., Kresse, O., Cohen, C. E., Wu, R., and Gu, H., 2011. Modeling of hydraulic-fracture-network propagation in a naturally fractured formation. *SPE Production & Operation*s. 26(04), 368-380.

Wiles, T.D., 1986. *Modeling of hydraulic fracture propagation in a discontinuous rock mass using displacement discontinuity method*. PhD. Thesis, University of Toronto, 168 pp.

Willis, J. R., 1967. A comparison of the fracture criteria of Griffith and Barenblatt. *Journal of the Mechanics and Physics of Solids*. 15(3), 151-162.

Witherspoon, P. A., Wang, J. S. Y., Iwai, K., and Gale, J. E., 1980. Validity of cubic law for fluid flow in a deformable rock fracture. *Water Resources Research*. 16(6), 1016-1024.

Wright, C.A., and Tanigawa, J.J., 1994. Real-time and post-frac 3D analysis of hydraulic fracture treatments in geothermal reservoirs. *nineteenth workshop on geothermal reservoir engineering, Stanford University, Stanford, CA*.

Xu, X. P., Needleman, A., 1994. Numerical simulations of fast crack growth in brittle solids. *Journal of the Mechanics and Physics of Solids*. 42(9), 1397-1434.

Zhang, Z., 2013. Discretized virtual internal bond model for nonlinear elasticity. *International Journal of Solids and Structures*. 50(22), 3618-3625.

Zhang Z., Ge X., 2005. A new quasi-continuum constitutive model for crack growth in an isotropic solid. *European Journal of Mechanics - A/Solids*. 24(2): 243-252.

Zhang Z., Ge X., 2006. Micromechanical modelling of elastic continuum with virtual multi-dimensional internal bonds. *International Journal for Numerical Methods in Engineering*. 65: 135-146.

Zhang, Z., Chen, Y., 2008. Numerical simulation for fracture propagation of multi-cracked rock materials using virtual multidimensional internal bonds. *Chinese Journal of Geotechnical Engineering*. 10, 015.

Zhang, Z., Chen Y., 2009. Novel numerical approach to jointed rock mass simulation: Element partition method. *Chinese Journal of Geotechnical Engineering*. 31(12), 1858-1865.

Zhang, Z., Chen, Y., 2009. Simulation of fracture propagation subjected to compressive and shear stress field using virtual multidimensional internal bonds. *International Journal of Rock Mechanics and Mining Sciences*. 46(6), 1010-1022.

Zhang, Z., Ge X., 2005. Micromechanical consideration of tensile crack behavior based on virtual internal bond in contrast to cohesive stress. *Theoretical and Applied Fracture Mechanics*. 43(3): 342-359.

Zhang, Z., Wang, D., Ge, X., 2013. A novel triangular finite element partition method for fracture simulation without enrichment of interpolation. *International Journal of Computational Methods*. 10(04).

Zhou, X., Ghassemi A., 2009. Finite element analysis of coupled chemo-poro-thermo-mechanical effects around a wellbore in swelling shale. *International Journal of Rock Mechanics and Mining Sciences.* 46.4: 769-778.

Zhang, Z., Zheng, H., Ge, X., 2013. Triangular element partition method with consideration of crack tip. *Science China Technological Sciences*. 56(8), 2081-2088.

Zoback, M. D., Healy, J. H., 1992. In situ stress measurements to 3.5 km depth in the Cajon Pass scientific research borehole: Implications for the mechanics of crustal faulting. *Journal of Geophysical Research: Solid Earth* (1978–2012), 97(B4), 5039-5057.